Innovative Pulsar Searching Techniques

or

Fantastic Pulsars and How to Find Them

Dissertation

zur

Erlangung des Doktorgrades (*Dr. rer. nat.*)

der

Mathematisch–Naturwissenschaftlichen Fakultät

der

Rheinische Friedrich–Wilhelms–Universität Bonn

vorgelegt von

Andrew David Cameron

aus

Sydney, Australia

Bonn 2018

Angefertigt mit Genehmigung der Mathematisch–Naturwissenschaftlichen Fakultät
der Rheinische Friedrich–Wilhelms–Universität Bonn

1. Referent: Prof. Dr. Michael Kramer [Supervisor]
2. Referent: Prof. Dr. Norbert Langer [2nd referee]
Tag der Promotion: 05.06.2018
Erscheinungsjahr: 2018

Diese Dissertation ist auf dem Hochschulschriftenserver der ULB Bonn unter
http://hss.ulb.uni-bonn.de/diss_online elektronisch publiziert

RHEINISCHE FRIEDRICH–WILHELMS–UNIVERSITÄT BONN

Abstract

by Andrew David Cameron

for the degree of

Doctor rerum naturalium

Pulsars are rapidly rotating, highly magnetised neutron stars which emit beams of electromagnetic radiation from their magnetic poles, most commonly in the radio spectrum. These massive and extremely compact objects have emerged as fantastic physical tools suitable to a wide variety of scientific applications, perhaps the most important being their role in testing and constraining of General Relativity and other alternative theories of gravity. This thesis presents the results of an ongoing search for new and scientifically-interesting pulsars in the High Time Resolution Universe South Low Latitude (HTRU-S LowLat) pulsar survey, and includes the discovery of PSR J1757−1854, the first relativistic binary pulsar to be discovered as part of this survey. Also presented in this thesis is a detailed study of the Fast Folding Algorithm (FFA), an additional pulsar searching technique capable of overcoming some of the limitations of more commonly used search techniques such as the Fast Fourier Transform (FFT), presenting a new avenue by which further pulsars discoveries may be made.

Chapter 1 of this thesis summarises the essential ideas surrounding the formation, structure and behaviour of pulsars in the radio regime and their interaction with the interstellar medium (ISM). Also discussed are some of the specific scientific investigations to which pulsars have been applied and which motivate ongoing pulsar searches, with particular emphasis on the milestones achieved to date in the study of gravitational theories through the use of relativistic binary pulsars. Chapter 2 then details the fundamentals of standard pulsar searching methodology, with extra attention given both to binary search techniques and the basic principles behind the FFA, a time-domain pulsar searching technique. A summary is also provided of the techniques involved in pulsar timing, one of the primary tools by which scientific information is extracted from discovered pulsars, with an additional focus once again given to the timing of relativistic binary pulsars. In order to set the context of the HTRU-S LowLat pulsar survey, Chapter 2 concludes with a summary of previous and current pulsar searches conducted of the Galactic-plane region.

The HTRU-S LowLat pulsar survey, along with its particular searching and processing methodology, is introduced in Chapter 3. This survey, conducted with the Parkes 64-m Radio Telescope in Australia, covers a region between $-80^\circ < l < 30^\circ$ and $|b| < 3.5^\circ$ and was conducted with the specific goal of dis-

covering new relativistic binary pulsars which can be applied to future tests of gravitational theories. To date, approximately 79 % of the survey has been processed through a novel 'partially-coherent segmented acceleration search' pipeline designed to optimise the detection of tight binary systems with short orbital periods. From the $\sim$ 44 % of the survey processed for this thesis, a total of 40 new pulsar discoveries are reported, at least 7 of which are in binary systems. Selected highlights include PSR J1618−4624, a millisecond pulsar (MSP) orbiting a carbon-oxygen-white dwarf (CO-WD) companion which, with an orbital period of 1.78 d and a spin period of only 5.93 ms, presents a challenge to current binary formation models. Two further MSPs with helium-white dwarf (He-WD) companions, PSRs J1537−5312 and J1547−5709, are also reported, along with a fourth MSP, the black widow system PSR J1745−23. Additionally, PSRs J1812−15 and J1831−04 are a pair of $\sim$ 1 s, nulling/intermittent pulsars which show evidence of acceleration, indicating possible binary systems. PSR J1706−4434 meanwhile exhibits glitching behaviour, while PSR J1653−45 is an eclipsing binary system with a likely orbital period on the order of months to years, appearing similar to the previously known PSR B1259−63. Finally, the full set of 100 pulsars discovered to date in the HTRU-S LowLat survey is compared to the background population of Galactic-plane pulsars, indicating that HTRU-S LowLat has uncovered a population of older, lower-luminosity pulsars. Evaluations of the survey yield and performance are also presented, indicating that while the $\sim$ 44 % of the HTRU-S LowLat survey presented in this thesis has been processed to a standard consistent with the earlier processing conducted by Ng et al. (2015), the survey appears to fall below its expected pulsar yield by $\sim$ 25 % in the case of young, slow pulsars and by as much as $\sim 150 - 250$ % in the case of MSPs.

The flagship discovery of the HTRU-S LowLat survey, PSR J1757−1854, is presented in Chapter 4. A 21.5-ms pulsar in a 4.4-h orbit around a neutron star (NS) companion, this double neutron star (DNS) system exhibits some of the most extreme relativistic qualities of any known radio pulsar, including the strongest observed relativistic effects due to gravitational wave (GW) damping. PSR J1757−1854 represents precisely the type of pulsar the HTRU-S LowLat survey and its search pipeline were designed to find. A 1.6-yr, multi-frequency, multi-telescope timing campaign has resulted in the measurement of five post-Keplerian (PK) parameters, allowing for three immediate tests of gravitational theories, and also allowing for the masses of the pulsar ($m_{\rm p} = 1.3384(9)\,{\rm M}_\odot$) and its companion neutron star ($m_{\rm c} = 1.3946(9)\,{\rm M}_\odot$) to be separated. The larger mass of the companion neutron star and the high orbital eccentricity provide important clues regarding the system's binary formation. Timing simulations suggest that a 3-σ measurement of both the contribution of Lense-Thirring precession to the rate of change of the semi-major axis as well as the relativistic deformation of the orbit will be possible within $\sim 7 - 9$ years. Both of these

quantities have remained poorly constrained in other relativistic binary pulsars, including both the Hulse-Taylor pulsar PSR B1913+16 and the Double Pulsar PSR J0737−3039, such that PSR J1757−1854 stands out as a unique laboratory for new tests of gravitational theories, particularly general relativity (GR).

Chapter 5 presents an in-depth study of the behaviour of the FFA, an alternative pulsar searching technique to the FFT. Although the FFT forms the backbone of most pulsar-searching efforts, including the pipeline currently employed on the HTRU-S LowLat survey, weaknesses in the FFT (including a susceptibility to red noise) leave it insensitive to pulsars with long rotational periods ($P > 1\,\mathrm{s}$). This sensitivity gap may result in a biased understanding of the true underlying pulsar population. The FFA, a coherent time-domain search technique, has the potential to overcome some of these biases, although many aspects of the behaviour of this search technique remain poorly understood, including its responsiveness to variations in pulse shape and to the presence of red noise. This chapter documents an extensive evaluation of the behaviour of the FFA with respect to variations in noise content and pulse shape using a custom software package FFANCY, including a comparison of the performance of the FFA against the FFT on real data taken from the HTRU-S LowLat survey. While the superiority of the FFA to the FFT in the long-period regime is demonstrated in both simulated and real data, there remains significant room for improvement in terms of the implementation and evaluation of the FFA and its evaluation algorithms.

Lastly, Chapter 6 closes with a summary of the most important scientific results derived as part of this thesis project. Additional discussion is given to the future of the HTRU-S LowLat survey, including improvements to be included in future survey re-processing and the next steps required in the further scientific exploitation of the pulsar discoveries reported in this thesis. Future goals for PSR J1757−1854, and their reliance on the next generation of radio telescopes and instrumentation, are also discussed. An overview is also given of the future role of the FFA and its ongoing development and implementation as part of the next generation of pulsar surveys, where it is already breaking ground in the discovery of long-period pulsars. Finally, the chapter concludes with a brief summary of the future telescopes and pulsar surveys that will be the drivers of pulsar science over the coming decades.

To my parents, John and Wendy.

The powerful play goes on, and you may contribute a verse.

Walt Whitman,
O Me! O Life!

Acknowledgements

This thesis, in all of its volume, constitutes the end result of the past three and a half years of my life, and it would not have been possible without the help and support of countless individuals. Naming names is always a slightly dangerous exercise, but I have done my best to ensure that these acknowledgements are as complete as possible.

First thanks go to my advisor, David Champion, who has been a constant source of support and guidance throughout every stage of my PhD. He has fueled my passion for science and the study of pulsars, inspired me to tackle new problems that I thought were beyond my limits, and has tolerated the often-excessive demands I placed on his time and attention. He has helped to shape me into the professional academic I now graduate as, and I feel grateful to count him as a friend as well as a colleague.

Significant thanks also go to my supervisor, Michael Kramer, who has played a similarly supportive role throughout the course of this project. He has backed and defended me at every stage of my professional development, given me multiple opportunities to gain a wide variety of academic experiences around the world, and I feel humbled by the responsibility he has entrusted in me to both complete the processing of the HTRU-S LowLat pulsar survey and to lead the study of its flagship discovery, the relativistic binary PSR J1757−1854.

Wider acknowledgements are owed to the staff of the MPIfR Fundamental Physics group, from whom I have learned so much and who have made this such a welcoming place to work throughout my time in Germany. Particular thanks go to Ewan Barr, Paulo Freire, Alessandro Ridolfi, Thomas Tauris and Norbert Wex, who collectively have worked as some of my closest collaborators and have shared with me a great deal of their expertise. Additional thanks also go to Ramesh Karuppusamy and Alex Kraus for their patience and assistance during my many observations with the Effelsberg telescope; to Laura Spitler and James McKee for their role as internal referees on several of my publications; and to Kira Kühn, for her constant optimism and helpfulness no matter what my problem was. To the students of the IMPRS who have been with me on this journey, I don't dare try to name all of you (you know who you are), however I do wish to specifically thank my office mates of the past several years, Eleni Graikou, Nataliya Porayko and Jason Wu, for having been such good company and for having put up with my many eccentricities for so long.

To save this section from becoming as lengthy as the rest of this thesis, the remaining academic acknowledgements are presented in a rapid-fire format. Thanks go to Emmanouil Angelakis, Rainer Mauersberger and Simone Pott of the IMPRS; to Gerrit Schellenberger, my IMPRS Student co-Representative; to Olaf Wucknitz, Ralph Eatough, Norbert Langer and Cees Bassa, the extra members of my Thesis Advisory Committee; to Alessandro Ridolfi (again) and Cherry Ng for the time spent reviewing and commenting on this thesis; to Marina Berezina and Eleni Graikou (again) for additional assistance with the Effelsberg telescope; to Barbara Menten and Tuyet-Le Tran for helping me to navigate the bureaucracy of this strange, new country; to the RZ staff

of both the MPIfR and the MPCDF for their constant assistance and understanding; to the members of the HTRU Collaboration for their ongoing support, as well as the members of the P860 and P789 Parkes observing projects for the many, many hours spent in observing the pulsars reported in this thesis; to Natalia Lewandowska, Duncan Lorimer, Ryan Lynch and Maura McLaughlin for their assistance with observations at the GBT; to Vladislav Kondratiev and Patrick Lazarus for their assistance in the portion of this research involving the FFA; and finally to Cherry Ng (again), for having given me such a fantastic starting point to work from and for helping me to find my feet back when this project first began.

Lastly, there are a number of personal acknowledgements to include. Thanks go to Thomas Weiß and the members of the Taekwon-Do Center Bonn; to my friends at the Köln Stammtisch for their company and patience with my terrible German language skills; to the staff of the English Shop Bonn for helping this town to feel just a little bit more like home; and to Nico and Tanja Buchmühlen, my oldest and best friends on this side of the world, along with Karsten Auchter, Mario Groß and so many, many others from that community who have lent me their support and friendship over the past several years. Finally, I wish to express my heartfelt thanks to my family, John, Wendy, Amy and Valerie Cameron for their ongoing support and encouragement throughout every crazy life change I've put myself through over the past several years; to Pauline Pounds, without whom I might never have found the courage to pursue my PhD in the first place and who has been a constant friend throughout every hardship I have been through in this project; and to my partner Robbie Spackman, who has been both my rock and my light at the end of the tunnel as I prepare to move back to Australia.

Contents

List of Figures

List of Tables

Nomenclature

Frequently used symbols

a / $a_{\rm orb}$	Orbital acceleration
$\dot{a}$	First derivative of orbital acceleration (jerk)
$a_{\rm p}$	Semi-major axis
$A_{\rm T}$	True anomaly
b	Galactic latitude
B	Bandwidth
$B_{\rm surf}$	Characteristic dipole surface magnetic field strength
c	Speed of light
d	Distance
e	Orbital eccentricity
E	Total pulse energy *or* pulse fluence
$\dot{E}$	Spin-down luminosity
f	Mass function *or* electromagnetic frequency
$f_{\rm c}$	Central observing frequency
$\Delta f_{\rm chan}$	Channel bandwidth
G	Gravitational constant *or* antenna gain
h_3	Orthometric amplitude
i	Orbital inclination angle
I	Moment of inertia
l	Galactic longitude
L	Luminosity
$m_{\rm c}$	Companion mass
$m_{\rm p}$	Pulsar mass
M	Total binary system mass
n	Braking index
$n_{\rm bin}$	Number of profile bins
$n_{\rm bits}$	Number of bits in data digitisation
$n_{\rm chan}$	Number of channels
$n_{\rm e}$	Electron number density
$n_{\rm p}$	Number of polarisation channels
$n_{\rm samp}$ / N	Number of samples
$n_{\rm FFT}$	Number of samples in FFT
P	Spin period
$\dot{P}$	First spin period derivative
P_0	FFA base period *or* pulsar birth period
$P_{\rm b}$	Orbital period
$\dot{P}_{\rm b}$	First derivative of orbital period

$P_{\rm thres}$	False-alarm power threshold
r	Shapiro range parameter
$r_{\rm orb}$	Ratio of data length over orbital period ($t_{\rm int}/P_{\rm b}$)
R	Neutron star radius
$R_{\rm S}$	Schwarzchild radius
s	Shapiro shape parameter *or* segment group number
S	Flux density *or* pulse height
$S_{\rm min}$	Characteristic minimum detectable flux density
S/N	Signal to noise ratio
$\mathrm{S/N}_{\rm min}$	Characteristic minimum detectable signal to noise ratio
$\Delta t_{\rm chan}$	Intrachannel smearing
$t_{\rm int}$	Integration time
$t_{\rm samp}$	Time sampling interval
T_0	Epoch of periastron
$T_{\rm asc}$	Epoch of ascending node passage
$T_{\rm rec}$	Temperature of the receiver
$T_{\rm sky}$	Temperature of the sky
$T_{\rm sys}$	Temperature of the observing system ($T_{\rm rec} + T_{\rm sky}$)
u	Eccentric anomaly
$V_{\rm T}$	Transverse velocity
$V_{\rm l}$	Line-of-sight velocity
W / w	Pulse width
W_{10}	Pulse width at 10 % of the pulse height
W_{50}	Pulse width at 50 % of the pulse height
x	Projected semi-major axis
$\dot{x}_{\rm LT}$	Lense-Thirring contribution to the rate of change of x
α	Right ascension (R.A.) or the angle between the magnetic and rotational axes
β	Digitisation degradation factor
γ	Gravitational redshift and time-dilation parameter (Einstein delay)
Δ_γ	Timing residual contribution of γ
δ	Declination (Dec.) or pulsar duty cycle
δ_θ	Relativistic orbital deformation
Δ_{δ_θ}	Timing residual contribution of δ_θ
θ	Angular offset
μ	Proper motion
ν	Spin frequency
π	Parallax
σ	Standard deviation
$\sigma_{\rm gauss}$	Gaussian equivalent sigma
ς	Orthometric ratio
$\tau_{\rm c}$	Characteristic age
$\tau_{\rm s}$ / $\tau_{\rm sc}$	Scattering time scale
ϕ	Rotational *or* pulse phase

φ	Orbital phase
ω	Longitude of periastron
$\dot{\omega}$	Relativistic rate of periastron advance
Ω	Longitude of ascending node *or* angular frequency
Ω_{SO}	Rate of geodetic precession

Numerical constants

π	$= 3.14156$
$1\,\mathrm{rad}$	$= 57.296°$
e	$= 2.7183$

Physical constants

Boltzmann's constant	$k_{\mathrm{B}} = 1.381 \times 10^{-16}\,\mathrm{erg\,K^{-1}}$
Gravitational constant	$G = 6.670 \times 10^{-11}\,\mathrm{m^3\,kg^{-1}\,s^{-2}}$
Speed of light	$c = 2.9979 \times 10^{8}\,\mathrm{m\,s^{-1}}$

Astronomical constants

Astronomical unit ($1\,\mathrm{AU}$)	$= 1.496 \times 10^{11}\,\mathrm{m}$
Earth mass ($1\,\mathrm{M_\oplus}$)	$= 5.974 \times 10^{24}\,\mathrm{kg}$
Jansky ($1\,\mathrm{Jy}$)	$= 10^{26}\,\mathrm{W\,m^{-2}\,Hz^{-1}}$
Julian light year ($1\,\mathrm{ly}$)	$= 9.460730472 \times 10^{15}\,\mathrm{m}$
Julian year ($1\,\mathrm{yr}$)	$= 3.15576 \times 10^{7}\,\mathrm{s}$
Parsec ($1\,\mathrm{pc}$)	$= 3.086 \times 10^{16}\,\mathrm{m}$
Solar mass ($1\,\mathrm{M_\odot}$)	$= 1.989 \times 10^{30}\,\mathrm{kg}$
Solar radius ($1\,\mathrm{R_\odot}$)	$= 6.960 \times 10^{8}\,\mathrm{m}$
$\mathrm{T_\odot}$	$= 4.925490947\,\mu\mathrm{s}$

Frequently used acronyms

ADC	Analogue-to-digital converter
ANU	Australian National University
ATNF	Australia Telescope National Facility
AXP	Anomalous X-ray pulsar
BCGS	Bonn-Cologne Graduate School of Physics and Astronomy
BH	Black hole
BPSR	The Berkeley Parkes Swinburne Recorder
CAASTRO	ARC Centre of Excellence for All-sky Astrophysics
CASPSR	The CASPER Parkes Swinburne Recorder
CDF	Cumulative distribution function
CO-WD	Carbon-oxygen white dwarf
CSIRO	Commonwealth Scientific and Industrial Research Organisation

DFB	Digital filter bank
DFT	Discrete Fourier transform
DM	Dispersion measure
DNS	Double neutron star
EFF	The 100-m Effelsberg Radio Telescope
EOS	Equation of state
FAST	Five-hundred-meter Aperture Spherical Telescope
FFA	Fast Folding Algorithm
FFT	Fast Fourier Transform
FPGA	Field-programmable gate array
FRB	Fast radio burst
FWHM	Full width at half maximum
GBT	The 100-m Robert C. Byrd Green Bank Telescope
GPS	Global Positioning System
GR	General relativity
GW	Gravitational waves
H-OH	Parkes H-OH 21-cm receiver
He-WD	Helium white dwarf
HMXB	High-mass X-ray binary
HTRU	The High Time Resolution Universe pulsar survey
HTRU-S LowLat	The High Time Resolution Universe South Low Latitude pulsar survey
IGM	Intergalactic medium
IMPRS	International Max Planck Research School
IMXB	Intermediate-mass X-ray binary
INAF	Istituto Nazionale di Astrofisica
ISM	Interstellar medium
JBO	The 76-m Lovell Telescope at the Jodrell Bank Observatory
KS	Kolmogorov-Smirnoff
LAT	Large Area Telescope
LIGO	Laser Interferometer Gravitational-Wave Observatory
LGM	Large Magellanic cloud
LMXB	Low-mass X-ray binary
LNA	Low noise amplifier
LO	Local oscillator
MAD	Median absolute deviation
MB20	Parkes 21-cm multibeam receiver
MJD	Modified Julian date
MPCDF	Max Planck Computing and Data Facility
MPIfR	Max-Planck-Institute für Radioastronomie
MS	Main sequence
MSP	Millisecond pulsar
NCI	National Computational Infrastructure
NF	Nulling fraction

NS	Neutron star
PALFA	Pulsar Arecibo L-band Feed Array survey
PDF	Probability distribution function
PFB	Polyphase filter bank
PICS	Pulsar image-based classification system
PK	Post-Keplerian
PKS	The Parkes 64-m Radio Telescope
PMPS	Parkes Multibeam Pulsar Survey
PSR	Pulsar
PSRCAT	ATNF Pulsar Catalogue
PTA	Pulsar timing array
RF	Radio frequencies
RFI	Radio frequency interference
RMS	Root mean square
RRAT	Rotating radio transient
SGR	Soft gamma repeaters
SKA	The Square Kilometre Array
SMC	Small Magellanic cloud
SNR	Supernova remnant
SSB	Solar system barycenter
S/N	Signal to noise ratio
SUPERB	Survey for Pulsars and Extragalactic Radio Bursts
TAI	International Atomic Time
TCB	Barycentric Coordinate Time
TDB	Barycentric Dynamical Time
TOA	Time of arrival
TOV	Tolman-Oppenheimer-Volkoff limiting mass
TT	Terrestrial Time
UTC	Coordinated Universal Time
UWB	Ultra-wideband receiver
WD	White dwarf

Chapter 1

Pulsars: An introduction

First discovered in 1967 as part of the serendipitous observation of a regularly pulsing radio signal by Antony Hewish and Jocelyn Bell (Hewish et al., 1968), pulsars are rapidly-rotating, highly-magnetised neutron stars (NSs) which emit beams of electromagnetic radiation (typically in the radio spectrum) along their magnetic axis. As they rotate, their lighthouse-like beams are observed as regular pulses of emission as they cut the line of sight between the pulsar and Earth. While individual pulses exhibit a great deal of variability (see e.g. Lorimer, D. R. and Kramer, M., 2005), when averaged over hundreds or thousands of pulses they produce a stable *pulse profile* which is more or less unique to each individual pulsar, providing one of the fundamental units of information by which pulsars are studied. An example of a pulse profile is provided in Figure 1.1.

In the intervening 50 years since their discovery, the field of pulsar astronomy has flourished, with over 2600 pulsars having been discovered as of the writing of this thesis[1]. As our body of knowledge of these sources has increased, pulsars have emerged as powerful physical tools, capable of probing multiple aspects of fundamental physics. This chapter presents a brief introduction to the subject of pulsars, including the fundamentals of their formation, structure and observed phenomenology, with a focus on their behaviour in the radio spectrum. Attention is given to the scientific applications of pulsars, with particular emphasis on the critical role of binary pulsars as laboratories capable of providing some of the most constraining strong-field tests to date of multiple theories of gravity, the most important being general relativity (GR).

Contents

[1] As per the ATNF Pulsar Catalogue (PSRCAT; Manchester et al., 2005), available at http://www.atnf.csiro.au/people/pulsar/psrcat

1.1 Historical context and motivation

1.1.1 Milestones of pulsar astronomy

The discovery of the first pulsar, PSR B1919+21, was made in 1967 at the Mullard Radio Astronomy Observatory (Hewish et al., 1968). Initially identified as a regular radio pulsation with a period of approximately 1.34 s, the *pulsar* (a portmanteau of 'pulsing star') was quickly recognised as an extra-terrestrial source due to its localised on-sky position, with a further lack of measurable parallax indicating that it was located beyond the solar system. This, along with the identification of similar signals elsewhere on the sky shortly after the initial discovery of PSR B1919+21, suggested the discovery of a new class of astrophysical object.

The rapid nature of the radio pulsations suggested that pulsars must be compact, with upper limits on their physical sizes being derived from the light-travel time across their pulsed emission (Hewish et al., 1968). This idea was reinforced by the discovery of both the Crab and Vela pulsars (Staelin & Reifenstein, 1968; Large et al., 1968a) which, rotating at much faster rates of 33 ms and 89 ms respectively, significantly further constrained the physical dimensions of the source objects. Pulsars were therefore hypothesised to consist of either a rotating white dwarf (WD) or a rotating NS, the collapsed core of a post-supernova star. The idea of a NS had first been proposed by Baade & Zwicky (1934), although no direct evidence of their existence had previously been found. Work conducted by Pacini (1967) and Gold (1968) both before and after the discovery of PSR B1919+21 laid a solid foundation in favour of the current pulsar NS model, which is further detailed in Section 1.2.

Since this initial discovery, a number of significant milestones have marked the development of pulsar astronomy throughout the years. The following, while not intended to be a comprehensive list, details some of the major developments of the past 50 years:

- **The first binary pulsar.** Identified in 1974 as part of a survey by the 305-m Arecibo Telescope, PSR B1913+16 Hulse & Taylor (1975a), also known as the 'Hulse-Taylor' pulsar after its discoverers Russel Hulse and Joseph Taylor, was the first example of a pulsar in a binary system. The 59-ms pulsar was determined to be in a ~ 7.75-h, highly-eccentric ($e = 0.62$) orbit around a likely NS companion,

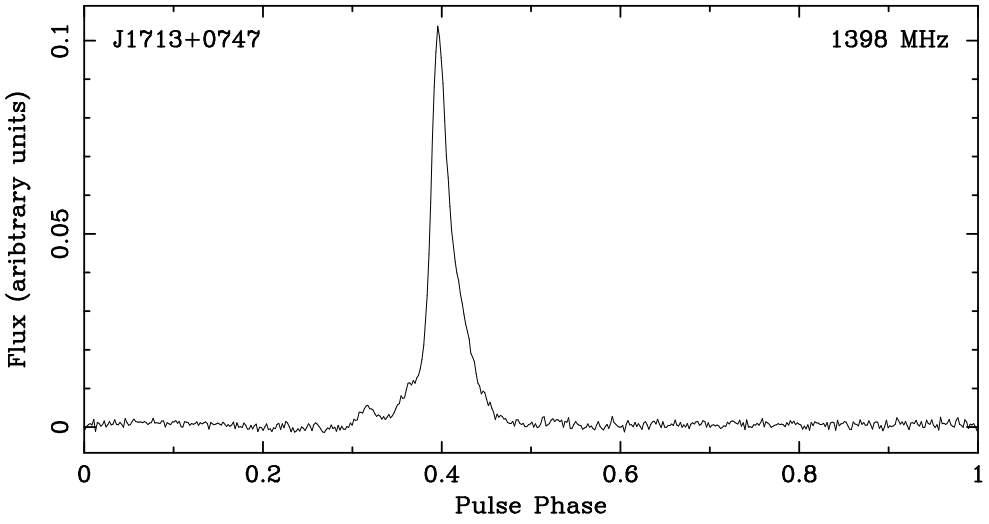

Figure 1.1: An example of a pulsar profile, in this case the profile of PSR J1713+0747, which has a rotational period of 4.57 ms. With an integration time of just over 2 min, this profile represents the average of $\sim 2.8 \times 10^4$ individual pulses.

also making the system the first example of a double neutron star (DNS) binary system. The discovery of the PSR B1913+16 shed light on multiple areas of investigation, including models of stellar evolution and pulsar formation.

- **The first millisecond pulsar (MSP).** This pulsar, PSR B1937+21, was discovered in 1982 by Backer et al. (1982) after suspicions arose about the nature of a compact, steep spectrum, scintillating radio source in the Vulpecula constellation. A series of observations conducted once again using Arecibo discovered the presence of a 1.56-ms (642-Hz) pulsar, representing the discovery of an entirely new class of pulsar, with an increased degree of rotational stability (see Section 1.4). The discovery of such a rapidly-rotating pulsar posed a number of challenges with regard to models of pulsar formation and evolution (see e.g. Shapiro et al., 1983; Taylor & Stinebring, 1986). PSR B1937+21 held the record for the fastest rotating pulsar until 2006, when it was surpassed by the 1.40-ms (716-Hz) pulsar PSR J1748−2446ad (Hessels et al., 2006).

- **The discovery of globular cluster and extragalactic pulsars.** While the typically low luminosities of the vast majority of pulsars have limited their discoverability to within the Milky Way Galaxy, a handful of pulsars have been discovered at greater distances. The first pulsar to be discovered in a globular cluster, PSR B1821−24A, was discovered in 1987 in the globular cluster M28 (Lyne et al., 1987), again following speculation regarding the identity of compact, steep spectrum radio source already identified within the cluster. According to PSRCAT, as of October 2017 a total of 145 pulsars are known to be associated with various globular clusters. Pulsars have also been identified further afield in

both the Large and Small Magellanic Clouds (LMC and SMC), the first being PSR B0529−66, a 0.976-s pulsar detected in the LMC (McCulloch et al., 1983). PSRCAT lists a total of 29 pulsars which have been identified in either the SMC or LMC as of October 2017. These discoveries not only improve our understanding of the pulsar luminosity distribution, but can also be used to inform astrometry and to probe the local Intergalactic Medium (IGM). Additionally, a handful of pulsar and pulsar candidates emitting in X-rays (the result of an accretion process from a binary companion) have been discovered in much more distant neighbouring galaxies, including M82 (Bachetti et al., 2014), M31 (Zolotukhin et al., 2017), NGC 5097 (Israel et al., 2017a) and NGC 7793 (Israel et al., 2017b).

- **The discovery of the first exoplanets.** Although the vast majority of exoplanet discoveries have been made using optical techniques, including spectral line analysis and planetary transit observations (Ollivier & Maurel, 2014), the *first* detection of exoplanets was made in 1992 via a pulsar timing analysis (see Section 2.6) of the 6.22-ms pulsar PSR B1257+12 (Wolszczan & Frail, 1992; Wolszczan, 1994). The system is home to three planetary objects of masses 3.4, 2.8 and 0.015 $M_\oplus$ which were detected as their orbits exerted a modulating influence on the arrival times of each pulse from the pulsar (see Section 2.6.3), demonstrating the power of the measurement precision achievable using pulsar timing techniques.

However, some of the most critical milestones in pulsar astronomy have been in relation to their applicability to the study of gravitational theories. For example, while it was the discovery of PSR B1919+21 which first earned Antony Hewish[2] a share of the 1974 Nobel Prize in Physics[3], it was not until the discovery of the Hulse-Taylor pulsar PSR B1913+16 and its demonstration of the existence of gravitational waves (GW) that pulsar astronomers were once again awarded the honour in 1993[4]. In fact, the study of gravitational theories (with particular emphasis on GR) through pulsars has emerged as one of their most fundamental applications and, as further discussed in Chapters 3 and 4, forms one of the primary motivations of this thesis. Therefore, the precise manner in which pulsars can be utilised to perform these tests, along with some the key achievements made in this regard, is summarised in the following section.

1.1.2 Testing gravity with pulsars: a fundamental application

Einstein's theory of GR has been the paradigm of gravitational theories for over a century, having been formally put forward in 1915 (Einstein, 1915a). Throughout that time, it has been subject to multiple tests designed to investigate the extent of the theory's predictive power. Initially, these tests consisted only of those in the 'quasi-stationary weak-field' regime of gravity (Wex, 2014), a description which includes the gravitational conditions encountered in our own solar system. Einstein himself proposed

[2]With the unfortunate exclusion of Jocelyn Bell
[3]https://www.nobelprize.org/nobel_prizes/physics/laureates/1974/press.html
[4]https://www.nobelprize.org/nobel_prizes/physics/laureates/1993/press.html

the first three so-called 'classical' tests of GR (Einstein, 1916). The first test required the theory to correctly account for the perihelion advance of Mercury (as well as other planetary bodies), something which previous Newtonian theories could not account for and which Einstein himself demonstrated that GR could (Einstein, 1915b). The second test describes the gravitational redshift expected as a consequence of the equivalence principle, caused by light having to escape from the gravitational field of its progenitor star. The third test describes the curvature of light around a gravitational body, which was first (crudely) demonstrated in the solar eclipse of 1919 (Dyson et al., 1920). A more recent fourth test proposed by Shapiro (1964) additionally accounts for the predicted time of the delay (the 'Shapiro delay') caused by both the curved path and the time dilation experienced within the gravitational field of the bending mass (see Section 2.6.3.3). To date, GR has continued to pass all four classical tests as well as multiple others in the weak-field regime, even with recent advances in technology allowing for considerably higher measurement precision (Wex, 2014; Will, 2014).

Pulsars, specifically those found in binary systems, allow for tests of gravity to be conducted in a new regime, the 'quasi-stationary strong-field' regime (see e.g. Wex, 2014), in which the masses involved move at speeds considerably lower than the speed of light but are themselves strongly self-gravitating (a condition which, as shown in Section 1.2.2, NSs satisfy). Pulsars are particularly advantageous in this regard, as their regular clock-like pulsations and rotational stability allow for the extraction of precise information regarding the orbits in which they are found (see Section 2.6). Furthermore, despite the unrivaled success of GR as a theory over its 100-yr lifespan, it is unlikely that the theory is a complete description of gravity (e.g. GR fails to adequately explain the role of gravity in quantum mechanics). Therefore, as well as testing GR to uncover its predictive limits, binary pulsars can also be used to test alternative theories of gravity which, while agreeing with GR in the weak-field regime, diverge from it in the strong-field regime and may yet surpass GR's predictive power under sufficiently-extreme conditions (for a review of these theories and the tests applicable to them, see Berti et al. (2015)).

Some of the tests to which binary pulsars are suited, and which are specifically related to the scientific content of this thesis, are described below. It should be noted that in addition to these tests, pulsars are also capable of testing gravitational theories through the use of pulsar timing arrays (PTAs), which are covered separately in Section 1.5.

1.1.2.1 Mass-mass tests and the existence of gravitational waves

In order to exploit the orbits of binary pulsars to test different theories of gravity, a parameterised post-Keplerian (PPK) formalisation is used, which describes the relativistic effects encountered in a binary pulsar system in a theory independent fashion (Damour & Taylor, 1992). This formalisation characterises the observable relativistic effects as a set of measurable post-Keplerian (PK) parameters, for which each theory of gravity possesses its own mathematical expression as a function of the masses of the two binary objects. These parameters and their expressions under GR are described

in more detail in Section 2.6.3.3, but in brief, they include (among others) the rate of periastron advance $\dot{\omega}$, the 'Einstein' delay γ (which describes the influence of gravitational redshift and second-order Doppler time-dilation effects), the rate of orbital period decay $\dot{P}_\mathrm{b}$, and the Shapiro delay[5] parameters r and s. Accurate measurements of any two of these parameters allow for the masses of the pulsar and its binary companion to be fixed under a particular theory of gravity. Each additional parameter then allows for a check of self-consistency to be conducted by determining if the newly measured parameter agrees with the previously fixed masses, constituting a strong-field 'mass-mass' test of gravity.

The first of these tests were enabled by the discovery of the first binary pulsar in 1974, PSR B1913+16 (Hulse & Taylor, 1975a). As noted previously, PSR B1913+16 is a DNS binary system in a 7.75-hr orbit with an eccentricity of $e = 0.62$. Within a year of its discovery, the rate of periastron advance had been measured at $\dot{\omega} = 4.22(4)\,^\circ\,\mathrm{yr}^{-1}$ (Taylor et al., 1976), with early measurements of γ and $\dot{P}_\mathrm{b}$ following only a few years later (Taylor et al., 1979). Together these constituted the first strong-field test of gravity, with the two most-precise PK parameters enabling a self-consistency mass-mass test of the third PK parameter. GR passed this initial test with flying colours, and it continues to do so even with ongoing timing of PSR B1913+16 producing evermore precise measurements of the PK parameters (Weisberg et al., 2010; Weisberg & Huang, 2016). Perhaps more importantly, as shown in Figure 1.2, the measurement of $\dot{P}_\mathrm{b}$ and its precise agreement with the predicted GR value provided the first indirect evidence of GW (Taylor & Weisberg, 1982). In other words, the observed orbital period decay agreed precisely with the energy loss predicted by GR due to the radiation of energy through GW as described by the quadrupole formula (see e.g. Peters, 1964; Weisberg & Huang, 2016; Wex, 2014; Will, 2014).

By far the most constraining tests of this type have been derived from the so-called 'Double Pulsar' PSR J0737−3039 (Burgay et al., 2003; Lyne et al., 2004), the only known example of two radio pulsars in a single binary system. Pulsar A is a recycled MSP with a period of approximately 22.7 ms, while pulsar B is a young, slow pulsar with a period of approximately 2.77 s. Both pulsars orbit each other with an orbital period of 2.45 hr and an eccentricity of 0.89. All five of the aforementioned PK parameters have been well measured in this system, providing an immediate three tests of gravitational theories (Kramer et al., 2006b). Additionally, the fact that we can time the pulses from both objects in the binary allows for the the semi-major axis (notated by x as described see Section 2.6.3) of each of their orbits to be measured independently, with the ratio of the two pulsar masses simply being the inverse of the ratio of theses axes. This mass ratio R provides an additional theory-independent fourth mass-mass test. The full mass-mass test is graphically depicted in Figure 1.3, with GR passing the most constraining test to within a published precision of only 0.05 % (Kramer et al., 2006b).

However, the tests described so far have focused only on those which most favourably constraining GR. For testing alternative theories of gravity, different types of

[5]The Einstein and Shapiro delays refer here to those encountered within the binary system, not those produced within our own solar system, although as described in Section 2.6.1, these solar system contributions may still need to be accounted for depending on the required analytical precision.

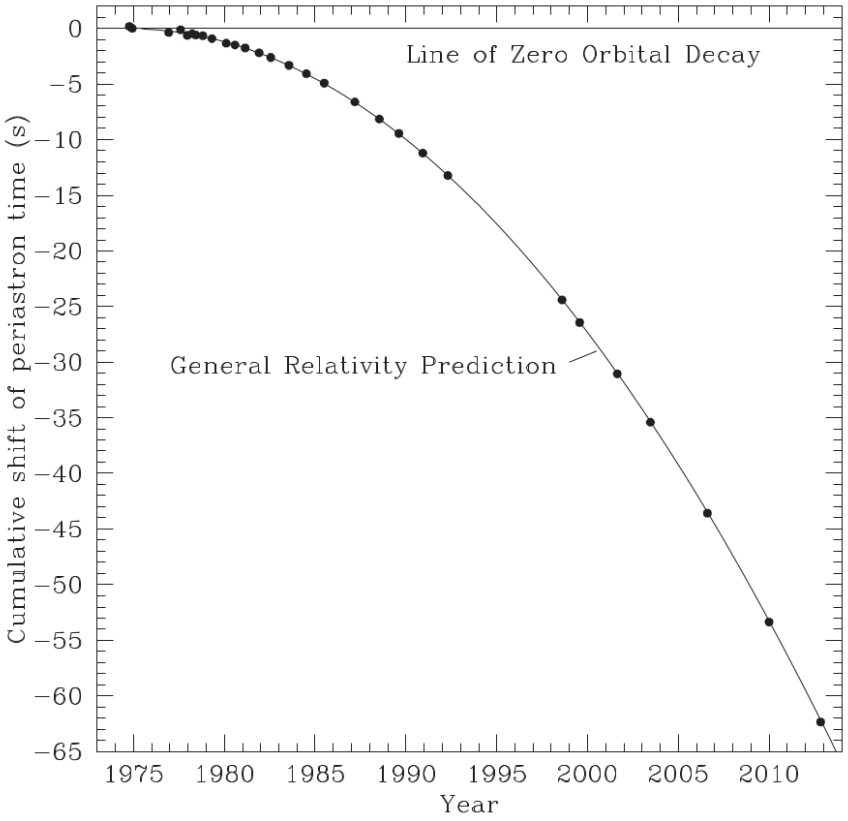

Figure 1.2: The cumulative shift in periastron time observed in PSR B1913+13. The 'General Relativity Prediction' curves indicates the change in periastron time expected from GR as a consequence of the emission of quadrupolar GW, while the straight 'Line of Zero Orbital Decay' indicates the classical expectation. The data points measured from PSR B1913+16 (with error bars typically too small to be visible) indicate a precise match to the GR prediction. Image from Figure 3 in Weisberg & Huang (2016), provided courtesy of Joel Weisberg.

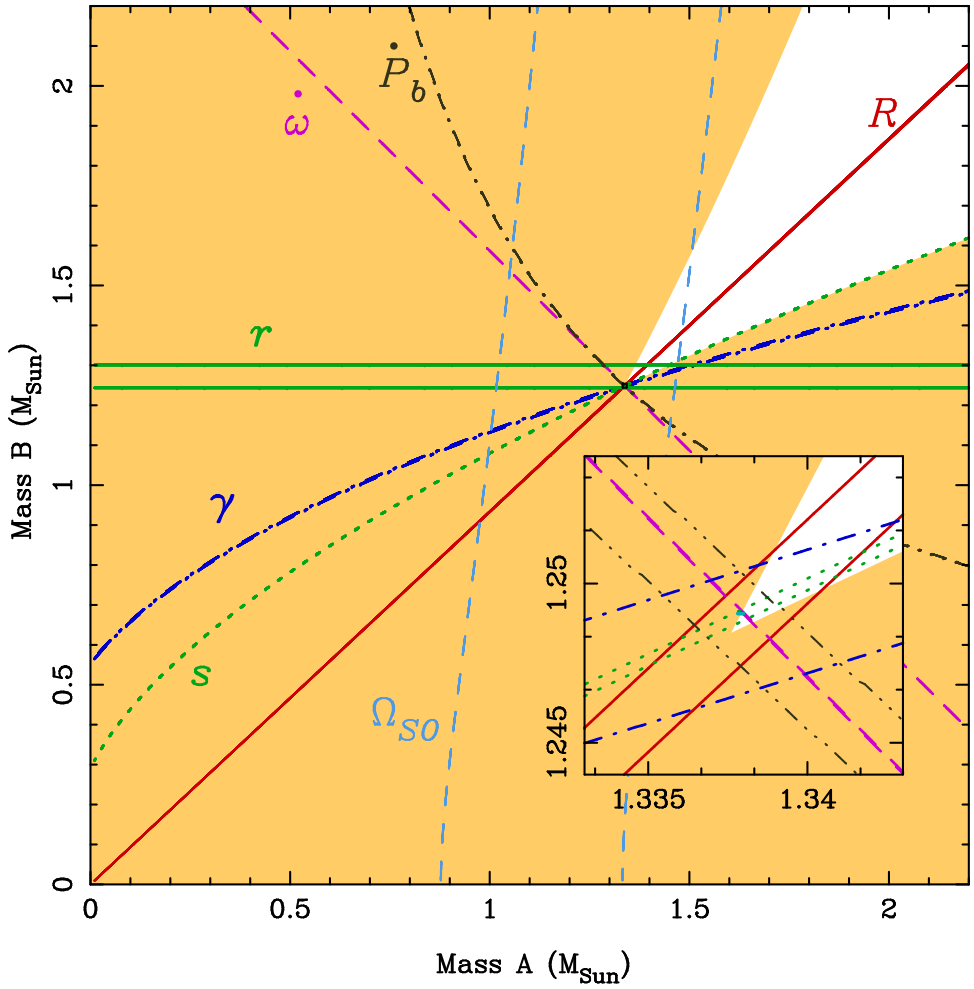

Figure 1.3: A mass-mass diagram of PSR J0737−3039, as characterised under the assumption of GR. Each set of lines correspond to the constraint placed by a particular parameter on the masses of pulsar A and pulsar B, and indicate the current error on the measured parameters. Included are the five PK parameters ($\dot{\omega}$, γ, $\dot{P}_{\rm b}$, r and s), the mass ratio (R) as determined from the measured semi-major axis of both orbits, and the geodetic precession rate of pulsar B ($\Omega_{\rm SO}$). The yellow region is excluded by orbital geometry, as it would require a value of $\sin i > 1$, where i is the inclination angle of the orbit with respect to the plane of the sky (see Section 2.6.3). The inset shows the region of common overlap of these constraints, indicating a common solution for the masses and that GR passes all four tests provided by PSR J0737−3039. Figure courtesy of Michael Kramer.

binary pulsar may be more advantageous. For example, the scalar-tensor family of gravitational theories predicts the existence of *dipolar* GW (as opposed to the *quadrupolar* waves shown to exist in the case of PSR B1913+16). In order to constrain the existence of dipolar GW, pulsar-WD binaries are typically ideal, as the two binary objects have significantly different masses and self-gravitational due to their differing compactness. Such asymmetry is vital in magnifying the measurable effects of any expected dipolar radiation (see e.g. Wex, 2014). To this end, pulsars such as PSR J1738+0333 (Antoniadis et al., 2012; Freire et al., 2012) and PSR J0348+0432 (Lynch et al., 2013; Antoniadis et al., 2013) provide the best current constraints on the dipolar radiation predicted by scalar-tensor theories, and rival the best solar-system based tests achieved with the Cassini space probe (Bertotti et al., 2003).

1.1.2.2 Precession and frame dragging tests

The existence of relativistic *spin-orbit coupling*, a consequence of higher-order post-Newtonian terms, results in a number of additional effects which can also serve as tests of gravity (see e.g. Wex, 2014). This coupling exists between the spin of the pulsar and the spin of the companion, and the spin of both objects to the angular momentum of the orbit itself. For a detailed analysis, Barker & O'Connell (1975) describes the measurable effects of these coupling terms as they apply to binary pulsars.

The most prominent consequence of spin-orbit coupling is that of *geodetic precession*, which describes the precession of the spin axis of the pulsar[6] about the total angular momentum of the binary system. This change in the orientation of the spin of the pulsar can lead to visible changes of the pulse profile over time as different parts of the radio beam become pointed along the line of sight to Earth. This secular profile change can be used to determine the rate of precession $\Omega_{\rm SO}$, the geometry of the pulsar's spin in relation to its orbit (Kramer, 1998), and even map the pulsar's emission region (see e.g. Desvignes et al., 2013a). As the predicted amount of geodetic precession is dependent on gravitational theory being considered, an accurate measurement of $\Omega_{\rm SO}$ can also provide an additional gravity test. This is seen in Figure 1.3, which shows the rate of precession $\Omega_{\rm SO}$ of PSR J0737−3039B[7] (Breton et al., 2008). Additional pulsars in which geodetic precession has been observed include PSRs B1913+16 (Weisberg et al., 1989; Kramer, 1998), B1534+12 (Stairs et al., 2004), J1141−6545 (Manchester et al., 2010) and J1906+0746 (Lorimer et al., 2006b).

A second precession effect is that of Lense-Thirring precession, a 'frame-dragging' relativistic effect whereby the plane of the orbit is itself seen to precess as a result of spin-orbit coupling (Barker & O'Connell, 1975; Damour & Schafer, 1988). To date, a measurement of Lense-Thirring precession in a binary pulsar has not yet been made, and as such it represents an as-yet unexplored test of gravity in the strong-field regime. Also, the magnitude of the Lense-Thirring precession effect is directly related to mo-

[6] Or the spin axis of the companion, although with the exception of PSR J0737−3039B, this precession is typically not measurable due to the lack of observed pulsations.

[7] As of March 2008, PSR J0737−3039B is no longer detectable in the radio spectrum, having precessed fully out of view (Perera et al., 2010)

ment of inertia of the pulsar, of which estimated measurements are rare. Constraining the magnitude of the Lense-Thirring effect in a binary pulsar would in theory lead to a precision measurement of this value (see Section 1.2.2 for further discussion of the importance of such a measurement).

One direct effect of Lense-Thirring precession is a change in the size of the semi-major axis of the orbit (x) over time. As further described in Chapter 4, the contribution of Lense-Thirring precession to the change in x (written as $\dot{x}_{\rm LT}$) is proportional to $\cot i$, where i is the inclination angle of the orbit (Damour & Taylor, 1992). Therefore, tests involving $\dot{x}_{\rm LT}$ are not well suited to pulsars whose orbits are highly inclined, as is the case for the Double Pulsar PSR J0737−3039 for which $i = 88.7^{+0.5}_{-0.8}$ (Kramer et al., 2006b). An alternative test available to PSR J0737−3039 involves measuring the Lense-Thirring contribution to the observed rate of periastron advance, given by $\dot{\omega}_{\rm obs} = \dot{\omega}_{\rm int} + \dot{\omega}_{\rm LT}$, where $\dot{\omega}_{\rm LT}$ is the Lense-Thirring contribution to the rate of periastron advance and $\dot{\omega}_{\rm int}$ is the intrinsic rate of periastron advance neglecting spin effects (Kehl et al., 2016). By using an additional well-measured PK parameter such as $\dot{P}_{\rm b}$ to fix the intrinsic value of $\dot{\omega}$, the Lense-Thirring contribution can therefore be constrained with respect to $\dot{\omega}_{\rm obs}$. With the development of next-generation radio telescopes such as the Square Kilometer Array[8] (SKA), this test is expected to produce a measurement of the Lense-Thirring effect in the PSR J0737−3039 within only a handful of years (Kehl et al., 2016).

1.1.2.3 The future of strong-field tests of gravity

Binary pulsars are no longer the only means of testing gravity in the strong-field regime. The first direct observations of GWs from the merger of two black holes (BHs) by the Laser Interferometer Gravitational-Wave Observatory (LIGO; Abbott et al., 2016), followed more recently by the observation of two merging NSs (Abbott et al., 2017b), mark a fundamental turning point in astrophysics. As well as providing a first look into the 'highly-dynamical strong-field' regime (Wex, 2014), these observations mark the first direct astrophysical observations conducted outside of the electromagnetic spectrum. However, it is anticipated that relativistic binary pulsars will be still be able to provide both competitive and complementary tests of gravitational theories against even the most advanced ground-based GW detectors (such as LIGO) that are currently foreseen (Shao et al., 2017).

Naturally, this will depend upon the continued discovery of ever-more relativistic binary pulsars. Such systems could include the types of pulsars already seen, including DNS binary systems and ever-more asymmetric pulsar-WD binary systems. One particularly promising binary type is that of a pulsar-BH binary, which although hypothesised has yet to be observed. The discovery of such a binary would allow for multiple new and improved tests of both GR and other gravitational theories, particularly if the pulsar was found to be in a tight enough orbit to probe the gravitational potential of the BH (for a summary, see e.g. Wex, 2014). To this end, a number of current and future-generation surveys (see Section 2.7) have been designed with the

[8] https://skatelescope.org/

specific aim of discovering both pulsar-BH systems and other relativistic binary pulsar systems. The High Time Resolution Universe South Low Latitude pulsar survey (HTRU-S LowLat; Keith et al., 2010; Ng et al., 2015), which forms the backbone of the work conducted in this thesis, was undertaken specifically with this goal in mind (see Sections 2.7.2 and 3.1.1 for further discussion), and the discovery of such a system forms a primary motivation of this project.

1.2 The basics of pulsars and neutron stars

As highlighted in the discussion thus far, great strides have been made in both the scientific understanding and application of pulsars. This includes a significant amount of progress in uncovering the answers to many of the fundamental questions surrounding pulsars, including the structure and composition of the NS interior, details of the pulsar emission mechanism, etc., although many aspects of these problems still remain the subject of ongoing discussion and debate. The resolutions to the complex and intricate questions which stem from these ongoing investigations are largely outside the scope of this thesis; instead, presented in this section is an overview of a set of simplified models which explain the basics of NS formation and the essential structure and properties of a typical pulsar.

1.2.1 Formation

A main sequence (MS) star essentially exists as a balance between the inward-acting force of gravity exerted by the star's mass, and the outward-acting force provided by the radiation pressure from the star's internal nuclear fusion. Once the star evolves to the point where its core environment can no longer sustain the process of nuclear fusion, gravitational collapse will inevitably take hold. This collapse results in one of three outcomes depending upon the original mass of the progenitor star. For lower mass stars ($M < 8\,\mathrm{M}_\odot$), the result is a WD, while for higher mass stars ($M > 25\,\mathrm{M}_\odot$), the collapse results in a BH. For intermediate mass stars ($8\,\mathrm{M}_\odot < M < 25\,\mathrm{M}_\odot$, although larger masses may be possible if the progenitor star's metallicity is sufficiently high) the end result is the production of a NS (Heger et al., 2003). The details of the mechanics of these collapse scenarios are largely beyond the scope of this thesis (for more in-depth reviews, see e.g., Woosley & Weaver, 1986; Tayler, R. J., 1994; Heger et al., 2003). An amalgamated, simplified overview of the portion relevant to the formation of NSs is presented here.

A typical scenario for the formation of a NS begins with a sufficiently massive progenitor star, early in its lifetime, converting hydrogen into helium through the process of nuclear fusion occurring at its core. As the star evolves, a core of non-fusing helium begins to accumulate at the center of the star. With no nuclear fusion process to provide any outward radiation pressure, the helium core contracts under its own gravity, until its density and temperature increase to the point where helium fusion becomes possible. This cycle continues throughout the lifetime of the star, resulting in the production of heavier and heavier elements until an iron core finally accumulates at the

center of the star. As before, this core begins to contract under its own self-gravitation, but even as its density and temperature increase, the iron core is unable to produce a self-sustaining nuclear fusion reaction, as any further fusion reactions require greater amounts of energy than they produce (Burbidge et al., 1957). Therefore, the collapse of the core is able to continue unarrested.

As the density of the collapsing core continues to increase, a state of electron degeneracy is reached which provides an additional outward pressure, temporarily halting the collapse. It is this degenerate electron pressure which stabilises the collapse of lower-mass stars (whose fusion processes have not yet reached iron production) and results in the stable formation of WDs. However, this process is only stable up to the Chandrasekhar limiting mass (Chandrasekhar, 1931) of $1.44\,\mathrm{M}_\odot$, a mass which is eventually exceeded by the mass of the iron core. Thus the final stage of the collapse continues in rapid fashion, within a timescale of seconds, halting only when the inner core becomes sufficiently compressed to be converted into the incompressible nuclear matter which composes a NS. This sudden change from a compressible to an incompressible core results in an outward shock wave in the still-collapsing outer layers of the core, which in addition to the prodigious amount of gravitational potential energy released during the collapse, triggers a supernova explosion (in this case a Type II or 'core-collapse' supernova). The outer layers of the progenitor star are subsequently blown away, revealing the newly formed NS which, depending upon its orientation of its rotational and magnetic axes with respect to the line-of-sight to the Earth, may or may not be detectable as a pulsar. The expelled material may itself result in the development of a supernova remnant (SNR).

1.2.2 Essential properties and the equation of state

The structure and composition of a NS depends delicately upon the exact *equation of state* (EOS) which governs the behaviour of matter at such ultra-high densities. A precise knowledge of the EOS would allow for the determination of many NS properties, including the relationships between the mass, radius, moment of inertia and their influence on the internal structure. However, as it is not possible to access and study this ultra-dense material here on Earth, the true EOS remains unknown, although multiple candidate models have been proposed, with the first such model predating the observational discovery of NSs (Oppenheimer & Volkoff, 1939). More recent reviews of the ongoing development of EOS models include Lattimer & Prakash (2001) and Özel & Freire (2016), along with references therein. Naturally, as one of the only current means of studying the behaviour of the ultra-dense matter of NSs, pulsars have the potential to serve as tools by which EOS models can be constrained, a topic further discussed in Section 1.5.

The canonical NS mass is typically taken as $m_\mathrm{p} = 1.4\,\mathrm{M}_\odot$ (see e.g., Lorimer, D. R. and Kramer, M., 2005), although the precise number chosen for this value varies from source to source. However, a range of potential NS masses are possible, with the minimum and maximum allowable masses being highly dependent on the EOS. An initial attempt to estimate a maximum NS mass was made by Oppenheimer &

Volkoff (1939). The Tolman-Oppenheimer-Volkoff limiting mass (TOV), analogous to the Chandrasekhar limiting mass for WDs, was initially determined to be only $0.7\,\mathrm{M}_\odot$. Modern re-calculations of the TOV suggest that NS masses as high as $3\,\mathrm{M}_\odot$ may yet be possible (Bombaci, 1996; Steiner et al., 2013; Chamel et al., 2013). Meanwhile, the minimum possible NS mass is currently estimated to be approximately $1.1 - 1.2\,\mathrm{M}_\odot$ (Goussard et al., 1998; Lattimer & Prakash, 2001). These theoretical predictions are progressively being supplemented by observational measurements of NS masses, made available primarily through pulsar timing (see Sections 1.5 and 2.6 for further details). Considering only those masses for which the measurement is well-constrained, the current set of NS masses spans a range of approximately $1.2 - 2.0\,\mathrm{M}_\odot$ (Özel & Freire, 2016).

The range of potential NS radii is more difficult to accurately quantify, as all estimates indicate an order of magnitude for the radius of only $\sim 10\,\mathrm{km}$, a tiny quantity in astronomical terms. Indeed, a canonical pulsar radius of $R = 10\,\mathrm{km}$ is typically adopted for many simple calculations. The true relationship between the mass and radius of a NS is, once again, finely sensitive to the EOS but, as outlined in Lorimer, D. R. and Kramer, M. (2005), it is possible to derive simple limits on the maximum and minimum radius of a NS largely in ignorance of the specifics of any particular EOS. Lattimer et al. (1990) and Glendenning (1992) derive the following expression for a lower NS radius limit R_{min}, based on the assumptions of the speed of sound in a NS being smaller than the speed of light, and that the EOS allows for smooth transitions in density:

$$R_{\mathrm{min}} \simeq \frac{3}{2} R_{\mathrm{S}} = \frac{3}{2}\left(\frac{2Gm_{\mathrm{p}}}{c^2}\right) = 6.2\,\mathrm{km}\left(\frac{m_{\mathrm{p}}}{1.4M_\odot}\right), \tag{1.1}$$

where R_{S} is the Schwarzchild radius[9] of the NS and m_{p} is the mass of the NS. Meanwhile, an upper radius limit can be derived by considering the rate of rotation at which a NS would destabilise. By equating the centripetal and gravitational acceleration at the surface of the NS, for a NS with rotational period P this maximum radius R_{max} can be shown to be given by:

$$R_{\mathrm{max}} \simeq \left(\frac{Gm_{\mathrm{p}}P^2}{4\pi^2}\right)^{1/3} = 16.8\,\mathrm{km}\left(\frac{m_{\mathrm{p}}}{1.4M_\odot}\right)^{1/3}\left(\frac{P}{\mathrm{ms}}\right)^{2/3}. \tag{1.2}$$

In the case of the fastest rotating pulsar, PSR J1748−2446ad, which has a period of only $P = 1.40\,\mathrm{ms}$ (Hessels et al., 2006), and assuming a canonical mass of $m_{\mathrm{p}} = 1.4M_\odot$, this gives a maximum radius estimate of $R_{\mathrm{max}} \simeq 21\,\mathrm{km}$.

With respect to a more realistic consideration of the role of the EOS, Steiner et al. (2013) derive limits on the radius of approximately $10.4 \leq R \leq 12.9\,\mathrm{km}$ for a $1.4M_\odot$ canonical pulsar. Additionally, techniques for measuring the true radii of NSs, such as spectroscopic measurements of thermal emission from the NS surface, have made significant progress in previous years. Multiple radius estimates are now available which are largely consistent with these theoretical predictions (see e.g. Özel & Freire, 2016, and references therein).

[9]For a given point-mass m, the Schwarzchild radius defines a sphere around the mass such that the escape velocity is equal to the speed of light c.

A few words should also be given to the general structure of a NS interior, although as with the EOS, this remains a subject of considerable ongoing discussion research. As once again outlined in Lorimer, D. R. and Kramer, M. (2005), a simplified 'standard' model of the NS interior includes a thin, solid, crystalline crust consisting of iron nuclei and degenerate elections. This is situated above a superfluid neutron 'sea' which forms the majority of the stellar interior, which itself is situated above a stellar core. The transitions between these layers are not necessarily well defined, occurring gradually as a function of the increasing density. Densities range from $10^9\,\mathrm{kg\,m^3}$ at the surface of the NS to $10^{17}\,\mathrm{kg\,m^3}$ at the outer boundary of the NS core, beyond which densities may increase sufficiently high so as to lead to the emergence of exotic forms of matter at the center of the star (see e.g., Weber, 2005).

1.2.3 The pulsar model

As Section 1.2.2 makes apparent, the precise structure and composition of NSs is far from simple, and this degree of complexity naturally extends to current models of pulsar behaviour and phenomenology. However, a number of useful results can be dervied from a relatively simple pulsar model as is depicted in Figure 1.4. Often referred to as the 'toy' or 'lighthouse' pulsar model, this model presents the pulsar as a rotating NS whose magnetic field is purely dipolar, surrounded by a vacuum, with a misalignment angle α between the magnetic and rotational axes. As shown in Figure 1.4, the magnetic field is divided into *closed* and *open* field lines by the *light cylinder*, an imaginary surface at which an object co-rotating with the pulse would move at the speed of light. The size of the emission beams, pointed along the pulsar's magnetic axis, is largely defined by the size of the open field-line region.

In reality, the assumptions which make up this simplified model do not hold true. For example, rather than a vacuum, the NS is typically surrounded by a plasma magnetosphere (see e.g. Goldreich & Julian, 1969). However, a full exploration of complex pulsar models is beyond the scope of this thesis, and the simple results dervied for the lighthouse model, while to be taken with a number of caveats, are sufficient for the purposes of the scientific discussion explored in Chapters 3 and 4. Therefore, the remainder of this section explores some of the consequences of this simplified model, largely following the discussion outlined in Lorimer, D. R. and Kramer, M. (2005).

The initial spin of a pulsar comes largely as a result of the conservation of angular momentum during the core-collapse of the progenitor supernova, although contributions to this spin as the result of a 'kick' imparted by the supernova have also been proposed (Spruit & Phinney, 1998). Over time, pulsar spin periods are observed to gradually increase as they lose rotational kinetic energy to other physical processes, including magnetic dipole radiation, high energy emission and the formation of pulsar winds[10]. This loss of energy $\dot{E}$, known as the *spin-down luminosity*, is described by

$$\dot{E} = -I\Omega\dot{\Omega} = 4\pi^2 I\dot{P}P^{-3}, \tag{1.3}$$

[10]This energy budget also includes the radio emission typically observed from pulsars, although this accounts for only a very small fraction of the spin-down energy.

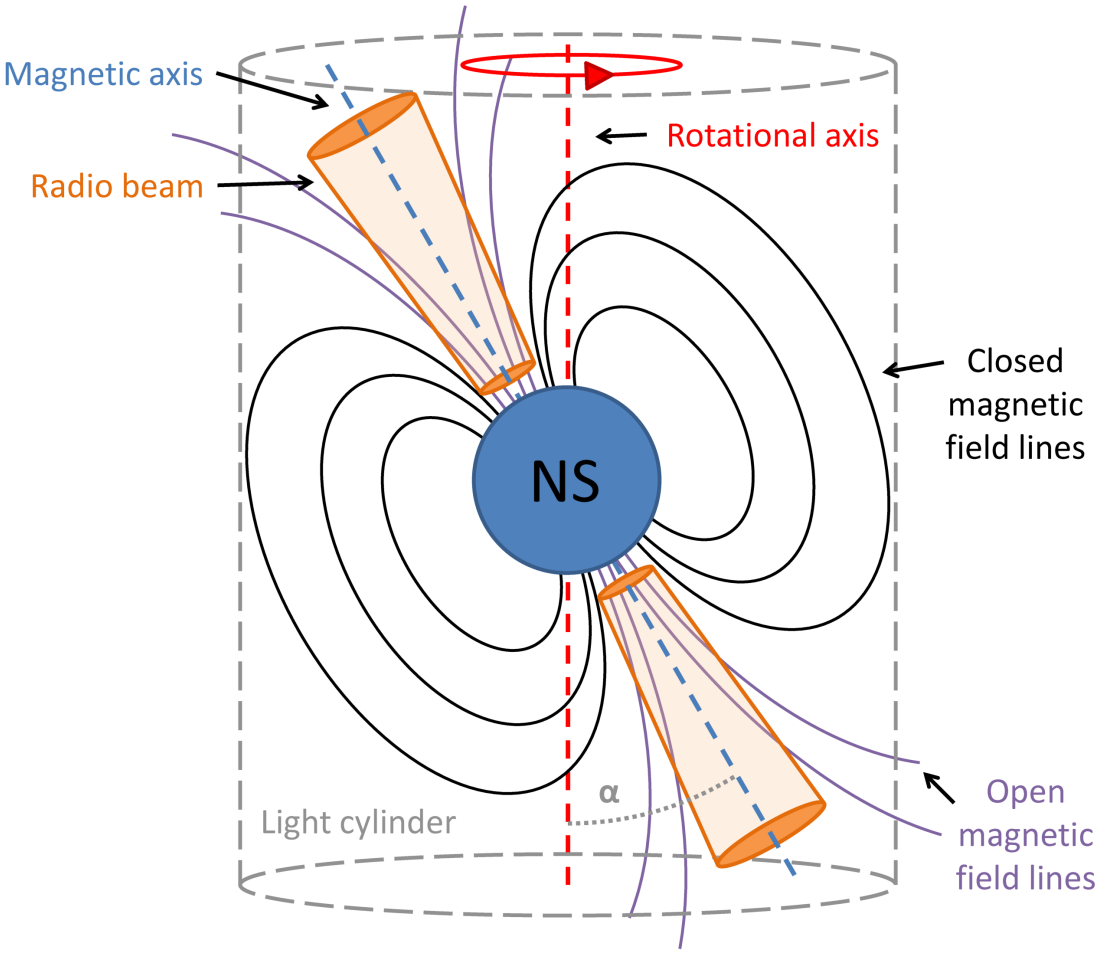

Figure 1.4: A simplified model of a pulsar, the so-called 'lighthouse' model, as explained in Section 1.2.3. Figure adapted from Lorimer, D. R. and Kramer, M. (2005).

where $\Omega = 2\pi/P$ is the angular frequency, P is the pulsar period, $\dot{P} = dP/dt$ is the rate of spin-down and

$$I = km_{\rm p}R^2 \tag{1.4}$$

is the pulsar's moment of inertia. Taking the simplified case of a sphere of uniform density (for which $k = 0.4$), and assuming the canonical pulsar mass and radius ($m_{\rm p} = 1.4M_\odot$ and $R = 10\,{\rm km}$ respectively) gives the canonical moment of inertia of $I \simeq 10^{38}\,{\rm kg\,m^2}$ and reduces Equation 1.3 to

$$\dot{E} \simeq 3.95 \times 10^{31}\,{\rm erg\,s^{-1}} \left(\frac{\dot{P}}{10^{-15}}\right)\left(\frac{P}{\rm s}\right)^{-3}. \tag{1.5}$$

The aforementioned magnetic dipole radiation arises from classical electrodynamics (see e.g., Jackson, 1962), which predicts the formation of electromagnetic waves from a rotating magnetic dipole. For a pulsar with a magnetic moment $|\mathbf{m}|$ and angle α between the magnetic and rotational axes, this magnetic dipole energy loss can be expressed as

$$\dot{E}_{\rm dipole} = \frac{2}{3c^3}\,|\mathbf{m}|^2\,\Omega^4 \sin^2\alpha. \tag{1.6}$$

Assuming for the present that this accounts for the overwhelming majority of the pulsar's spin-down luminosity, Equations 1.3 and 1.6 can be equated to give

$$\dot{\Omega} = \left(\frac{2\,|\mathbf{m}|^2 \sin^2\alpha}{3Ic^3}\right)\Omega^3 \tag{1.7}$$

Substituting for the pulsar's rotational frequency $\nu = 1/P$ and generalising Equation 1.7 to a power law results in

$$\dot{\nu} = -K\nu^n, \tag{1.8}$$

where K is typically taken as a constant, and n describes the *braking index*. From Equation 1.7 it is clear that in the case of pure magnetic dipole braking where $\dot{E} = \dot{E}_{\rm dipole}$, the braking index $n = 3$. However, as previously described, other energy loss mechanisms may also play significant roles and may modify the true value of n for a given pulsar. By differentiating and re-arranging Equation 1.8 to give

$$n = \frac{\nu\ddot{\nu}}{\dot{\nu}^2}, \tag{1.9}$$

it can be seen that by measuring the value of $\ddot{\nu}$ for a given pulsar, an estimate for n may be derived. Such measurements of $\ddot{\nu}$ are typically only possible in young pulsars with high rates of spin-down, but unfortunately, timing noise (Hobbs et al., 2010; Shannon & Cordes, 2010) and pulsar glitches (see Section 1.4.3) are both common among these pulsars, making accurate measurements difficult. Recent techniques are making progress in overcoming these restrictions (see e.g., Espinoza et al., 2017, for recent braking index measurements made possible through glitch modeling), although the current set of braking index measurements is still limited, with measured values

ranging between approximately $0.9 \leq n \leq 2.8$ (see e.g., Ho & Andersson, 2012, and references therein).

An approximate age T for a given pulsar can be derived by integrating Equation 1.8 which, expressed in terms of the pulsar period P results in

$$T = \frac{P}{(n-1)\,\dot{P}} \left[1 - \left(\frac{P_0}{P} \right)^{n-1} \right], \tag{1.10}$$

where P_0 is the birth period of the pulsar and $n \neq 1$. If one again assumes pure magnetic dipole braking ($n = 3$) and adding the assumption that the pulsar's birth period $P_0 \ll P$, the so-called *characteristic age* τ_c can be derived, defined as

$$\tau_c \equiv \frac{P}{2\dot{P}} \simeq 15.8\,\mathrm{Myr} \left(\frac{P}{\mathrm{s}} \right) \left(\frac{\dot{P}}{10^{-15}} \right)^{-1}. \tag{1.11}$$

However, while τ_c can provide a useful first estimate of the age of a given pulsar, it should be treated with a degree of caution, as its built-in assumptions are unlikely to hold true in all but a handful of cases. This is especially true in the case of MSPs (see Section 1.4.1), which have undergone a different evolutionary history to the standard spin-down model presented thus far and can as a result appear to have almost any value of τ_c (Tauris, 2012), including values greater than a Hubble Time (e.g. PSR J1938+2012, Stovall et al., 2016).

Maintaining the assumption of pure magnetic dipole braking, an expression for the surface magnetic field of the pulsar, B_{surf}, can also be derived as

$$B_{\mathrm{surf}} = \sqrt{\frac{3c^3 I P \dot{P}}{8\pi^2 R^6 \sin^2 \alpha}}. \tag{1.12}$$

Substituting the typical values for a canonical pulsar ($I = 10^{38}\,\mathrm{kg\,m^2}$ and $R = 10\,\mathrm{km}$), and additionally assuming that $\alpha = 90°$ (i.e., that the pulsar is an *orthogonal rotator*) reduces Equation 1.12 to

$$B_{\mathrm{surf}} = 3.2 \times 10^{19}\,\mathrm{G}\sqrt{P\dot{P}} \simeq 10^{12}\,\mathrm{G} \left(\frac{\dot{P}}{10^{-15}} \right)^{1/2} \left(\frac{P}{\mathrm{s}} \right)^{1/2}. \tag{1.13}$$

As with the characteristic age τ_c, the high likelihood that any given pulsar will not reflect the assumptions behind Equation 1.13 means that this expression for the surface magnetic field B_{surf} should be treated with some caution, and is best taken only as an order-of-magnitude estimate. Applying Equation 1.13 to the general pulsar population[11] provides a typical B_{surf} range of $10^{11} - 10^{13}\,\mathrm{G}$. This range agrees generally well with actual measurements of B_{surf} derived from the study of cyclotron processes in the X-ray spectra of isolated and binary NSs (see e.g., Coburn et al., 2002; Bignami et al., 2003).

[11] Not including MSPs (see Section 1.4.1) and magnetars (see Section 1.4.4), which posses markedly different values of B_{surf}.

1.3 Propagation effects

The focus of this introduction now turns from the structure and properties of NSs to the observed properties of the radio pulsations themselves. Due to interactions of these radio signals with the interstellar medium (ISM), several propagation effects can occur which can influence our observations of these pulses. Some of the main effects include pulse dispersion, pulse scattering and scintillation. Understanding these propagation effects is critical in order to understand the properties of the underlying pulsar signal. Each of these effects is described in the subsections below.

1.3.1 Pulse dispersion

Each of a pulsar's individual pulses departs simultaneously across a broad electromagnetic frequency range, although for the purposes of this thesis focus is kept only on the radio component of this pulse. Pulse *dispersion* describes the delay in arrival times of the lower-frequency components of each pulse, a consequence of the frequency dependence of the pulse's group velocity as it travels through ionised components of the ISM. The phenomenon was first observed during early studies of the first discovered pulsar, PSR B1919+21 (Hewish et al., 1968). An example of the effect of pulse dispersion on PSR B1706−44 is presented in Figure 1.5.

The amount of dispersion affecting a pulsar's signal is typically characterised by the *dispersion measure* (DM). The DM is defined as the integration of the electron density of the ISM along the line of sight between the observer and the pulsar, i.e.

$$\mathrm{DM} = \int_0^d n_\mathrm{e}\,\mathrm{d}l\,\mathrm{cm}^{-3}\,\mathrm{pc}, \tag{1.14}$$

where d is the distance to the pulsar and n_e is the electron density in units of cm^{-3}. The delay in arrival time between two frequency components of the same broadband signal is related to the DM by

$$\Delta t \simeq \mathcal{D} \times \left(f_1^{-2} - f_2^{-2}\right) \times \mathrm{DM} \tag{1.15}$$

where the dispersion constant $\mathcal{D} \simeq 4.15 \times 10^6\,\mathrm{ms}$ (Manchester & Taylor, 1972). In the case of PSR B1706−44, which has a spin period of 102-ms and a DM of $75.7\,\mathrm{cm}^{-3}\,\mathrm{pc}$, Equation 1.15 indicates a delay between 1200 and 1500 MHz of approximately 78.5-ms, or approximately 77 % of the spin period of the pulsar. The magnitude of this delay is reflected in Figure 1.5.

As demonstrated by Equation 1.14, the DM value along a particular line of sight is approximately analogous to the distance to the pulsar. However, this relationship depends on the precise distribution of n_e throughout the Galaxy. A crude estimate of the distance can be derived by assuming a constant value of n_e, with a typical value taken as $n_\mathrm{e} \simeq 0.03\,\mathrm{cm}^{-3}$ (e.g. Ables & Manchester, 1976). However, in reality the true Galactic distribution of n_e is far from uniform. A more accurate approach has been to use independently calibrated measurements of pulsar distances (via techniques such as the measurement of parallax or HI absorption lines) in order to construct more

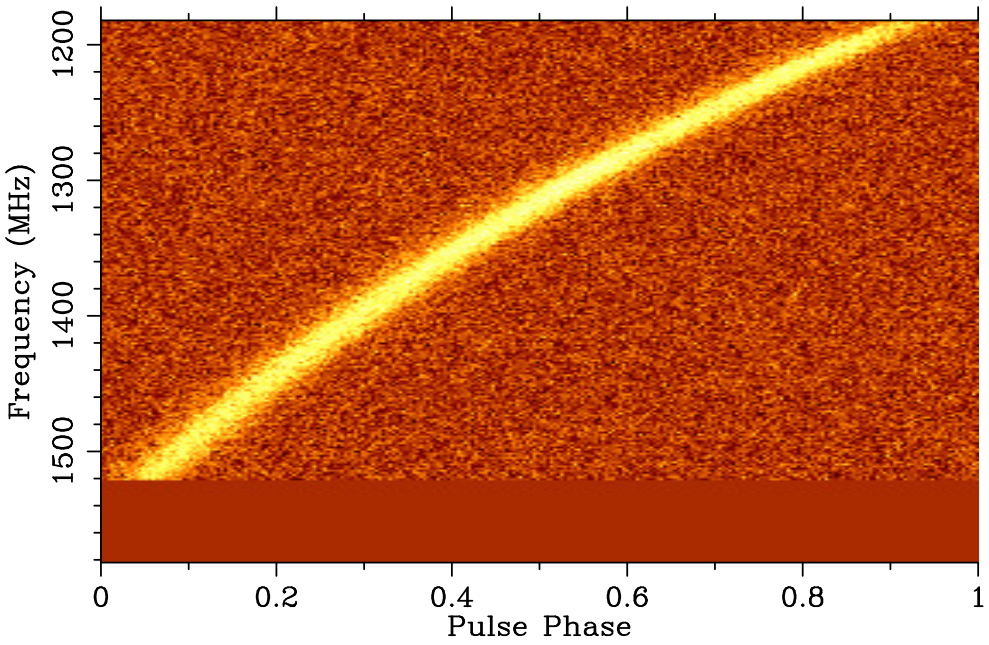

Figure 1.5: The effect of dispersion on pulsar signals, in this case using the example of PSR B1706−44, a 102-ms pulsar with a dispersion measure (DM) of $75.7\,\mathrm{cm}^{-3}\,\mathrm{pc}$, observed here as part of the HTRU-S LowLat survey. In this plot of frequency versus pulse phase (integrated over $\sim 4.2 \times 10^4$ pulses), it can be seen that the higher frequency signal components arrive first (pulse phase being analogous to time), causing a characteristic quadratic sweep across the frequency band.

elaborate models of the true Galactic n_e distribution. These models include more complex descriptions of major Galactic structures, such as the disk and spiral arms where the density is typically at its highest, as well as identifiable local variations such as nebulae and supernova remnants. Examples include the long-standing NE2001 model (Cordes & Lazio, 2002, 2003) as well as the more recent YMW16 model (Yao et al., 2017).

1.3.2 Pulse scattering

While spatially coherent at its point of origin, a pulsar's radiation can also be impacted by scattering caused by turbulence in the ISM. The effect of this turbulence is to cause perturbations in the refractive index of the ISM, bending the incoming pulsar radiation along different lines of sight, thereby modifying its path length. This in turn modifies the arrival time of the radiation as it reaches the observer, detectable as an offset in pulse phase, which when summed across the distribution function of potential paths can result in a significantly broadened pulse profile. This broadened or scattered pulse shape can typically be modeled as a convolution of the 'true' pulse shape with a one-sided exponential decay function. The $1/e$ time constant of this exponential function is referred to as the *scattering time*, or τ_s (see, e.g., Lorimer, D. R. and Kramer, M., 2005).

As with DM, the amount and nature of scattering experienced by a given pulsar's radiation is dependent on the distribution and behaviour of the ISM, modeling which can present a serious challenge. A typical strategy is to assume a Kolmogorov spectrum of turbulence in the ISM (see, e.g. Armstrong et al., 1995), along with a thin-screen model (Scheuer, 1968), which reduces the scattering experienced along the entire line of sight to a single scattering screen midway between the pulsar and the observer. This basic model works well for a significant portion of pulsars, however, multiple instances of pulsars requiring more in-depth scattering models have been reported (see, e.g. Lewandowski et al., 2013).

The presence of scattering in pulsar observations is in many case undesirable, as it can lower the overall signal to noise ratio (S/N) and thereby make the scattered pulsar harder to detect. It can also obscure features in the pulse profile which could otherwise reveal additional information about the structure of the pulsar's emission region or improve the pulsar's timing accuracy (see Section 2.6). As a direct prediction of the thin-screen model, $\tau_s \propto f^{-4}$, where f is the frequency of the observation. In other words, the scattering time decreases at higher electromagnetic frequencies. An observational example of this is presented in Figure 1.6. Therefore, observing at higher frequencies can help to avoid the effects of scattering. τ_s also correlates strongly with DM Bhat et al. (2004), such that pulsars with higher values of DM are more likely to experience higher values of τ_s.

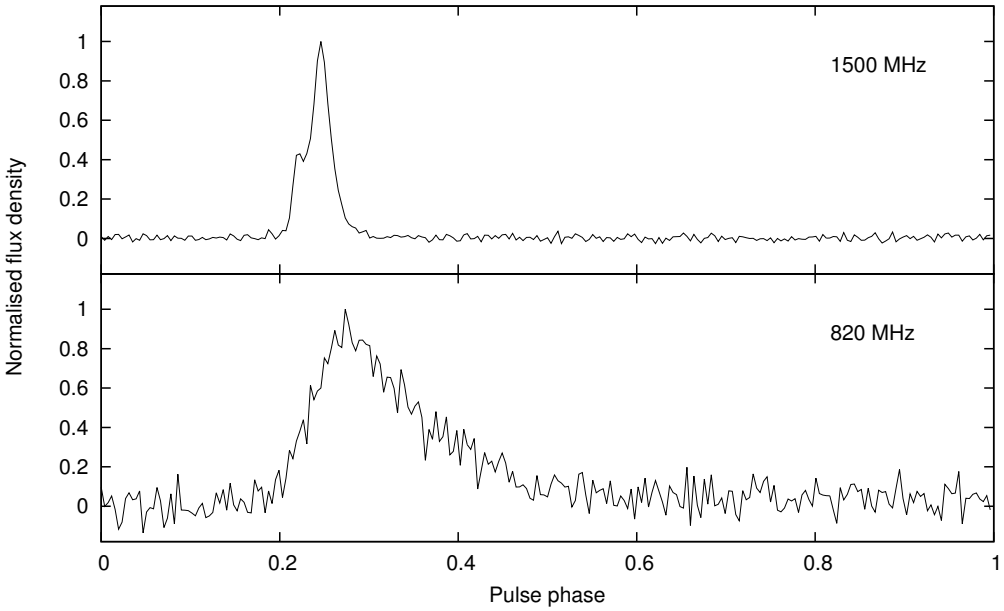

Figure 1.6: Multi-frequency profiles of PSR J1757−1854 (see Chapter 4), observed at both 1500 and 820 MHz with the Green Bank Telescope (GBT). In each case, the peak of the profile has been normalised to 1. The effect of scattering, which causes a broadening of the apparent pulse shape at lower frequencies along with an exponential tail, can clearly be seen.

1.3.3 Interstellar scintillation

An additional effect of the ISM, and one that is closely related to pulse scattering, is that of interstellar *scintillation*. First observed by Lyne & Rickett (1968) as strong modulations of observed pulsar intensity, the effect is analogous to the optical 'twinkling' of stars observed through Earth's atmosphere. These modulations can be extreme enough to render an otherwise bright pulsar almost impossible to detect while it is 'scintillated-down' (Cordes, 2002). Modulations in intensity (also referred to as *scintils*) are observed in both the frequency and time domains, with a characteristic scintillation bandwidth of $\Delta f \propto f^4$ for a given observing frequency f. As with pulse scattering, the effect is described by the thin-screen model (Scheuer, 1968), which predicts a diffraction pattern resulting from the interference of the phase-offset components of the pulsar's originally-coherent signal. Δf also scales in inverse proportion to pulsar distance and therefore to DM (see, e.g. Sutton, 1971; Backer, 1975), meaning that the effects of scintillation are more commonly observed in nearby pulsars with low values of DM.

1.4 The pulsar zoo: a diverse population

An enormous range of variety has been noted in the observational characteristics, physical configurations, evolutionary history and other properties of the over 2600 pulsars that have been discovered to date. The classification of pulsars into various categories has been a useful way of studying these patterns of behaviour in greater detail, and to build models which describe and explain the underlying mechanisms at work. One of the primary goals of pulsar astronomy is to eventually reconcile these different pulsar categories into a fully-encompassing model of pulsar behaviour, describing how pulsars can transition from one category to another as they evolve over time.

A useful tool in the study of pulsar behaviour has been the so-called P-$\dot{P}$ diagram, which characterises pulsars by their two most readily observable properties, their spin period P and rate of spin-down $\dot{P}$. Such a diagram can be used to provide insights into the evolutionary histories of the pulsar population because, as noted in Section 1.2.3, a pulsar's characteristic age τ_c (as well as its surface magnetic field $B_{\rm surf}$ and spin-down luminosity $\dot{E}$) can be approximately determined by its values of P and $\dot{P}$. In this sense, the P-$\dot{P}$ diagram is analogous to the Hertzsprung-Russel diagram, which tracks the evolution of conventional stars as a function of their luminosity and effective temperatures. An example P-$\dot{P}$ diagram for the general pulsar population is displayed in Figure 1.7.

Although the evolutionary history of each individual pulsar will vary significantly, a 'typical' pulsar's evolutionary history as described in Lorimer, D. R. and Kramer, M. (2005) is expected to begin in the upper left region of the P-$\dot{P}$ diagram, with a short birth spin period on the order of 30 ms (see e.g. Gonthier et al., 2002; Johnston & Karastergiou, 2017). It is in this region of the P-$\dot{P}$ diagram in Figure 1.7 that we

[12] http://www.physics.mcgill.ca/~pulsar/magnetar/main.html

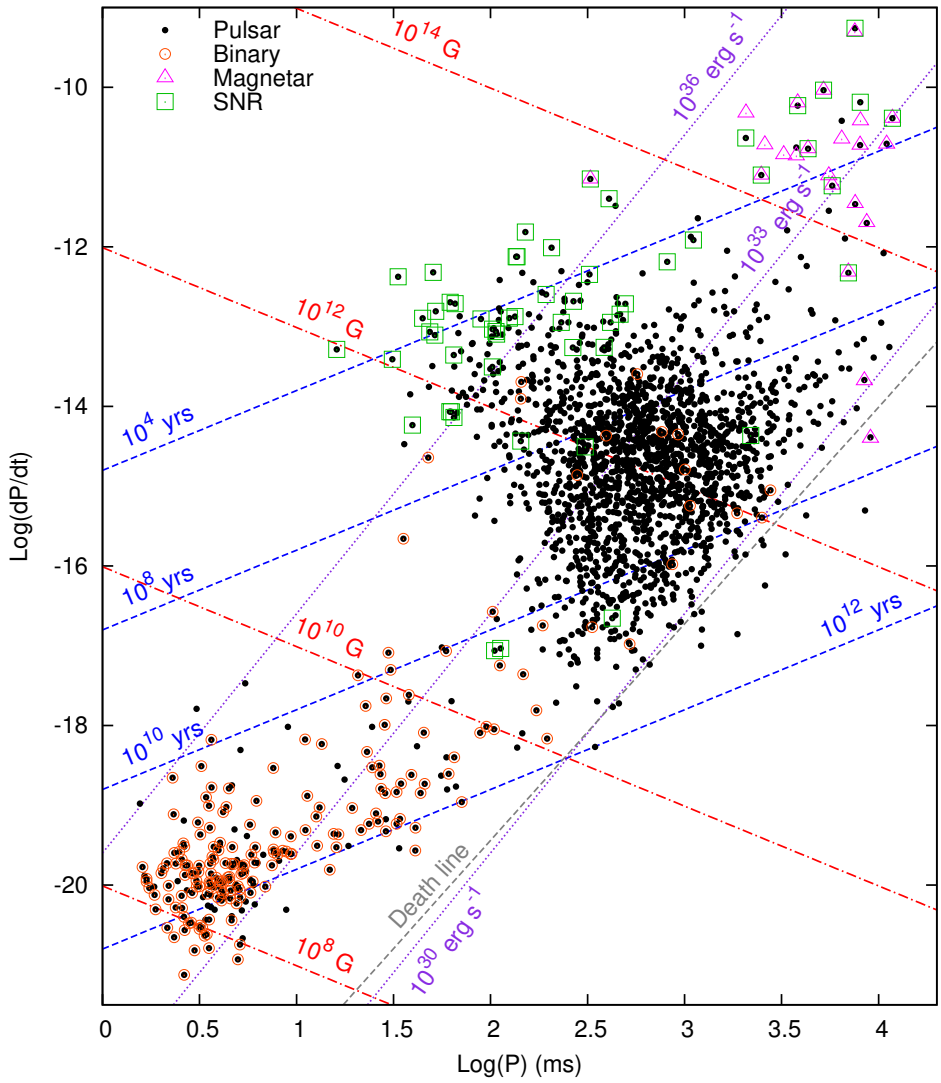

Figure 1.7: A P-$\dot{P}$ diagram, with axes presented in logarithmic scale. Black dots indicate the 2109 known pulsars which as of April 2017 have listed values for both P and $\dot{P}$ in PSRCAT. Orange circles indicate known binary pulsars. Green squares indicate pulsars with known SNR associations. Pink triangles indicate the 21 known magnetars which as of April 2017 have listed values for both P and $\dot{P}$ in the McGill Online Magnetar Catalog[12] (Olausen & Kaspi, 2014). Lines of constant characteristic age τ_c, surface magnetic field $B_{\rm surf}$ and spin-down luminosity $\dot{E}$ (as defined in Section 1.2.3) are depicted in blue, red and purple respectively. The pulsar 'death line' shown at the lower right is as defined by Equation 9 in Chen & Ruderman (1993), and marks the approximate edge of the pulsar 'graveyard', beyond which the pulsed radio emission from NSs is expected to cease.

see the highest concentration of SNR associations (see, e.g. Staelin & Reifenstein, 1968; Gotthelf et al., 2000; Camilo et al., 2002). This serves as strong evidence for the young ages of these pulsars, as SNRs have only a lifetime on the order of 10^4 years before they dissipate and fade into the background ISM (see e.g. Frail et al., 1994). Additionally, the typically-high birth velocity of pulsars (see e.g. Faucher-Giguère & Kaspi, 2006) will also cause them to move away from the positions of their progenitor supernova, although in comparison to SNR lifetime estimates, this effect plays a lesser role. Over a subsequent timescale of $10^5 - 10^6$ years, the pulsar experiences a gradual spin-down, moving towards the lower right of the P-$\dot{P}$ diagram, before encountering a so-called pulsar 'death line' (see e.g. Chen & Ruderman, 1993) after approximately 10^7 years. Beyond this point, the drop in electric potential required for the production of radio emission exceeds the maximum which can be achieved in the pulsar's magnetosphere, and the NS becomes undetectable as a pulsar. It should be noted that the multiple death lines that have been proposed to date are largely theoretical, and a small number of pulsars (e.g. PSR J2144−3933; Young et al., 1999; Zhang et al., 2000) are found in the so-called 'graveyard' region which exists beyond these lines, posing further questions regarding pulsar emission mechanisms.

Outlined in the remainder of this section are some of the major pulsar categories that have been determined thus far. This list is not intended to be comprehensive, and chooses to focus on those pulsar categories which are most relevant to the later science chapters.

1.4.1 Millisecond and binary pulsars

Millisecond pulsars are a population of pulsars marked by their extremely short spin periods, low rates of spin-down and high rotational stability. Although the precise definition of MSPs varies between sources, for consistency and simplicity this thesis broadly adapts the definition used by Ng (2014), defining an MSP as a pulsar with $P < 30\,\mathrm{ms}$ and $\dot{P} < 10^{-17}$ (unless otherwise noted). MSPs also typically possess much lower magnetic field strengths than non-MSPs, typically around $10^8 - 10^9\,\mathrm{G}$. The low $\dot{P}$ criterion distinguishes MSPs from very young pulsars with short post-birth periods, which spin down towards the death line over considerably shorter timescales. The distinction between MSPs and the so-called 'normal' pulsar population can be seen most effectively in the P-$\dot{P}$ diagram presented in Figure 1.7, with the MSP population forming a distinct 'island' towards the lower left of the diagram.

The mechanism responsible for the formation of MSPs involves the interaction of a young, normal pulsar with a stellar binary companion (see e.g. Alpar et al., 1982). There exist a variety of specific evolutionary channels through which MSPs are believed to be formed (for detailed reviews, see e.g. Bhattacharya & van den Heuvel, 1991; Phinney & Kulkarni, 1994; Tauris & van den Heuvel, 2006) and it is likely that the evolution of each MSP is slightly different. However a simplified version proceeds as follows, with an accompanying schematic in Figure 1.8. The scenario begins with two MS stars bound in a binary system, at least one of which is of sufficient mass to act as the progenitor

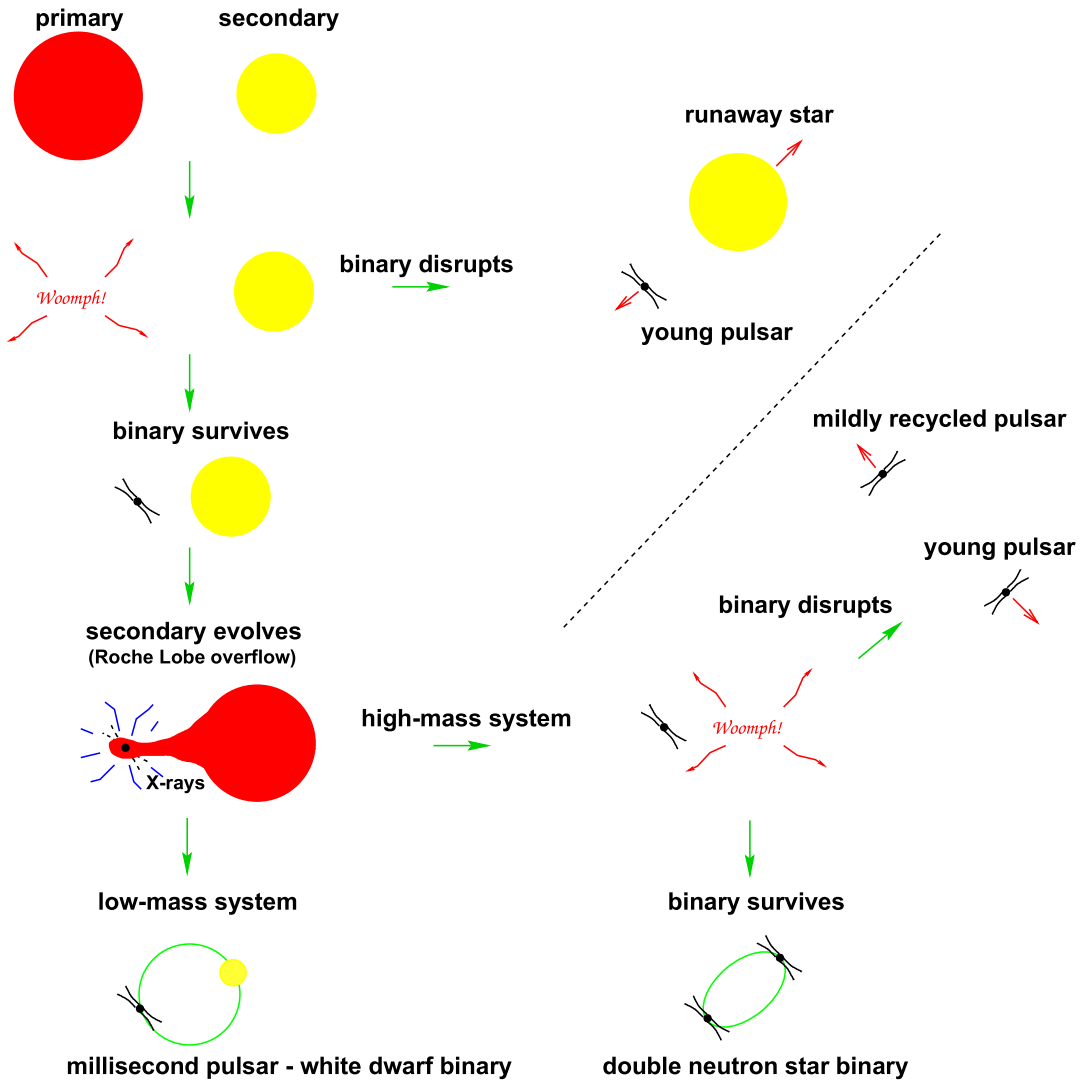

Figure 1.8: A simplified cartoon schematic of some of the major formation channels of pulsar binary systems. Further explanation is provided in Section 1.4.1. Diagram from Figure 7 in Lorimer (2008), used under Creative Commons licensing[13].

of a supernova explosion. The more massive of the two stars evolves more rapidly than its companion via the mechanism outlined in Section 1.2.1, eventually reaching the point of supernova and resulting in the formation of a NS. Should the binary system not survive the disruption caused by the supernova, the two objects become unbound, resulting in the production of a young, isolated, normal pulsar. In the event that the binary is not disrupted by the supernova, the eventual evolution of the remaining MS star causes it to expand, eventually leading to a process of Roche-lobe overflow (RLO) where the outer layers of stellar material are no longer gravitationally bound to the star. This stellar material is then able to accrete onto the pulsar, resulting in an exchange of angular momentum which spins-up or 'recycles' the pulsar to very short rotational periods (Bisnovatyi-Kogan & Komberg, 1974) as it transitions to an MSP. This same recycling process also leads to a significant reduction of the surface magnetic field of the MSP (Shibazaki et al., 1989) and typically results in a high-degree of circularisation of the binary orbit due to the exchange of tidal forces between the pulsar and its binary companion (Phinney & Kulkarni, 1994). During the accretion and recycling process, the binary system may also be observable in X-rays as a low, intermediate or high-mass X-ray binary (LMXB/IMXB/HMXB), depending upon the masses of the progenitor stars (Tauris & van den Heuvel, 2006). Recycling continues until an equilibrium point is reached between the inward gravitational pressure of the infalling accreted material and the outward radiation pressure of the NS (Bhattacharya & van den Heuvel, 1991).

The eventual fate of the MS companion, and by extension the binary system as a whole, depends largely upon the companion's initial mass. If the companion is sufficiently massive so as to undergo its own supernova event, and assuming that the orbit is not disrupted as a result, then a DNS system can result. The asymmetric kick imparted to the system by the second supernova typically decircularises the orbit, resulting in larger values of eccentricity (Ihm et al., 2006). The second-formed NS may or may not be detectable as a pulsar by the time of its observation, as no further recycling in the system is possible. It therefore experiences a much shorter lifetime than its MSP companion before reaching the death line where its pulsed emission is expected to cease, reducing the chances of a detection being made. Of the 11 confirmed DNS systems listed by PSRCAT as of October 2017, only the Double Pulsar PSR J0737−3039 (Burgay et al., 2003; Lyne et al., 2004) has been detected both through the pulsations of the recycled pulsar (pulsar A) and its younger, unrecycled binary companion (pulsar B)[14]. For an in-depth review on the formation of DNS systems, see Tauris et al. (2017).

A more common fate for MSP binary systems occurs when the companion MS star is not of sufficient mass to undergo a supernova. Following an accretion period as long as 10^8 years (Lorimer, D. R. and Kramer, M., 2005), the evolution of the companion eventually terminates as it sheds its outer layers and becomes a WD. This long period of recycling typically imbues pulsar-WD binary systems with some of the shortest pulsar rotational periods and the most circularised orbits (the record for the lowest measured eccentricity in a pulsar binary, $e = 1.14(10) \times 10^{-7}$, is currently held by the WD binary PSR J1909−3744 (Reardon et al., 2016)). Depending on the precise evolution

[14]See footnote 7.

of the binary system and the initial mass of the binary companion, the resulting WD companion can either be a lighter helium-white dwarf (He-WD), typically possessing a mass of $m_{\rm WD} < 0.45\,{\rm M}_\odot$ (Tauris & van den Heuvel, 2006), or less-commonly a heavier carbon-oxygen-white dwarf (CO-WD) (see e.g. Lazarus et al., 2014) or oxygen-neon-magnesium-white dwarf (ONeMg-WD).

However, a number of binary pulsars have emerged in recent years which challenge some of these basic models. For example, the discovery of PSR J1903+0327 (Champion et al., 2008) marked the first discovery of a recycled MSP in a highly eccentric orbit ($e = 0.44$), defying the above-outlined models relating to orbital circularisation as a natural consequence of the recycling process. Subsequent investigation of this pulsar has both identified the binary companion as a MS star and suggested a likely formation scenario involving a triple system, from which the stellar companion responsible for recycling the pulsar has since been ejected (Freire et al., 2011; Portegies Zwart et al., 2011). This proposed progenitor triple is potentially similar to the only currently-known stellar pulsar triple system, PSR J0337+1715 (which contains a MSP and two WDs, see Ransom et al., 2014), and may also bear similarities to the earlier MSP triple system PSR B1620−26 (which contains a MSP, WD and a third object of planetary mass, see e.g. Thorsett et al., 1999; Sigurdsson et al., 2003). More recently, a family of eccentric MSP-WD systems has been identified which pose further challenges to the standard recycling models (see e.g. Antoniadis, 2014; Barr et al., 2017). Beyond their abnormally high eccentricities, these pulsars appear to have been recycled in the standard fashion, and the process of determining explanatory models for these unusual systems is currently ongoing.

There also exists a minority population of isolated recycled pulsars. As the recycling process is believed to require a binary companion, much discussion exists about the multiple channels by which these isolated MSPs are thought to be able to form (for a brief summary, see e.g. Levin et al., 2013). As indicated in Figure 1.8, one such path involves the disruption of a potential DNS system during the second supernova explosion, instead leading to two isolated pulsars, one of which is at least partially recycled (see e.g. Camilo et al., 1996; Lorimer et al., 2004). Another scenario involves so-called 'black widow' pulsars (see Section 1.4.1.1), which MSPs in the process of ablating their binary companions, the end result of which may be an isolated MSP.

A diversity of binary pulsar behaviour also exists beyond the recycled pulsars. For example, excluding the aforementioned PSR J0737−3039B which has a rotational period of $P = 2.773\,{\rm s}$, the longest period pulsar currently known in a binary system is PSR J1822−0848 (Faulkner et al., 2004), with a period of $P = 2.505\,{\rm s}$. Despite being unrecycled, the pulsar orbits a He-WD companion in a wide orbit with an orbital period of $P_{\rm b} \simeq 287\,{\rm days}$ (Lorimer et al., 2006a). Additionally, as with PSR J1903+0327, unrecycled pulsars are also found around MS binary companions. Currently, the three longest $P_{\rm b}$ pulsar binaries are all unrecycled pulsars orbiting MS companions, with the longest being PSR J2032+4127 (Abdo et al., 2009) whose $P_{\rm b} = 8.6(12) \times 10^3\,{\rm d}$ or approximately 24 years (Lyne et al., 2015).

1.4.1.1 The 'spider' pulsars

Two classes of binary MSPs which warrant separate discussion are the so-called 'black widow' and 'redback' pulsars, which are often collectively referred to as the 'spider' pulsars (see, e.g. Roberts, 2013). Black widows and redbacks both describe MSPs found in tight binary systems ($P_b < 24\,h$) which are observed to undergo regular eclipses. The primary observational difference between the two spider classes is the mass range of their companions; black widows are orbited by extremely light companions ($m_c \ll 0.1M_\odot$), while redbacks feature heavier companion masses ($0.2M_\odot < m_c < 0.4M_\odot$). Since the first black widow was discovered (PSR B1957+20; Fruchter et al., 1988), at least 40 have now been identified[15], while at least 22 redbacks have been discovered[16] since the identification of the first redback pulsar (PSR J1023+0038; Archibald et al., 2009). In both spider classes, the observed eclipses are believed to occur as a result of the pulsar ablating its companion through an irradiative process (Kluzniak et al., 1988; Ruderman et al., 1989), resulting in the production of an intra-binary field of material capable of eclipsing the pulsar during *superior conjunction*, the point in the orbit where the pulsar passes directly behind the binary companion with respect to the line of sight to the observer.

These spider pulsars are of particular note as they represent new insights into the evolutionary processes involved in the formation of MSPs. As noted previously, black widows have been proposed as a step in the formation of isolated MSPs, as the continued ablation of the companion leads to eventual dynamic disruption of the binary system (King et al., 2005). Meanwhile, redback pulsars are to believe to represent an evolutionary step between LMXBs and recycled MSPs (see e.g. Roberts, 2013; Jia & Li, 2015), where the mass transfer between a non-degenerate companion and the pulsar may have temporarily halted. This is demonstrated by the example of the first redback pulsar, PSR J1023+0038, which was shown to have lost an earlier-observed accretion disk (Wang et al., 2009), suggesting that the spin-recycling fueled by the binary companion had only recently halted, with the pulsar having depleted the remaining material in the accretion disk.

1.4.2 Nulling, intermittent & mode changing pulsars

First directly noted by Backer (1970a), *nulling* pulsars are pulsars whose emission appears to abruptly switch between 'off' and 'on' states. During 'off' intervals, no pulsed emission is detected from the pulsar. Although the terms are sometimes used interchangeably, in this thesis the term 'nulling pulsar' is used to refer to pulsars whose 'off' states are of a timescale on the order of individual pulse periods to as long as several minutes, while an 'intermittent pulsar' is defined as one whose 'on' and 'off' states have much longer timescales, from hours to days or even years in extreme cases. The fraction of time a pulsar spends in its 'off' state is referred to as its *nulling fraction*. 'Off' phases can also be accompanied by a change in the pulsar's spin properties (see,

[15] https://apatruno.wordpress.com/about/millisecond-pulsar-catalogue/
[16] See footnote 15.

e.g. Kramer et al., 2006a).

A potentially related pulsar phenomenon is that of *mode changing*. First observed by Backer (1970b) in the pulsar PSR B1237+25, the term describes a pulsar whose pulsed emission appears to abruptly change between multiple discrete 'modes'. While this is primarily seen in a change in the shape of the pulse profile, changes in luminosity (see, e.g. Sobey et al., 2015), spin properties (see, e.g. Lyne et al., 2010) and other parameters may also be observed.

Both the nulling and mode-changing behaviours are likely linked to highly-ordered changes in the pulsar emission process (Lorimer, D. R. and Kramer, M., 2005), with recent work (see, e.g. Lyne et al., 2010) suggesting that global changes in the configuration of the pulsar magnetosphere may be responsible, although the mechanisms responsible for these changes are not yet understood. Nulling, intermittent and mode-changing pulsars may actually be manifestations of the same phenomenon, with nulling simply representing an extreme case of mode-changing behaviour, or an emission mode too weak to be detectable by current telescopes (see, e.g. Young et al., 2015).

1.4.3 Glitching pulsars

A pulsar *glitch* is marked by a sudden increase in the pulsar's rotational frequency, followed by a slow relaxation towards the original spin period. However, permanent post-glitch changes to the spin period are often observed even well after the relaxation phase, (see, e.g. Yuan et al., 2017). The phenomenon was first observed in the Vela pulsar (Radhakrishnan & Manchester, 1969), and Vela remains a particularly glitch-prone pulsar to this day. Glitches are typically associated with a younger pulsar population (see, e.g. Shemar & Lyne, 1996) and are relatively uncommon, with only 482 glitches spanning 168 pulsars having been published as of October 2017[17] (Espinoza et al., 2011), although as the detection of a glitch involves observing the pulsar within a specific window of time, the potential for a selection bias exists in the estimation of the glitch rate.

The physical mechanism responsible for glitches remains a subject of ongoing discussion, due in part to the limited number of glitches available for study and their unpredictable occurrences. Early models, such as those put forward by Baym et al. (1969), suggested that 'starquakes' in the crust of the NS might be responsible. In such a model, the oblate crust of the NS cracks under strain caused by the pulsar's natural long term spin-down. This change in the crust modifies the moment of inertia of the pulsar, thereby inducing a spin-up event through the conservation of angular momentum. However, this model fails to account for multiple details of the glitch phenomenon (see, e.g. Ruderman, 1976). The currently favoured model (see, e.g. Anderson & Itoh, 1975; Ruderman, 1976; Alpar et al., 1981) explains glitches as the result of a coupling interaction between pinned regions of localised vorticity which form in the neutron superfluid region of the NS, and the crust of the NS itself. As these vorticity regions become pinned and unpinned, they can induce a rapid transfer of angular momentum to the crust of the NS, thereby producing the observed spin-up.

[17] http://www.jb.man.ac.uk/pulsar/glitches.html

1.4.4 Magnetars

A portmanteau of 'magnetic star', the term *magnetar* refers to a particular class of unusually energetic NSs whose surface magnetic fields appear to be exceptionally strong, on the order of $B_{\rm surf} \simeq 10^{14}$ to 10^{15} G, representing the strongest magnetic fields in the Universe. First proposed by Duncan & Thompson (1992), magnetars form an explanatory model for two observationally-defined, high-energy astrophysical phenomenon, soft gamma repeaters (SGRs) and the anomalous X-Ray pulsars (AXPs) (for a review, see Woods & Thompson, 2006). As the X-ray luminosities observed from these sources are well beyond the available $\sim 10^{33}$ ergs s^{-1} that can be provided by a rotationally-powered source such as a conventional radio pulsar, magnetars are believed to be powered directly by their decaying, high-strength magnetic fields (Thompson & Duncan, 1995; Kaspi, 2004). A secondary consequence of this strong magnetic field is a rapid spin-down of the rotational period, and as such magnetars are typically found with longer spin periods between approximately 2 to 12 seconds[18] (Olausen & Kaspi, 2014).

Initially, magnetar emission was thought to be limited only to high energy wavelengths, such as the gamma and X-ray bands. However, further observations have since demonstrated that magnetars can also be observed in the radio spectrum. The previously-discovered AXP magnetar XTE J1810−197 was identified as a transient, pulsating radio source following an X-ray outburst in 2003 (Camilo et al., 2006), with a second AXP magnetar, 1E 1547.0−5408, shown to display radio pulsations shortly thereafter (Camilo et al., 2007). Radio observations have also led to the direct discovery of new magnetars, the first being PSR J1622−4950 (Levin et al., 2010). Radio observations were also employed in the confirmation of perhaps the most scientifically-significant magnetar discovered to date, PSR J1745−2900 (Eatough et al., 2013b). PSR J1745−2900 lies within ~ 3 arcsec of Sgr A*, the supermassive BH at the center of the Milky Way Galaxy, and is considered likely to be in a bound orbit around Sgr A* (Bower et al., 2015). If this is the case, PSR J1745−2900 may be able to act as a rare probe of the environment surrounding the BH[19]. PSR J1745−2900 also holds the record for the highest radio frequency detection of any pulsar, having been observed as high as 291 GHz (Torne et al., 2017), and as such may provide additional clues into the processes of both pulsar and magnetar radio emission.

1.5 Scientific applications of pulsars

In addition to the tests of strong-field gravity as outlined in Section 1.1.2, pulsars can also serve a wide variety of additional scientific applications, many of which have already been touched on as part of the earlier discussions in this chapter. These applications provide additional motivation for the ongoing search, discovery and study of ever more diverse pulsars. The following list outlines a number of fields of scientific interest to which pulsars are able to make significant contributions. Note once again that this

[18] See footnote 12

[19] Unfortunately, PSR J1745−2900 has neither sufficient proximity to Sgr A* or timing precision to serve as the long-sought relativistic pulsar-BH binary described in Section 1.1.2.3 (Wex, 2014).

list is not intended to be exhaustive, but simply serves to demonstrate the versatile number of applications which pulsars can serve.

- **Direct detection of gravitational waves.** While relativistic binary pulsars serve well as laboratories for testing gravitational theories in the quasi-stationary strong-field regime, and are also capable of indirectly detecting the presence of GW (see Section 1.1.2), a network of MSPs with extremely high timing precision (≤ 100 ns; see e.g. Jenet et al., 2005) known as a *pulsar timing array* can potentially be applied to directly detect gravitational waves in the nano-Hz frequency band. A GW signal detected by such an array would produce a correlated residual signature amongst the individual residuals from each of the timed pulsars. Compared to ground-based detectors, which to date have picked up the mergers of stellar-mass BH-BH (Abbott et al., 2016) and DNS binary systems Abbott et al. (2017b), PTAs are expected to be sensitive to the stochastic GW background produced by merging supermassive BH-BH systems (see e.g. Sesana, 2013) as well as other cosmological processes (see e.g. Maggiore, 2000). To date, three separate pulsar timing array projects are underway, including the Parkes Pulsar Timing Array (PPTA; Manchester et al., 2013), the European Pulsar Timing Array (EPTA; Kramer & Champion, 2013), and the North American Nanohertz Observatory for Gravitational Waves (NANOGrav; McLaughlin, 2013), which combined form the International Pulsar Timing Array (IPTA; Manchester & IPTA, 2013). The challenges associated with this technique mean that a detection of GW via PTAs has yet to be made. Ongoing monitoring of existing PTA pulsars and the discovery of additional high timing precision pulsars, as well as the development of next-generation telescopes such as MeerKAT[20] and the SKA, will be crucial in reaching this important scientific goal.

- **The behaviour of matter at ultra-high densities.** Although already discussed in detail in Section 1.2.2, it is worth reiterating that pulsars currently provide one of the only means of probing matter at the ultra-high densities found in NSs and determining the EOS[21]. As each proposed EOS makes predictions regarding the limiting masses, radii and spin periods of pulsars, discovering new pulsars which push quantities to even further extremes allows for certain EOS to be ruled out. For example, the two most-massive pulsars to date, PSR J1614−2230 ($1.97(4)\,M_\odot$; Demorest et al., 2010) and PSR J0348+0432 ($2.01(4)\,M_\odot$; Antoniadis et al., 2013) rule out a number of EOS which predict the formation of 'exotic' matter within the NS (Demorest et al., 2010). Furthermore, a constrained measurement of the moment of inertia of a NS, which directly relates to the mass and radius of the star, would provide significant further constraints on the EOS (see e.g. Lattimer & Schutz, 2005; Kehl et al., 2016). Additionally, the study of other phenomena such as pulsar glitches can be used to further probe the me-

[20] http://www.ska.ac.za/science-engineering/meerkat/

[21] The recent GW observation of a DNS merger (Abbott et al., 2017b) provides a new avenue for studying the EOS of NSs (see e.g. Abbott et al., 2017a)

chanics of the NS interior (see Section 1.4.3), providing further insight into the behaviours of matter at these densities.

- **Plasma physics in extreme environments.** Since the early days of pulsar astronomy, it has been recognised that a plasma-filled magnetosphere plays a critical role in the pulsar emission process (Goldreich & Julian, 1969), although the precise mechanics of this process remain an ongoing source of discussion (for a recent review, see Cerutti & Beloborodov, 2017). The plasma which surrounds the NS is subject to very high densities and strong magnetic fields, and as with the study of ultra-high density matter, pulsars represent one of the only means of studying the behaviour of plasma under these conditions. As described in Section 1.4.2, the nulling and mode-changing behaviour observed in many pulsars, along with the timing noise observed in others, are thought to be linked to global changes in the pulsar magnetosphere (Lyne et al., 2010). Studying these aspects of pulsar behaviour may therefore allow for models of the behaviour magnetosphere to be developed (see e.g. Yuen & Melrose, 2017). The observed interaction between the magnetospheres of the two pulsars in PSR J0737−3039 also provides a number of unique opportunities to explore and test aspects of plasma physics under these extreme conditions (see Kramer & Stairs, 2008, and references therein).

- **The structure of the Galaxy and the ISM.** As discussed in Section 1.3 the effects of pulse dispersion, scattering and scintillation can all be used as tools to probe the structure of the ISM along various lines of sight, the results of these studies having been used to construct a number of the electron density distribution throughout the Galaxy. Any observing variation in these characteristics (for example, a variation in DM or the observing scattering time τ_s) can also be used to probe dynamic changes in the ISM (see e.g. Maitia et al., 2003). In addition, pulsars can also be used as excellent probes of the *magnetic* structure of the Galaxy, as the effect of Faraday rotation alters the polarisation characteristics of the incoming pulsar signal as it traverses the ISM (see e.g. Han, 2013).

- **Processes of stellar and binary evolution.** The observed abundance and variety of pulsar binary systems (as briefly reviewed in Section 1.4.1) can provide a great deal of information regarding the processes of stellar and binary evolution which exist within both the disk of the Galaxy as well as in surrounding globular clusters, which are subject to different star-forming and evolutionary conditions (see e.g. Freire, 2013). In a sense, binary pulsars act as fossil records of the binary processes which led to their formation, with the discovery of ever more unusual systems such as the pulsar triple system (Ransom et al., 2014) or the new class of eccentric MSPs (see e.g. Antoniadis, 2014; Barr et al., 2017) motivating further research into how these systems are able to form. Indeed, some of the binary pulsars reported in this thesis pose their own unique evolutionary questions, including PSR J1618−4624 (see Section 3.4.2) and PSR J1757−1854 (see Chapter 4).

- **Determining the properties of the true pulsar population.** Despite the discovery of over 2600 pulsars to date and the breadth of pulsar behaviour which they encapsulate, it is estimated that there may be as many as $\sim 10^5$ active radio pulsars within the Galaxy[22] which beam towards the Earth (Faucher-Giguère & Kaspi, 2006), and are therefore potentially detectable. Furthermore, the population of pulsars which have been discovered thus far are subject to a number of selection biases, although these vary from survey to survey (see Section 2.7). For example, the limited flux density sensitivity of current and previous pulsar surveys, although having vastly improved over the years, provides a selection bias in terms of both luminosity and distance, while limitations in sampling time and bandwidth channelisation have discriminated against the detection of MSPs. Biases introduced by the choice of data-reduction technique, such as the noise limitations of the Fast Fourier Transform (FFT; Lazarus et al., 2015), or by the availability of the computational resources necessary to conduct searches with sufficiently-fine resolution also play a role. Only by continuing to combat these selection biases and conduct further searches for the remaining population of pulsars can we hope to determine a more accurate understanding of the full pulsar population and thereby develop better models of the behaviour of pulsars as a unified class of objects, and this goal forms one of the primary motivations of the all-sky HTRU survey (Keith et al., 2010) and its Galactic-plane component (HTRU-S LowLat) on which this thesis focuses.

1.6 Thesis outline

This thesis represents the culmination of over three years of intensive research, with the goal of both developing and applying new and innovative pulsar searching techniques in order to facilitate the discovery of new and scientifically-interesting pulsars. In particular, the ultimate goal of this research project has been the discovery of new relativistic pulsar binaries, capable of further pushing the limits of tests of GR and other gravitational theories. The primary purpose of this chapter has been to lay out a basic understanding of the workings and variety of the pulsar population, to justify the role that pulsars play in both tests of gravitational theories and a wide range of other scientific areas, and to provide motivation for the research conducted in this project. The remainder of this thesis is structured as follows:

- **Chapter 2** provides an overview of the means by which pulsars are discovered through the process of pulsar searching. This includes a description of the hardware setup required to conduct a pulsar observation, as well as a number of fundamental techniques and algorithms involved in conducting a large scale, blind pulsar search. Also described are the basics of pulsar timing, a process by which information about a pulsar's behaviour can be determined with extremely high precision, and which serves as one of the primary tools in the scientific exploitation of pulsars. The chapter concludes with a brief overview of those pulsar

[22] Not counting those found in globular clusters or the SMC/LMC

surveys whose focus has been along the Galactic plane, the region studied by the HTRU-S LowLat survey (on which this thesis focuses).

- **Chapter 3** documents the results of the processing of the latter $\sim 50\,\%$ of the HTRU-S LowLat survey through the 'partially-coherent segmented acceleration search', which has resulted in the discovery of 40 new pulsars, of which at least 7 are in binary systems. Provided in this chapter are the properties of all 40 new pulsars, 23 of which have full timing solutions, as well as in-depth analyses of some of the more scientifically-interesting discoveries. Also included are a summary of the search strategy, an assessment of the survey's performance with regard to the expected number of pulsar re-detections and the encountered number of pulsar non-detections, as well as a comparison of the population of 100 pulsars (to date) which have been discovered in the HTRU-S LowLat survey to the previously-known Galactic-plane pulsar population.

- **Chapter 4** highlights PSR J1757−1854, a newly-discovered relativistic binary and the flagship discovery of the HTRU-S LowLat survey. Included is a description of the 1.6-year multi-frequency, multi-telescope timing campaigns carried out during the follow-up of PSR J1757−1854, a summary of its remarkable relativistic qualities and likely evolutionary history, and a discussion regarding the new tests of GR and other gravitational theories which PSR J1757−1854 is likely to enable within the next $7 - 9$ years.

- **Chapter 5** presents an in-depth investigation of a pulsar-searching technique known as the Fast Folding Algorithm (FFA). Included is an analysis of the behaviour of the algorithm as a pulsar-searching tool under theoretical ideal conditions, as well as a trial of the technique on real-world observational data taken from the HTRU-S LowLat survey. This trial also includes a comparison of the FFA's performance to that of the FFT, which currently forms the backbone of the majority of pulsar searches.

- **Chapter 6** closes this thesis with a brief summary of the results and conclusions derived from this research, as well as an overview of anticipated future work.

Chapter 2

Methods of pulsar discovery and exploitation

If Chapter 1 represents the 'what' and 'why' of pulsars and the reasons for their ongoing scientific study, then this chapter is very much intended to provide the 'how' and the 'where'. Summarised here are the essential methods and techniques by which pulsars are first discovered as part of pulsar surveys, and then scientifically exploited through the process of pulsar timing. These discussions are presented in mostly generic terms, but with specific focus on those aspects which are most relevant to the scientific content presented in this thesis. Therefore, particular attention is given to the role played by the Fast Fourier Transform (FFT) and the Fast Folding Algorithm (FFA), as well as the techniques involved in discovering, solving and timing pulsars in binary systems. The chapter concludes with a brief review of the history of pulsar surveys undertaken along the Galactic plane both past and present, thereby setting the High Time Resolution Universe pulsar survey (HTRU; Keith et al., 2010) in its appropriate context.

Contents

2.1 Data acquisition

The process of acquiring an astrophysical radio signal involves three core components; the physical telescope antenna, the frontend (which collects, amplifies and mixes the received signal) and the backend (which converts the received signal into a format which can be easily processed). A typical schematic of these components is presented in Figure 2.1. Although an in-depth overview of the data acquisition system is beyond the scope of this thesis, a summary of those points important to the science in later chapters is presented here.

2.1.1 Telescope basics

Pulsars are among the weakest radio sources known and, as noted in Chapter 1, suffer from a number of effects which can further reduce their detectability. For example, at lower observing frequencies pulsars may experience scattering effects (see Section 1.3.2) while at higher frequencies their flux density is seen to decrease (see, e.g. Bates et al., 2013). As a result of this combination of factors, large single-dish telescopes capable of observing at intermediate frequencies between approximately $0.4 - 3\,\mathrm{GHz}$ have served as the backbone of pulsar astronomy. Current notable examples include the 64-m Parkes Radio Telescope (Australia), the 100-m Effelsberg Radio Telescope (Germany), the 76-m Lovell Telescope at the Jodrell Bank Observatory (UK), the 100-m Green Bank Telescope (GBT; USA) and the 305-m Arecibo Telescope (USA). The majority of single-dish telescopes share the same essential configuration: a symmetric, parabolic surface designed to focus incoming radio frequencies (RF) to a central focal point, at which are mounted a number of interchangeable receivers. Additionally, a number of telescopes have the ability to redirect the incoming RF to a secondary focal point at which additional receivers are made available.

Two quantities which come into play in the later science chapters of this thesis are are the telescope beam *full width at half maximum* (FWHM) and the telescope *gain*. As a single-dish telescope points at a particular on-sky location, its specific geometry (typically a circular aperture with parabolic curvature) causes it to act as a diffraction grating, generating an aperture illumination pattern or *power pattern*. Typically this pattern consists of one central beam, with the telescope's sensitivity strongest at the center of the beam (aligning with the telescope *boresight*, the optical axis of the telescope) and with decreasing sensitivity as the angular offset from the beam center (θ) increases. The primary beam may also be surrounded by *side lobes* where the telescope's sensitivity experiences a minor, localised increase. An example of a telescope power pattern can be seen in Figure 2.2. The diameter of the primary beam is typically characterised by the FWHM, the angular diameter of the region at

which the response of the beam falls to half its central peak value. Modeling the power pattern as a Bessel function (see e.g. Rohlfs & Wilson, 2000) allows the FWHM to be defined as

$$\mathrm{FWHM} = 1.02\,\mathrm{rad}\frac{\lambda}{\eta D} \simeq 58.4^{\circ}\frac{\lambda}{\eta D} \tag{2.1}$$

where λ is the wavelength of the incoming RF, D is the telescope diameter and η is a dimensionless quantity describing the telescope efficiency.

Meanwhile, the telescope gain describes the raw sensitivity of the telescope. As described in Lorimer, D. R. and Kramer, M. (2005), the gain G can be defined as

$$G = \frac{\eta\pi D^2}{8k_{\mathrm{B}}} \tag{2.2}$$

where k_{B} is Boltzmann's constant. As $G \propto D^2$, and the measured signal to noise ratio (S/N) of a given pulsar in a particular observation scales linearly with G (see Equation 2.23), a larger telescope typically delivers significant advantages when undertaking pulsar observations.

2.1.2 Frontends

The telescope *frontend* typically refers to the initial portion of the receiving system which collects and amplifies the incoming RF signal before later down-converting it to a lower frequency. The signal path begins with the receiver *feed horn*, which is placed at the focal point of the telescope and gathers the incoming RF. A probe inside the feed-horn then samples the RF signal at two orthogonal polarisations, converting the raw electromagnetic waves into a series of analog voltages. Despite the focal amplification provided by the design of the telescope, the incoming signal is still remarkably weak, therefore a low-noise amplifier (LNA) is applied to the signal. In order to mitigate the introduction of thermal noise, the LNA is cryogenically cooled, typically to temperatures on the order of a few tens of Kelvin. Following the LNA, the signal is then processed through a *bandpass filter* in order to sample a specific frequency band of the incoming RF. Additional filters may also be employed at this stage to mitigate specific instances of RFI (see Section 2.2.1), along with additional RF amplifiers as required by the specific observing system under consideration.

At this point in the signal path, the RF signal is typically passed through a *mixer* in order to down-convert it to a lower intermediate frequency (IF). This is necessary both because it reduces the cable transmission losses of the signal, which are more pronounced at higher frequencies, and because low-noise signal-processing components operating at lower frequencies are much easier to produce. Therefore, the RF signal (at frequency f_{RF}) is mixed with a monochromatic signal of frequency f_{LO} produced by a *local oscillator* (LO) in a process known as *heterodyning*. This mixing process produces a resulting IF at $f_{\mathrm{IF}} = f_{\mathrm{RF}} - f_{\mathrm{LO}}$, which is further isolated by a second bandpass filter. The signal is then processed through a chain of additional IF amplifiers in order to achieve stable amplification, before being transmitted via cable to the backend system.

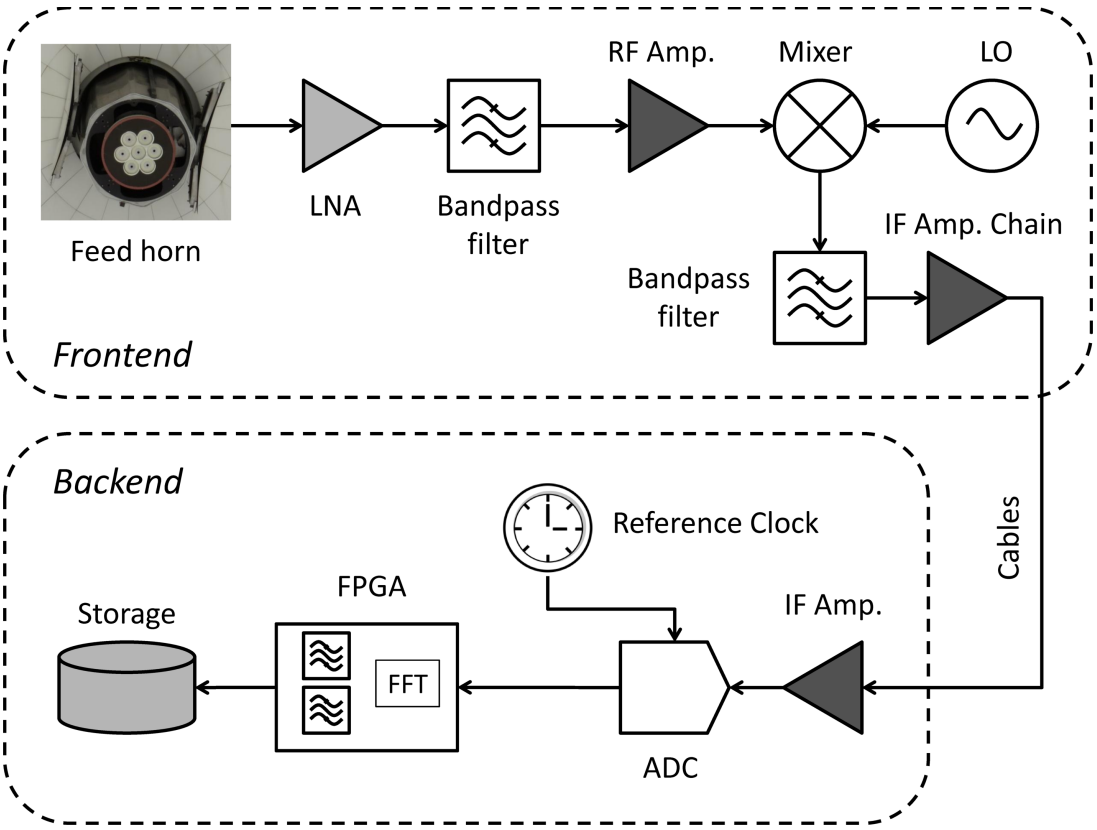

Figure 2.1: A schematic of the signal path of an example telescope frontend and backend, as described in detail in Sections 2.1.2 and 2.1.3. The backend configuration displayed here is that of a polyphase filter bank (PFB), which performs the bulk of its processing in its field-programmable gate array (FPGA). The inset FPGA schematic depicts both the FFT processing step and the channelisation of the signal through multiple narrow-band bandpass filters.

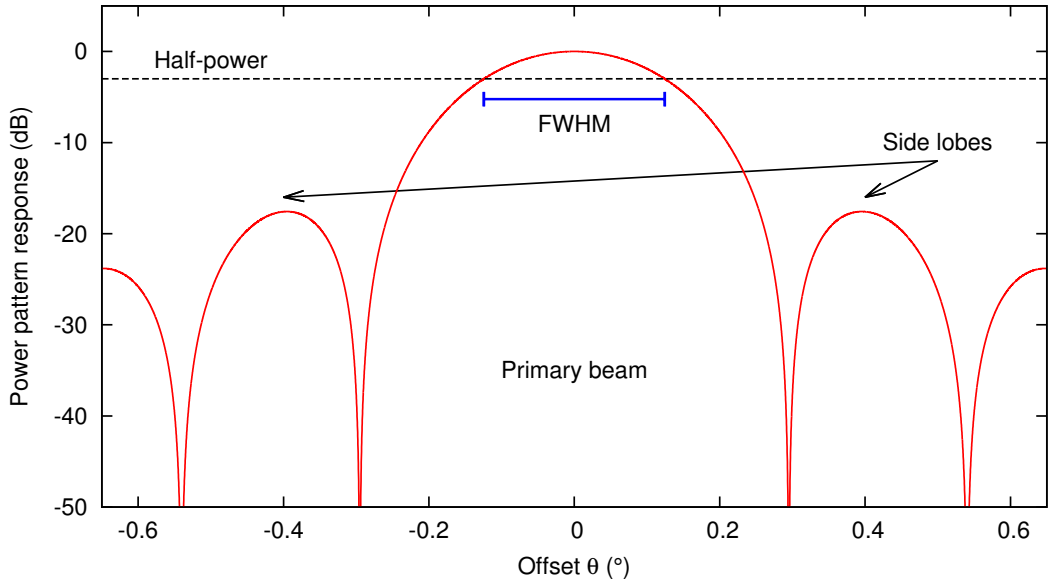

Figure 2.2: An example of the power pattern of a circularly-symmetric parabolic telescope as function of the offset from the central position of the beam (θ). The vertical scale is presented in dB with the maximum power at the center of the primary beam taken as the reference power. The FWHM of the primary beam is also displayed. Although the power pattern generally decreases with increasing $|\theta|$, side lobes (localised increases in the pattern) are also encountered. The configuration of these side lobes is dependent on the precise geometry of the telescope.

2.1.3 Backends

The telescope *backend* is responsible for the sampling and conversion of the IF signal into a useful digital format for processing and long-term storage. While the frontend is typically designed as a general purpose instrument, allowing it to be used for multiple astrophysical applications, backends are typically much more specialised. Two common backend types are of particular interest in pulsar observations:

- **Polyphase filter banks (PFB)** - After additional amplification, the incoming IF signal is first digitised into n-bit numbers using an analogue-to-digital converter (ADC) sampling at the Nyquist frequency so as to preserve the original signal. Each digital sample is timestamped using a high-precision reference clock such as a hydrogen maser. The digitised IF signal is then passed through a field-programmable gate array (FPGA) which processes discrete blocks of data through a FFT (see Section 2.3.1), resulting in the production of Fourier spectrum every few microseconds. This process also involves the channelisation of the data, dividing it into narrow frequency channels so as to minimise the effects of intra-channel dispersive smearing (see Section 2.2.2). Depending upon the intended application of the data, the resulting Fourier spectra may be handled in one of several ways. For search-mode data (intended to allow for the discovery of a pulsar whose spin period and other properties are unknown), the spectra are integrated to give sampling rates on the order of tens of microseconds, with the two orthogonal polarisation signals also having been summed together as this information is typically not required for search applications. The data is then written out to a long-term storage medium for later analysis. Alternatively, filterbank data recorded in timing mode (for a pulsar whose properties have previously been determined) will be folded according to the changing period of the pulsar being observed, producing a compact timing archive (see Sections 2.4 and 2.6) which is then written to storage. An example PFB backend configuration is portrayed in Figure 2.1.

- **Baseband sampling** - One significant disadvantage of the PFB is that it allows only for *incoherent* de-dispersion, where individual frequency channels can be re-aligned in post-processing, but the intrachannel dispersive smearing remains, lowering the signal-to-noise ratio (S/N) of an observed pulsar (see Section 2.2.2). This effect can be removed through the process of *coherent* de-dispersion, which requires access to the raw complex IF voltages as produced by the telescope frontend. In its simplest form, *baseband sampling* (see e.g., Stairs et al., 2000; Lorimer, D. R. and Kramer, M., 2005) involves mixing the IF signal with a secondary LO. This process produces two mixed signals, the second signal having been mixed with the same LO signal but with an applied phase shift of 90°. Combining these two signals allows for the digital sampling through additional ADCs of complex-valued baseband data, retaining both the amplitude and phase of the original IF voltages. Coherent de-dispersion can then be achieved by applying an inverse transfer function to the baseband voltages, with the transfer func-

tion being specific to the dispersion measure (DM) of the pulsar being observed (Hankins, 1971; Hankins & Rickett, 1975). Hence, this observing mode is only practical when the DM of the pulsar is previously known, making it impractical for pulsar searching. The resulting baseband data may either be written to disk as-is for later processing, folded on-line as part of coherently de-dispersed timing observations, or itself converted to channelised filterbank-format search mode data after having been coherently de-dispersed. This final mode is useful when observing known pulsars whose spin properties have not been well established, especially in the case of binary pulsars.

2.2 Standard searching methods

In the 50 years since the discovery of the first pulsars, a comprehensive suite of tools, techniques and algorithms have been developed in order to search for the signals of increasingly-weak, undiscovered pulsars in observational data. These techniques are typically assembled into a *pulsar search pipeline*, a standardised chain of data reduction and search techniques built to facilitate the processing of large amounts of observational data in a systematic and reproducible fashion. Common software packages employed in modern search pipelines include SIGPROC[1] (Lorimer, 2011) and PRESTO[2] (Ransom, 2001), both of which can be used to implement the majority of the pulsar searching techniques detailed in this chapter.

Although each pipeline will be custom-tailored to suit the needs of each individual search, a typical overall structure tends to emerge. An example of one such pipeline is shown in Figure 2.3. For clarity, this example pipeline is color-coded to represent three basic, common stages:

- **Initial standard search techniques (red):** a set of techniques largely common to all pulsar search pipelines, including RFI mitigation and de-dispersion. The remainder of this section deals with these techniques.
- **The pulsar searching algorithm (blue):** the core pipeline algorithm which produces the list of initial pulsar candidates. A sophisticated pipeline may operate using multiple algorithms in parallel, with the choice of algorithm playing a large role in the types of pulsars to which the pipeline is sensitive. A selection of search algorithms are detailed in Section 2.3.
- **Candidate optimisation and review (green):** techniques involved in efficiently selecting those pulsar candidates which may represent true pulsar discoveries. The precise methods involved are often dependent on the choice of pulsar search algorithm, with common approaches detailed in Section 2.4.

This structure of the example pipeline in Figure 2.3 approximately conforms to the structure of the pipeline applied to search for pulsars in the High Time Resolution

[1] http://sigproc.sourceforge.net
[2] http://www.cv.nrao.edu/ sransom/presto

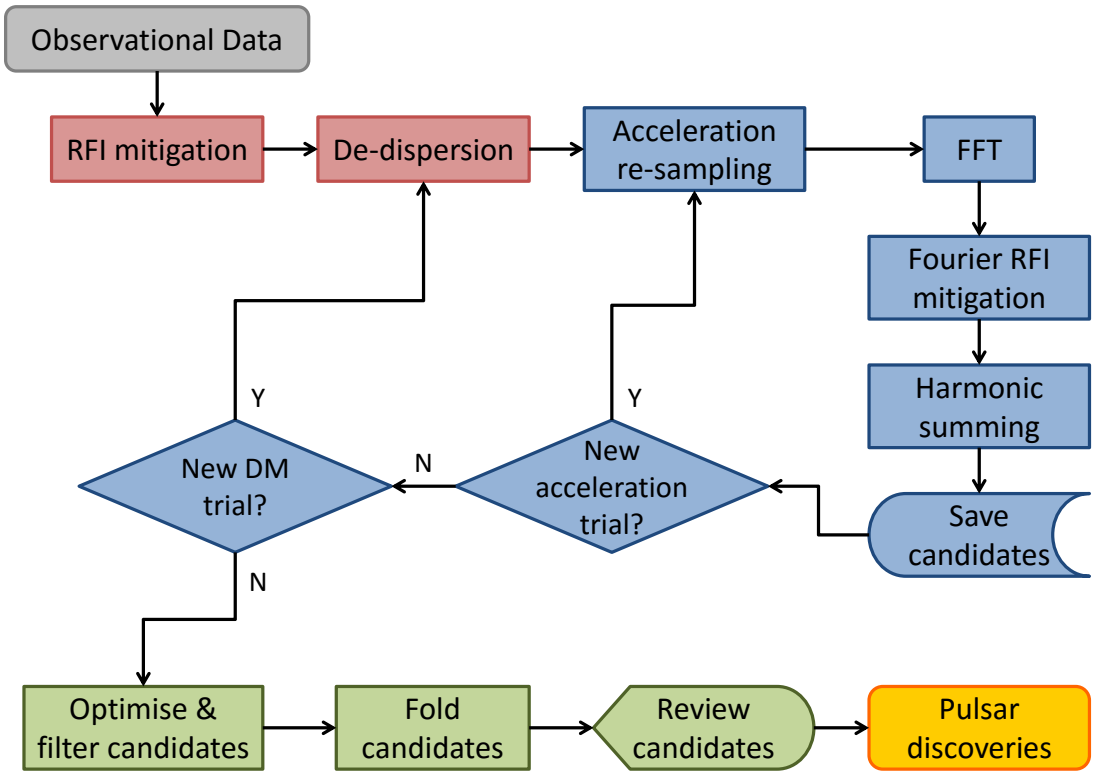

Figure 2.3: An example of a typical pulsar search pipeline. This pipeline is based around an FFT periodicity search with an additional acceleration-search component designed to search for binary pulsars. Further description is provided in Section 2.2.

Universe South Low Latitude pulsar survey (HTRU-S LowLat; Ng et al., 2015), as described in Chapters 3 and 4. In both cases, the core search algorithms of these pipelines use a periodicity search based around an FFT (see Section 2.3.1), coupled with an acceleration search designed to compensate for any unknown binary motion of an undiscovered pulsar (see Section 2.3.3). As such, much of the discussion of pulsar search algorithms presented in this chapter focuses both on Fourier-based periodicity searches and on current binary searching techniques, with the specific implementation applied to HTRU-S LowLat further discussed in Section 3.1. Some focus is also given in this chapter to the FFA, with a much more comprehensive discussion presented in Chapters 5. Additional pulsar searching algorithms such as those involved in single-pulse searches (for recent work see e.g., Burke-Spolaor et al., 2011; Devine et al., 2016; Adámek & Armour, 2016) are largely outside the scope of this thesis, and are not discussed here.

2.2.1 RFI mitigation

Radio frequency interference (RFI) refers to any terrestrial radio signal, both natural and man-made, which can interfere with astrophysical radio observations. As radio

telescope observing systems are specifically designed to detect extremely weak radio signals, even moderate sources of RFI can cause an astrophysical signal to be entirely obscured, either by saturating the receiver or, in the case of modulated or otherwise semi-periodic RFI, by overwhelming a pulsar search pipeline with large quantities of false candidates. Although electrical devices which deliberately transmit in the radio band (such as mobile phones, satellites, airport and military radars, etc.) do account for a significant portion of RFI instances, **any** improperly shielded electrical device can produce significant RFI, up to and including the computing systems at the observatory itself and even the AC oscillation associated with the mains power supply. These instances come in addition to naturally-occurring sources of RFI, lightning being an obvious example. With the ever-increasing prevalence of electrical technology, especially wireless and other transmitting devices, mitigating the influence of RFI is an ever-increasing challenge, and it remains a necessary first step in any pulsar search pipeline.

With regard to pulsar observations, a number of techniques currently exist that are designed to target specific types of RFI which occur in different observing regimes. These techniques are summarised in the following sections. Note that some of these methods, such as RFI mitigation in the Fourier regime, are specific to particular pulsar searching algorithms and may be applied at later stages in the pipeline (as per the example in Figure 2.3). However, for completeness they have been included here as part of an overall discussion of RFI mitigation techniques.

2.2.1.1 Time domain

As RFI is generated by terrestrial sources, it is unlikely to show the effects of (apparent) dispersion[3]. As a result, one extremely useful RFI-mitigation technique is to generate a time series (see Section 2.2.2) at DM $= 0\,\mathrm{cm}^{-3}\,\mathrm{pc}$. One can then statistically analyse this time series by comparing each data sample (or group of samples) to the approximately-Gaussian distribution expected from the averaging together of the individual frequency channels in the original filterbank observation. Any sample identified as an outlier, and therefore having likely been contaminated by RFI, can either be 'clipped' to a given threshold value or replaced by Gaussian noise constructed to match the surrounding clean data samples. This technique is most sensitive to the mitigation of short-duration, impulsive RFI.

2.2.1.2 Frequency domain

Certain varieties of RFI are localised to specific, narrow electromagnetic frequency bands. Therefore, by integrating an observation in time across the length of the observation, the frequency *bandpass* of the observation can be statistically analysed to determine which frequency channels contain excessive power due to the presence of narrow-band RFI. Afterwards, as with time-domain RFI, the affected data can either

[3]The recent example of 'perytons' being a notable exception (Petroff et al., 2015b).

be replaced by zeroes or by Gaussian noise sampled from the surrounding uncontaminated data. Although this form of RFI mitigation can be conducted in a manner specific to each individual observation, commonly-occurring RFI sources specific to each telescope may often by targeted by the use of a static channel mask, which can be applied either in post-processing after the data has been recorded or, as noted in Section 2.1.2, as part of the RF signal path itself.

2.2.1.3 Fourier domain

Periodic or semi-periodic RFI, which may be too weak to be directly detected in either the time or frequency domains, may reveal itself after a time series has been processed through a Fourier transform (see Section 2.3.1). Figure 2.4 shows an example of this type of RFI contamination, with individual instances of Fourier domain RFI sometimes being referred to as a *birdie*. This type of RFI can be particularly problematic in pulsar searching, as these false birdie signals can overwhelm a list of pulsar candidates, which is derived from analysing those Fourier bins which have locally-high Fourier S/N (see Section 2.3.1.3). Similarly, it can be difficult to distinguish between a birdie and a genuine pulsar candidate without additional information, making this type of RFI harder to remove. One strategy is to use a fixed list of previously-identified birdie frequencies to mask out known RFI signals (see e.g., Keith et al., 2010). Contaminated regions of the Fourier spectrum can then be replaced (as per the time and frequency-domain techniques) either by setting the affected bins to zero or by replacing them with Gaussian noise sampled from the surrounding spectrum. While this strategy can be effective, if the mask is applied too broadly it can also accidentally mask the signal of a real pulsar which may be close to a known RFI source.

2.2.1.4 Red noise

An additional form of interference is *red-noise* contamination. As opposed to the other forms of RFI described in this section, which typically comes from external sources, red noise occurs as a result of longer-term variations often within the observing setup itself, such as thermal variations in the receiver. This causes the baseline of the otherwise Gaussian noise observed in a typical time series to gradually vary with time. Processing the time series through a Fourier transform (see Section 2.3.1) reveals this noise as large increase in Fourier power present at very low frequencies (the 'red' end of the spectrum). Depending upon the timescale of the red noise present in a given observation, this increase in Fourier power can overwhelm the signal of long-period pulsars ($P \gtrsim 1\,\mathrm{s}$), causing a reduction in their detectability (see e.g., Lazarus et al., 2015). Searches based in the time domain such as the FFA may also suffer from the influence of red noise, although with differing response characteristics to searches based in the Fourier domain (see Chapter 5 for a detailed review). An example of red noise contamination in both the time and Fourier domains can be seen in Figure 2.5.

Techniques exist to mitigate red noise in both the time and Fourier domains. In the time domain, a time series can be de-reddened through the use of a running median

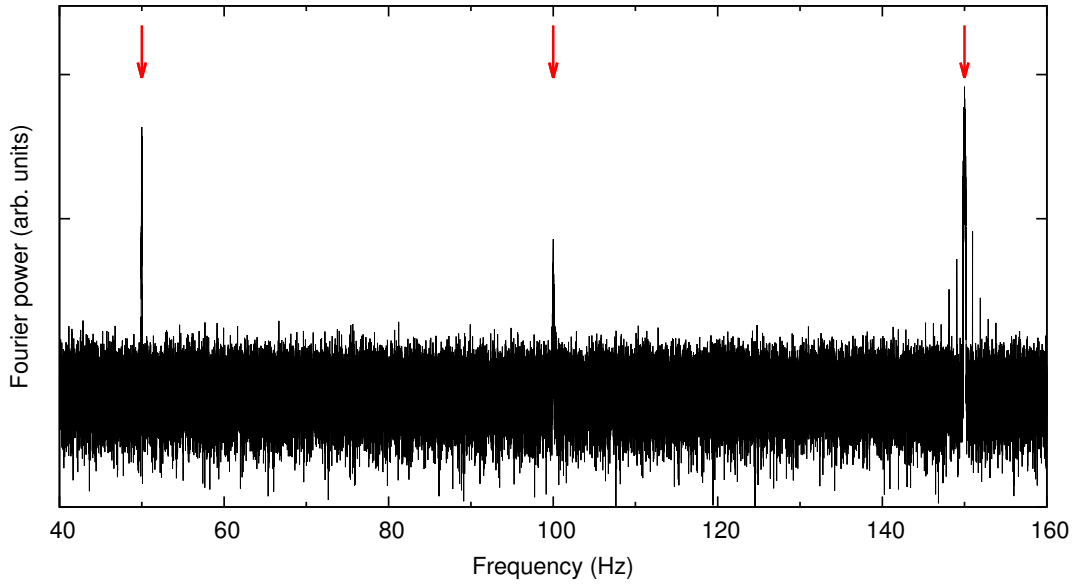

Figure 2.4: An example of a periodic RFI signal present in the DM = 0 cm^{-3} pc Fourier power spectrum of an observation from HTRU-S LowLat. The marked RFI instance at 50 Hz is caused by contamination from the 50-Hz AC signal of the Australian mains power supply, with harmonically-related instances of RFI also marked at 100 and 150 Hz.

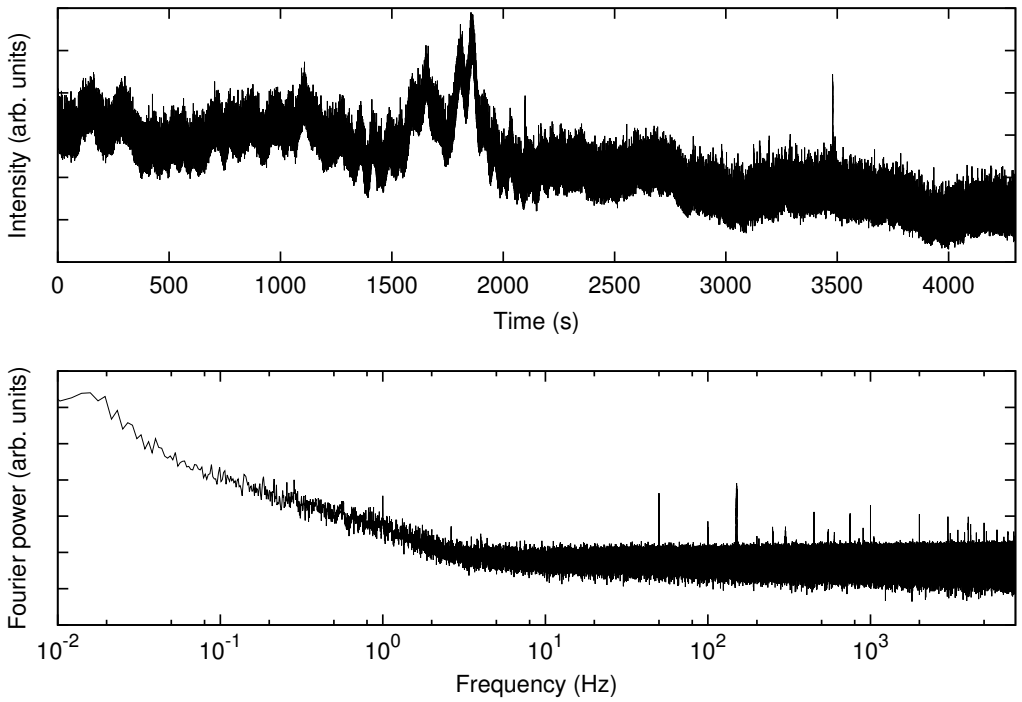

Figure 2.5: A demonstration of the effects of red-noise contamination. Shown here is the DM = $0\,\mathrm{cm}^{-3}\,\mathrm{pc}$ time series (top) and corresponding Fourier power spectrum (bottom) of an observation from HTRU-S LowLat. The effect of red noise in the time domain is seen in the gradual oscillation of the baseline of the time series. These long-period, low-frequency oscillations cause the significant increase in Fourier power seen below approximately 3 Hz.

filter. In this technique, the median is calculated for n samples in the time series within a designated filter window. The median of these samples is then subtracted from a given sample within the window (typically the sample closest to the center of the window), the result of which is then written into a new, de-reddened time series at the same position. The filter is then advanced by one sample in the original, unaltered time series and the process is repeated, until an entire de-reddened time series is created. The choice of the filter size n is key, as only red noise of a timescale greater than n will be removed by such a filter. Optimally, n should be chosen so as to be larger than the longest pulsar period being searched for, but sufficiently small so as to mitigate the majority of the red noise contamination. A corresponding technique known as *spectral whitening* is also available in the Fourier domain, where the Fourier spectrum itself is passed through a running median filter and normalised such that its root mean square (RMS) approaches unity. However, this technique may be likely to suppress the Fourier power of any long-period pulsar along with the red noise power itself, limiting its usefulness in the search for such pulsars (van Heerden et al., 2017).

2.2.1.5 Multibeam techniques

For observations taken with multibeam receivers (receivers capable of simultaneously observing with multiple beams at separate on-sky locations), a number of specialised RFI removal techniques are available. This comes as a consequence of the fact that any true astrophysical point source (such as a pulsar) is highly likely to be detectable only in a single beam[4], while terrestrial sources of RFI are likely to be simultaneously detectable in many beams. One such technique, designed to mitigate impulsive RFI sources in the time domain, is the 'eigenvector decomposition' method described by Kocz et al. (2012). In this technique, the DM $= 0\,\mathrm{cm}^{-3}\,\mathrm{pc}$ time series is generated for each beam of a multibeam receiver. These time series are then cross-correlated to form a matrix for each time sample, which is then decomposed into its eigenvector and eigenvalue components. The number of eigenvalues in which a given signal appears reflects the number of beams in which it was detected for a given sample, and by setting appropriate thresholds, terrestrial RFI sources which occur in a sufficient number of beams can be flagged and removed.

An alternative multibeam RFI excision technique which operates in the Fourier domain was developed as part of the HTRU-S LowLat processing pipeline (Ng, 2014; Ng et al., 2015). Once again, the DM $= 0\,\mathrm{cm}^{-3}\,\mathrm{pc}$ time series is produced for each beam of the multibeam receiver. These time series are then passed through a Fourier transform to produce a Fourier spectrum for each beam. A bin-by-bin analysis of the Fourier spectra from each beam can then be used to assess the number of beams for which the power in a certain Fourier bin exceeds a particular threshold, and therefore whether a particular periodic signal can be classified as RFI. This technique, along with

[4]Particularly bright pulsars (e.g. PSR B1641−45) are known to spill into neighbouring beams depending on the particular beam geometry of the receiver in question, in part due to their detection by side lobes. However, as the work in this thesis concentrates on the discovery and observation of particularly faint pulsars, this can largely be ignored for the purposes of this discussion.

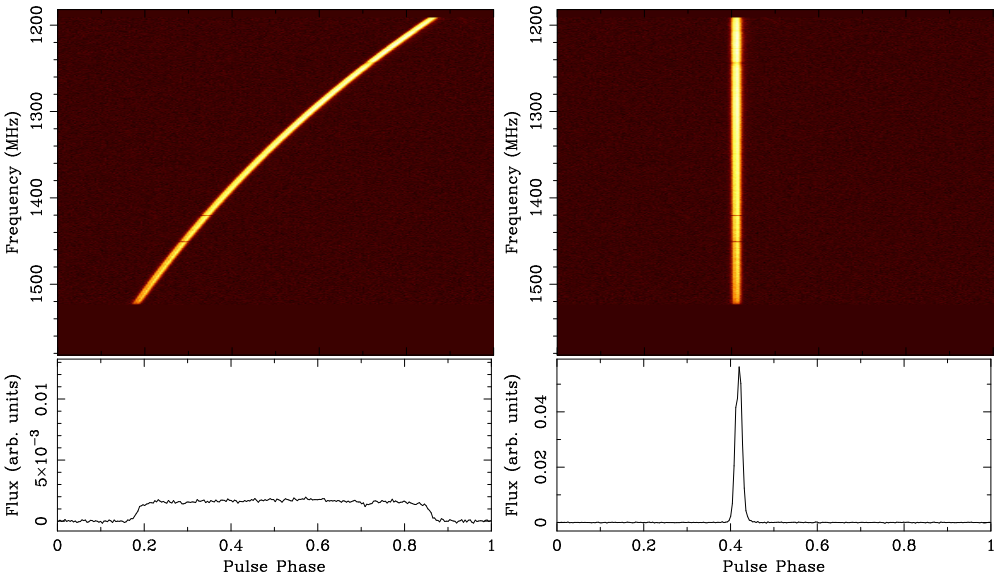

Figure 2.6: An example of the effects of dispersive smearing, as seen in PSR B1323−62 (DM = 318.8 $\mathrm{cm}^{-3}\,\mathrm{pc}$) as observed by HTRU-S LowLat. The top-left plot shows a dispersed pulse, integrated in time and plotted in terms of pulse phase versus observing frequency. Further integrating this dispersed pulse in frequency produces the smeared pulse profile shown in the bottom-left plot, resulting in a reduction of the pulse's S/N. Meanwhile, the top-right and bottom-right plots show the same observation after it has been correctly de-dispersed, resulting in a recognisable sharp pulse, maximising the pulse's S/N.

additional RFI mitigation strategies employed by the HTRU-S LowLat pulsar survey, is also explored in Section 3.1.2.1.

2.2.2 De-dispersion

Following RFI excision, the next stage of the standard pulsar search pipeline is that of *de-dispersion*, in which the observation is integrated in frequency to produce a single-channel *time series*. As described in Section 1.3.1 and defined by Equation 1.15, a dispersive delay is introduced between the top and bottom of the frequency band as a result of each pulse passing through and interacting with the ISM. If this delay is not properly corrected for during de-dispersion, then the effect will be to smear out each pulse in time, dramatically reducing the detectability of the pulsar by later search algorithms. An example of this dispersive smearing effect is shown in Figure 2.6.

As noted in Section 2.1.3, the ideal method of de-dispersing an observation is through *coherent de-dispersion*, which is able to de-disperse the incoming pulses in real time before writing the corrected baseband data to storage. However, this technique relies on prior knowledge of the DM of the pulsar being observed, which remains unknown in a blind pulsar search. Therefore, we rely instead on *incoherent de-dispersion*,

which is able to approximately de-disperse a channelised filterbank observation to any arbitrary value of DM. We can consider the observation as a two-dimensional array of samples in both time and frequency, defining $\mathcal{S}_{jl}$ as the j^{th} time sample of the l^{th} frequency channel. For a filterbank with n_{chans} channels, we can defined a de-dispersed time series $\mathcal{T}_j$ as

$$\mathcal{T}_j = \sum_{l=1}^{n_{\text{chans}}} \mathcal{S}_{j+k(l),l}, \tag{2.3}$$

where $k\,(l)$ is the nearest integer number of time samples corresponding the dispersion delay at the l^{th} frequency channel. From Equation 1.15, we can define this delay by

$$k\,(l) = \left\lfloor \left(\frac{t_{\text{samp}}}{4.15 \times 10^6\,\text{ms}}\right)^{-1} \left(\frac{\text{DM}}{\text{cm}^{-3}\,\text{pc}}\right) \left[\left(\frac{f_l}{\text{MHz}}\right)^{-2} - \left(\frac{f_1}{\text{MHz}}\right)^{-2}\right] \right\rfloor, \tag{2.4}$$

where t_{samp} is the sampling time of the observation, f_l is the frequency of the l^{th} channel and f_1 is defined as highest frequency channel ($l = 1$). The act of de-dispersing the observation at a given DM value can therefore be seen as a sliding of the frequency channels alongside each other by the required dispersive delay $k\,(l)$ before adding the channels together to produce the time series.

However, even if the incoherent de-dispersion process is correctly applied, a small amount of *intrachannel smearing* will remain, due to the dispersive delay across each individual frequency channel. When $\Delta f_{\text{chan}} \ll f$, where Δ_{chan} is the channel bandwidth and f is the channel frequency, this intrachannel smearing Δt_{chan} can be calculated as

$$\Delta t_{\text{chan}} = \left(\frac{8.3 \times 10^6}{\text{ms}}\right) \left(\frac{\text{DM}}{\text{cm}^{-3}\text{pc}}\right) \left(\frac{\Delta f_{\text{chan}}}{\text{MHz}}\right) \left(\frac{f}{\text{MHz}}\right)^{-3}. \tag{2.5}$$

Since we are considering a blind pulsar survey in which the DM of any given pulsar is unknown, a large number of DM values must be trialled, such that at least one of them falls close enough to the true DM of any unknown pulsar present in the observation so as to render it detectable. This then poses a challenge of optimisation with relation to the step size, ΔDM; if the step size is too small, then computational resources are wasted on separate DM trials which deliver essentially identical results, while too large a step size may result in the sensitivity of the search to an unknown pulsar being significantly reduced because its true DM fell too far between trial DMs for its signal to be recoverable, as a consequence of excessive smearing. Lorimer, D. R. and Kramer, M. (2005) determine a sensible ΔDM by equating it to a dispersive delay of t_{samp} across the observation bandwidth B, such that each DM step can at most smear the de-dispersed profile by a single time sample. This can be expressed mathematically through a rearrangement and enumeration of Equation 2.5 to give

$$\text{DM}_i = 1.205 \times 10^{-7}\,\text{cm}^{-3}\,\text{pc}\,(i-1)\,t_{\text{samp}}\left(f^3/B\right), \tag{2.6}$$

where f is the central observing frequency and i represents the number of the DM trial. Note that as with Equation 2.5, this assumes that $B \ll f$, which may not be true

in all cases, especially as the observing bandwidths of modern receivers and backends continue to increase[5].

Under the de-dispersion scheme outlined by Equation 2.6, at $i = n_{\text{chans}} + 1$ the dispersive delay becomes $n_{\text{chans}} \times t_{\text{samp}}$ i.e., the intrachannel dispersion delay $\Delta t_{\text{chan}} = t_{\text{samp}}$. This marks the so-called *diagonal DM*. Once $i = 2 \times (n_{\text{chans}} + 1)$ and the second diagonal DM is reached, the intrachannel smearing will have increased to $\Delta t_{\text{chan}} = 2t_{\text{samp}}$, such that neighbouring pairs of samples can essentially be counted as the same sample. This allows for the time series to be downsampled by a factor of two for all further DM trials, a process which can be repeated with each doubling of the diagonal DM. This saves computational expense at higher DM values as a result of the decrease of t_{samp} and the corresponding increase in ΔDM allowing for fewer DM trials.

2.3 Pulsar searching algorithms

2.3.1 The Fast Fourier Transform (FFT)

As a pulsar's defining characteristic is that of its regular, periodic radio pulsations, by far the most popular searching algorithms involve the use of the *Fourier transform*, which decomposes a given signal into its periodic components. An analysis of the resulting *Fourier spectrum*, which plots Fourier power as a function of frequency, can then be performed to determine if any periodic signal (such as a pulsar) is present in the data. As a pulsar time series consists of a series of discrete samples rather than a smooth continuous function, it is necessary to use the discrete Fourier transform (DFT). Pulsar searches typically employ an implementation of the DFT known as the *Fast Fourier Transform* (FFT; Cooley & Tukey, 1965), so-named because it dramatically improves the efficiency of the DFT, reducing the number of required operations from $O\left(N^2\right)$ to $O\left(N \log_2 N\right)$ over a data set of N samples in length. Such is the utility of the FFT that within just two years of the discovery of the first pulsar, the FFT had already become a standard algorithm for pulsar searching (Burns & Clark, 1969).

2.3.1.1 The discrete Fourier transform

For a discretely-sampled time series $\mathcal{T}_j$ consisting of N samples, the k^{th} complex Fourier component $\mathcal{F}_k$ of the DFT is defined as

$$\mathcal{F}_k = \sum_{j=0}^{N-1} \mathcal{T}_j \exp\left(-2\pi i j k / N\right), \tag{2.7}$$

where $i = \sqrt{-1}$. For a time series uniformly sampled in intervals of t_{samp}, the frequency[6] ν of the k^{th} Fourier component is given by $\nu_k = k/\left(N t_{\text{samp}}\right) = k/t_{\text{int}}$ where t_{int} is the integration length of the time series. From this, it can be inferred that the width of a

[5] For example, the recently-installed VEGAS backend at the GBT has a nominal observing bandwidth of 1.5 GHz, comparable in magnitude to the central observing frequencies of the majority of current pulsar radio observations.

[6] Not to be confused with an electromagnetic observing frequency f.

single Fourier bin is given by $\Delta\nu = 1/t_{\rm int}$ which (in the case of $k = 1$) also represents the lowest detectable frequency. Meanwhile, the highest detectable frequency is naturally given by the Nyquist frequency which, given the sampling time of $t_{\rm samp}$, occurs at $\nu_{\rm Nyq} = 1/(2t_{\rm samp})$, corresponding to $k = N/2$ such that $1 \leq k \leq N/2$.

As the Fourier components $\mathcal{F}_k$ are complex values (capable of representing both the amplitude and phase of the original periodic signal), some care must be taken in the production of the resulting Fourier spectrum. Most commonly this takes the form of a Fourier *power* spectrum, defined by

$$\mathcal{P}_j = \mathrm{Re}\,(\mathcal{F}_j)^2 + \mathrm{Im}\,(\mathcal{F}_j)^2\,, \tag{2.8}$$

where $\mathcal{P}_j$ is the $j^{\rm th}$ frequency component of the Fourier power spectrum. Alternatively, the Fourier spectrum is sometimes given as an *amplitude* spectrum, where $\mathcal{A}_j = \left|\sqrt{\mathcal{P}_j}\right|$. In this thesis, all references to the 'Fourier spectrum' refer to the power spectrum unless otherwise noted.

A primary limitation of the DFT is that as a consequence of its discrete nature, its response in frequency is not uniform. Instead, it is 'tuned' to its specific frequency components (given by ν_k), with intermediate frequencies suffering from a degradation in sensitivity, an effect referred to as 'scalloping' (see, e.g. Middleditch et al., 1993). For a non-integer r for which $\nu_r = r/t_{\rm int}$, chosen such that ν_r lies within the same Fourier bin as ν_k (i.e. $|\nu_k - \nu_r| < \Delta\nu/2$), Ransom et al. (2002) demonstrate that the loss of Fourier power can be described by

$$\mathcal{P}_r = \mathcal{P}_k\,\mathrm{sinc}^2\left[\pi\,(k - r)\right]. \tag{2.9}$$

In the worst case where $|k - r| = 1/2$, this results in a power loss of $\sim 60\,\%$, although the average power loss of signal at an arbitrary ν_r is only $\sim 23\,\%$ (van der Klis, 1989). This loss of response to intermediate frequencies can be combated in multiple ways. One basic technique is to 'pad' the time series out with zero-valued samples. These samples add no extra noise or signal, but increase N and thereby decrease $\Delta\nu$, allowing for a finer resolution in the Fourier spectrum. An alternative technique known as *interbinning* (van der Klis, 1989), one of a number of Fourier interpolation techniques, estimates the Fourier amplitude at the half-integer point between two neighbouring frequencies by interpolating their Fourier amplitudes, such that

$$\mathcal{A}_{k+(1/2)} \simeq \frac{\pi}{4}\left(\mathcal{A}_k - \mathcal{A}_{k+1}\right). \tag{2.10}$$

This technique improves the worst-case Fourier power response $\mathcal{P}_r = \mathcal{A}_r^2$ from the previous reduction of $\sim 60\,\%$ to a reduction of only $\sim 14\,\%$. Multiple additional techniques for improving the response of the DFT are available, with a detailed review provided by Ransom et al. (2002).

2.3.1.2 Harmonic summing

Following the application of the FFT to a given time series, along with any Fourier RFI mitigation techniques (see Section 2.2.1), one could in theory analyse the resulting

cleaned Fourier spectrum in order to determine the presence of any potential pulsar candidates. However, while the power of a perfectly sinusoidal signal would be collected in a single Fourier bin by the FFT, pulsars have much narrower, sharper pulse profiles, with typical *duty cycles* $\delta = W/P$ of only a few percent (where W is the pulse width and P is the pulse period). As a result, the Fourier power of a pulsar ends up distributed among both its fundamental spin frequency as well as multiple *harmonics*, integer multiples or divisions of the fundamental frequency. This distribution of Fourier power, if uncorrected, renders the pulsar significantly harder to detect.

First proposed by Taylor & Huguenin (1969), the technique of *incoherent harmonic summing* is a common technique used to recover some of the Fourier power lost to harmonic frequencies (this method is incoherent as it does not take into account any phase information of the initial periodic signal). As demonstrated in Figure 2.7, this technique involves 'stretching' the fundamental spectrum by a factor of 2, before adding it to the original, unstretched spectrum. Note that this addition takes place using the **amplitude** spectrum $\mathcal{A}_j$. Since the Fourier S/N of a periodic signal in the k^{th} frequency bin is proportional to its amplitude $\mathcal{A}_k$ via

$$\mathrm{S/N}_k = \frac{\left(\mathcal{A}_k - \overline{\mathcal{A}}\right)}{\sigma_{\mathcal{A}}}, \tag{2.11}$$

where $\overline{\mathcal{A}}$ is the mean of $\mathcal{A}_j$ and $\sigma_{\mathcal{A}}$ is the local root mean square, the addition of a fundamental and harmonic signal of roughly equal power results in an amplitude increase of the order of a factor of 2, a power increase of the order of a factor of 4, and an increase in S/N of the order of a factor of $\sqrt{2}$ (since the noise $\sigma_{\mathcal{A}}$ of the combined amplitude spectra increases by $\sqrt{2}$).

By repeating this process of harmonic summing, the power of additional harmonics can be recaptured. Typical pulsar software sums up to 16 harmonics, which is sufficient for pulsars with duty cycles $\delta > 0.02$ (Ransom et al., 2002). However, for pulsars with $\delta \gtrsim 0.3$, harmonic summing can actually result in a degradation of Fourier sensitivity, since these pulsars produce far less harmonic Fourier signals and hence attempting to sum the higher non-existent harmonics only results in the addition of noise into the fundamental Fourier detection. For this reason, it is typical to separately evaluate the resulting spectra from **each** stage of the harmonic summing process during the later candidate-selection stage.

2.3.1.3 False-alarm probabilities and candidate selection

In order to determine whether a given signal in a Fourier spectrum constitutes a real detection, or is simply the result of random noise, its significance must first be quantified via an analysis of the noise response of the DFT. For a white-noise time series which follows an approximately Gaussian probability distribution function (PDF), both the real and imaginary Fourier components will also approximately conform to a Gaussian PDF. The PDF of the Fourier power spectrum, which incorporates both of these components, will therefore follow a χ^2 distribution with $n = 2$ degrees of freedom which itself reduces to an exponential PDF. An integration of this PDF shows that the

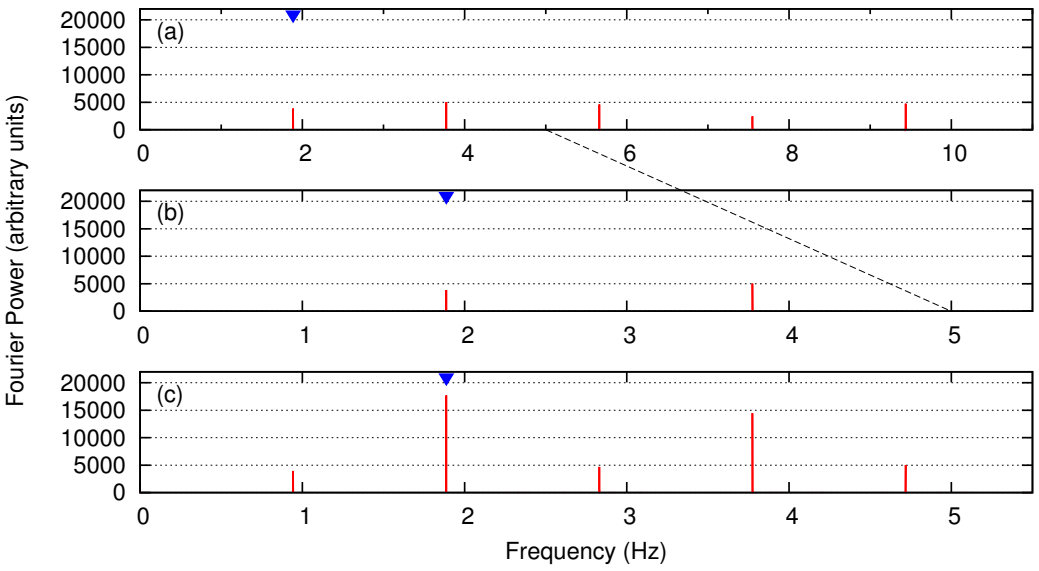

Figure 2.7: A demonstration of how incoherent harmonic summing can be used to recover Fourier power. Plot (a) shows a whitened Fourier power spectrum for PSR B1323−62 as observed in HTRU-S LowLat. The fundamental spin frequency ($\nu_0 = 1.887\,\mathrm{Hz}$) is indicated by the blue arrow, and a number of signals at harmonic frequencies (at multiples of ν_0) are also visible. In plot (b), the spectrum is stretched by a factor of 2, as indicated by the dashed line. In plot (c), the spectra in plots (a) and (b) are added together via their **amplitude** spectra (the square root of the power spectra), so that the Fourier power of the second harmonic ($2\nu_0 = 3.774\,\mathrm{Hz}$) is added to the fundamental, resulting in a stronger Fourier signal.

probability of the power $\mathcal{P}$ in a given Fourier bin exceeding a threshold power $\mathcal{P}_{\text{thresh}}$, otherwise known as the *false-alarm probability*, is simply proportional to $\exp(\mathcal{P}_{\text{thresh}})$. Note that with the addition of m harmonic sums as part of the Fourier analysis, the PDF is modified to a χ^2 distribution with $2m$ degrees of freedom. Further details on the evaluation of the false-alarm probability are available in Lorimer, D. R. and Kramer, M. (2005).

A suitable $\text{S/N}_{\text{thresh}}$, based on an analysis of the Fourier amplitude spectrum as described by Equation 2.11, can be established by setting the value of $\mathcal{P}_{\text{thresh}}$ such that the number of false alarm events expected for a number of trials n_{trials} is equal to one. Lorimer, D. R. and Kramer, M. (2005) demonstrates that $\text{S/N}_{\text{thresh}}$ can therefore be expressed by

$$\text{S/N}_{\text{thresh}} = \frac{\sqrt{\ln(n_{\text{trials}})} - \sqrt{\pi/4}}{\sqrt{1-\pi/4}} \simeq \frac{\sqrt{\ln(n_{\text{trials}})} - 0.89}{0.46}. \tag{2.12}$$

Assuming the standard, non-accelerated periodicity search of the HTRU-S LowLat survey as described in Section 2.1.2.6 of Ng (2014), with time series consisting of 2^{26} samples each (resulting in 2^{25} Fourier samples), de-dispersed at 1069 trial values of DM and searched independently with an FFT incorporating five harmonic sums, we arrive at $n_{\text{trials}} = 2^{25} * 1069 * 5 = \simeq 1.8 \times 10^{11}$ by multiplying these individual factors together. By Equation 2.12, this results in an $\text{S/N}_{\text{thresh}} \simeq 9$. However, the influence of non-Gaussian RFI in the data is likely to cause the true value of $\text{S/N}_{\text{thresh}}$ to rise slightly and, as discussed further in Section 3.2.1, this calculation is not entirely applicable to the segmented search applied to the HTRU-S LowLat survey as part of this thesis.

2.3.2 The Fast Folding Algorithm (FFA)

An alternative approach to finding periodic signals in an observational time series $\mathcal{T}_j$ is to simply fold the time series directly over a number of trial periods to produce a collection of folded pulse profiles. These profiles can then be assessed, either manually or analytically, in order to determine their likelihood of representing the detection of a genuine pulsar candidate. The *Fast Folding Algorithm* (FFA; Staelin, 1969) represents a particularly efficient means of producing these folded profiles. A comprehensive investigation and review of the properties of the FFA, including methods by which its folded profiles may be evaluated, is presented in Chapter 5. However, a brief review of the core algorithm mechanics is presented here for completeness.

Consider a time series $\mathcal{T}_j$ consisting of N samples, to be searched at a period of P_0 samples (multiplying by the sampling time t_{samp} converts P_0 into units of time). Assuming that N/P_0 is an integer, a single folded profile p_k (where k indicates number of the profile bin) can be produced by breaking down $\mathcal{T}_j$ into N/P_0 segments (that each contain P_0 samples) and summing them together, such that for $0 \leq k < P_0$, the folded profile is given by

$$p_k = \sum_{j=0}^{N/P_0-1} \mathcal{T}_{k+jP_0}. \tag{2.13}$$

The FFA, as shown in the schematic in Figure 2.8, builds upon this foundation to produce N/P_0 **separate** folded profiles for a given base period P_0. Note that in the standard FFA implementation shown in Figure 2.8, the condition $N/P_0 = 2^n$ (where n is an integer) must hold. The production of each folded profile is broken down into a series of smaller addition steps whose results are stored in the intermediate columns, with n additions performed per sample of each folded profile. The folded profiles produced by the FFA span a range of trial periods between P_0 and $P_0 + 1$ samples inclusive, with the trial period of the i^{th} profile given by

$$P_i = P_0 + \frac{iP_0}{N - P_0}, \tag{2.14}$$

where $0 \leq i < N/P_0$. This is achieved by adding relative shifts between segments before adding them together at the various steps of the FFA. The arrows in Figure 2.8 indicate which segments are being added together at each step, with the number in each vertex indicating the relative shift in position. By modifying Equation 2.13 to account for these shifts, the resulting folding profiles p_{ki} (indicating the k^{th} bin of the i^{th} folded profile) can be described by

$$p_{ki} = \sum_{j=0}^{N/P_0-1} \mathcal{T}_{k+jP_0+q}, \tag{2.15}$$

where

$$q = \lfloor jP_i \rceil \bmod P_0. \tag{2.16}$$

The rounding function ensures that only integer samples are selected, while the modulo function allows for wrapping within each segment of $\mathcal{T}_j$ during the addition process. The necessity of this is seen in the example of $p_{0,3}$ in Figure 2.8, indicated by the red path. Without wrapping, a trial period of $P_3 = 4$ samples would result in the addition of $\mathcal{T}_{12}$, which is not present in the data set, and so $\mathcal{T}_9$ is summed in its place via a wrap in the $j = 3$ segment.

The key advantage of the FFA is that by storing the intermediate results of each addition step, rather than directly summing the folded profiles as per Equation 2.15, redundant operations are avoided. The computational cost of producing the N/P_0 folded profiles is thereby reduced from $O\left(N^2\right)$ to $O\left(N \log_2\left(N/P_0\right)\right)$. However, despite this computational efficiency, the FFA has seen relatively little use as a searching tool in large-scale pulsar surveys as, in comparison to the FFT, it has remained computationally expensive (Lorimer, D. R. and Kramer, M., 2005). A detailed comparison of the relative advantages and disadvantages of the FFT and the FFA is included as part of the work in Chapter 5.

2.3.3 Binary pulsar search algorithms

So far this discussion of pulsar searching algorithms has considered only the case of isolated pulsars, whose spin periods can be assumed to be approximately constant over

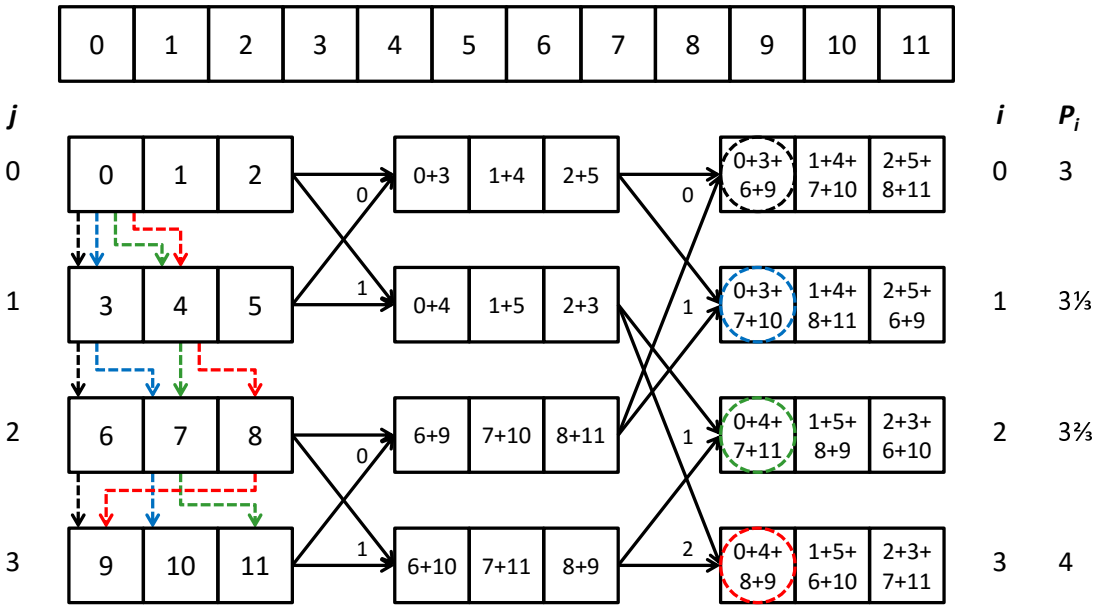

Figure 2.8: A schematic diagram of an example of the FFA. This examples uses a data set of $N = 12$ samples with a base period of $P_0 = 3$ samples. The data set is broken into $N/P_0 = 4$ segments (enumerated by j on the left-hand side). The solid black arrows indicate which segments are added together at each step, with the number in each vertex indicating the shift to be applied between the segments before adding them together. In this example, there are $n = 2$ addition steps, where $N/P_0 = 2^n$. The FFA results in $N/P_0 = 4$ folded profiles (enumerated by i on the right-hand side, with periods P_i in samples). The dashed arrows indicate the samples required to form the first bin ($k = 0$) of each folded profile. Note that the red path is forced to wrap at the final step, due to the lack of a sample $\mathcal{T}_{12}$. Figure adapted from Staelin (1969) and Lorimer, D. R. and Kramer, M. (2005).

the course of a search observation[7]. However, the apparent spin period of a pulsar will be modulated by the presence of any binary motion, a manifestation of the Doppler Effect as the pulsar's line-of-sight velocity changes. This effect is particularly prominent in binary systems with short orbital periods. If this effect is left uncorrected, it can degrade the signal of the pulsar both in the Fourier domain (smearing the Fourier power among multiple bins) and in the time domain (the changing apparent spin period causing a smearing of the signal in time), reducing its detectability. Presented here is an overview of a selection of additional algorithms designed to mitigate these effects and allow for the detection of pulsars in binary systems, once again focusing on those which are at the core of the science presented in this thesis.

2.3.3.1 Time-domain resampling

If the Keplerian orbit of a pulsar is fully known, an observational time series can be resampled so as to transform it from the Earth-bound reference frame of the observer to an inertial reference frame with respect to the pulsar, essentially negating its orbital motion and rendering it stationary. Such a transformation, known as *time-domain resampling*, can be expressed using an extended Doppler correction, which relates the time in the observer's frame t to the time in the inertial frame τ via

$$\tau\left(t\right) = \tau_0 \left(1 + \frac{V_1\left(t\right)}{c} + \ldots\right), \tag{2.17}$$

where $V_1\left(t\right)$ gives the line-of-sight velocity of the pulsar, τ_0 represents a normalisation constant (see e.g. Camilo et al., 2000) and higher order (v/c) terms are ignored. Resampling can be performed either by a process of linear interpolation (see e.g. Middleditch & Kristian, 1984) or by adding and removing samples to compensate for the drifting phase change between the two reference frames.

In theory, this coherent transformation can fully correct for the orbital motion of a pulsar. However, since in a blind search the orbit of the pulsar is unknown, this would require a comprehensive search of the five Keplerian orbital parameters (see Section 2.6.3), which for large-scale surveys remains computationally impractical. The simplified version of this technique which is usually applied in pulsar searches makes the assumption that the orbital motion of the pulsar can be approximated by a constant acceleration a, i.e. $V_1\left(t\right) = at$. Different trial values of the acceleration a can then be applied in order to quadratically stretch or squeeze the time series in order to approximately correct for the presence of any orbital motion (see e.g. Johnston & Kulkarni, 1991), after which the time series can be searched as normal through search algorithms such as the FFT or FFA. This technique is the primary binary searching method employed in this thesis, and an example of its application to PSR J1431−5740 can be seen in Figure 2.9. The quadratic change in the apparent period of the pulsar

[7]Search observations with long integration times, such as those from HTRU-S LowLat, can require corrections to account for the change in the apparent spin period of the pulsar caused by the orbital motion of the Earth, a process known as *barycentering*. As this correction is typically of far more importance in the process of pulsar timing, it is discussed in Section 2.6.1.

as seen in Figure 2.9a indicates that the pulsar's motion can be approximated well by a constant acceleration. Figure 2.9b shows the same observation after the application of time-domain resampling at a constant acceleration of $a = 0.42\,\mathrm{m\,s^{-2}}$, which for this pulsar almost completely corrects for the effects of the orbital motion.

As with de-dispersion, care must be taken in choosing an acceleration step size so as to maximise computational efficiency without losing sensitivity by under-sampling the search space. One approach, as outlined in Lorimer, D. R. and Kramer, M. (2005), is to consider the effect of the resampling in the Fourier domain. Under the assumption of a constant acceleration a, the rate at which the apparent spin frequency (ν) of the pulsar drifts in the reference frame of the observer ($|\dot{\nu}|$) is given by

$$|\dot{\nu}| = \frac{\nu_0 a}{c}, \tag{2.18}$$

where ν_0 is the spin frequency of the pulsar in its inertial frame. Remembering from Section 2.3.1 that the width of each Fourier bin is given by $\Delta\nu = 1/t_{\mathrm{int}}$, the number of bins drifted by an accelerated signal over the interval t_{int} is given by

$$N_{\mathrm{drift}} = \frac{|\dot{\nu}|\, t_{\mathrm{int}}}{\Delta\nu} = \frac{a\nu_0 t_{\mathrm{int}}^2}{c}. \tag{2.19}$$

An acceleration step size can then be determined by stipulating that the number of Fourier bins drifted in a single acceleration step should be less than one, from which it can be inferred using Equation 2.19 that

$$\Delta a < \frac{c}{\nu_0 t_{\mathrm{int}}^2}. \tag{2.20}$$

An alternative approach presented by Eatough et al. (2013a) is to consider the smearing of the accelerated signal in the time domain. Under this method, an acceleration step size is chosen such that for a pulsar whose actual value of acceleration falls exactly halfway between two neighbouring acceleration trials, the maximum smearing in time experienced over the length of the observation will be equal to $t_{\mathrm{acc}} = 4t_{\mathrm{samp}}$. Due to the quadratic nature of the time smearing, this restriction means that 50 % of the pulsar signal will be smeared by less than t_{samp}. As derived by Eatough et al. (2013a), the acceleration step size which follows from this formulation can be expressed by

$$\Delta a = \frac{64 c t_{\mathrm{samp}}}{t_{\mathrm{int}}^2}. \tag{2.21}$$

Additionally, care must be taken when considering the applicability of the assumption of constant acceleration. Ng et al. (2015) (and earlier Johnston & Kulkarni, 1991) demonstrated that, in the case of circular orbits, the technique of time-domain resampling works best where

$$r_{\mathrm{orb}} = \frac{t_{\mathrm{int}}}{P_{\mathrm{b}}} \lesssim 0.1, \tag{2.22}$$

where t_{int} is the length of the observation being searched. This can present a limitation of this technique in terms of ability to detect pulsars with short orbital periods.

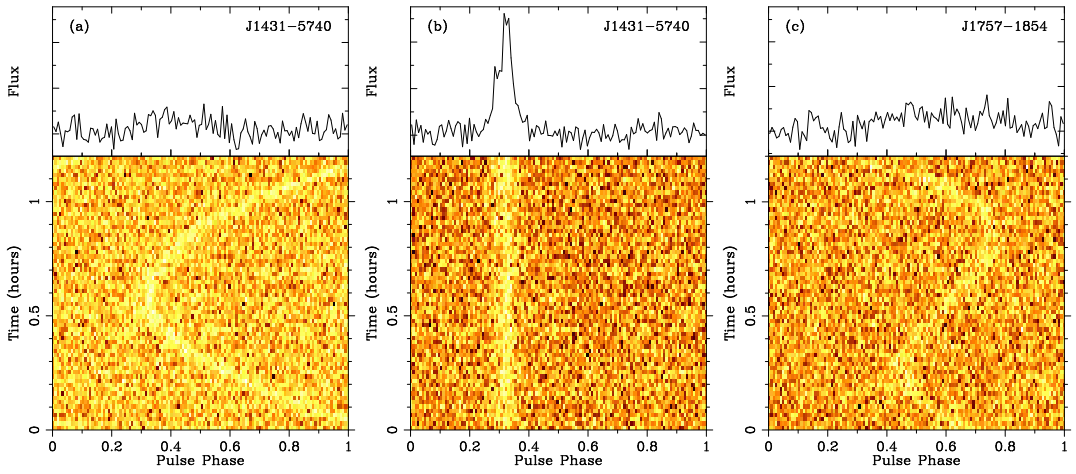

Figure 2.9: A demonstration of the application and limitations of the time-domain resampling acceleration search technique. Plot (a) shows a HTRU-S LowLat observation of PSR J1431−5740, a binary millisecond pulsar (MSP) with an orbital period of $P_\mathrm{b} = 2.73\,\mathrm{d}$, without having been corrected for its orbital motion. Plot (b) shows the same observation after the application of time-domain resampling using a constant acceleration of $a = 0.42\,\mathrm{m\,s^{-2}}$. Plot (c) shows the HTRU-S LowLat observation of PSR J1757−1854, a relativistic binary with $P_\mathrm{b} \simeq 4.4\,\mathrm{h}$ (see Chapter 4), after correction for a constant acceleration of $a = -30\,\mathrm{m\,s^{-2}}$. The remaining cubic trend in the apparent pulsar period indicates the presence of 'jerk', and that the assumption of constant acceleration over the entire observation is not appropriate.

Figure 2.9 also displays the example of PSR J1757−1854, a pulsar discovered as part of this thesis work and reported in Chapter 4. Figure 2.9c shows the HTRU-S LowLat observation in which this pulsar was first discovered, after having been resampled at an acceleration of $a = -30\,\mathrm{m\,s^{-2}}$. With an orbital period of $P_\mathrm{b} \simeq 4.4\,\mathrm{h}$ and an integration time of $t_\mathrm{int} = 4300\,\mathrm{s}$ implying an $r_\mathrm{orb} \simeq 0.27$, it is clear that the assumption of constant acceleration is not sufficient to correct for the orbital motion of this pulsar[8], with the residual cubic trend in Figure 2.9c indicating the presence of significant '*jerk*' (the rate of change of acceleration, $\dot{a}$). One proposed solution to this limitation is the 'partially-coherent segmented acceleration search' (Ng et al., 2015), which forms the backbone of the pipeline search pipeline employed in this thesis and is discussed in detail in Section 3.1.2.

The constant acceleration technique of time domain resampling remains one of the techniques of choice in the ongoing search for new pulsar binaries, and is currently deployed as part of the SIGPROC pulsar software package. Notable contributions that have been made using this technique include the discovery of 9 MSP binaries in the globular cluster 47 Tucane (Camilo et al., 2000), the re-analysis of the Parkes Multibeam

[8]PSR J1757−1854 also possesses a high eccentricity of $e \simeq 0.606$, which breaks the assumption of circularity used to calculate the ideal value of $r_\mathrm{orb} \lesssim 0.1$. The implications of eccentricity in the application of the time-domain resampling technique are discussed in Section 3.1.2.2.

Pulsar Survey (PMPS; Manchester et al., 2001) conducted by Eatough et al. (2013a), and as already described, the processing of the first half of the HTRU-S LowLat pulsar survey (Ng et al., 2015). This technique is also being applied as part of the first-pass processing of the Survey for Pulsars and Extragalactic Fast Radio Bursts (SUPERB; Keane et al., 2018).

2.3.3.2 Match filtering

An alternative coherent binary searching technique which operates in the Fourier domain, and which has been used as part of the follow-up work on a number of the newly discovered pulsars reported in this thesis, is the technique of *match filtering*, also known as the *correlation technique* (Ransom et al., 2002). As opposed to time-domain resampling, which works to correct the effects of any orbital motion prior to the application of an FFT, the match filtering technique attempts to predict the shape of the smeared pulsar signal as it would appear in a Fourier spectrum after the application of an FFT to an uncorrected time series. This shape can then be used to characterise a matched filter, which for a given acceleration will have a width in Fourier bins $N_{\rm drift}$ as given by Equation 2.19. In the ACCELSEARCH program (part of the PRESTO software package), the value $N_{\rm drift}$ is also referred to as the z parameter, which sets the maximum width of the matched filter to be applied in the search.

Once a given matched filter of width $N_{\rm drift}$ has been been calculated, it can then be cross-correlated with the Fourier spectrum of the uncorrected time series, thereby re-summing the otherwise smeared Fourier power and resulting in a much stronger detection of the accelerated pulsar. For a search of a single time series de-dispersed at a single trial DM, the match filtering technique stands out as computationally superior to the technique of time domain resampling, as a number of different matched filters corresponding to different trial accelerations can be applied to the same Fourier spectrum from a single FFT, while the time domain resampling technique requires one FFT per acceleration trial.

Alongside time domain resampling, match filtering continues to see widespread use as a binary pulsar search technique. The first application of this technique resulted in the discovery of PSR J1807−2459A in the globular cluster NGC 6544 (Ransom et al., 2001) which, with $P_{\rm b} = 1.7\,{\rm h}$ has the fourth-shortest orbital period of any binary pulsar currently known. Additional successes of this technique include the discovery of a number of eccentric binary MSPs, including PSR J1946+3417 (Barr et al., 2013) and PSR J1835−3259A (DeCesar et al., 2015), as well as the discovery of a number of binary pulsars in the Green Bank Northern Celestial Cap (GBNCC) pulsar survey (Stovall et al., 2014).

2.3.3.3 Additional techniques

Although time-domain resampling and match filtering are the primary acceleration search techniques employed in this thesis, additional search techniques are also available, some of which are briefly summarised here:

- **Stack/slide searches:** Developed by Faulkner et al. (2004), the 'stack/slide' search technique first divides an observational time series into smaller segments which are then independently Fourier transformed. This is advantageous in two ways. Firstly, by shortening the integration time $t_{\rm int}$ of each segment, the changing apparent period of the pulsar as induced by the orbital motion has less time to drift, while as described in Section 2.3.1.1, a reduced $t_{\rm int}$ also increases the size of each Fourier bin. Both of these effects result in the signal of the pulsar drifting by fewer Fourier bins in each segment. The resulting Fourier spectra are then 'stacked' and, in a similar manner to the frequency channels in a de-dispersion trial, are made to 'slide' against each other at various offsets before being added together. Should a binary system be present, the slide offset corresponding to the period drift caused by the orbit will result in the emergence of a stronger signal in the summed spectra. One key disadvantage of this technique is that it is incoherent by virtue of its segmented nature, and hence does incur a subsequent loss in sensitivity compared to other, coherent acceleration techniques.

- **Phase modulation searches:** Developed by Ransom (2001), Jouteux et al. (2002) and Ransom et al. (2003), the phase-modulation search is of most use in the event that $t_{\rm int} \gg P_{\rm b}$, i.e., that multiple orbits are covered by a single observation. Another Fourier-domain technique, this search takes advantage of the fact that over multiple orbits, the modulation of the apparent pulse period will produce a regular Fourier pattern consisting of multiple sidebands spaced around the fundamental period. As these sidebands are spaced at intervals corresponding to $P_{\rm b}$, applying a *second* Fourier search to the initial power spectrum will result in a significant detection at the corresponding frequency, allowing $P_{\rm b}$ to be approximately determined. However, one disadvantage of this technique is that extracting additional information about the orbit of the pulsar, including its orbital phase φ, eccentricity e and semi-major axis x (see Section 2.6.3) is often non-trivial, and typically requires additional searching and/or processing of the sidebands.

2.4 Candidate optimisation and review

Following the application of either the FFT or the FFA, a candidate list of suspected pulsar signals is typically produced, and includes the pulse period, DM and acceleration of the candidate pulsar signal. In the case of the FFT, this candidate list is derived from an analysis of the amplitude spectra, taking periodic signals whose S/N (according to Equation 2.11) lies above the $\mathrm{S/N}_{\rm thresh}$ given by Equation 2.12. In the case of the FFA, separate techniques for deriving a candidate list are presented in greater detail in Chapter 5.

This list is then typically subjected to further optimisation techniques in order to reduce the number of candidates, a process typically referred to as *candidate sifting*. For example, as shown in Section 2.3.1.2, a pulsar spinning at a given fundamental frequency will be present at multiple harmonic frequencies in a Fourier spectrum. If

the S/N of these harmonic Fourier components is greater than S/N_{thresh}, then the same pulsar may produce multiple harmonic candidate signals at similar values of DM. With this in mind, candidate signals whose DM values are sufficiently close together can then be grouped by looking for matching harmonic periods, a process which typically involves searching for matches to candidate pulsar period over a range of trial fractions. A pulsar candidate may also be detected multiple times at a number of closely-spaced DM trials or acceleration values, which can also be grouped so as to reduce the size of the candidate list, with the retained candidate being the one with the highest S/N.

Once the sifting process is complete, the final candidate list is then used to fold the RFI-cleaned observation according to the period, DM and acceleration of each candidate signal to produce a *folded archive*. The folding process involves first de-dispersing the observation according to the DM of the pulsar, before summing the observation in time about the predicted phase of the candidate pulsar, such that samples which correspond to the same phase of the pulse are added together. In order to retain information about the pulsar, it is common practice to not fully sum the observation in time or frequency when producing an archive. Instead, *sub-integrations* are produced at regular intervals (typically on the order of seconds to minutes), with frequency *sub-bands* being produced in a similar fashion. The resulting archive (with dimensions of time, electromagnetic frequency and phase) can then be inspected so as to determine the likelihood of the signal representing the detection of a true pulsar, typically after an optimisation search designed to probe the local parameter space around the candidate so as to maximise its folded S/N[9].

Examples of these diagnostic plots, as produced by the PSRCHIVE[10] (Hotan et al., 2004; van Straten et al., 2012) program PDMP, are shown in both Figures 2.10 and 2.11. In each case, the top-left plot shows a colour map showing how the S/N of the candidate signal changes as the DM (vertical axis) and the period (horizontal axis) of the pulsar are modified. The blue crosshairs indicate the optimal solution. The top-right plot shows the same optimisation for acceleration (in units of $\mathrm{m\,s^{-2}}$), but in only one dimension. The central-left plot shows the signal of the pulsar phase versus time, with the blue line once again indicating the optimal solution for the period and acceleration of the candidate signal. The central-right plot shows a phase versus frequency plot, with the blue line again showing the optimal DM of the candidate signal. These optimal values are then used to create the final folded profile at the bottom of the plot, with the optimised values listed alongside the folded S/N.

Historically, these diagnostic plots have been inspected by eye[11] in order to determine whether or not a candidate signal represents noise, RFI, or an actual pulsar. A

[9] Note that the folded S/N differs from the Fourier S/N. Although the two terms are typically analogous to each other, care must be taken when making this comparison. For further discussion, see Chapter 5.

[10] http://psrchive.sourceforge.net

[11] Machine learning and other automated techniques are increasingly being applied to the problem of pulsar-candidate inspection, as the number of candidates continues to grow as surveys become more complex and data-intensive, especially with the development of big-data telescopes such as MeerKAT[12] and the Square Kilometre Array[13] (SKA). For recent examples, see Zhu et al. (2014) and Lyon et al. (2016).

typical pulsar signal is indicated by a well-constrained DM-period solution away from $0\,\mathrm{cm}^{-3}\,\mathrm{pc}$, a well-constrained acceleration solution, and continuous signals in both the time and frequency plots. An example of such a pulsar is given by PSR B1715−40 in Figure 2.10. However, these are only general rules of thumb, and behaviour such as nulling, scintillation or scattering (see Chapter 1) can alter this ideal picture. An example of this is given by PSR J1054−5946 in Figure 2.10. As a nulling pulsar, PSR J1054−5946 does not give a continuous signal in the phase versus time plot, but shows ideal characteristics in all other respects. Once a candidate pulsar signal has been reviewed and flagged as being a likely new pulsar, a new observation is typically performed so as to confirm it as an astrophysical source.

However, despite the development and application of increasingly sophisticated RFI-mitigation techniques (as are described in Section 2.2.1), it is not uncommon to encounter leftover RFI signals during the candidate review stage, and so techniques for recognising and classifying these signals must also be honed. Examples of RFI are provided in Figure 2.11. The example on the left indicates an archive which has been overwhelmed by RFI, such that the diagnostic plot displays no useful information. The example on the right is particularly deceptive, as it appears at first glance to resemble a pulsar signal. However, the DM-period solution in the top-left plot indicates a DM consistent with $0\,\mathrm{cm}^{-3}\mathrm{pc}$, consistent with a terrestrial source. The same signal was also identified in other simultaneously recorded telescope beams, again pointing to its identity as terrestrial RFI rather than an astrophysical point source.

2.5 Survey sensitivity

At a basic level, the sensitivity of a given pulsar survey (or even a single pulsar observation) is characterised by the radiometer equation for pulsars, which as described in Lorimer, D. R. and Kramer, M. (2005), can be expressed as

$$S_{\mathrm{min}} = \frac{\beta\,(\mathrm{S/N}_{\mathrm{thresh}})\,T_{\mathrm{sys}}}{G\sqrt{n_{\mathrm{p}}t_{\mathrm{int}}B}}\sqrt{\frac{W}{P-W}}. \tag{2.23}$$

In this expression, S_{min} is the minimum detectable flux density in mJy corresponding to the cutoff value of $\mathrm{S/N}_{\mathrm{thresh}}$, t_{int} is the integration time of each observation in seconds, n_{p} is the number of recorded polarisations, B is the observation bandwidth in MHz, G is the gain of the telescope expressed in K Jy^{-1} (see Section 2.1.1), and β is a correction factor accounting for losses during signal digitisation and other miscellaneous effects. T_{sys} (measured in K) is the *system temperature*, which describes a number of thermal noise contributions to the observation, including those from the telescope receiver T_{rcvr} and the sky temperature T_{sky}. The T_{sky} contribution varies greatly as a function both of observing frequency and sky position, generally increasing towards lower Galactic latitudes. Finally, P is the spin period of the pulsar being observed, while W is the width of the pulse profile, typically given as either the FWHM of the pulse profile (sometimes denoted as W_{50}) or an equivalent top-hat pulse, such that the integral of the top-hat profile is equal to the integral of the original pulse profile.

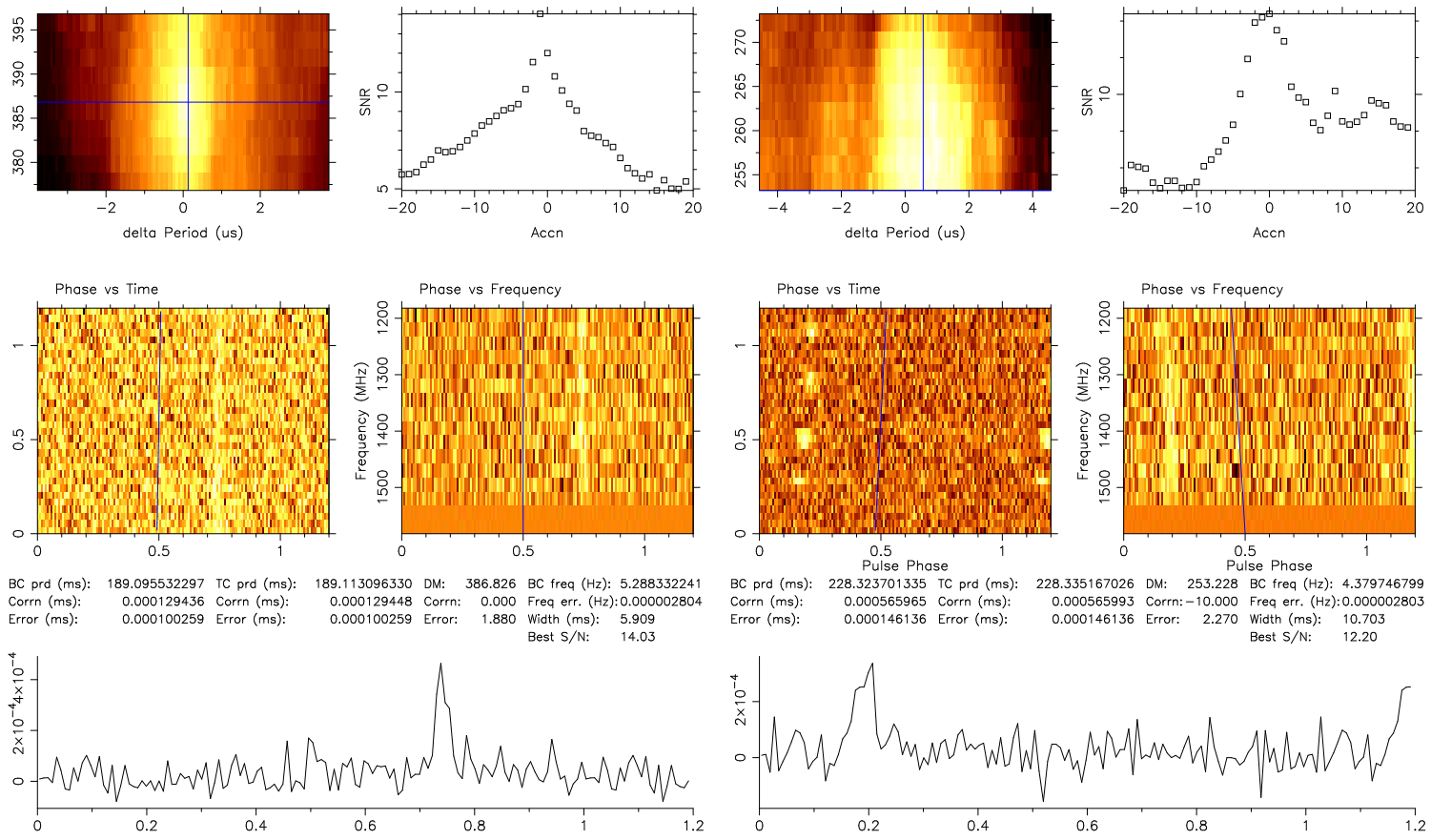

Figure 2.10: Examples of pulsar detections in the HTRU-S LowLat pulsar survey. PSR B1715−40 is shown on the left, while the nulling pulsar PSR J1054−5946 is shown on the right.

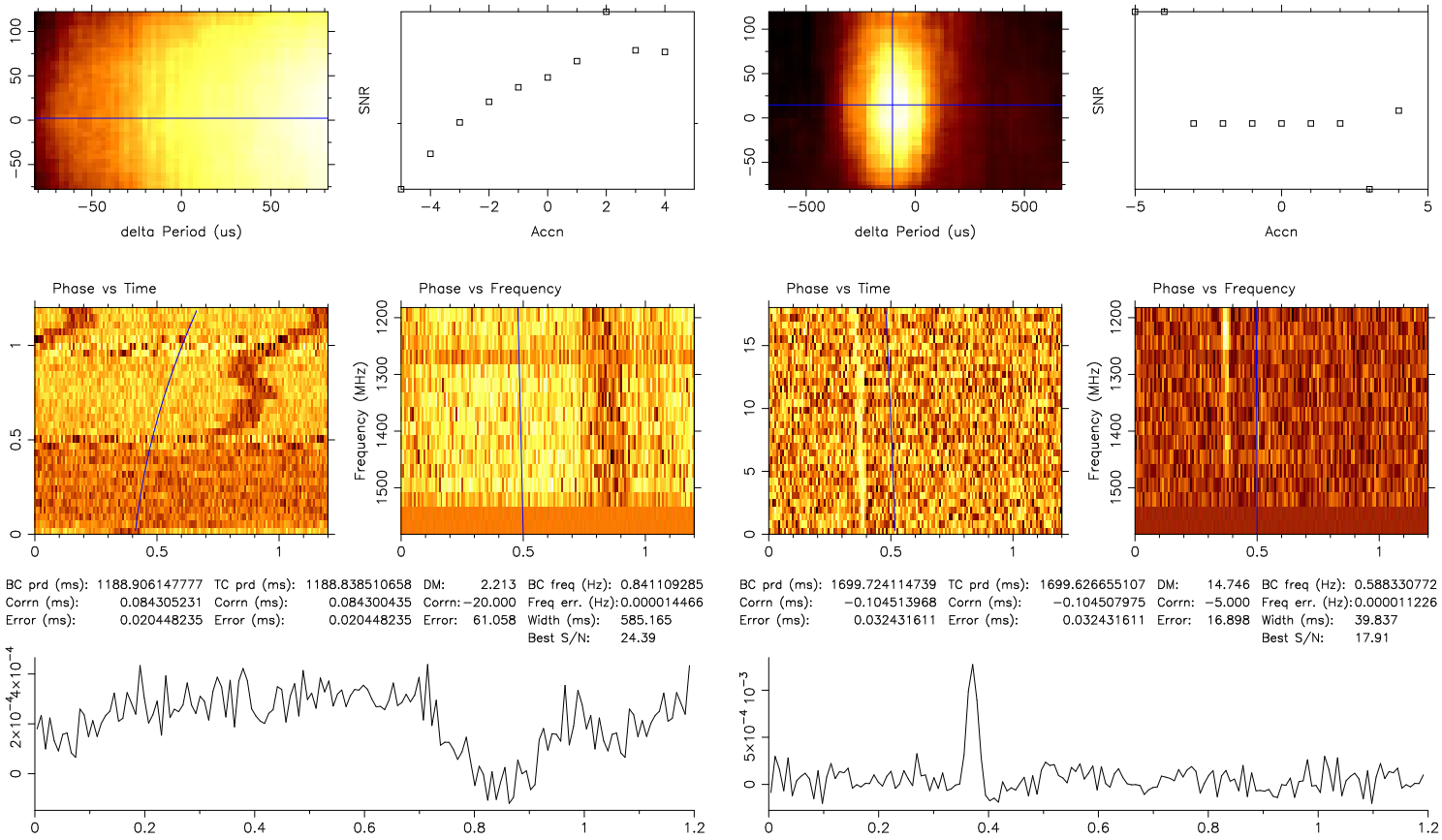

Figure 2.11: Examples of RFI contamination in the HTRU-S LowLat pulsar survey. The RFI signal on the left has overwhelmed observation, rendering the diagnostic plots meaningless. The signal on the right appears pulsar-like, but is given away as RFI by its DM being indistinguishable from $0\,\mathrm{cm}^{-3}\,\mathrm{pc}$.

However, this ideal calculation is complicated by a number of additional factors. For example, the intrinsic pulse width of a pulsar $W_{\rm int}$ may be smeared to produce a wider effective pulse width $W_{\rm eff}$ as a consequence of the true DM of the pulsar lying between DM trials. A similar smearing effect occurs in high DM pulsars, for which the intrachannel DM smearing becomes progressively worse (see Section 2.2.2). These larger $W_{\rm eff}$ values cause a reduction in survey sensitivity per Equation 2.23, as the minimum flux density required to detect a pulsar increases (Dewey et al., 1985). These smearing effects are also more problematic in the case of MSPs, as the number of time samples over which the smearing occurs exert a larger proportional influence over the shape of an MSP profile. The choice of smaller frequency channel bandwidths and smaller sampling times can assist in the mitigation of these effects.

Even neglecting dispersive smearing, the properties of MSPs present additional difficulties for survey detection. For example, a survey with insufficient time resolution may lack enough samples to be able to resolve the pulse profile of an MSP, a limitation which affected many previous-generation pulsar surveys (see Section 2.7.1). Further, MSPs typically possess inherently larger pulse duty cycles $\delta = W/P$ than the rest of the 'normal' pulsar population (see e.g. Kramer et al., 1998). As the final square root term in Equation 2.23 can be rewritten as $\sqrt{\delta/(1-\delta)}$, a larger value of δ can be seen to further decrease the sensitivity of a given survey to MSPs.

Finally, although the radiometer equation is typically considered a standard means of evaluating the sensitivity of a survey, its failure to account for the influence of RFI and in particular the red noise content of the survey mean that its application should be considered limited at best. These limitations are highlighted by Lazarus et al. (2015), and are further discussed in the context of the FFT and the FFA in Chapter 5.

2.6 Pulsar timing

Once a new pulsar has been discovered and confirmed, its initial properties (such as its spin period, position, etc.) are only known to a relatively imprecise degree. The next step in its scientific exploitation is to produce a high-precision, descriptive model of the pulsar through the process of *pulsar timing*. Such a model is called a *timing model*, or alternatively a *pulsar ephemeris*. The timing process involves observing the pulsar at closely-spaced intervals (typically between days and weeks apart) over a typical span of at least one year, with the typical interval between these observations referred to as the *observational cadence*. Pulsar timing can at times be a highly-nuanced technique, and the description provided here will be limited to those aspects most relevant to this thesis (for a more complete overview, see e.g., Lorimer, D. R. and Kramer, M., 2005; Edwards et al., 2006).

The goal of each timing observation is to determine a fundamental quantity known as the pulse *time of arrival* (TOA). This is a timestamp which marks the arrival time of an individual pulse from the pulsar being observed. As a pulse profile has some finite width, the TOA refers to a specific *fiducial point* on the pulse profile (for example, the profile peak). Additionally, in order to ensure the stability of the pulse profile

between separate TOAs and to reduce the TOA uncertainty, an integrated profile (see e.g. Figure 1.1) consisting of several hundred to several thousand averaged pulses (integrated in time and frequency using the folding method described in Section 2.4) is typically used, with the TOA value then defined as the arrival time of the pulse closest to the midpoint of the span of the averaged pulses (Lorimer, D. R. and Kramer, M., 2005). The actual value of the TOA is typically determined by cross-correlating the integrated profile against a noise-free analytic template profile known as a *standard profile*, which is typically expressed as the summation of several Gaussian components (Foster et al., 1991; Kramer et al., 1994).

The high degree of long-term rotational stability found in pulsars means that it is possible to develop timing models which are capable of predicting the arrival times of every single rotation of a given pulsar to within a very small fraction of the pulsar's rotational pulse phase. Such a model is typically referred to as being *phase-connected*, and phase-connection constitutes a basic requirement in order for a timing model to be considered an accurate description of a pulsar's behaviour. With a phase-connected model, it is possible both to unambiguously account for every single rotation of the pulsar between observations which are separated in time, and to predict the arrival times of future pulses. However, as this prediction extends further into the future, a larger and larger error in arrival times is likely to accumulate. When the accumulated error amounts to a substantial fraction of the pulse period, the relation between predicted and actual pulse arrival times is no longer unambiguous, and the model is said to have lost phase-connection. The span of time required for a timing model to lose phase-connection varies greatly, but in general terms, a model constructed using higher-cadence observations over a longer time span will retain phase-connection further into the future.

A pulsar timing model is developed and refined by minimising the least-squares fit of the difference between the measured and predicted TOAs, known as the *timing residuals*. Mathematically the expression to be minimised can be expressed as

$$\chi^2 = \sum_i \left(\frac{N(t_i) - n_i}{\sigma_i} \right)^2 \tag{2.24}$$

where $N(t_i)$ represents each measured arrival time in units of rotational phase, n_i represents the nearest integer to each $N(t_i)$ and σ_i is the TOA error in units of rotational phase. Ideally, a well fit model should result in a Gaussian distribution of the post-fit residuals, with a root-mean-square that is comparable to the TOA uncertainties themselves (Lorimer, D. R. and Kramer, M., 2005). When determining the timing solution for a newly discovered pulsar, it is common practice to first develop a solution using high-cadence TOAs over a short timespan until phase-connection is achieved, fitting only for timing parameters whose effects are expected to dominate over shorter timescales. During this process, it is often necessary to add and subtract rotational phases from the model in the gaps between observations where the behaviour of the pulsar is not well known, in order to find the absolute minimum value of χ^2 and produce an accurate timing model. Freire & Ridolfi (in prep.) describe a particular

algorithm whereby a large number of unknown phase gaps can be efficiently solved via an iterative process, even with a large number of unfit timing parameters. As the timing model is improved over a longer timespan, the observational cadence can be gradually decreased, with additional timing parameters which contribute over longer time scales being fit for as required.

A number of software packages have been developed to assist in the derivation of pulsar timing solutions. Data manipulation and analysis is typically carried out with the PSRCHIVE software package, which includes a full suite of tools required to reduce pulsar data into a set of TOAs. The actual timing analysis, wherein the timing residuals are used to develop and refine a phase-connected timing solution, is typically conducted using either the TEMPO[14] or TEMPO2[15] (Hobbs et al., 2006; Edwards et al., 2006) software packages.

2.6.1 Time corrections and barycentering

When a TOA is first calculated, it is derived from the local time standard of the observatory at which the data was recorded, typically provided by a hydrogen maser or other relatively stable timing source (see Section 2.1.3). However, this local time standard is not necessarily of sufficient accuracy for pulsar timing, as despite their stability, local observatory clocks are known to drift and glitch over time. In order to be converted to a standard *topocentric* (Earth-bound) reference time, each TOA is transformed through a series of corrections designed to account for any errors in the timing process.

The local observatory timestamp of the TOA is first converted into the time standard of the Global Positioning System (GPS), before being further converted into Coordinated Universal Time (UTC). The drift between these three time standards is constantly monitored, with bulletins of corrections (e.g. CircularT[16]) being published regularly. An additional conversion, which accounts for the accumulated number of leap seconds which have been added to UTC, transforms the timestamp into International Atomic Time (TAI) via

$$\mathrm{TAI} = \mathrm{UTC} + \Delta T, \tag{2.25}$$

where ΔT is the sum of all added and subtracted leap seconds (which as of December 31st, 2016 stands at $\Delta T = 37\,\mathrm{s}$). One final conversion transforms TAI into Terrestrial Time (TT) via

$$\mathrm{TT} = \mathrm{TAI} + 32.184\,\mathrm{s}. \tag{2.26}$$

The TT standard is intended to represent idealised geocentric time (Seidelmann & Fukushima, 1992), with the SI second as its unit, and is the final stage in the conversion of the TOA timestamp to a standardised topocentric value.

However, we have still not arrived at a suitable reference frame for pulsar timing. For example, two observatories observing a pulsar simultaneously will, due to their

[14] http://tempo.sourceforge.net/
[15] http://www.atnf.csiro.au/research/pulsar/tempo2/
[16] http://www.bipm.org/jsp/en/TimeFtp.jsp?TypePub=Circular-T

physical separation, measure the same incoming pulse at different times, complicating multi-telescope timing campaigns. Worse still, the rotation of the Earth both around its own axis and around the Sun render any topocentric reference frame non-inertial. To resolve these problems, all TOAs must be further transformed to the solar system center-of-mass, also known as the solar system barycenter (SSB), such that they become *barycentric*. Although not a perfectly inertial reference frame (due to the acceleration of the solar system in the Galactic potential), the approximation is suitably precise for the purposes of pulsar timing. For a TOA already converted to TT, $t_{\rm topo}$, Lorimer, D. R. and Kramer, M. (2005) provide an expression for the following barycentric corrections,

$$t_{\rm SSB} = t_{\rm topo} - \frac{\mathcal{D} \times {\rm DM}}{f^2} + \Delta_{\rm R\odot} + \Delta_{\rm S\odot} + \Delta_{\rm E\odot}. \tag{2.27}$$

In this expression, the second term (where $\mathcal{D}$ is defined as per Section 1.3.1) represents the delay required to convert a TOA recorded at central frequency $f_{\rm c}$ (in MHz) and a given DM (in $\rm cm^{-3}\,pc$) to a TOA of 'infinite frequency', thereby removing the effect of dispersion and allowing for TOAs at multiple frequencies to be handled simultaneously. The third term represents the Römer delay, and describes the delay of the arrival of a given pulse between the observatory and the SSB. Calculating the Römer delay relies on accurate knowledge of the mass and position of all major solar system objects, for which a *planetary ephemeris* (such as the DE405 or DE421 models produced by the Jet Propulsion Laboratory[17]) is used. Accurate knowledge of the geographical location of the observatory is also required to complete the calculation. The remaining terms, $\Delta_{\rm S\odot}$ and $\Delta_{\rm E\odot}$ describe contributions from the Shapiro and Einstein delays respectively, caused by the gravitational potential of both individual planets, the Sun, and the solar system as a whole. These two concepts are treated in more detail with respect to binary pulsar timing in Section 2.6.3. Additional corrections, such as delays induced by the solar wind, may also be considered, but are beyond the scope of this thesis.

Equation 2.27 results in a conversion from the TT standard to the Barycentric Dynamical Time (TDB). An alternative and increasingly-used barycentric time standard is Barycentric Coordinate Time (TCB), which runs as a TDB clock would at the SSB but without the influence of the solar system's gravitational potential. Therefore, there is an accumulative difference between these two time standards which accounts for the relativistic delay, with the conversion (as defined by IAU 2006 Resolution B3[18]) given by

$$t_{\rm TCB} = (t_{\rm TDB} - L_{\rm B} t_{\rm init} - \Delta_{\rm T})\,(1 - L_{\rm B})^{-1} \tag{2.28}$$

where $t_{\rm TCB}$ and $t_{\rm TDB}$ are in units of MJD, $t_{\rm init}$ = MJD 43144.0003725, $\Delta_{\rm T} = -(6.55/86400) \times 10^{-5}$ days and $L_{\rm B} = 1.550519768 \times 10^{-8}$.

2.6.2 Standard timing parameters

A typical pulsar timing model contains several timing parameters which are fundamental in adequately describing a given pulsar's behaviour. As noted previously, each

[17] https://ssd.jpl.nasa.gov/?ephemerides#planets
[18] https://www.iau.org/static/resolutions/IAU2006_Resol3.pdf

of these parameters has differing characteristic timescales, and errors in the modeled values of these parameters can cause the appearance of characteristic trends in the pulsar's timing residuals. Some of these trends are depicted in Figure 2.12. Pulsar timing parameters can be divided into three main categories. The first category, known as the *spin parameters*, includes

- the **spin period** P, which if incorrectly fit for introduces a linear trend into the timing residuals (see Figure 2.12b). Alternatively, a timing model may fit for the **spin frequency** F.
- the **spin period derivative** $\dot{P}$, which if incorrectly fit for introduces a quadratic trend into the timing residuals, centered about a chosen period reference epoch (see Figure 2.12c). Equivalently, a timing model may fit for the **spin frequency derivative** $\dot{F}$.

Additional spin period derivatives may also be included in order to correct for *timing noise* (long-term residual trends which lack a readily-apparent physical explanation), but unlike $\dot{P}$, which describes the physical spin-down of the pulsar as described in Section 1.2.3, higher-order derivatives typically lack predictive power, serving only to describe the observed noise. Furthermore, in the case of a glitching pulsar (see Section 1.4.3), multiple values of P and $\dot{P}$ (referenced at different epochs) will be required to describe the pre- and post-glitch spin states of the pulsar.

The second category of timing parameters, known as the *astrometric parameters*, includes but is not limited to

- the pulsar's **position**, including both the **right ascension** (denoted α or R.A.) and **declination** (denoted δ or Dec.) of the pulsar. An error in position causes the Römer delay to be incorrectly calculated, resulting in a sinusoidal trend in the residuals with a period of one year (see Figure 2.12d) which corresponds to the Earth's orbit around the Sun. Over short time spans, the partial sinusoidal residual trend is difficult to distinguish from the parabolic trend caused by an incorrect $\dot{P}$ and so a timing span on the order of a year is typically required in order to break this degeneracy.
- the **dispersion measure**, which can only be fit for as part of a timing analysis if multi-frequency TOAs are available. An incorrect value of DM can be highlighted by plotting the timing residuals as a function of frequency instead of time.
- the **proper motion** of the pulsar, which is measurable if the pulsar is moving relative to the SSB. The transverse component of the velocity, V_{T}, can be described by the proper motion parameters $\mu_{\mathrm{T}} = \sqrt{\mu_\alpha^2 + \mu_\delta^2}$, where μ_α and μ_δ are the angular components of the proper motion of the pulsar in α and δ respectively. μ_{T} is typically expressed in milliarcseconds per year ($\mathrm{mas\,yr^{-1}}$), and any error in μ_{T} produces a sinusoidal residual trend with a period of one year and a steadily-increasing amplitude (see Figure 2.12d), as it causes an increasingly large error in position. Note that in order to convert the angular proper motion

$\mu_{\rm T}$ into the physical transverse velocity $V_{\rm T}$, the distance to the pulsar d must also be taken into account.

Finally, the third category of timing parameters, the *binary parameters*, must also be fit for when dealing with a pulsar in a binary system. As a large portion of the science in this thesis involves the development of timing solutions of binary pulsars, these parameters receive a more thorough treatment in Section 2.6.3.

2.6.3 Binary pulsar timing

An extra level of difficulty is introduced in the timing of pulsars in binary systems. As noted in the discussion of acceleration searches (see Section 2.3.3), a pulsar in an orbit will experience a modulation of its apparent spin period due to its changing line-of-sight velocity and the associated Doppler effect. In other words, the pulsar itself is in a non-inertial reference frame and experiences its own Römer delay $\Delta_{\rm R\odot}$ between its orbital position and the barycenter of the binary system. Therefore, the timing model of a binary pulsar must not only account for the standard astrometric and spin parameters as already discussed, but must also account for the parameters of the pulsar's orbit in order to fully account for the additional Römer delay. A typical orbital parameterisation is given by the classical five *Keplerian parameters* which, with reference to the orbital schematics in Figure 2.13, are defined as

- the **orbital period** $P_{\rm b}$, typically measured in days.
- the orbital **eccentricity** e which, given a *semi-major axis* $a_{\rm p}$ and a *semi-minor axis* $b_{\rm p}$ as indicated in Figure 2.13a, is defined by

$$e = \sqrt{1 - \left(\frac{b_{\rm p}}{a_{\rm p}}\right)^2}. \tag{2.29}$$

- the **longitude of periastron** ω, defined as the angle between the *ascending node* and *periastron* in the direction of motion of the pulsar, as indicated in Figure 2.13b.
- the **epoch of periastron** T_0, a reference point in time at which the pulsar passed through periastron.
- the **projected semi-major axis** $x = a_{\rm p} \sin i$, where $a_{\rm p}$ is the semi-major axis of the orbit (typically measured in light-seconds) and i is the orbital *inclination angle* as indicated in Figure 2.13. The inclination angle i is defined so that an orbit edge-on to the line of sight has $i = 90°$. Due to the fact that it is only possible to measure the pulsar's projected orbital motion along the line of sight, $a_{\rm p}$ and i are inseparable without additional information.

A typical timing implementation of this standard parameterisation, used to calculate and fit the timing residuals from each binary parameter, is given by the BT model

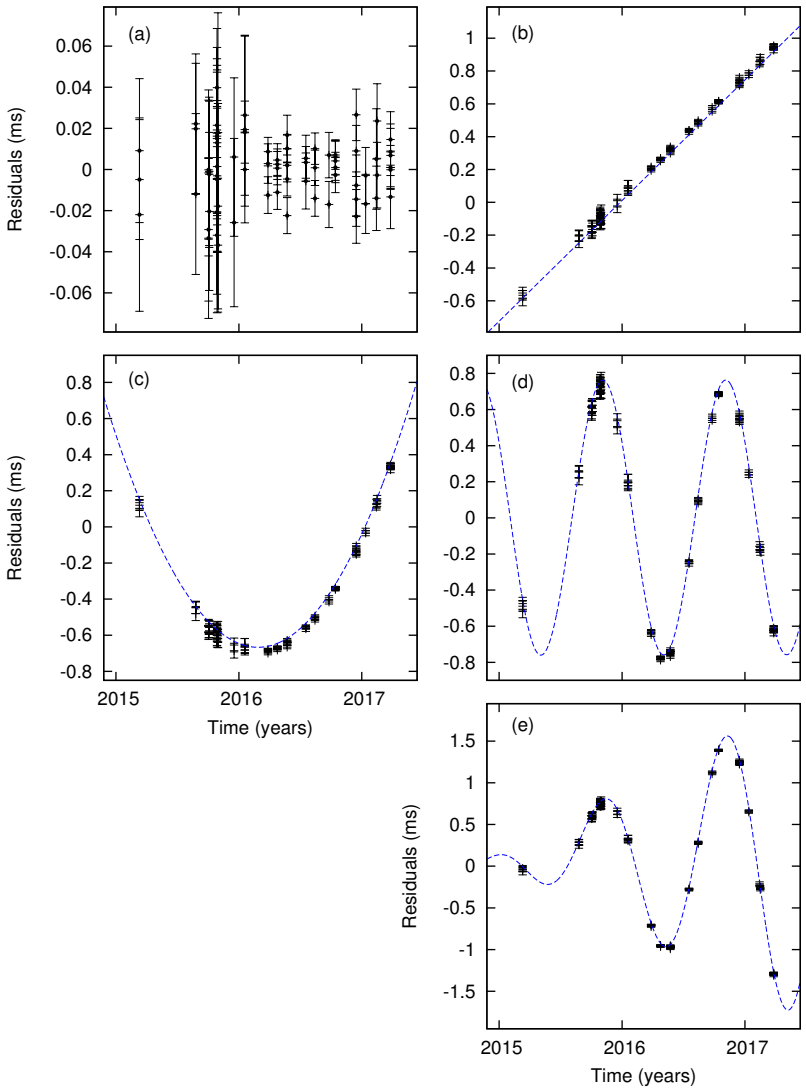

Figure 2.12: A demonstration of the effects of incorrect timing parameters on pulsar timing residuals. Plot (a) displays the residuals of the newly-discovered PSR J1547−5709 (see Chapter 3) after the application of a phase-connected, well-fit timing model. The residuals are approximately Gaussian in distribution. Each of the remaining plots shows the same model with an offset applied to a single timing parameter: (b), an offset to the spin period of $\Delta P = -10^{-10}$ ms, resulting in a linear trend; (c), an offset to the spin period derivative of $\Delta\dot{P} = -7.5 \times 10^{-21}$, resulting in a quadratic trend; (d), an offset to the declination of $\Delta\delta = 0.5$ arcsec, resulting in a sinusoidal trend with a period of 1 yr; (e), an offset to the proper motion in declination of $\Delta\mathrm{PM}_\delta = -500\,\mathrm{mas\,yr^{-1}}$, resulting in a sinusoidal trend with a period of 1 yr and a steadily increasing amplitude. Note the differing vertical scales of each plot.

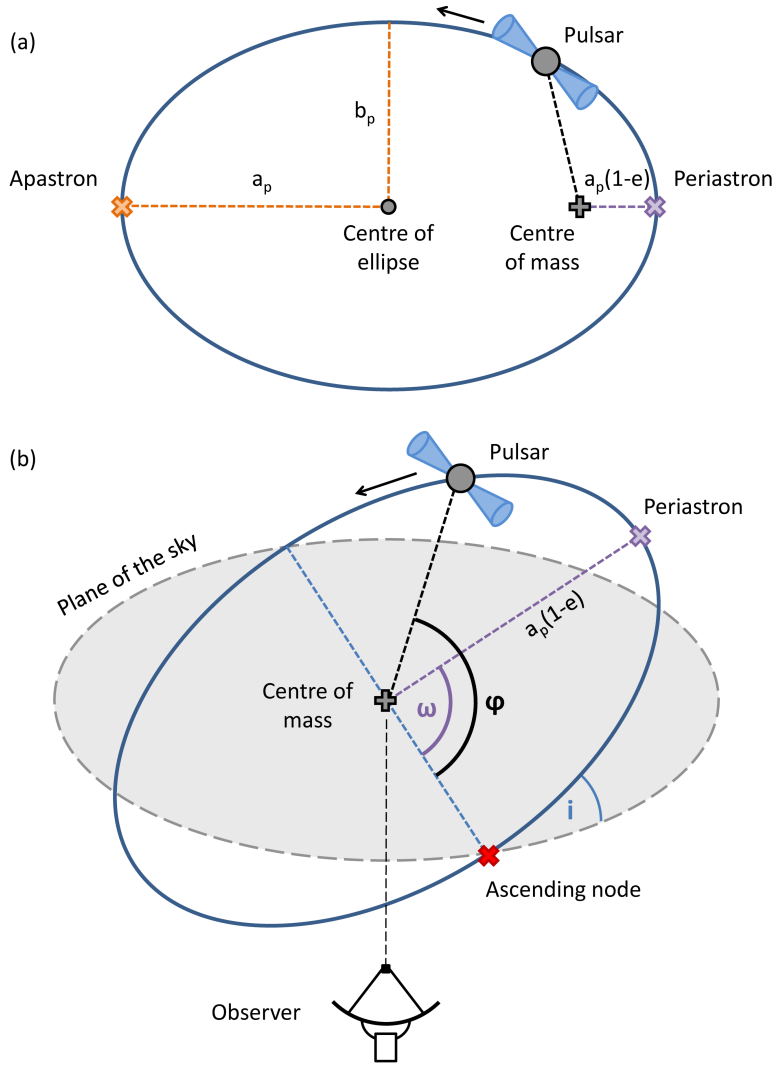

Figure 2.13: A schematic diagram of the Keplerian orbital parameters and other associated quantities. Plot (a) displays the *semi-major axis* $a_{\rm p}$ and the *semi-minor axis* $b_{\rm p}$ of the elliptical orbit, with the *eccentricity* defined as $e = \sqrt{1 - (b_{\rm p}/a_{\rm p})^2}$. As the pulsar and its binary companion both orbit the center of mass (located at one of the foci of the ellipse), *periastron* marks their point of closest separation, while *apastron* marks their point of furthest separation. In plot (b), we see the orbit as viewed by an Earth-based observer. The *plane of the sky* (marked in grey) is perpendicular to the line of sight and is fixed to the center of mass of the orbit. The plane of the sky is intersected by the *plane of the orbit* (marked in blue) at an *inclination angle* i. The *ascending node* is defined as the point where the pulsar crosses the plane of the sky traveling away from the observer. The *orbital phase* φ is the angle between the ascending node and the position of the pulsar, while the *longitude of periastron* ω is the angle between the ascending node and the position of periastron. Note that for illustrative purposes, the orbits depicted in plots (a) and (b) have differing eccentricities.

(Blandford & Teukolsky, 1976). However alternative models and parameterisations are often called for depending on the particular pulsar in question. For example, one shortcoming of the BT model is its inability to adequately constrain e, ω and T_0 as they become increasingly poorly defined in the case of extremely circular orbits. The ELL1 model (Wex 1998 unpublished work, see Lange et al., 2001) is designed to work around this limitation, replacing e and ω with $\varepsilon_1 = e \sin \omega$, $\varepsilon_2 = e \cos \omega$ and referring to the epoch of the ascending node $T_{\rm asc}$ (as opposed to the epoch of periastron T_0) as a reference point in time. The original Keplerian parameters can then be derived via

$$e = \sqrt{\varepsilon_1^2 + \varepsilon_2^2}, \tag{2.30}$$

$$\omega = \arctan\left(\varepsilon_1/\varepsilon_2\right), \tag{2.31}$$

$$T_0 = T_{\rm asc} + \frac{P_{\rm b}}{2\pi} \arctan\left(\varepsilon_1/\varepsilon_2\right). \tag{2.32}$$

2.6.3.1 Developing a binary solution

While for isolated pulsars, an initial estimate of the pulsar period is typically sufficient to begin developing a fully phase-connected timing model, further information is required in the case of binary pulsars. Specifically, it is typically necessary to first develop an approximate orbital solution. As has been noted at multiple points throughout this thesis, the orbital motion of a pulsar causes a modulation of the pulsar's apparent orbital period. To first order, this modulation of the apparent pulsar period P can, as outlined in Freire et al. (2001), be described by

$$P\left(A_{\rm T}\right) \simeq P_{\rm int}\left(1 + \frac{V_1\left(A_{\rm T}\right)}{c}\right), \tag{2.33}$$

where $P_{\rm int}$ is the intrinsic spin period of the pulsar, $A_{\rm T}$ is the *true anomaly*, describing the angle between periastron and the position of the pulsar with respect to the center of mass of the orbit[19], and $V_1\left(A_{\rm T}\right)$ is the line-of-sight velocity as a function of the true anomaly, defined by

$$V_1\left(A_{\rm T}\right) = \frac{2\pi}{P_{\rm b}} \frac{x}{\sqrt{1-e^2}} \left[\cos\left(\omega + A_{\rm T}\right) + e\cos\omega\right]. \tag{2.34}$$

By taking care to account for the orbit motion of the Earth by using barycentric period measurements, the changing apparent pulsar period can be fit to these expressions and therefore allow for the determination of an approximate orbital solution. This technique works best when observations are recorded with a high cadence, so as to both mitigate the effects of additional, unsolved timing parameters such as $\dot{P}$ and to sufficiently sample the orbit of the pulsar. The program FITORBIT[20] provides a current implementation of this technique, and has been used in developing the orbital solutions of many of the new binary systems reported in Chapter 3.

[19] Expressions describing $A_{\rm T}$ as a function of time can be found in Equations 8.17 and 8.18 of Lorimer, D. R. and Kramer, M. (2005).

[20] https://github.com/gdesvignes/fitorbit

For pulsars which lack sufficient cadence for this technique, Freire et al. (2001) describe an alternative approach which takes advantage of the changing apparent acceleration of the pulsar, as well as its changing apparent spin period. This allows for the 'sense' of the period-change to be determined (i.e. whether the period is increasing or decreasing) for an individual measurement of the spin period. As described by Freire et al. (2001), the changing line-of-sight acceleration of the pulsar can be described to first order by

$$a_1\left(A_{\rm T}\right) = -\left(\frac{2\pi}{P_{\rm b}}\right)^2 \frac{x}{\left(1-e^2\right)^2}\left(1+e\cos A_{\rm T}\right)^2 \sin\left(\omega + A_{\rm T}\right). \tag{2.35}$$

Equations 2.33 and 2.35 can then be plotted parametrically to form a *period-acceleration diagram*, which forms a closed loop over one orbital period of the pulsar[21]. A period-acceleration diagram for PSR J1757−1854 (see Chapter 4), a pulsar whose orbital solution was made possible by this technique, can be seen in Figure 2.14. Measurements of the changing barycentric period and acceleration between observations can be then be used in conjunction with this diagram to estimate the orbital parameters.

For some pulsars, it may be sufficient to estimate a single measurement for both the period and acceleration per observation. However, for in the case of more extreme orbits such as that of PSR J1757−1854 where the period and acceleration are both changing rapidly, more advanced techniques may be required. In the case of PSR J1757−1854, this involved modeling the changing period and acceleration in each observation with a Taylor series using as many period-derivative terms as could be measured to a 3-σ significance, and then using the Taylor series expansion to reconstruct the approximate period and acceleration change over the duration of the observation in the period-acceleration diagram. An example of this fitting technique is also given in Figure 2.14.

2.6.3.2 Mass function

Information regarding the mass of the binary companion can be derived directly from measured Keplerian parameters of a given binary system. This is achieved via the *mass function*,

$$f\left(m_{\rm p}, m_{\rm c}\right) = \frac{\left(m_{\rm c}\sin i\right)^3}{\left(m_{\rm p}+m_{\rm c}\right)^2} = \frac{4\pi^2}{{\rm T}_\odot}\frac{x^3}{P_{\rm b}^2} \tag{2.36}$$

where $m_{\rm p}$ and $m_{\rm c}$ are the respective masses of the pulsar and its companion in units of the solar mass $\mathrm{M}_\odot$, and ${\rm T}_\odot = \left(G\mathrm{M}_\odot/c^3\right) = 4.925490947\,\mu s$. However, the companion mass $m_{\rm c}$ cannot be precisely determined using the mass function alone, due both to the unknown pulsar mass $m_{\rm p}$ and the unknown inclination angle i. In lieu of additional constraints, a range of masses for $m_{\rm c}$ can be estimated by taking the canonical pulsar mass of $m_{\rm p} = 1.4\,\mathrm{M}_\odot$ (as described in Section 1.2.2). With this assumed pulsar mass, setting $i = 90°$ (the case of an edge-on orbit) allows for a determination of the minimum companion mass, while taking an inclination angle of $i \simeq 26°$ allows for a constraint

[21] This assumes a Keplerian orbit. Post-Keplerian effects (see Section 2.6.3.3 and Figure 2.14) will change the shape of the curve with time.

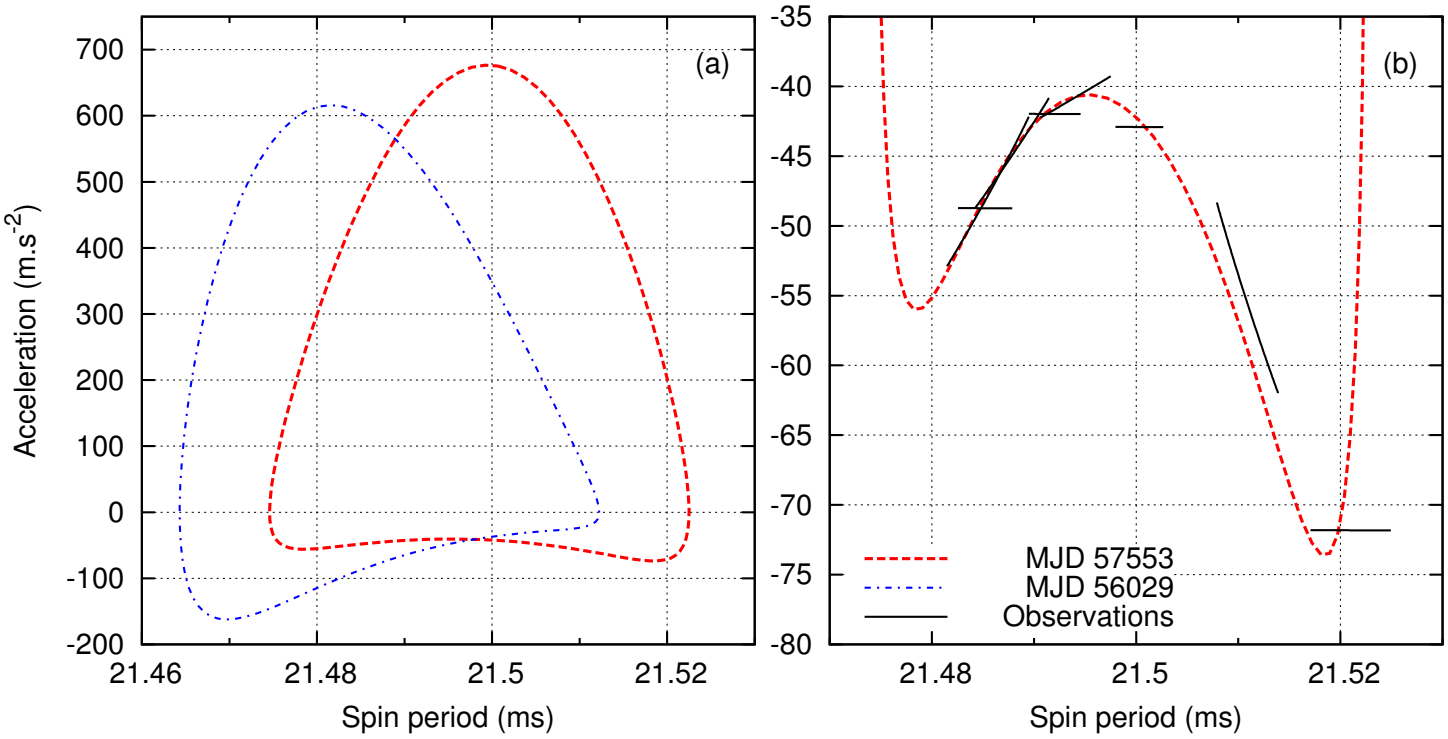

Figure 2.14: Period-acceleration curves for PSR J1757−1854, one of the pulsars reported in this thesis (see Chapter 4). Plot (a) shows the period-acceleration curve of the pulsar as measured at two separate epochs, MJD 57553 (the epoch at which the pulsar's orbit was solved) and MJD 56029 (the epoch at which the pulsar was discovered). Although the pulsar traces an approximately-closed loop in the period-acceleration diagram as it completes each orbit, the rate of periastron advance (see Section 2.6.3.3) in PSR J1757−1854 causes the line-of-sight projection of the orbit to gradually change over time, accounting for the two separate curves. Plot (b) shows the Taylor series reconstructions of the changing period and acceleration (black) plotted against the curve of the solved orbit. Figure adapted from the Proceedings of the International Astronomical Union Vol. 337 (Cameron et al., submitted).

of the maximum companion mass at a confidence level of 90 % (Lorimer, D. R. and Kramer, M., 2005).

2.6.3.3 Relativistic binaries and the post-Keplerian parameters

For pulsars in tight binary systems, especially those with compact companions such as white dwarves (WDs), neutron stars (NSs) and (theoretically) black holes (BHs), the standard Keplerian parameters (which are rooted in classical Newtonian mechanics) are fundamentally insufficient to model the relativistic effects which are observed in the resulting strong-field gravitational regime. The required relativistic corrections are typically described through the *post-Keplerian* (PK) *parameters*. Each of these PK parameters produce their own characteristic timing residual signatures (Damour & Deruelle, 1986), and can therefore be accounted for by the process of pulsar timing. The role of these parameters in allowing for tests of gravitational theories such as general relativity (GR) has already been discussed in Chapter 1, however, it is worth repeating that these parameters have been enumerated in a theory-independent fashion (see e.g. Damour & Taylor, 1992), i.e., they are measurable independent of any particular gravitational theory and can therefore be used to test and constrain them. The first three 'standard' PK parameters, along with their relations as determined GR (Damour & Deruelle, 1985, 1986; Taylor & Weisberg, 1989; Damour & Taylor, 1992) and with all masses in units of $\mathrm{M}_\odot$, include

- the time-averaged **rate of periastron advance**[22] $\dot{\omega}$, or the rate at which the orientation of the orbit rotates through space, defined by

$$\dot{\omega} = 3\mathrm{T}_\odot^{2/3} \left(\frac{P_\mathrm{b}}{2\pi}\right)^{-5/3} \left(1-e^2\right)^{-1} \left(m_\mathrm{p}+m_\mathrm{c}\right)^{2/3}. \tag{2.37}$$

- the **gravitational redshift and time-dilation parameter** γ, sometimes referred to as the **Einstein delay**, which describes the relativistic dilation experience by the pulsar signal as it traverses the gravitational potential of the binary system, defined by

$$\gamma = \mathrm{T}_\odot^{2/3} e \left(\frac{P_\mathrm{b}}{2\pi}\right)^{1/3} \frac{m_\mathrm{c}\left(m_\mathrm{p}+2m_\mathrm{c}\right)}{\left(m_\mathrm{p}+m_\mathrm{c}\right)^{4/3}}. \tag{2.38}$$

- the **orbital period derivative** $\dot{P}_\mathrm{b}$, the rate at which the orbital period decreases due to the emission of gravitational waves (GW), defined by

$$\dot{P}_\mathrm{b} = -\frac{192\pi}{5}\mathrm{T}_\odot^{5/3} \left(\frac{P_\mathrm{b}}{2\pi}\right)^{-5/3} f\left(e\right) \frac{m_\mathrm{p} m_\mathrm{c}}{\left(m_\mathrm{p}+m_\mathrm{c}\right)^{1/3}} \tag{2.39}$$

  where

$$f\left(e\right) = \frac{\left(1+\left(73/24\right)e^2+\left(37/96\right)e^4\right)}{\left(1-e^2\right)^{7/2}}. \tag{2.40}$$

[22] The instantaneous value of $\dot{\omega}$ varies as a function of orbital phase. Quoted values of $\dot{\omega}$ refer to its value averaged over a single orbit.

Two further 'standard' PK parameters describe the *Shapiro delay* (Shapiro, 1964) encountered as the pulsar moves behind its binary companion with respect to the observer's line of sight which, as noted previously in Section 1.4.1.1, is an orientation known as *superior conjunction*. As the signal of the pulsar passes close to the binary companion, it experiences a relativistic delay as a result of traversing the companion's gravitational field. This delay originates not just from the extra path length introduced as the curved spacetime surrounding the companion bends the pulsar's signal around it, but also from the time dilation induced by this curved spacetime. A demonstration of the characteristic residual signature of Shapiro delay as a function of orbital phase can be seen in Figure 2.15. The two Shapiro delay PK parameters, along with the formulations under GR, are

- the **range** parameter r, defined by

$$r = \mathrm{T}_{\odot} m_{\mathrm{c}}. \tag{2.41}$$

- the **shape** parameter, defined by

$$s = \sin i = \mathrm{T}_{\odot}^{-1/3} x \left(\frac{P_{\mathrm{b}}}{2\pi}\right)^{-2/3} \frac{(m_{\mathrm{p}} + m_{\mathrm{c}})^{2/3}}{m_{\mathrm{c}}}. \tag{2.42}$$

Two additional PK parameters are the **orbital deformation parameters**, which describe relativistic corrections to the shape of the pulsar's orbit. They are defined in GR by

$$\delta_{\theta} = \mathrm{T}_{\odot}^{2/3} \left(\frac{P_{\mathrm{b}}}{2\pi}\right)^{-2/3} \frac{\left(3m_{\mathrm{p}}^2 + 6m_{\mathrm{p}}m_{\mathrm{c}} + 2m_{\mathrm{c}}^2\right)}{(m_{\mathrm{p}} + m_{\mathrm{c}})^{4/3}} \tag{2.43}$$

$$\delta_{\mathrm{r}} = \mathrm{T}_{\odot}^{2/3} \left(\frac{P_{\mathrm{b}}}{2\pi}\right)^{-2/3} \frac{\left((7/2)\, m_{\mathrm{p}}^2 + 6m_{\mathrm{p}}m_{\mathrm{c}} + 2m_{\mathrm{c}}^2\right)}{(m_{\mathrm{p}} + m_{\mathrm{c}})^{4/3}} \tag{2.44}$$

The degree to which each of these PK parameters is measurable varies greatly depending upon the binary system in question. For example, a pulsar in a circular orbit will make the measurement of $\dot{\omega}$ more difficult due to the poorer constraints available on both ω and T_0. Similarly, measurement of the Shapiro delay parameters r and s relies upon the binary being close to edge-on in its inclination in order for the binary companion to pass close to the line-of-sight during superior conjunction. The parameters δ_{θ} and δ_{r} present particular detection challenges. Currently, δ_{r} is considered unmeasurable due to its covariance with other orbital and spin parameters (Damour & Taylor, 1992), while the measurability of δ_{θ} is related both to e (which determines the magnitude of the residual timing signature) and to $\dot{\omega}$ (which determines the time scale required to separate the effect from the residual signature of γ). The precise expression for timing residual contribution of δ_{θ} is provided in Damour & Deruelle (1986), and is discussed further in Chapter 4. To date, δ_{θ} has only been measured to low precision in both the Hulse-Taylor pulsar (PSR B1913+16; Weisberg & Huang, 2016) and the Double Pulsar (PSR J0737−3039; Kramer et al., in prep.).

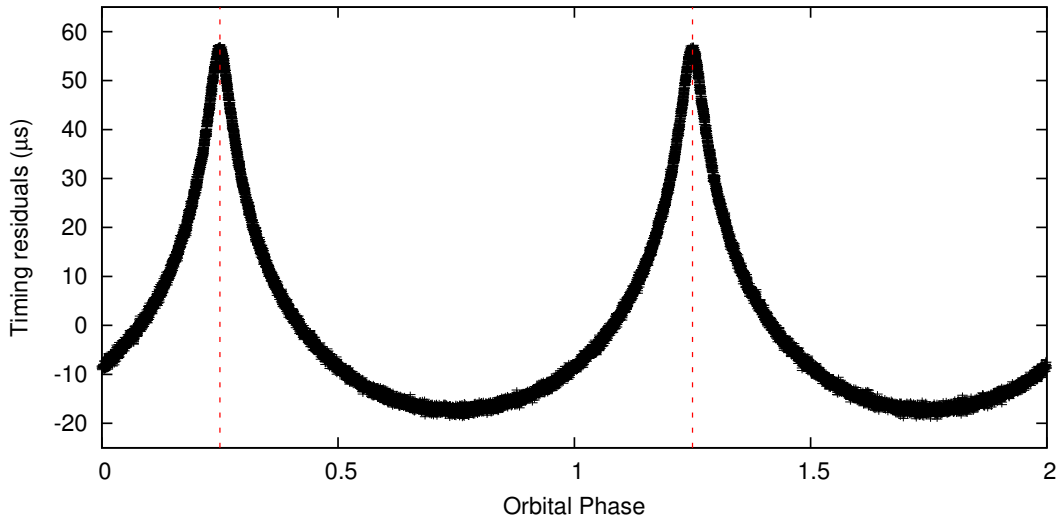

Figure 2.15: The timing residual signature exhibited by Shapiro delay in a relativistic binary system, plotted as function of orbital phase. Shown are the simulated TOAs for a hypothetical circular, edge-on binary system, with all timing parameters except for the Shapiro delay having been correctly fit for, such that only the Shapiro delay residual signature is visible. The dashed red lines indicate the position of superior conjunction, the point in the orbit where the pulsar passes directly behind the companion object, thus causing the maximum delay in the received pulsar emission.

The defining timing model used to describe relativistic binaries is the DD model (Damour & Deruelle, 1985, 1986), which incorporates the required relativistic corrections (including the PK parameters) in a theory-independent fashion, and thereby allows for tests of multiple gravitational theories to be conducted. In addition, multiple variants of this model are also in common use, depending on the required application. For example, the DDGR model (Taylor, 1987; Taylor & Weisberg, 1989) assumes the correctness of GR and thereby ensures consistency between the PK parameters according to their GR definitions, only fitting for $m_{\rm p}$ and $m_{\rm c}$. Another variant, the DDH model (Freire & Wex, 2010), was designed to allow for easier separation and constraint of the Shapiro delay by reparameterising it as the orthometric amplitude h_3 and orthometric ratio ς. These relate to the standard Shapiro parameters r and s via

$$\varsigma = \sqrt{\frac{1-\overline{c}}{1+\overline{c}}} \tag{2.45}$$

where

$$\overline{c} = \sqrt{1-s^2} = |\cos i|\,, \tag{2.46}$$

and

$$h_3 = r\varsigma^3. \tag{2.47}$$

One further model, the DDS model (Kramer et al., 2006c,b), re-parameterises the Shapiro shape parameter s as $z_s = -\ln(1-s)$, thereby allowing for better uncertainty estimation in highly-inclined binaries such as the PSR J0737−3039.

2.7 An overview of Galactic-plane pulsar surveys

This chapter concludes with a brief overview of the current state of pulsar surveys. A fully comprehensive review is beyond the scope of this thesis, however, a degree of historical context regarding the most significant survey projects is important in order to understand the relative position of the bulk of the scientific results presented in the remainder of this thesis. With this in mind, particular attention is given to those surveys whose focus has been on observations of the Galactic plane, the region surveyed by the HTRU-S LowLat pulsar survey.

2.7.1 Previous generation surveys

Following the initial discovery of the first pulsar by Hewish et al. (1968), a number of early pulsar surveys began in earnest so as to uncover as many of these new objects as possible. This first generation of pulsar surveys, including the first Molonglo transit survey with the Molonglo Cross Telescope (MOL1; Large et al., 1968b; Turtle & Vaughan, 1968; Large et al., 1969; Vaughan & Large, 1972) and the first Jodrell Bank transit survey with the 76-m Lovell Telescope (JB1; Davies et al., 1970; Davies & Large, 1970; Davies et al., 1973), were conducted at central frequencies between 400−430 MHz and by today's standards seem very technologically limited. For example, MOL1 observed using only two 2-MHz channels with the output of the telescope written to a chart recorder and inspected by eye (Large et al., 1968b).

Even in these early surveys, the fundamental relationship between the Galactic plane and the distribution of the pulsar population was recognised quickly, with both MOL1 and JB1 devoting additional observational resources to the Galactic plane. Both Large et al. (1968b) and Wielebinski et al. (1969) observed a clustering of pulsars observed towards the Galactic plane in the discoveries of MOL1, but noted a 'zone of avoidance' along the central regions of the plane where comparatively few pulsars had been detected. This zone was a likely consequence of both of these surveys' limited sensitivity and their technologically-limited ability to de-disperse pulsed signals from deeper in the plane, for which the effects of dispersion would be more pronounced. These limitations were partially addressed by both the first Arecibo survey (AR1; Hulse & Taylor, 1974, 1975b), which also observed at 430 MHz with the 305-m Arecibo Radio Telescope but employed 32 channels across an 8-MHz bandwidth and thereby allowed for better mitigation of the effects of dispersion, and the second Molonglo survey (MOL2; Manchester et al., 1978), an all-sky survey which employed 4 channels across a 4-MHz bandwidth for its observations of the Galactic-plane region. Of all these early surveys, MOL2 was perhaps the most successful, discovering 155 pulsars and more than doubling the known pulsar population, although with the Hulse-Taylor binary pulsar among its discoveries (Hulse & Taylor, 1975a), the AR1 survey was not short on success.

Later Galactic-plane surveys continued in the following decades, with continual improvements in technology allowing for a constant flow of new discoveries. New receivers with larger bandwidths and increasingly-fine channelisation allowed for weaker pulsars to be detected at greater and greater values of DM, while increasingly-fine time sampling allowed for the discovery of the first MSP (PSR B1937+21; Backer et al., 1982). Additional surveys of this era which specifically targeted the Galactic plane in the $400-430$-MHz range include the second and third Arecibo surveys (AR2, AR3; Segelstein et al., 1986; Stokes et al., 1986; Nice et al., 1995), the Green Bank short-period survey (GB3; Stokes et al., 1985) (which was conducted with the since-destroyed Green Bank 300-ft telescope), and the Parkes Southern Pulsar survey (PKS70; Manchester et al., 1996; Lyne et al., 1998) (conducted with the Parkes 64-m Radio Telescope). The last of these surveys, PKS70, was conducted with a 32-MHz bandwidth, 256 channels and a sampling time of only $t_{\rm samp} = 300\,\mu$s. The survey employed an offline, software-based pulsar search pipeline, closely resembling the setup still used by current-day pulsar surveys.

In addition to the surveys described thus far, which were all conducted within the vicinity of $400-430$ MHz, a number of Galactic-plane surveys were also undertaken at higher frequencies, particularly in the vicinity of 1.4 GHz. Major Galactic-plane surveys conducted at this frequency include the second Jodrell Bank survey (JB2; Clifton & Lyne, 1986; Clifton et al., 1992) and the Parkes 20-cm survey (PKS1; Johnston et al., 1992a). As noted previously in Section 1.3.2, searching at higher frequencies reduces the effects of pulse scattering, hence allowing these surveys to penetrate deeper into the Galactic ISM, with a significant fraction of the discovered pulsars from both surveys being reported at higher values of DM. Another advantage of the change to higher frequency was the availability of receivers with larger bandwidths, with JB2 observing

Table 2.1: Basic parameters of the Parkes 21-cm 13-multibeam receiver (MB20). The gain, full width at half maximum (FWHM), and beam ellipticity of each concentric ring of telescope beams (see Figure 2.16) is listed. Also provided is the coma lobe, a quantity which describes the geometric aberration effects which result from placing a particular beam at an offset from the boresight of the telescope. Table adapted from Keith et al. (2010).

Beam	Centre	Inner Ring	Outer Ring
Gain, G (K Jy^{-1})	0.735	0.690	0.581
FWHM (arcmin)	14.0	14.1	14.5
Ellipticity	0.0	0.03	0.06
Coma lobe (dB)	-	17	14

across 40 MHz and PKS1 observing over a maximum bandwidth of 320 MHz, increasing the sensitivity of these observations as per Equation 2.23. However, as indicated by Equation 2.1, a key disadvantage of observing at higher frequencies is the resulting smaller FWHM of the telescope beam. As a result, surveys as higher frequencies require more individual observations to map the same region of sky, reducing the overall efficiency of the survey due to the larger corresponding time requirements.

2.7.1.1 The Parkes Multibeam Pulsar Survey

Commencing in 1997, the Parkes Multibeam Pulsar Survey (PMPS; Manchester et al., 2001), once again conducted with the Parkes 64-m Radio Telescope, represents a significant milestone in the history of pulsar surveys, and is arguably the most successful pulsar survey undertaken to date, discovering over of 830 pulsars. The focus of the survey was exclusively on the Galactic plane, covering a region between $260° < l < 50°$ and $|b| < 5°$ (See Figure 2.17). The success of the survey was due in large part to the development of the Parkes 21-cm multibeam receiver (MB20; Staveley-Smith et al., 1996), a 13-beam focal plane array receiver originally designed for surveys of neutral hydrogen. A summary of the critical parameters of the MB20 receiver is provided in Table 2.1. The 13 survey beams, arranged in two concentric hexagonal rings with one central beam (see Figure 2.16), greatly improved the survey efficiency of the receiver over the earlier PKS1 1.4-GHz pulsar survey in that it could observe 13 on-sky positions simultaneously. This counteracted the disadvantage of the smaller FWHM of each beam ($\sim 0.24°$ for each beam in the case of the MB20 receiver, as per Table 2.1) due to observing at higher frequencies, while continuing to mitigate the effects of interstellar scattering. Coupled with a large bandwidth of ~ 300 MHz, integration times of $t_{\rm int} = 35$ min and a sampling time of $t_{\rm samp} = 250\,\mu$s, the PMPS was able to probe much deeper into the Galactic plane than earlier pulsar surveys and ensured its sensitivity to a wide range of pulse periods, including MSPs.

The many successes of the PMPS are too numerous to list in full detail. How-

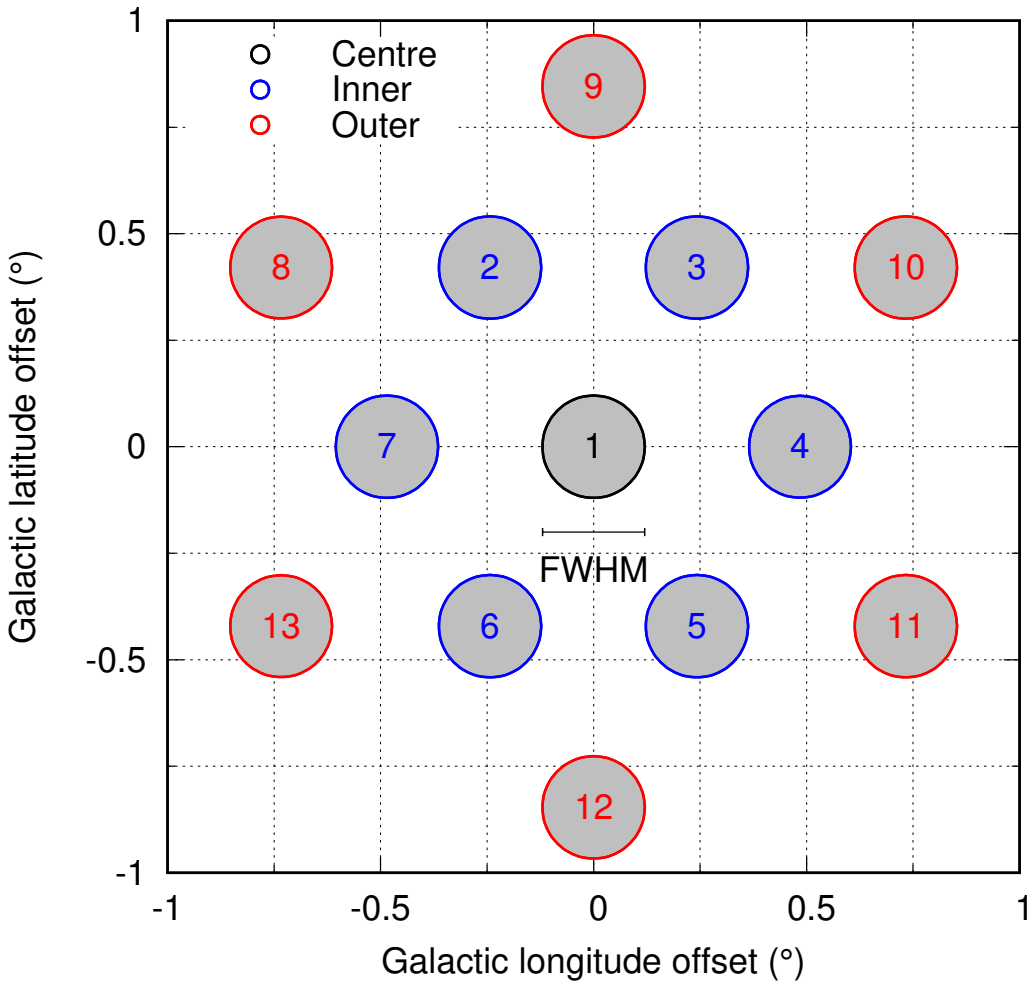

Figure 2.16: On-sky beam configuration of the Parkes 21-cm 13-multibeam receiver (MB20). The 13 beams are configured into three groups as shown, the centre beam (black), the inner ring (blue) and the outer ring (red). Note that while the relative positions of the beams with respect to each other are fixed, their absolute on-sky orientation may change between epochs due to changes in the rotation of the receiver. The parameters of each beam group vary slightly as per Table 2.1, with the full width at half maximum of the central beam being 14 arcmin ($\sim 0.24°$).

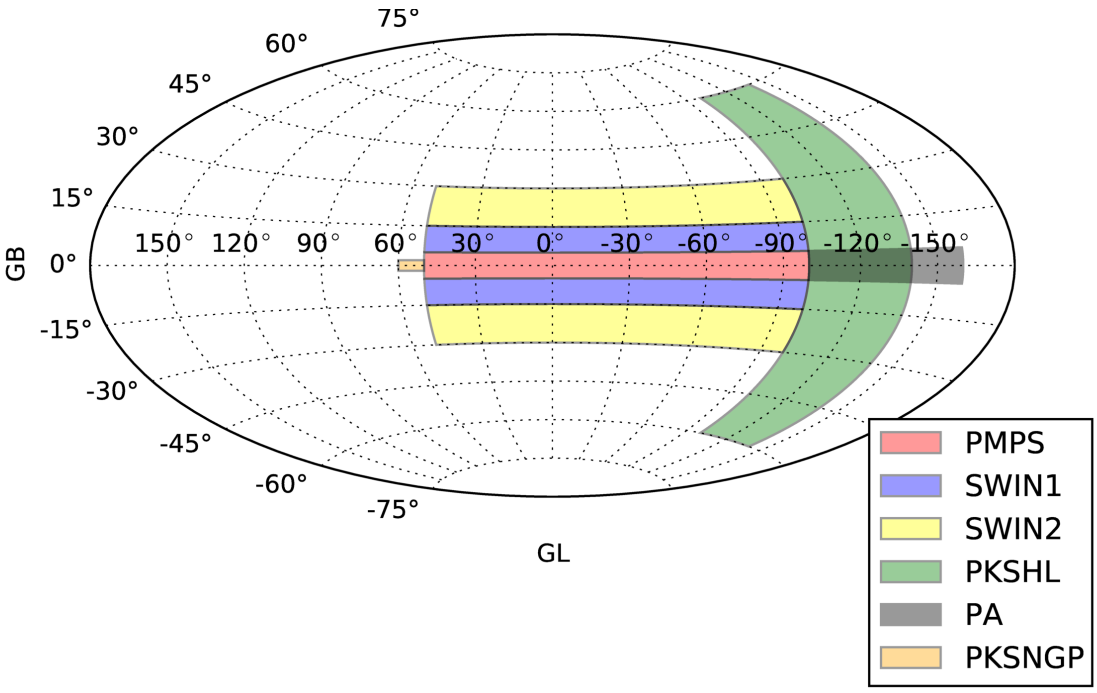

Figure 2.17: Sky coverage of PMPS-era pulsar surveys, projected in Galactic coordinates. A brief explanation of each survey is given in Sections 2.7.1.1 and 2.7.1.2.

ever, selected highlights include the discovery of the first Rotating Radio Transients[23] (RRATs, McLaughlin et al., 2006; Keane et al., 2010), the discovery of the relativistic binary system PSR J1141−6545 (Kaspi et al., 2000), and the discovery of three double neutron star (DNS) binary systems, PSRs J1753−2240 (Keith et al., 2009a), J1756−2251 (Faulkner et al., 2004) and J1811−1736 (Lyne et al., 2000). In addition, the large population of pulsars discovered by the survey (Manchester et al., 2001; Morris et al., 2002; Kramer et al., 2003; Hobbs et al., 2004; Lorimer et al., 2006a) enabled a much greater understanding of the Galactic pulsar population (Lorimer et al., 2006a). Furthermore, even though the observations of the PMPS were completed in 2002, multiple reprocessing efforts have continued to yield new discoveries. These include the discovery of 28 pulsars through the use of new candidate sorting techniques (Keith et al., 2009b), the discovery of 16 pulsars through a coherent time-domain acceleration search (Eatough et al., 2013a), the discovery of 24 pulsars through the 'Einstein@Home' distributed computing project (Knispel et al., 2013) and one of the first applications of a 'neural network' candidate classification system, resulting in the discovery of one further pulsar (Eatough et al., 2010a).

[23]RRATs are a class of pulsar characterised by sporadic, single bright pulses of inferred Galactic origin, and are generally beyond the scope of this thesis. For a review, see Keane et al. (2011).

2.7.1.2 Additional Parkes multibeam surveys

The PMPS was by no means the only Galactic-plane pulsar survey to take advantage of the capabilities of the MB20 receiver. The Perseus Arm Pulsar Survey (PA; Burgay et al., 2013a), conducted between 2004 and 2009, was designed as a southern extension of the PMPS away from the Galactic center, observing with an identical setup to the PMPS and covering a sky region between $200° < l < 260°$ and $|b| < 5°$. The PA survey resulted in the discovery of 14 additional pulsars. Simultaneously, the Parkes Northern Galactic Plane survey (PKSNGP; Lorimer et al., 2013) extended the PMPS north, covering a small region of the Galactic plane between $50° < l < 60°$ and $|b| < 2°$. With half the sampling time ($t_{\rm samp} = 125\,\mu$s) and double the integration time ($t_{\rm int} = 70$ min) of the PMPS, the survey allowed for a much deeper probe into the Galactic plane, and resulted in the discovery of 17 pulsars.

A number of other Parkes surveys were also conducted with the MB20 receiver, but did not cover or specifically focus on the Galactic-plane region. The Parkes High-Latitude survey (PKSHL; Burgay et al., 2006), conducted between 2000 and 2003, observed at a similar range of Galactic longitudes to the PA survey, covering $220° < l < 260°$, but extended the Galactic latitude range to $|b| < 60°$. With only $t_{\rm int} = 265$ s per observation, the sensitivity of this survey in the Galactic-plane region was significantly lower than in both the PMPS and PA surveys, although 6 of the the 18 new discoveries reported by PKSHL were found within $|b| < 5°$. PKSHL also holds the distinction of having discovered the Double Pulsar (PSR J0737−3039A/B; Burgay et al., 2003; Lyne et al., 2004), the importance of which has already been discussed in Section 1.1.2. In addition, the first (SWIN1; Edwards et al., 2001) and second (SWIN2; Jacoby et al., 2009) Swinburne intermediate-latitude surveys, conducted in 1998−1989 and 2001−2002 respectively, observed the same Galactic longitude region as the PMPS, but at Galactic latitude regions of $5° < |b| < 15°$ and $15° |b| < 30°$ respectively. Together, SWIN1 and SWIN2 discovered a combined total of 109 pulsars. The sky coverage of the PKSHL, SWIN1 and SWIN2, PA and PKSNGP surveys are displayed in Figure 2.17.

2.7.2 The High Time Resolution Universe survey

The High Time Resolution Universe (HTRU) project consists of two separate current-generation surveys, the northern (HTRU-N) and southern (HTRU-S) surveys, which together represent the first true all-sky pulsar survey. HTRU-N (Barr et al., 2013) is currently being conducted by the 100-m Effelsberg telescope in Germany, with survey observations having commenced in 2010. HTRU-S (Keith et al., 2010) was conducted using the Parkes 64-m radio telescope, with all observations having been completed as of 2014. These surveys are further divided into specialised regions based primarily on Galactic latitude, the LowLat ($|b| < 3.5°$), MedLat ($|b| < 15°$) and HiLat ($|b| > 15°$ in the case of HTRU-N, and all latitudes such that $\delta < +10°$ in the case of HTRU-S). Each of these sub-surveys is specifically tailored in its design so as to make HTRU one of the most sensitive pulsar surveys ever conducted, particularly along

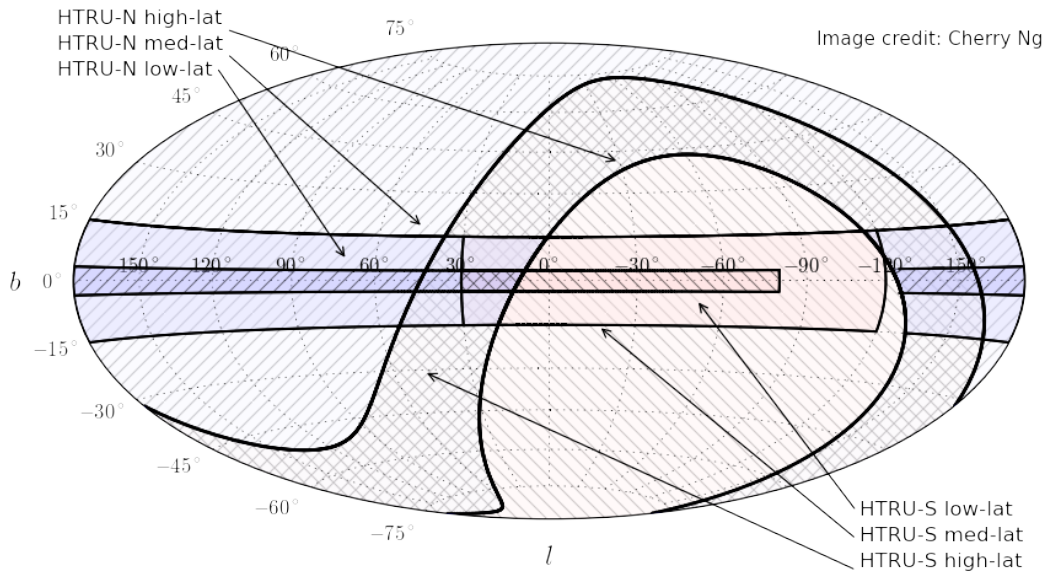

Figure 2.18: Regions of the HTRU pulsar survey. Red-shaded areas with '\' hatching indicate the HTRU-South (HTRU-S) survey, while blue-shaded areas with '/' indicate the HTRU-North (HTRU-N) survey. Each survey is divided into three regions, the low-latitude (LowLat), medium-latitude (MedLat) and all-sky high-latitude (Hilat) regions as indicated. Full survey parameters are available in Table 2.2. Figure from Ng (2014).

the Galactic plane. Figure 2.18 shows the sky coverage and overlap between all six survey regions, while Table 2.2 lists the parameters of each survey component. The full HTRU survey project is supported by the international HTRU Collaboration, with the responsibility for ongoing data-processing and follow-up primarily shared between the Max-Planck-Institute für Radioastronomie (MPIfR) in Germany, the Swinburne University of Technology and the Australia Telescope National Facility (ATNF) in Australia, the Istituto Nazionale di Astrofisica (INAF) in Italy and the University of Manchester in the UK.

As with the earlier PMPS, the HTRU-S survey was conducted using the MB20 receiver, however, increases in signal and data processing allow for much greater sensitivity both in terms of flux density as well as an increased sensitivity to MSPs. As described in Table 2.2, all HTRU-S observations were recorded with the Berkeley Parkes Swinburne Recorder[24] (BPSR) backend system, recording dual-polarisation polyphase filterbank search-mode data recorded across 1024 channels at a channel bandwidth of $\Delta f_{\rm chan} \simeq 391\,\mathrm{kHz}$ across a total usable bandwidth of 400 MHz, drastically reducing the effects of dispersive smearing. However, due to RFI from the *Tharuya 3* satellite, the usable bandwidth was reduced to only 340 MHz, with 870 usable channels remaining. A

[24] http://astronomy.swin.edu.au/pulsar/?topic-bpsr

Table 2.2: Observing specifications of the HTRU-N and HTRU-S pulsar surveys. Table adapted from Ng (2014).

	HTRU-N			HTRU-S		
Telescope	Effelsberg 100-m			Parkes 64-m		
Receiver	7-Beam			MB20		
Backend	PFFTS			BPSR		
Peak gain, G ($\mathrm{K\,Jy^{-1}}$)	1.5			0.735		
Receiver temperature, T_{rec} (K)	21			23		
Digitisation bit-count, n_{bits}	8			2		
Number of polarisations, n_{p}	2			2		
Central frequency, f_{c} (MHz)	1360			1352[a]		
Bandwidth, B (MHz)	240			340[a]		
Number of channels, n_{chan}	512			870[a]		
Channel bandwidth, Δf_{chan} (kHz)	468.75			390.625		
Sampling time, t_{samp} (μs)	54.6			64		
Region of declination, δ (°)	$\delta > -20$			$\delta < +10$		
Survey region	HiLat	MedLat	LowLat	HiLat	MedLat	LowLat
Region of Galactic longitude, l (°)	–	–	–	–	$-120 < l < 30$	$-80 < l < 30$
Region of Galactic latitude, b (°)	$\lvert b\rvert > 15$	$\lvert b\rvert < 15$	$\lvert b\rvert < 3.5$	–	$\lvert b\rvert < 15$	$\lvert b\rvert < 3.5$
Integration time, t_{int} (s)	90	180	1500	270	540	4300
Number of beams, N_{beams}	1066135	375067	87395	443287	95056	15990
Mean sky temperature[b], T_{sky} (K)	5	8	11	1.0	2.5	7.6
Characteristic minimum sensitivity[c], S_{min} (mJy)	0.61	0.34	0.13	0.40	0.30	0.13
Number of samples per beam, n_{samp}	1.6×10^6	3.3×10^6	27.4×10^6	$\sim 2^{22}$	$\sim 2^{23}$	$\sim 2^{26}$
Data size per beam (GB)	0.8	1.6	13.4	1.0	2.0	16.6
Total data size (TB)	818	576	1118	435	190	263

[a] Original survey conducted with $f_{\mathrm{c}} = 1382\,\mathrm{MHz}$, $B = 400\,\mathrm{MHz}$ and $n_{\mathrm{chan}} = 1024$, however the upper 60 MHz of the band was rendered unusable by RFI. These parameters therefore reflect the usable band.

[b] Values of T_{sky} extrapolated from the 408-MHz sky-map presented in Haslam et al. (1981).

[c] Derived for a pulsar with a spin period of only a few milliseconds and a duty cycle $\delta = 0.3$ as per (Ng, 2014).

Table 2.3: Characteristic minimum detectable flux densities ($S_{1400,\mathrm{min}}$) of the HTRU-S LowLat survey. Maximum, mean and minimum values of $S_{1400,\mathrm{min}}$ are provided with respect to the approximate range of duty cycles δ of both the population of normal pulsars and MSPs (defined here as having $P < 30\,\mathrm{ms}$. Table from Ng et al. (2015).

	MSPs		Normal pulsars	
	δ (%)	$S_{1400,\mathrm{min}}$ (mJy)	δ (%)	$S_{1400,\mathrm{min}}$ (mJy)
min	0.28	0.013	0.014	0.0030
mean	11.54	0.092	4.21	0.053
max	65.31	0.35	57.29	0.29

sampling time of $t_{\mathrm{samp}} = 64\,\mu\mathrm{s}$ also significantly increases the sensitivity of the survey to MSPs compared to the earlier PMPS, whose t_{samp} of only $250\,\mu\mathrm{s}$ was almost 4 times as large. Further details of the HTRU-S setup and strategy are available in Keith et al. (2010).

Meanwhile, the HTRU-N survey represents one of the first large-scale blind pulsar surveys to be conducted with the Effelsberg telescope. Data was recorded using a 21-cm 7-multibeam receiver[25] (one hexagonal ring with a central beam) in conjunction with the Effelsberg Pulsar Fast Fourier Transform Spectrometer (PFFTS) backend. The PFFTS is capable of recording polyphase filterbank search-mode data in dual polarisations with 512 channels at a channel bandwidth of $\Delta f_{\mathrm{chan}} \simeq 469\,\mathrm{kHz}$ across a usable bandwidth of 240 MHz with a sampling time of $t_{\mathrm{samp}} = 54.6\,\mu\mathrm{s}$. Further details of the HTRU-N setup and strategy are available in Barr et al. (2013).

The majority of the scientific content of this thesis focuses on the LowLat portion of the HTRU-S survey (HTRU-S LowLat; Ng et al., 2015), which represents the direct technological successor to the PMPS. A comparison between some of the basic parameters of these two surveys is given in Table 2.4. Covering the densest regions of the Galactic plane with an integration time of $t_{\mathrm{int}} = 72\,\mathrm{min}$ (twice that of the PMPS), the HTRU-S LowLat survey represents one of the deepest blind pulsar surveys of the Galactic plane ever recorded. Table 2.3 lists the estimated sensitivity of the HTRU-S LowLat survey to both normal pulsars and MSPs, with respect to the survey sensitivity discussion in Section 2.5 and the parameters listed in Table 2.2. The goals and search strategy of the HTRU-S LowLat survey are further discussed in Section 3.1, with additional information available in Ng (2014) and Ng et al. (2015).

2.7.2.1 Discovery highlights

Not including the 40 new pulsar discoveries described in this thesis in Chapters 3 and 4, HTRU-S has published the discovery of approximately 190 pulsars (Keith et al., 2010; Levin et al., 2010; Bates et al., 2011; Bailes et al., 2011; Burke-Spolaor et al., 2011; Keith et al., 2012; Bates et al., 2012; Burgay et al., 2013b; Ng et al., 2014; Bates et al., 2015), including 60 from the HTRU-S LowLat survey (Ng et al., 2015), while HTRU-N

[25] http://www3.mpifr-bonn.mpg.de/div/electronic/content/receivers/21cm.html

Table 2.4: A direct comparison of the basic survey parameters of the PMPS and HTRU-S LowLat, showing the technological improvement achieved by the HTRU-S LowLat pulsar survey. Shown are the sky coverage in Galactic coordinates, the central frequencies (f_c), number of channels (n_{chan}), channel bandwidth (Δf_{chan}), total bandwidth (B), sampling time (t_{samp}) and integration time (t_{int}) of each survey. PMPS parameters are taken from Manchester et al. (2001), while HTRU-S LowLat parameters are as they appear in Table 2.2.

Survey	Sky coverage	f_c (MHz)	n_{chan}	Δf_{chan} (MHz)	B (MHz)	t_{samp} (μs)	t_{int} (s)
PMPS	$-100° < l < 50°$ $\lvert b\rvert < 5°$	1374	96	3	288	250	2100
HTRU-S LowLat	$-80° < l < 30°$ $\lvert b\rvert < 3.5°$	1352	870	0.391	340	64	4300

has published the discovery of an additional 17 pulsars (Barr et al., 2013; Berezina et al., 2017). Some particular discovery highlights include the discovery of the 'pulsar-planet' binary PSR J1719−1438 (Bailes et al., 2011) (the so-called 'Diamond planet' binary, due to the suspected identity of the companion as the crystalline remains of a carbon-white dwarf) and the discovery of a radio-loud magnetar, PSR J1622−4950 (Levin et al., 2010).

However, perhaps one of the most notable contributions of the HTRU survey has been the detection of the first significant population of Fast Radio Bursts (FRBs) (Thornton et al., 2013; Petroff et al., 2015a,c; Champion et al., 2016). FRBs are millisecond-scale radio bursts typically found at high Galactic latitudes, and whose dispersive delay appears to exceed the expected contribution from the Milky Way Galaxy along their line of sight, suggesting an extragalactic origin. FRBs are also typically one-off events, with only one repeating FRB identified to date (Spitler et al., 2016). Although the first FRB was detected by Lorimer et al. (2007), it was not until the HTRU survey that a sufficient population was uncovered so as to fully establish FRBs as a new class of radio transient, a result both of the high time resolution of the survey as well as its fine channelisation contributing to an overall lack of dispersive smearing at high values of DM.

2.7.3 Additional current generation surveys

A number of additional pulsar surveys conducted with current-generation technology are either ongoing or have recently been completed. However, only a handful of these focus on the Galactic-plane region. The most relevant of these current generation surveys to the HTRU survey is the Survey for Pulsars and Extragalactic Radio Bursts (SUPERB; Keane et al., 2018), which to date has published the discovery of 10 new pulsars. In broad terms, the observing setup of SUPERB matches that of HTRU, employing the Parkes 64-m Radio Telescope and its MB20 receiver alongside the BPSR

search-mode backend with identical bandwidth, channelisation and sampling rates. However, SUPERB differs from HTRU in three key respects:

- As one of the primary goals of SUPERB is the detection of FRBs and other radio transient sources, it employs an integration time of only $t_{\rm int} = 9\,$min, equivalent to that of HTRU-S MedLat and more than double that of HTRU-S HiLat. This renders SUPERB more sensitive both to radio transients and other pulsars at high Galactic latitudes where FRBs appear to be more favourably detected (Petroff et al., 2014), but less sensitive in the region of the Galactic plane.

- Advances in parallel-processing technology have allowed for SUPERB to be processed in *real time* for both transients and pulsars so as to allow for immediate follow-up of any identified sources, although as with HTRU, observations are also written to long-term storage media for a later offline analysis. The development of real-time processing and candidate identification techniques is a critical step towards the implementation of next-generation pulsar surveys.

- In order to fully complement the observations of HTRU, the positions of the SUPERB survey beams have been designed to most-sensitively observe the sky positions to which HTRU was least sensitive. This includes both targeting the central MB20 beam at positions which in HTRU would only have been covered by an outer beam of the MB20, as well as introducing a half-FWHM offset in position so as to place the most sensitive portion of each SUPERB beam in the weakest portion of the coincident HTRU beams.

Another current-generation Galactic-plane survey is the Arecibo Pulsar survey using ALFA (PALFA; Cordes et al., 2006). Observing at 1.4 GHz, PALFA spans two regions of the Galactic plane between $|b| < 5°$, one towards the Galactic center ($32° < l < 77°$) and the other covering the Galactic anti-center ($168° < l < 214°$), an almost identical region of coverage to the original AR1 survey. Having commenced in 2004, the impressive gain of up to 10.4 K Jy^{-1} provided by Arecibo's 305-m antenna, combined with the 7-multibeam ALFA receiver and a sampling time of $t_{\rm samp} = 64\,\mu$s makes PALFA a particularly efficient and sensitive survey to both normal pulsars and MSPs. As a consequence of its high gain, it is able to reduce its integration time to a maximum of $t_{\rm int} = 134\,$s, reducing the influence of the effects of any binary motion (which as shown in Figure 2.9 can cause smearing of the signal in time if uncorrected) without having to conduct extensive acceleration searches or other binary search techniques. To date, PALFA has discovered in excess of 140 pulsars (see e.g. Cordes et al., 2006; Nice et al., 2013; Lazarus et al., 2015; Lyne et al., 2017b), with particular highlights including the discovery of a highly-eccentric, fully-recycled MSP PSR J1903+0327 (Champion et al., 2008) and the relativistic binary pulsar PSR J1906+0746 (Lorimer et al., 2006b). The PALFA survey is also complemented by the SPAN512 survey (Desvignes et al., 2013b) begun in 2012 at the Nançay Radio Telescope. Observing at 1.5 GHz with a sky coverage of $74° < l < 150°$ and $3.5° < |b| < 5°$, the survey extends the region of the Galactic plane covered by PALFA.

Additional contemporary surveys which do not focus on the Galactic-plane region include the the Arecibo 327-MHz driftscan survey (AO327; Deneva et al., 2013, 2016), the GBT 350-MHz (GBT350; Lynch & Bank North Celestial Cap Survey Collaborations, 2013) and the Green Bank North Celestial Cap (GBNCC; Stovall et al., 2014) surveys (both conducted by the 100-m GBT), the 322-MHz GMRT High Resolution Southern Sky survey (GHRSS; Bhattacharyya et al., 2016) and the 140-MHz LOFAR Pilot Pulsar Survey and LOFAR Tied-Array Survey (LPPS & LOTAAS; Coenen et al., 2014). For a more comprehensive summary of the full list of pulsar surveys and their parameters, see Lyon et al. (2016).

Chapter 3

Pulsar discoveries and other results from the HTRU-S Low Latitude pulsar survey

This chapter documents the results obtained from the processing of $\sim 44\,\%$ of the HTRU-S Low Latitude (HTRU-S LowLat) pulsar survey. Included is an overview of the structure and methodology behind the 'partially-coherent segmented acceleration search' pipeline which has been applied to the survey, as well as assessment of the performance of this pipeline on the 44 % of the survey processed during this research project. This assessment explores the ability of the pipeline to detect previously known pulsars, as well as accounting for those pulsars it could not re-detect, and indicates that the survey and its pipeline have performed approximately as expected, and have remained consistent in their performance with the results obtained from the $\sim 50\,\%$ of the survey processed previously by Ng et al. (2015).

Particular focus is given here to the discovery and timing of 40 new pulsars identified within the survey region. At least seven of these pulsars appear to be in binary systems, with two additional binary candidates. These include three millisecond pulsar-white dwarf (MSP-WD) systems (PSRs J1537−5312, J1547−5709 and J1618−4624), two long-period pulsars which display both nulling/intermittent behaviour and evidence of acceleration (PSRs J1812−15 and J1831−04), a pulsar with an orbital period on the order of months to years and a suspected main sequence (MS) companion (PSR J1653−45), a new black-widow system (PSR J1745−23), and one of the most relativistic pulsar binary discovered to date (PSR J1757−1854, further documented in exclusive detail in Chapter 4). Other pulsars of interest include a glitching pulsar (PSR J1706−4434), a nulling pulsar (PSR J1810−17) and an isolated intermittent pulsar (PSR J1854−05). The chapter concludes with an assessment of the total yield of newly-discovered pulsars in comparison to earlier predictions, and also analyses the properties of the 100 pulsars discovered within the HTRU-S LowLat survey with respect to the known pulsar population within the survey area.

The results of this work are intended for eventual publication and have included the efforts of additional collaborators. My primary contributions to this work have included the processing of all survey data analysed for this thesis project, as well as the review of all resulting pulsar candidates; the leading of the majority of the applications directly related to this processing, including observing time applications with the Parkes 64-m Radio Telescope and processing time applications with the ARC Centre of Excellence for All-sky Astrophysics (CAASTRO); the coordination and planning of the majority

of follow-up pulsar timing observations, including personally conducting a significant fraction of the required observations with Parkes; and performing the complete set of analyses presented in this chapter, including the pulsar timing analyses, population analyses and the pipeline performance evaluation.

Contents

3.1 The HTRU-S LowLat pulsar survey

3.1.1 Survey goals

While the general goal of *any* pulsar survey can largely be characterised as the discovery of new pulsars, the primary goal of the HTRU-S LowLat pulsar survey has been the discovery of relativistic binary pulsars. As described in Section 1.1.2, these binary systems can serve as excellent laboratories for developing tests of gravitational theories such as general relativity (GR), with the Double Pulsar PSR J0737−3039 (Burgay et al., 2003; Lyne et al., 2004) currently standing as the ultimate example of such a gravitational laboratory. The region of sky surveyed by HTRU-S LowLat (see Table 2.2), which comprises the densest portion of the Galactic disk, is expected to contain the highest proportion of these systems (Belczynski et al., 2002). Compact binary systems with short orbital periods ($P_b < 12\,h$) are of particular interest, as these systems are likely to display the significant relativistic effects, allowing for new and improved tests and limits well beyond those available from current binary pulsars.

An important secondary goal of the survey involves the discovery of low-luminosity pulsars too weak to have detected by earlier pulsar surveys. This is made possible by the unprecedented 72-min observations employed by HTRU-S LowLat. Characterising the population statistics of low-luminosity pulsars will allow for a greater understanding of the pulsar population as a whole, and will be vital in the planning of future pulsars surveys to be undertaken with next generation radio telescopes such as MeerKAT[1], the Square Kilometre Array[2] (SKA) and the Five-hundred-meter Aperture Spherical Telescope[3] (FAST), which are likely to probe even deeper into this regime. Finally, the long observation times are also favourable to capturing various transient radio phenomena, including fast radio bursts (FRBs), pulsar glitches (see Section 1.4.3) and both nulling and intermittent pulsars (see Section 1.4.2).

3.1.2 The partially-coherent segmented acceleration search pipeline

The portion of the HTRU-S LowLat survey presented in this chapter has been processed exclusively through the 'partially-coherent segmented acceleration search', which is documented in detail in both Ng (2014) and Ng et al. (2015). A summary of this pipeline and its principles of operation are presented here. In large part, the pipeline resembles the 'standard' Fourier-domain pulsar searching technique presented in Chapter 2, but also incorporates a number of specific features designed to maximise its sensitivity to compact, relativistic binary systems.

3.1.2.1 RFI mitigation

A key component of the partially-coherent segmented acceleration search is its comprehensive suite of RFI mitigation techniques. The most basic of these involves an imple-

[1] http://www.ska.ac.za/science-engineering/meerkat/
[2] http://skatelescope.org/
[3] http://fast.bao.ac.cn/en/

mentation of the frequency-channel zapping technique as described in Section 2.2.1.2, with its implementation to this pipeline described by Keith et al. (2010). Two additional RFI techniques designed to exploit the HTRU survey's use of the Parkes 21-cm multibeam receiver (MB20; Staveley-Smith et al., 1996) are also employed by this pipeline. The first of these is the time-domain eigenvector-decomposition method described by Kocz et al. (2012) and outlined in Section 2.2.1.5. A cutoff of $6\,\sigma$ is applied to remove any signal which appears in more than four beams, and a further cutoff of $4\,\sigma$ is applied to remove any signal which appears in all thirteen beams of a given survey observation (collectively referred to here as an observation *pointing*[4]).

The second multibeam technique, designed specifically for this survey, is a dynamic Fourier-domain technique intended to avoid the use of fixed Fourier RFI lists. While somewhat effective in removing Fourier-domain RFI, fixed Fourier RFI lists do not account for the time variability of Fourier RFI sources, whose periodic properties may change over time (hence altering their properties in the Fourier spectrum) or which may not always be active during every observation. The essentials of the alternate technique employed in this thesis involve the dynamic masking of Fourier RFI which occurs in multiple beams above a given power threshold, as also described in Section 2.2.1.5. In the case of the HTRU-S LowLat survey, this threshold is specified at $P_{\mathrm{thresh}} \simeq 19$ (Ng et al., 2015). Any Fourier bin whose power exceeds P_{thresh} in four or more beams for a single pointing is flagged as periodic RFI and removed as per the procedure outlined in Section 2.2.1.3 for fixed Fourier RFI.

3.1.2.2 Acceleration search strategy

As noted in Section 2.3.3, the presence of binary motion can limit the sensitivity of standard periodicity searches due to the Doppler shift caused by pulsar's line-of-sight motion. Fully correcting for this unknown orbital motion introduces a large additional parameter search space which presents considerable computational challenges to thoroughly analyse. To overcome this, our pipeline uses the 'time-domain resampling' technique outlined in Section 2.3.3.1. In short, this technique assumes that the orbital motion of a pulsar can be represented by a constant acceleration a over the span of a given observation such that the line-of-sight velocity can be expressed by $V_{\parallel}(t) = at$. If this assumption remains true (i.e. that the 'jerk' or rate of change of acceleration $\dot{a} \simeq 0\,\mathrm{m\,s^{-3}}$), then each de-dispersed time series to be searched by the pipeline can be quadratically resampled so as to remove the effect of the orbital motion over the course of the observation. As described in Equation 2.22, this technique works best (in the case of circular orbits) when the parameter $r_{\mathrm{orb}} = t_{\mathrm{int}}/P_{\mathrm{b}} \lesssim 0.1$, where t_{int} is the integration time of the observation.

Under the same assumption of a circular orbit, it is possible to determine the maximum acceleration ($|a_{\mathrm{max}}|$) expected for a particular orbital period P_{b} and set of

[4] An individual beam within a pointing is typically referred to first by the pointing's UTC timestamp, indicating the start time of the observation, followed by the number of the individual beam (see Figure 2.16). For example, 2012-07-18-05:13:39/07 refers to beam 07 in the pointing observation which began at 2012-07-18-05:13:39 UTC.

masses for the pulsar and its binary companion. According to Kepler's third law, this is given by

$$|a_{\max}| = \left(\frac{2\pi}{P_{\rm b}}\right)^{4/3} (\mathrm{T}_{\odot} f)^{1/3}\, c, \tag{3.1}$$

where c is the speed of light, $\mathrm{T}_{\odot} = 4.925490947\,\mu$s and f is the mass function as defined by Equation 2.36, which is maximised in the case of an edge-on orbit, i.e., an inclination angle of $i = 90°$. Assuming a canonical pulsar mass of $m_{\rm p} = 1.4\,\mathrm{M}_{\odot}$, the maximum orbital acceleration for any binary system can be determined as a function of the companion mass $m_{\rm c}$ and the orbital period $P_{\rm b}$. Figure 3.1 presents the $|a_{\max}|$ curves for three potential circular binary scenarios involving neutron stars (NS), white dwarves (WD) and black holes (BH):

- A NS-WD binary system with a WD mass of $m_{\rm c} = 0.2\,\mathrm{M}_{\odot}$
- A NS-NS binary system[5] with a companion NS mass of $m_{\rm c} = 1.4\,\mathrm{M}_{\odot}$
- A hypothetical NS-BH binary system with a BH mass of $m_{\rm c} = 10\,\mathrm{M}_{\odot}$

Also plotted in Figure 3.1 are the acceleration ranges of all binary pulsars listed in the ATNF Pulsar Catalogue[6] (PSRCAT Manchester et al., 2005) as of October 2017 with $P_{\rm b} < 12\,$h and $|a_{\max}| > 1\,\mathrm{m\,s^{-2}}$. Note that a number of these pulsars (notable examples including PSRs B1913+16 and B2127+11C) display acceleration ranges which exceed the $|a_{\max}|$ curves corresponding to their binary type. This is due to the high eccentricity of these systems, however the highly eccentric nature of these binaries implies that only a small fraction of the orbital period $P_{\rm b}$ is spent during this high-acceleration, high-jerk phase. The majority of these eccentric orbits is spent at much lower accelerations during which the assumption of constant acceleration approximately holds, although the optimal value of $r_{\rm orb}$ will be modified both as a function of eccentricity and of the orbital phase at which the observation is made.

3.1.2.3 Partially-coherent segmentation

The full-length of each HTRU-S LowLat observation (as noted in Table 2.2) is $t_{\rm int} = 4300\,$s, which according to Equation 2.22 implies a sensitivity to $P_{\rm b} \gtrsim 12\,$h. In order to optimise the sensitivity of each observation to shorter orbital periods, we adopt a segmented search strategy. Each observation is broken down into full-length ($s = 1$), half-length ($s = 2$), quarter-length ($s = 4$) and eighth-length ($s = 8$) segments, resulting in 15 segments in total. This segmenting provides sensitivity to progressively shorter orbital periods, with the $t_{\rm int}$ of each segment and its optimal $P_{\rm b}$ range described in Table 3.1. However, with each additional halving of the observation length $t_{\rm int}$, the raw flux-sensitivity of the segments correspondingly lowers by a factor of $\sqrt{2}$. Our strategy aims to strike an ideal balance between these two considerations, optimising our ability to detect binary systems with small values of $P_{\rm b}$ while retaining as much of the observation length and therefore as much flux-sensitivity as possible.

[5] Also referred to as a double neutron star (DNS) binary system.
[6] http://www.atnf.csiro.au/people/pulsar/psrcat

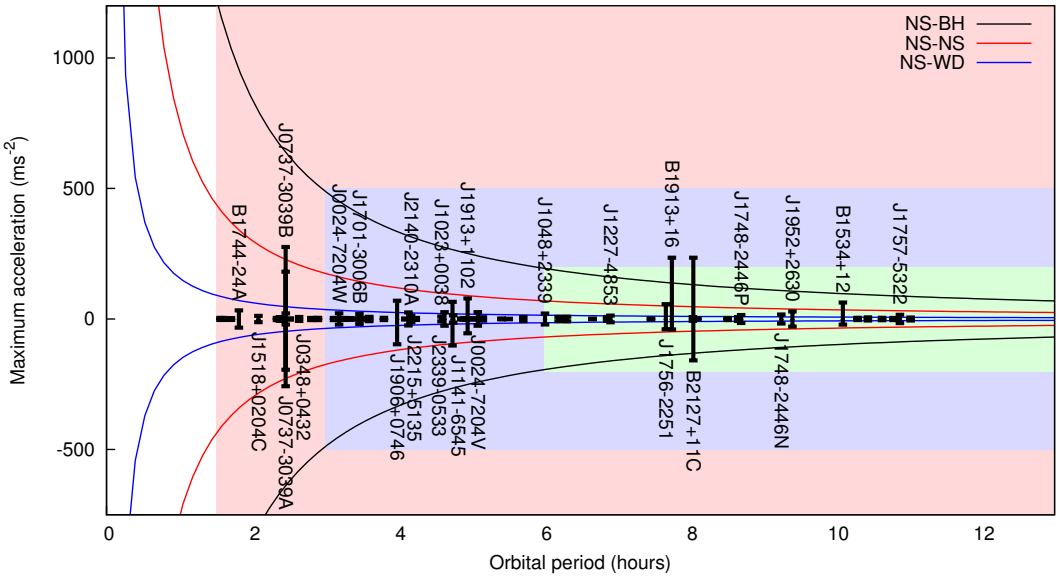

Figure 3.1: The maximum orbital acceleration of selected circular pulsar binary systems (NS-WD, NS-NS and NS-BH) as a function of orbital period. Over-plotted in black are the current line-of-sight acceleration ranges of all binary pulsars listed in PSRCAT as of October 2017 with $P_\mathrm{b} < 12\,\mathrm{h}$ and $|a_\mathrm{max}| > 1\,\mathrm{m\,s^{-2}}$ (labels are provided only for pulsars with $|a_\mathrm{max}| > 20\,\mathrm{m\,s^{-2}}$). The coloured regions indicate the search space probed by each level of the segmented search, $s = 1$ (no colour), $s = 2$ (green), $s = 4$ (blue) and $s = 8$ (red). Figure based on Figure 3.12 from Ng (2014), updated to include additional recently discovered binary systems.

Table 3.1: A summary of the 15 individual segments searched as part of the partially-coherent segmented acceleration search, including the number of segments s in each group, their P_b sensitivity and acceleration search ranges ($|a_\mathrm{min}|$ to $|a_{max}|$). Each group of segments spans the entire full-length observation without overlap.

Segment	s	t_int (s)	Min. P_b (h)	$\lvert a_\mathrm{min}\rvert$ ($\mathrm{m\,s^{-2}}$)	$\lvert a_\mathrm{max}\rvert$ ($\mathrm{m\,s^{-2}}$)
Full-length	1	4300	12	0	1
Half-length	2	2150	6	0	200
Quarter-length	4	1075	3	0[a]	500
Eighth-length	8	537	1.5	0	1200

[a] See footnote 7.

With this strategy in mind, acceleration search ranges can be chosen by considering the discussion presented in Section 3.1.2.2. Adopting the hypothetical NS-BH scenario as a limiting case, and using the minimum P_b to which each segment is sensitive (as listed in Table 3.1), it is possible to derive appropriate acceleration search ranges[7] for the $s = 2, 4, 8$ segments. These acceleration ranges are also listed in Table 3.1, and are reflected in the colour scheme of Figure 3.1. Meanwhile, the comparably-narrow acceleration search range adopted for the full-length $s = 1$ segment is intended to optimise sensitivity to mildly-accelerated binary systems in wider orbits. Finally, our choice of acceleration search step size for each segment is adopted from Eatough et al. (2013a) as discussed in Section 2.3.3.1.

The final configuration of the partially-coherent segmented acceleration search pipeline is presented in the schematic in Figure 3.2. In addition to the segmented structure, additional levels of downsampling are incorporated as a function of DM. The six DM groups shown in Figure 3.2 are specified in terms of the diagonal DM (see Section 2.2.2). As the effects of dispersive smearing halve the effective time resolution $t_{\rm samp}$ once the DM exceeds a value of $2 \times {\rm DM}_{\rm diag} = 122\,{\rm cm}^{-3}\,{\rm pc}$, all dispersion trials with ${\rm DM} > 2 \times {\rm DM}_{\rm diag}$ are downsampled[8], with additional downsampling taking place with each doubling of this value up to a maximum ${\rm DM} = 3000\,{\rm cm}^{-3}\,{\rm pc}$. Each of the 15 segments of a given observation beam is searched coherently through the acceleration and Fourier search specified in Figure 3.2, but is processed independently to each of the other segments, even those of the same group, hence rendering the pipeline only 'partially-coherent'.

3.1.3 Candidate identification and confirmation

Although a consideration of false-alarm statistics indicates an approximate ${\rm S/N}_{\rm min} \simeq 9$ (see Section 3.2.1), we conservatively consider each pulsar candidate produced by the pipeline with a ${\rm S/N} > 8$, folding and manually inspecting each candidate by eye in order to assess the likelihood of the candidate representing a true pulsar discovery. Promising candidates are then re-observed with the Parkes 64-m Radio Telescope in order to confirm them as pulsars should they be re-detected. Once confirmed, regular timing observations of each pulsar are conducted with a cadence of approximately one month, supplemented by intervals of higher cadence observations as required to obtain a phase-connected solution. Those pulsars with declinations $\delta < -30°$ are timed exclusively at Parkes, while those with $\delta > -30°$ are typically passed to Jodrell Bank to be observed using the 76-m Lovell Telescope.

Our confirmation strategy is to re-observe each candidate using a set of gridded observations. Each grid is offset from the position of the original observation in order

[7] Earlier data processing in this thesis included an acceleration search gap in the $s = 4$ segment between $|a| < 200\,{\rm m\,s}^{-2}$, a feature also present in the processing conducted by Ng et al. (2015). This gap was filled as part of later processing.

[8] It has since been identified that this value is incorrect, resulting from a revised bandwidth size due to the presence of persistent RFI in the HTRU-S LowLat data (see Section 2.7.2). The correct value should be $2 \times {\rm DM}_{\rm diag} = 104\,{\rm cm}^{-3}\,{\rm pc}$, however as the original value results only in some additional redundant processing and not in any sensitivity loss, it has been retained for consistency.

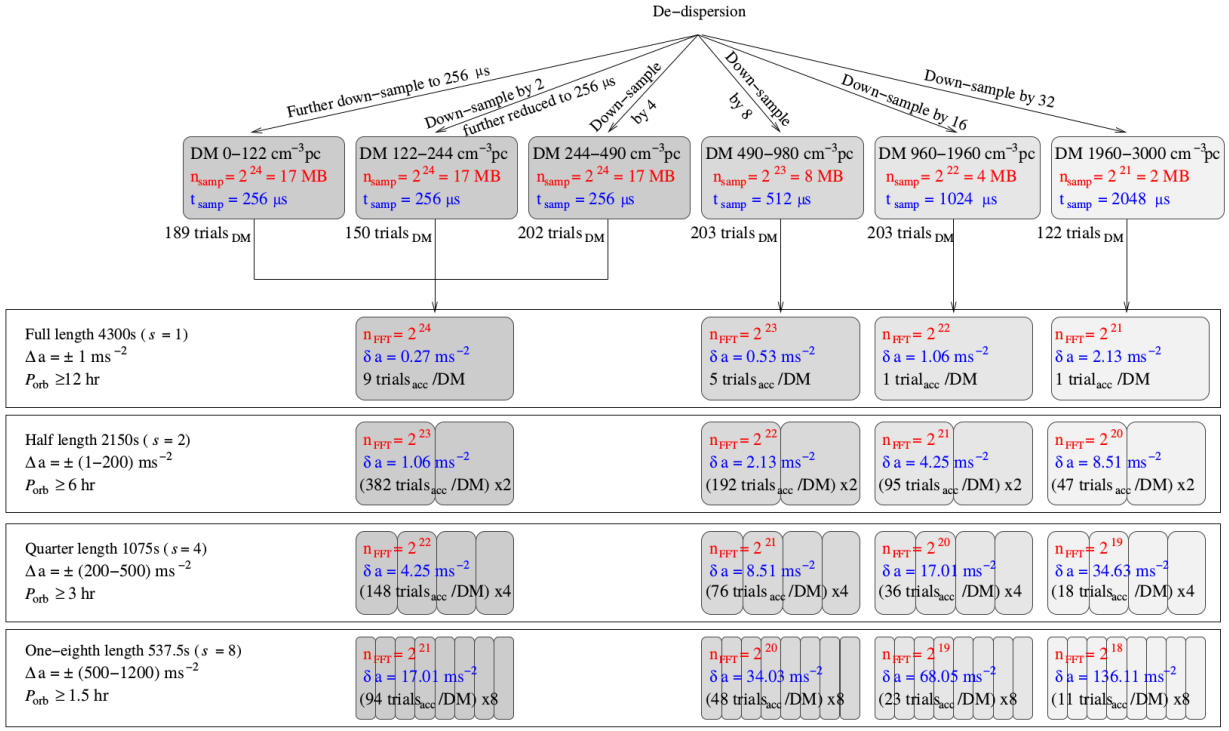

Figure 3.2: A schematic overview of the partially-coherent segmented acceleration search pipeline employed on HTRU-S LowLat. Following de-dispersion, each time series undergoes further downsampling according to its DM and is processed as one of six DM groups. Listed in each DM group is the DM range, number of samples in each time series (n_{samp}), effective sampling time t_{samp} and number of DM trials ($\mathrm{trials}_{\mathrm{DM}}$). Each time series is then passed to the four segmentation levels ($s = 1, 2, 4, 8$). Each segment of a time series is coherently searched independently through a time-domain resampling acceleration and Fourier search. Listed are the integration time of each segment, the acceleration search range (Δa) and acceleration step size (δa), the number of Fourier transform samples (n_{FFT}) and the number of acceleration trials per DM ($\mathrm{trials}_{\mathrm{acc}}$/DM). Image from Figure 3.13 in Ng (2014)

to determine an improved measurement of the pulsar's position by interpolating the positions of the beams in which the pulsar is detected, based upon the relative S/N of each detection. This allows future timing observations to place the pulsar as close as possible to the center of the telescope beam, maximising the S/N of each pulsar and reducing the time required in order to observe it. Additionally, as noted in Table 2.1, the central beam of the Parkes MB20 receiver has a full width at half maximum (FWHM) at 1.4 GHz of 0.24°, larger than the approximately 0.2° FWHM of the Jodrell Bank telescope beam. Accurate gridding ensures that a pulsar visible at Parkes will also be visible within the beam at Jodrell Bank without additional searching.

Figure 3.3 shows the 'Ring-of-3' grid configuration used in order to increase the efficiency of our confirmation observations. The three grids (A-B-C) are arranged in a triangular configuration such that they are separated from each other by the beam FWHM, and are offset from the central discovery position by $\sim 0.139°$. Typically, each of these grids is observed in turn until the pulsar is re-detected, using a reduced $t_{\rm int}$ designed to re-detect the candidate pulsar at S/N = 10. If no re-detection is made in any of the offset grids (A-B-C), additional confirmation observations may be taken at the discovery position (D). Alternatively, some pulsars may be observed only at the grid D position if they are likely to be influenced by factors such as scintillation, nulling, intermittency or binary motion which may confuse the gridding process. If available, archival data from the Parkes Multibeam Pulsar Survey (PMPS; Manchester et al., 2001) as well as data from the HTRU-S Medium Latitude survey (see Section 2.7.2) may also be searched in order to obtain additional information regarding the position and timing properties of the new pulsar.

3.1.4 Status of survey processing

Processing of the survey data has been conducted across multiple supercomputers throughout the duration of this project. Current processing efforts are primarily handled by the 4488-core 'Hercules' cluster, managed by the Max Planck Computing and Data Facility (MPCDF), with secondary candidate and data review being conducted on the 64-core 'Miraculix' computer at the Max-Planck-Institut für Radioastronomie (MPIfR). A significant amount of data processing conducted in this project was also performed using the 57,472-core cluster 'Raijin' as administered by the CAASTRO. Earlier processing which assisted in the 60 discoveries documented in Ng et al. (2015) was conducted by the 1492-node Sun Constellation cluster 'Vayu' and the 156-node SGI cluster 'XE' (both of which were operated by the NCI but have since been decommissioned), as well as the 1456-core supercomputer 'HYDRA' operated by the Jodrell Bank Observatory.

Of the 1230 scheduled pointings which comprise the HTRU-S LowLat pulsar survey, 536 ($\sim 44\,\%$) have been processed through the partially-coherent segmented acceleration search detailed in Section 3.1.2 as part of this thesis project. This is in addition to the 618 pointings ($\sim 50\,\%$) which were previously processed by Ng et al. (2015), of which 180 ($\sim 15\,\%$) have only been processed through a 'standard', non-acceleration search (for details, see Keith et al., 2010). A further 51 pointings encountered an error

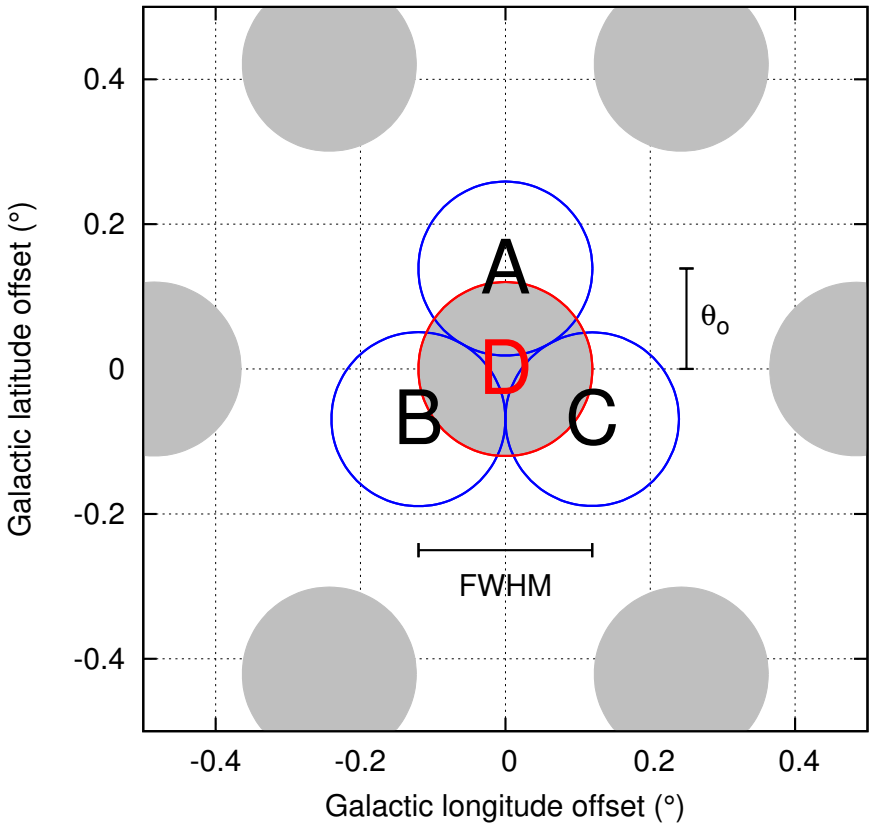

Figure 3.3: Pulsar candidate confirmation gridding strategy of the HTRU-S LowLat pulsar survey. The gray circles depict the positions and sizes of the central and inner beams of the MB20 receiver, which have a FWHM of $\sim 0.24°$ (see Table 2.1). The red circle marks the size of the beam in which pulsar was discovered (grid D), while the triangular configuration of blue circles mark the confirmation grids (grids A-B-C). These confirmation grids are configured such that they are each separated from each other by the FWHM, and are each offset from Grid D by $\theta_o = 0.24°/\sqrt{3} \simeq 0.139°$.

during processing, either due to data corruption or an error in the operation of the pipeline, in which case they may yet be recoverable in future processing attempts. In total, these 1205 pointings account for $\sim 98\,\%$ of the entire HTRU-S LowLat pulsar survey, with $\sim 94\,\%$ having been successfully processed and reviewed.

A graphical representation of the processing status of the survey is presented in Figure 3.4, which shows the spatial distribution of the survey beams within the Galactic-plane region. Unprocessed beams are marked by grey circles, indicating the size of the on-sky telescope beam, while beams which resulted in processing errors are marked in purple. Beams processed by Ng et al. (2015) are indicated in blue, while those beams processed by this thesis project are indicated in red. The positions of previously known pulsars are marked by gold triangles, while the 60 pulsars reported by Ng et al. (2015) are marked by blue diamonds. The 40 newly-discovered pulsars reported in this chapter (as detailed in Section 3.3) are indicated in black.

3.2 Re-detections of known pulsars

In order to verify that the processing pipeline is performing as expected in terms of its sensitivity, a complete record of the expected re-detections of previously known pulsars in the survey region has been maintained. For each survey beam, the current PSRCAT parameters of each nearby pulsar, including the pulsar's spin period P, its effective pulse width $W_{\rm eff}$ (which we approximate as W_{50}, the width of the pulse at 50 % of its peak value) and its flux density at 1.4 GHz, S_{1400} have been recorded. Due to the non-uniform response of the telescope beam (see Section 2.1.1), any offset of the pulsar from the center of the beam will cause a reduction in its apparent flux density, and correspondingly a reduction in its apparent S/N. In order to account for this effect, we approximate the response pattern of the telescope beam as a Gaussian curve and calculate the expected apparent flux density $S_{\rm exp}$ of the pulsar, given by

$$S_{\rm exp} = S_{1400} e^{-\theta^2/2\sigma^2}, \tag{3.2}$$

where θ is the offset in degrees and σ is related to the FWHM of the telescope beam by

$$\sigma = \frac{\rm FWHM}{2\sqrt{2\ln 2}}. \tag{3.3}$$

As noted previously the beams of the Parkes MB20 receiver have a FWHM of approximately 0.24°, resulting in $\sigma \simeq 0.1°$. Based upon the modified value of $S_{\rm exp}$, the expected S/N ($\rm S/N_{exp}$) is then derived using the radiometer equation (Equation 2.23) along with the aforementioned PSRCAT parameters of the pulsar and the survey parameters listed in Table 2.2. For those pulsars for which a W_{50} is not recorded, a value of $W_{50} = P/2$ is assumed in order to maintain consistency with Ng et al. (2015), while for those pulsars with no published value of S_{1400}, no calculation of $\rm S/N_{exp}$ is made.

In total, from the $\sim 44\,\%$ of the HTRU-S LowLat survey processed in this thesis project, we report 755 individual re-detections of a total of 390 unique pulsars. Considering all survey data processed to date, including the 50 % processed by Ng et al.

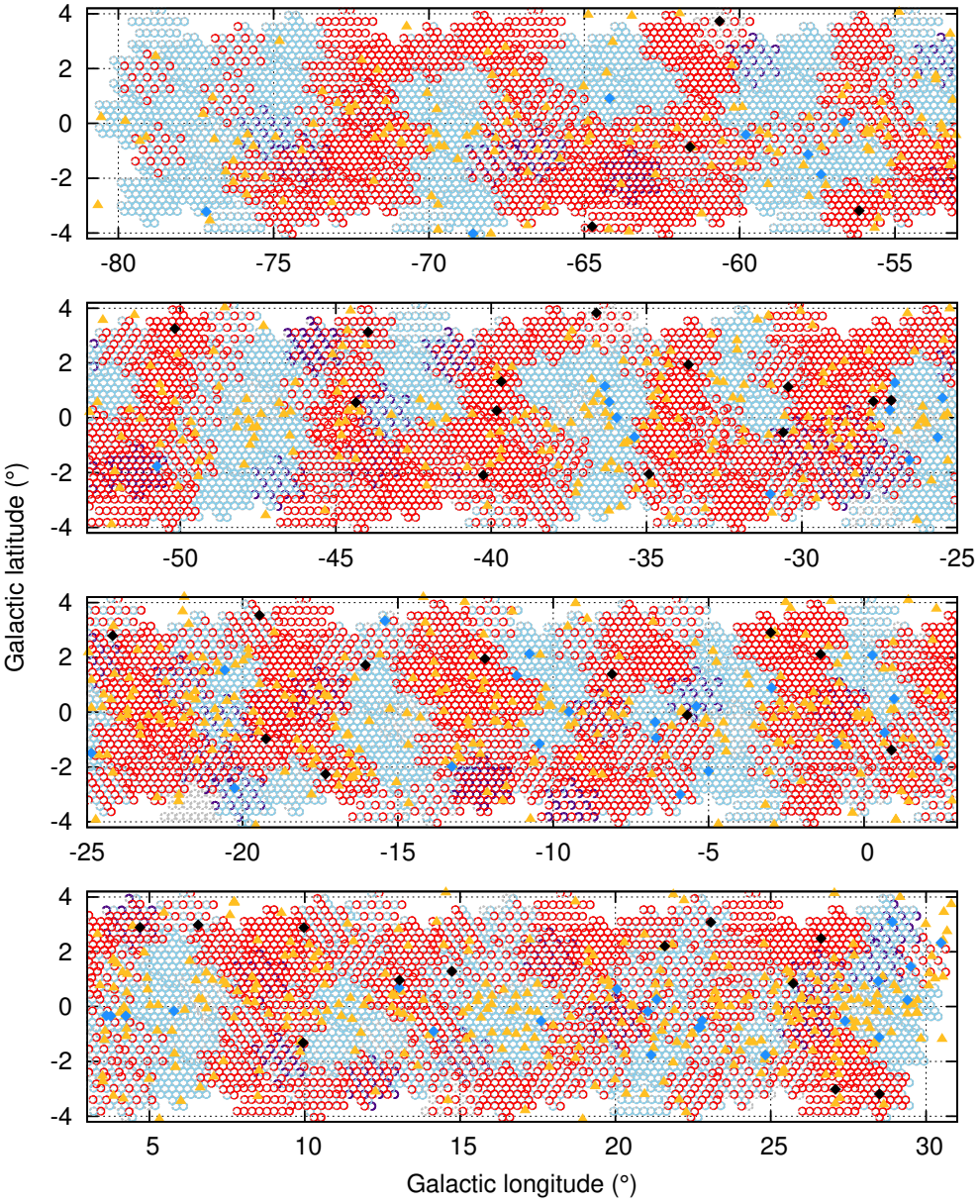

Figure 3.4: On-sky distribution of the 1230 scheduled pointings of the HTRU-S LowLat pulsar survey, each with 13 beams. Beams processed for this thesis are marked by red circles, with each circle representing the on-sky size of the telescope beam. Those beams processed in Ng et al. (2015) are marked in blue. Unprocessed beams are marked in grey. Beams which encountered an error during processing are marked in purple. Newly discovered pulsars from this thesis project are indicated in black, while the 60 discoveries reported by Ng et al. (2015) are indicated by blue diamonds. Previously known pulsars in the field are also indicated by gold triangles.

(2015), this results in a combined total of 1667 pulsar re-detections spanning a combined total of 649 unique pulsars (this number being less than the sum of the totals from each portion of the survey due to the mutual overlap in the individual pulsars detected in each half). A full record of the optimal[9] re-detections of each of the 390 unique pulsars re-detected in the 44 % of the survey data processed in this thesis can be found in Appendix A.

Figure 3.5 shows a comparison of the calculated S/N_{exp} against the measured S/N (S/N_{obs}) for the pulsar re-detections made in the portion of the survey processed for this thesis. As the response pattern of the telescope beam deviates from our Gaussian approximation outside of the beam FWHM, and also becomes complicated by the presence of side-lobes, all re-detections with an offset θ from the center of the beam greater than FWHM/2 = 0.12° (totaling 434 pulsars) have been excluded from this comparison. Also excluded are 2 pulsars without a recorded S_{1400}, for which S/N_{exp} cannot be calculated. Finally, 93 re-detections were excluded due to the position of the relevant survey beams being sufficiently ambiguous to prevent an accurate determination of θ and hence allow for an accurate determination of S/N_{exp}. The cause of this ambiguity appears to have been caused by an error in the recorded position of each beam at the time the survey was taken, affecting the header information of each filterbank observation file. While a technique for correcting the affected beams has been developed, we have excluded the re-detections made in these beams in order to ensure an accurate analysis. In total, after accounting for these caveats, 226 pulsar re-detections remain for the purposes of this analysis.

As can be seen in Figure 3.5, the overwhelming majority of re-detections fall close to the 1:1 relation as expected. However, the division of data points around this relation is not symmetric, with 163 re-detections (approximately 72 %) having $S/N_{exp} > S/N_{obs}$. As noted by both Keith et al. (2010) and Ng et al. (2015), this is potentially the result of a reporting bias, where the highest values of S/N observed during each known pulsar's initial set of observations tend to be reported (the variation in S/N between observations being due to scintillation and other potential instrumental effects), leading to higher catalogue values of S_{1400} which in turn lead to higher values of S/N_{exp}. The potential effect of scintillation can also be seen in panel (b) of Figure 3.5, which plots the ratio of $S/N_{exp}/S/N_{obs}$ as a function of catalogue DM. The scatter of re-detections is seen to increase towards lower DM values where the effects of scintillation are most prominent (see Section 1.3.3).

3.2.1 Non-detections of known pulsars

In addition to our recorded pulsar re-detections, we also note the presence of several non-detections of pulsars expected to be detectable above the threshold S/N (S/N_{min}). In a 'conventional' pulsar survey, an assessment of S/N_{min} can be derived in a straightforward manner using an assessment of the false-alarm statistics presented in Sec-

[9]Defined as the re-detection of the pulsar in the beam with the smallest angular offset θ from the pulsar position. In the event that the beams in which the pulsar was re-detected have ambiguous positions, the highest S/N_{obs} detection is used. See Appendix A for further details.

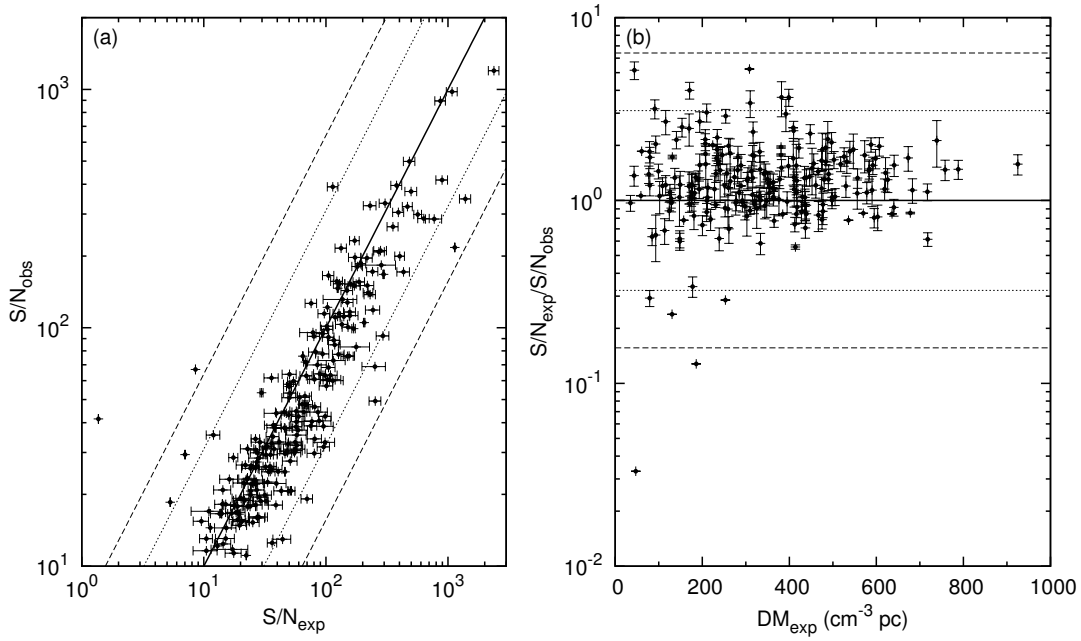

Figure 3.5: A comparison of the expected versus observed S/N values (S/N_{exp} and S/N_{obs} respectively) for pulsars re-detected in the 44 % of the HTRU-S LowLat survey processed in this thesis. Plot (a) shows S/N_{obs} plotted against S/N_{exp}, while plot (b) shows $S/N_{exp}/S/N_{obs}$ plotted against the PSRCAT DM for each re-detected pulsar. The bold line in each case represents the 1:1 relation, while the surrounding dashed lines extending outwards from the 1:1 line indicate contours containing 95 % and 99 % of the re-detections respectively.

tion 2.3.1.3 with respect to the number of dependent trials (n_{trials}). However, in the case of the partially-coherent segmented acceleration search, this method is complicated by the multiple-pass, segmented nature of the search (see Figure 3.2), which involves different numbers of both dependent and independent trials. As a conservative assessment, we have calculated the S/N_{min} for each iteration of the segmented search ($s = 1, 2, 4, 8$), considering only the number of dependent trials. From this, we derive a lower limit of $S/N_{\text{min}} \simeq 9.3$. The true value of S/N_{min} is likely to be higher, as this estimate fails to consider the complete search-space of the pipeline simultaneously, as well as the presence of RFI which will raise the survey's noise floor. However, given this value's approximate consistency with the value of $S/N_{\text{min}} = 9$ quoted in Ng et al. (2015), and that erring towards a lower value of S/N_{min} is preferable, we assume the same value as Ng et al. (2015) when assessing the non-detections encountered in the portion of the survey data processed in this thesis. In addition, for the reasons described in Section 3.2 we also restrict our analysis to those non-detections with an offset less than 0.12° and whose beam position is unambiguous.

Under these criteria, we identify 21 non-detections spanning 21 unique pulsars. These pulsar non-detections are listed in Table 3.2, along with the beam, angular offset θ, S/N_{exp} and PSRCAT spin period P_{cat} and DM_{cat}. For each non-detection, a manual fold of the relevant beam using the current PSRCAT ephemeris of the pulsar was also conducted. In 18 cases this manual analysis resulted in a re-detection of the pulsar, with the S/N_{eph} also listed in Table 3.2. We note that none of the listed pulsars are known to be in binary systems. A number of these non-detections can be accounted for as follows:

- PSRs J1322−6329, J1501−5637, J1709−4342 and J1733−2837 all suffered from the influence of significant RFI in their corresponding observations, such that additional cleaning of the data beyond the standard RFI mitigation employed by our pipeline was required in order to re-detect the pulsar.

- PSR J1550−5418, the magnetar also known as AXP 1E 1547.0−5408, is known to experience significant radio variability including spans of apparent non-emission (Camilo et al., 2007), accounting for its non-detection both by the pipeline and the later ephemeris fold.

- PSR J1709−4401 has been previously noted by Tiburzi et al. (2013) to be an intermittent pulsar, accounting for its non-detection both by the pipeline and the later ephemeris fold.

- PSRs J1524−5819 and J1611−4811 were both re-detected by the ephemeris fold, but with $S/N_{\text{eph}} < S/N_{\text{min}}$. Therefore, the non-detection by the search pipeline of these two pulsars is not unexpected. Similarly, the ephemeris fold of PSR J1509−5850 only resulted in $S/N_{\text{eph}} = 9.4$ which, while technically above the S/N_{min}, is sufficiently close that it can likely be grouped into this category.

- PSR J1747−2958 was discovered by Camilo et al. (2002) in a search of the Mouse Nebula. Its interaction with this nebula, combined with a relatively-

low DM, makes it susceptible to scintillation. Apparent flux variability due to this effect has already been observed in this pulsar's discovery observations. PSR J1747−2958 was also not detected by Ng et al. (2015), and remains undetectable here even after the ephemeris fold.

- With a relatively-long catalogue period of $P_{\rm cat} = 1388\,\mathrm{ms}$ and a $\mathrm{S/N_{eph}}$ significantly weaker than its $\mathrm{S/N_{exp}}$, the non-detection of PSR J1819−1131 is attributed to likely confusion with red noise, reducing its detectability in the Fourier domain.

- The profile of PSR J1822−1617 displays a wide pulse shape with a duty cycle of $\delta \simeq 14\,\%$ and evidence of a scattering tail, consistent with its high DM. This wide profile, in combination with a weak ephemeris fold of $\mathrm{S/N_{min}} = 10.2$, may have contributed the pulsar's non-detection.

However, we are at present unable to account for the non-detection of 9 of the pulsars listed in Table 3.2. Although some of these pulsars were only weakly detected (as low as $\mathrm{S/N_{eph}} = 10.2$), as their ephemeris folds remain above our $\mathrm{S/N_{min}}$ detection threshold they cannot be disregarded. Considering these non-detected pulsars in comparison to the set of re-detected pulsars, we calculate that $\sim 2\,\%$ of expected pulsars have been missed during the processing of the $\sim 44\,\%$ of the HTRU-S LowLat survey data processed in this thesis. This is comparable with the $\sim 1\,\%$ non-detection rate reported for the $\sim 50\,\%$ processed by Ng et al. (2015), indicating that the more-recently processed data has been analysed to an approximately equivalent sensitivity.

3.2.2 Binary re-detections

As the goal of the partially-coherent segmented acceleration search pipeline is to enhance our sensitivity to binary pulsars, we have also maintained a record of the observed S/N of each re-detected binary pulsar across each searched segment. A total of 17 unique binary pulsars were detected across 28 individual survey beams. The highest S/N re-detections and corresponding acceleration values (a) of each pulsar across all segments are listed in Table 3.3, along with the catalogue orbital period ($P_{\rm b}$) and eccentricity (e) of each binary as well as the calculated limiting accelerations ($a_{\rm max}$ and $a_{\rm min}$) along the line of sight at the epoch of each observation. As indicated by the listed values of $P_{\rm b}$, the majority of these pulsars (up to and including PSR J1431−5740) are of sufficiently-long orbital periods so as to be easily detectable without the need for a segmented acceleration search. These long-$P_{\rm b}$ pulsars are typically detected at maximum S/N in the full-length observation, with the S/N of the detection in each subsequent segment falling by roughly $\sqrt{2}$ until the pulsar falls below the survey noise floor and is rendered undetectable. This general observed trend is subject to a number of minor caveats:

- Due to the fact that, as listed in Table 3.1, the quarter-length segments are only searched at $500 > |a| > 200\,\mathrm{m\,s^{-2}}$ (much higher than the $a_{\rm max}$ or $a_{\rm min}$ of the pulsars listed in Table 3.3), the detections in the quarter-length segments typically break this trend with a significantly reduced S/N.

Table 3.2: Pulsars with a $S/N_{exp} > S/N_{min} = 9$ which were not detected by the partially-coherent segmented acceleration search pipeline as applied to the $\sim 44\,\%$ of the HTRU-S LowLat survey processed in this thesis project. Only pulsars with an offset θ within the FWHM of the telescope beam (a maximum offset of 0.12°) and with unambiguous beam positions are listed. In addition to the inspecting the results of the search pipeline, each beam was also folded directly using the latest PSRCAT ephemeris for the non-detected pulsar. Where this was successful in recovering the pulsar, the relevant S/N_{eph} is also listed.

PSR name	Pointing/Beam	θ (°)	P_{cat} (ms)	DM_{cat} ($cm^{-3}\,pc$)	S/N_{exp}	S/N_{eph}	Comments
J1031−6117	2012-07-18-05:13:39/07	0.12	306.411	506.8	10.5	12.7	Weak, close to beam FWHM, but unambiguous in ephemeris fold.
J1233−6344	2012-04-01-10:19:04/02	0.094	756.892	495.0	11.7	12.4	Weak, but unambiguous in ephemeris fold.
J1301−6310	2011-12-22-15:34:56/09	0.075	663.830	86.1	17.8	15.1	XRS (Prinz & Becker, 2015). Unambiguous in ephemeris fold.
J1309−6526	2012-04-14-10:01:12/03	0.091	398.292	340.0	20.3	10.8	Weak detection.
J1322−6329	2012-04-05-14:47:06/10	0.096	2764.209	659	26.6	13.0	Significant RFI contamination. Pulsar only detectable in ephemeris fold after additional cleaning.
J1501−5637	2011-12-13-18:40:47/11	0.11	782.949	258.0	18.2	11.0	Significant RFI contamination.
J1509−5850	2012-04-03-19:16:00/03	0.094	88.922	140.6	13.4	9.4	HE pulsar (Weltevrede et al., 2010). Weakly detected in ephemeris fold, close to S/N_{min}.
J1524−5819	2012-08-01-10:10:14/07	0.096	961.043	406.6	15.9	8.8	Weakly detected in ephemeris fold, below S/N_{min}.
J1550−5418	2011-07-14-05:40:23/01	0.022	2069.833	830.0	114.0[a]	-	Magnetar, AXP 1E 1547.0−5408 (Camilo et al., 2007).
J1611−4811	2011-12-27-19:03:07/08	0.047	1296.850	221.0	12.4	8.6	Weakly detected in ephemeris fold, below S/N_{min}.
J1633−4805	2011-12-30-19:34:06/13	0.096	710.830	1120.0	15.0	14.4	Unambiguous in ephemeris fold.
J1709−4342	2011-12-12-05:16:53/02	0.10	1735.898	281.0	15.7	17.0	RFI contamination.
J1709−4401	2012-09-24-06:43:27/01	0.026	865.235	225.8	233.0	-	Intermittent (Tiburzi et al., 2013).
J1733−2837	2011-12-07-03:42:23/03	0.070	768.185	225.0	14.4	15.5	Significant RFI contamination.
J1738−3107	2011-12-22-22:10:51/03	0.10	549.498	735.0	19.3	12.3	Weak, but unambiguous in ephemeris fold.
J1747−2958	2012-08-03-09:31:42/08	0.061	98.814	101.5	21.0	-	Discovered by Camilo et al. (2002) with $S_{1400} = 0.25\,mJy$. Associated with the Mouse Nebula, with flux variability likely due to interstellar scintillation. Also undetected by Ng et al. (2015).
J1755−2534	2012-07-26-12:48:29/02	0.12	233.541	590.0	10.6	11.6	Weak, close to beam FWHM, but unambiguous in ephemeris fold.
J1801−2115	2012-03-30-22:36:23/01	0.078	438.113	778.8	14.3	10.2	Weak detection.
J1819−1131	2012-08-05-08:17:44/02	0.069	1388.137	578.0	17.7	11.4	Weak, but unambiguous in ephemeris fold. Possible red noise confusion.
J1819−1717	2012-07-26-14:01:59/03	0.12	393.522	405.0	14.9	14.6	Unambiguous in ephemeris fold.
J1822−1617	2012-07-25-14:25:48/12	0.064	831.156	647.0	11.3	10.2	Wide pulse profile with $\delta \simeq 14\,\%$, appears to be scattered.

[a] For pulsars with no published pulse width, an effective pulse width of $W_{eff} = P_{cat}/2$ is used to calculate S/N_{exp}.

- The full-length detections of PSRs J1216−6410 and J1748−3009 were made at harmonics, reducing their apparent S/N.
- While the majority of reported accelerations are consistent with the calculated acceleration limits of a_{max} and a_{min}, the increasingly large ambiguity of $\dot{P}$ which occurs over shorter integration lengths (an effect exacerbated by weak pulsar detections) means that some reported acceleration values may exceed these limits. This effect is most prominent in the eighth-segment detections given their short duration of only $t_{\mathrm{int}} = 9\,\mathrm{min}$.

More interesting behaviour is observed as P_{b} shrinks to the point where r_{orb} (as defined by Equation 2.22) begins to approach 0.1 for the full-length observation (corresponding to a critical orbital period of $P_{\mathrm{b,crit}} = 12\,\mathrm{h}$). Although PSRs J1435−6100 and J1802−2124 have orbital periods of $P_{\mathrm{b}} = 32.5$ and $16.8\,\mathrm{h}$ respectively, both in excess of $P_{\mathrm{b,crit}}$, they experience comparatively large extremes of acceleration, a consequence of their heavier carbon-oxygen white dwarf (CO-WD) companions (Camilo et al., 2001; Ferdman et al., 2010). This is likely responsible for the non-detections of both pulsars in their full-length segments, which as listed in Table 3.1 are only searched to $|a| < 1\,\mathrm{m\,s^{-2}}$. Instead, the highest S/N detections of both pulsars are in their half-length segments, which are searched with a larger acceleration range. Although this is not a significant problem for the search conducted in this thesis, which specifically targets pulsars with $P_{\mathrm{b}} < P_{\mathrm{b,crit}}$, it does represent a parameter space to which our pipeline may not be sensitive, as weaker pulsars with similar orbital parameters may not have sufficient flux density for detections in only the half-length segment, requiring the flux sensitivity of the full-length observation in order to be identified.

Furthermore, the two beams in which PSR J1802−2124 was detected highlight the dependence of the search sensitivity on the orbital phase φ at which a given pulsar was observed. Although the lower acceleration values observed in beam 2011-12-30-23:14:07/02 allow for a detection of the pulsar within the narrow acceleration search range of the full-length segment, both the full-length and half-length segment detections show the presence of jerk ($\dot{a}$), which is at its maximum magnitude in a circular orbit when $a \simeq 0\,\mathrm{m\,s^{-2}}$. It is at this orbital phase that the $r_{\mathrm{orb}} \simeq 0.1$ approximation is least applicable, with a smaller r_{orb} being favoured (Ng et al., 2015). This further contributes to the non-optimal detection of the pulsar in the full-length observation, with the half-length segment providing a more favourable value of r_{orb} and allowing for a higher S/N. By contrast, the detection of PSR J1802−2124 in beam 2011-10-12-04:24:15/07 occurs at an acceleration close to a_{max} where the jerk $\dot{a} \simeq 0$. The role of jerk in each of these detections is presented in Figure 3.6.

Finally, PSR J1141−6545 represents the only short-P_{b}, relativistic binary redetected during this portion of the survey processing. The pulsar experiences high line-of-sight accelerations (the limits of which change with time due to a rate of periastron change of $\dot{\omega} \simeq 5.31^{\circ}\,\mathrm{yr^{-1}}$) (Bhat et al., 2008), and is also moderately eccentric with $e = 0.17$, making it a unique test case for the segmented acceleration search pipeline. In all four beams in which the pulsar was detected, the maximum S/N detection occurred in the half-length segment, for which $r_{\mathrm{orb}} = 0.13$. With an $r_{\mathrm{orb}} = 0.06$, the

Table 3.3: Re-detections of binary pulsars from the $\sim 44\%$ of the HTRU-S LowLat survey processed in this thesis project. Each re-detected pulsar is listed along with its PSRCAT values of orbital period P_b and eccentricity e, and the observed spin period P_{obs} and DM_{obs}. Also listed are the calculated maximum and minimum values of acceleration (a_{max} and a_{min} respectively) along the line of sight at the epoch of each beam in which the pulsar was re-detected. The re-detections with the highest S/N from each segment group (and their corresponding acceleration a) are also reported.

PSR name	P_b (h)	e	a_{max} ($m\,s^{-2}$)	a_{min} ($m\,s^{-2}$)	Pointing/Beam	P_{obs} (ms)	DM_{obs} ($cm^{-3}\,pc$)	Full-length S/N	Full-length a ($m\,s^{-2}$)	Half-length S/N	Half-length a ($m\,s^{-2}$)	Quarter-length S/N	Quarter-length a ($m\,s^{-2}$)	Eighth-length S/N	Eighth-length a ($m\,s^{-2}$)
B1800−27	9672.7	0.00051	0.0006	−0.0006	2011-12-11-05:59:48/03	334.420	161.3	-[b]	-	29.9	−2.1	18.9	−232.7	17.7	−23.6
					2012-10-01-06:42:41/10	334.412	165.0	54.8	−0.2	41.0	1.0	16.9	−211.4	23.6	−6.6
B1820−11	8586.3	0.79	0.005	−0.006	2011-12-23-01:58:46/13	279.821	428.0	91.2	0.6	65.6	0.03	28.2	206.4	34.0	−23.6
					2011-12-31-00:27:33/12	279.824	416.5	16.1	−0.7	13.5	−2.1	-	-	-	-
					2012-07-22-12:33:52/09	279.837	424.9	14.2	0.3	12.4	2.1	-	-	-	-
J1822−0848	6883.9	0.059	0.002	−0.002	2012-04-02-18:07:28/13	2504.472	189.7	18.6	−0.2	13.4	−17.0	-	-	-	-
					2012-04-12-17:41:06/13	2504.459	185.5	67.0	0.06	47.4	3.1	27.3	202.1	25.6	−40.7
J1740−3052	5544.7	0.58	0.07	−0.08	2012-07-21-10:23:16/05	570.380	738.0	83.2	−0.5	59.9	0.03	21.0	−202.9	32.3	−6.6
J1751−2857	2657.9	0.00013	0.004	−0.004	2012-12-14-00:34:43/05	3.915	43.0	16.0	0.06	14.9	0.03	-	-	-	-
J1125−5825	1833.7	0.00026	0.009	−0.009	2011-10-04-20:14:39/07	3.102	124.9	20.9	0.0	14.9	0.03	-	-	-	-
					2011-12-27-13:47:20/07	3.102	124.9	24.8	0.0	17.7	0.03	-	-	-	-
					2011-12-20-18:13:43/06	3.102	124.9	17.5	0.0	12.7	0.03	-	-	-	-
J1727−2946	967.4	0.046	0.06	−0.06	2011-10-12-03:10:49/04	27.086	61.3	15.1	0.0	11.3	0.03	-	-	-	-
J1811−1736	450.7	0.83	0.98	−4.8	2011-12-31-22:59:57/01	104.148	475.2	40.5	0.9	29.4	0.03	11.3	202.1	16.0	−6.6
J1454−5846	298.2	0.0019	0.27	−0.27	2012-12-30-17:34:08/06	45.244	115.6	19.9	−0.2	14.6	0.03	-	-	-	-
J1811−2405	150.5	0.0000016	0.23	−0.23	2012-08-05-14:33:10/04	2.661	60.8	24.9	0.3	22.1	0.03	-	-	-	-
J1337−6423	114.8	0.00002	0.91	−0.91	2012-01-02-01:12:28/09	9.425	259.3	16.5	0.6	-	-	-	-	-	-
J1216−6410	96.9	0.0000068	0.29	−0.29	2012-04-13-09:24:34/09	3.540	47.4	35.4[a]	0.0	41.2	0.03	-	-	24.0	−6.6
J1748−3009	70.4	0	0.24	−0.24	2012-11-30-04:17:16/08	19.367	418.6	11.7[a]	0.06	-	-	-	-	-	-
J1431−5740	65.4	0.0000043	0.48	−0.48	2011-12-23-16:52:20/07	4.111	131.3	18.7	0.3	12.4	0.03	-	-	-	-
J1435−6100	32.5	0.000011	5.3	−5.3	2011-12-14-19:52:54/06	9.351	114.1	-	-	20.9	−3.2	-	-	14.2	−6.6
					2011-12-22-16:53:19/07	9.350	114.1	-	-	12.5	3.1	-	-	-	-
J1802−2124	16.8	0.0000025	12.1	−12.1	2011-10-12-04:24:15/07	12.649	149.9	-	-	16.6	11.6	-	-	-	-
					2011-12-30-23:14:07/02	12.652	148.9	12.9	1.1	17.0	3.1	-	-	-	-
J1141−6545	4.7	0.17	56.5	−108.9	2012-02-18-20:27:49/05	394.152	114.8	191.5	−1.0	285.9	−7.4	123.1	−202.9	162.7	−40.7
					2012-02-18-20:27:49/11	394.029	118.2	-	-	12.7	−80.8	-	-	-	-
			57.5	−108.2	2012-07-23-00:10:48/07	394.034	114.8	31.0	−0.7	46.7	−77.6	23.7	−198.7	28.2	−6.6
					2012-07-23-00:10:48/08	394.151	117.1	13.3	0.6	18.3	−9.6	8.7	−202.9	10.8	−6.6

[a] Indicates that the highest S/N detection for that segment was found at a harmonic.

[b] The full-length segment for beam 2011-12-11-05:59:48/03 suffered a processing error, resulting in the non-detection of B1800−27 in this segment.

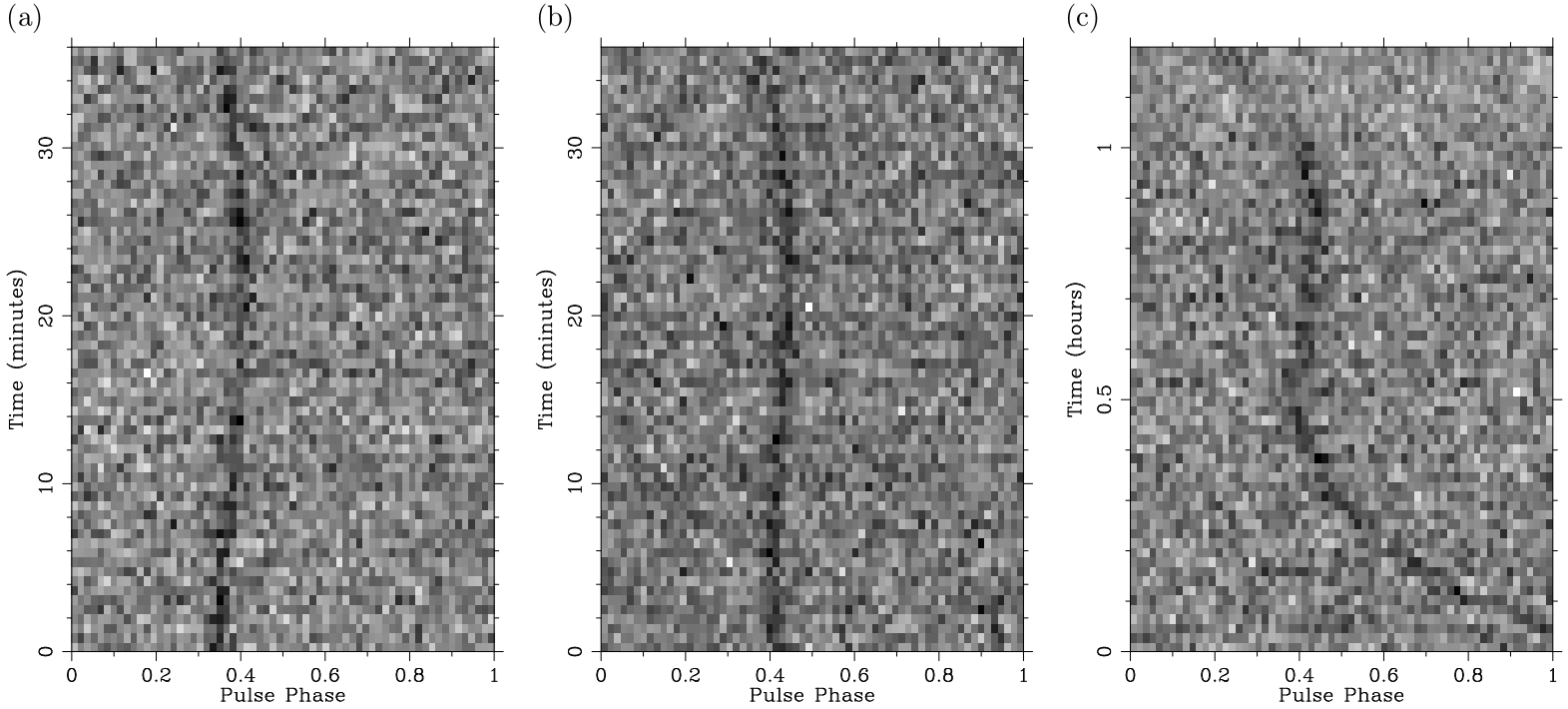

Figure 3.6: The effect of orbital phase φ on the detectability of PSR J1802−2124 by a time-domain resampling acceleration search. Plot (a) shows a half-length pipeline detection of the pulsar in beam 2011-10-12-04:24:15/07 at an orbital phase where the observed acceleration $a = 11.6\,\mathrm{m\,s^{-2}}$ is close to a_{max} and where the jerk $\dot{a} \simeq 0$. The slight parabolic curve indicates that the true acceleration of the pulsar is slightly offset from the detected value. Plots (b) and (c) show the best half and full-length segment detections respectively from beam 2011-12-30-23:14:07/02, recorded at a different orbital phase where $|a|$ is low while the jerk $|\dot{a}|$ is close to its maximum amplitude. The effect of jerk can be seen as a cubic trend in the sub-integrations, and becomes worse over the full-length observation.

quarter-length segments are also ideally suited to a detection of the pulsar, and had these segments been searched at smaller values of acceleration it is likely the detected S/N in these segments would have been consistent with the expected $\sqrt{2}$ reduction in S/N from the half-segment values. However, the stronger S/N of the half-segment detections indicates the a successful application of the segmented-search strategy to a relativistic binary pulsar. Note that for the two beams from each pointing in which the pulsar was detected, a discrepancy exists between the two reported half-length acceleration values. This is likely a result of the pulsar's long spin period P which, as with decreasing $t_{\rm int}$, increases the ambiguity of the measured $\dot{P}$ and hence also increases the ambiguity of the measured value of a. This effect can also be seen in the half-length detection of PSR J1822−0848 in beam 2012-04-02-18:07:28/13.

3.3 Newly-discovered pulsars

A total of 40 new pulsars, including 7 confirmed binary pulsars and a further 2 candidate binary pulsars, have been discovered in the $\sim 44\,\%$ of survey data processed and reviewed as part of this research project. A full listing of these pulsars is provided in Table 3.4, including the folded S/N values at which each candidate was initially detected by the processing pipeline ($\mathrm{S/N_{HTRU}}$). 39 of these pulsars have been successfully confirmed through re-observation with the Parkes Radio Telescope, using the gridding strategy outlined in Section 3.1.3. The remaining pulsar, PSR J1831−04, displays evidence of nulling and/or intermittency in its discovery observation (see Section 3.4.6), and is considered sufficiently unambiguous in its discovery observation so as to be self-confirming[10].

Timing observations for each pulsar were conducted by both the Parkes 64-m Radio Telescope and the Jodrell Bank 76-m Lovell Telescope, with the latter timing the majority of pulsars above a declination of $\delta \simeq -30°$ as per the procedure outlined in Section 3.1.3. Timing observations at Parkes were typically conducted with an approximately monthly cadence, while Jodrell Bank timing observations of were conducted with an irregular cadence, with observations of each pulsar typically every one to three weeks. Parkes observations were conducted using two receivers, the MB20 receiver and the H-OH 21-cm receiver (H-OH). The two timing backends employed at Parkes include a Digital Filter Bank backend system (currently DFB4), which is capable of only incoherent de-dispersion, and the CASPER Parkes Swinburne Recorder[11] (CASPSR), which is capable of coherent de-dispersion. Additionally, search-mode filterbank data taken using the Berkeley Parkes Swinburne Recorder[12] (BPSR) to HTRU specifications (see Table 2.2) was also used in the early timing stages of multiple pulsars, particularly those in binary systems. Jodrell Bank observations were conducted using the Single-

[10] A pulsar is typically considered *self-confirming* if it is observed with a high S/N, exhibits broadband and continuous emission, and has a DM constrained away from $0\,\mathrm{cm^{-3}}\,\mathrm{pc}$, such that the likelihood of it not representing a genuine pulsar detection are extremely remote.

[11] http://www.astronomy.swin.edu.au/pulsar/?topic=caspsr

[12] http://www.astronomy.swin.edu.au/pulsar/?topic=bpsr

Table 3.4: The mean flux density (S_{1400}), pulse widths (W_{50} and W_{10}) and derived luminosity (L_{1400}) of the 40 pulsar discoveries reported in this chapter. Also listed are the S/N at which each pulsar was detected in the survey (S/N_{HTRU}), and if available, the S/N of the pulsar in the PMPS (S/N_{PMPS}). Where a detection in the PMPS is only tentative, an upper limit on S/N_{PMPS} has been specified. Values in parentheses, where available, represent standard 1-σ uncertainties on the final digit. The derived luminosity is based on DM distance estimates, using the NE2001 model (left column; Cordes & Lazio, 2002) and the YMW16 model (right column; Yao et al., 2017).

PSR name	S/N_{HTRU}	S/N_{PMPS}	S_{1400} (mJy)	W_{50} (ms)	W_{10} (ms)	L_{1400} (mJy kpc^2)	
J1136−65	11.8	-	-	28.1	50.6	-	-
J1210−6322	11.6	< 7.0	0.151(15)	70.0	128.1	18.0	13.8
J1223−5856	34.9	-	0.377(12)	61.5	90.8	10.6	8.6
J1300−6602	13.5	< 7.0	0.119(15)	26.2	75.2	21.5	28.9
J1345−58	15.4	8.2	-	13.4	30.2	-	-
J1430−5712	13.2	-	0.092(16)	12.9	35.0	0.81	1.4
J1434−5943	13.3	< 6.3	0.17(2)	43.1	58.0	0.94	1.7
J1504−5659	14.2	< 7.4	0.11(2)	49.4	61.1	6.0	14.1
J1507−5800	11.1	8.2	0.20(3)	9.13	70.2	7.5	7.0
J1513−6013	18.0	8.9	0.20(4)	36.0	65.8	6.5	12.4
J1514−53	10.2	9.4	-	7.50	13.7	-	-
J1537−5312	14.8	-	0.410(17)	1.86	2.60	3.4	3.8
J1547−5709	17.5	-	0.42(2)	0.260	1.00	1.5	3.1
J1557−5151	17.2	-	0.310(18)	28.6	62.4	23.3	13.0
J1603−5312	14.0	9.0	0.25(5)	25.1	45.7	4.4	2.4
J1612−50	12.0	-	-	21.7	39.4	-	-
J1615−49	14.2	< 7.7	-	54.6	63.4	-	-
J1618−4624	15.1	-	0.29(3)	0.321	1.08	1.6	2.7
J1634−4229	19.9	-	0.16(2)	23.2	91.1	7.3	57.5
J1653−41	15.8	8.8	-	26.0	47.5	-	-
J1653−45	11.2	-	-	15.9	29.1	-	-
J1704−3756	11.3	-	0.134(15)	11.6	21.2	4.7	31.1
J1706−4434	16.9	-	0.19(2)	12.1	22.0	14.5	70.9
J1719−3458	13.7	10.2	0.20(2)	21.2	26.4	10.2	53.3
J1726−29	16.6	8.8	-	9.62	18.1	-	-
J1731−33	11.6	-	-	48.4	88.7	-	-
J1734−2859	10.4	6.6	0.13(2)	11.5	21.0	3.2	17.1
J1745−23	14.3	-	-	0.660	1.22	-	-
J1749−21	16.9	10.8	-	121.3	153.2	-	-
J1753−28	19.8	8.2	-	3.90	7.85	-	-
J1757−1854	13.3	-	0.25(4)	0.705	1.80	13.7	96.0
J1810−1709	13.9	-	0.45(4)	101.3	298.4	38.3	94.7
J1812−15	42.5	-	-	18.7	34.2	-	-
J1812−20	23.2	10.7	-	102.8	392.0	-	-
J1822−07	11.4	-	-	10.1	18.5	-	-
J1822−0902	16.5	12.4	-	5.25	7.11	-	-
J1831−04	18.4	-	-	15.3	28.1	-	-
J1835−06	16.2	8.6	-	29.0	53.6	-	-
J1851−06	9.5	< 6.6	-	50.2	63.9	-	-
J1854−05	23.0	-	-	12.6	23.3	-	-

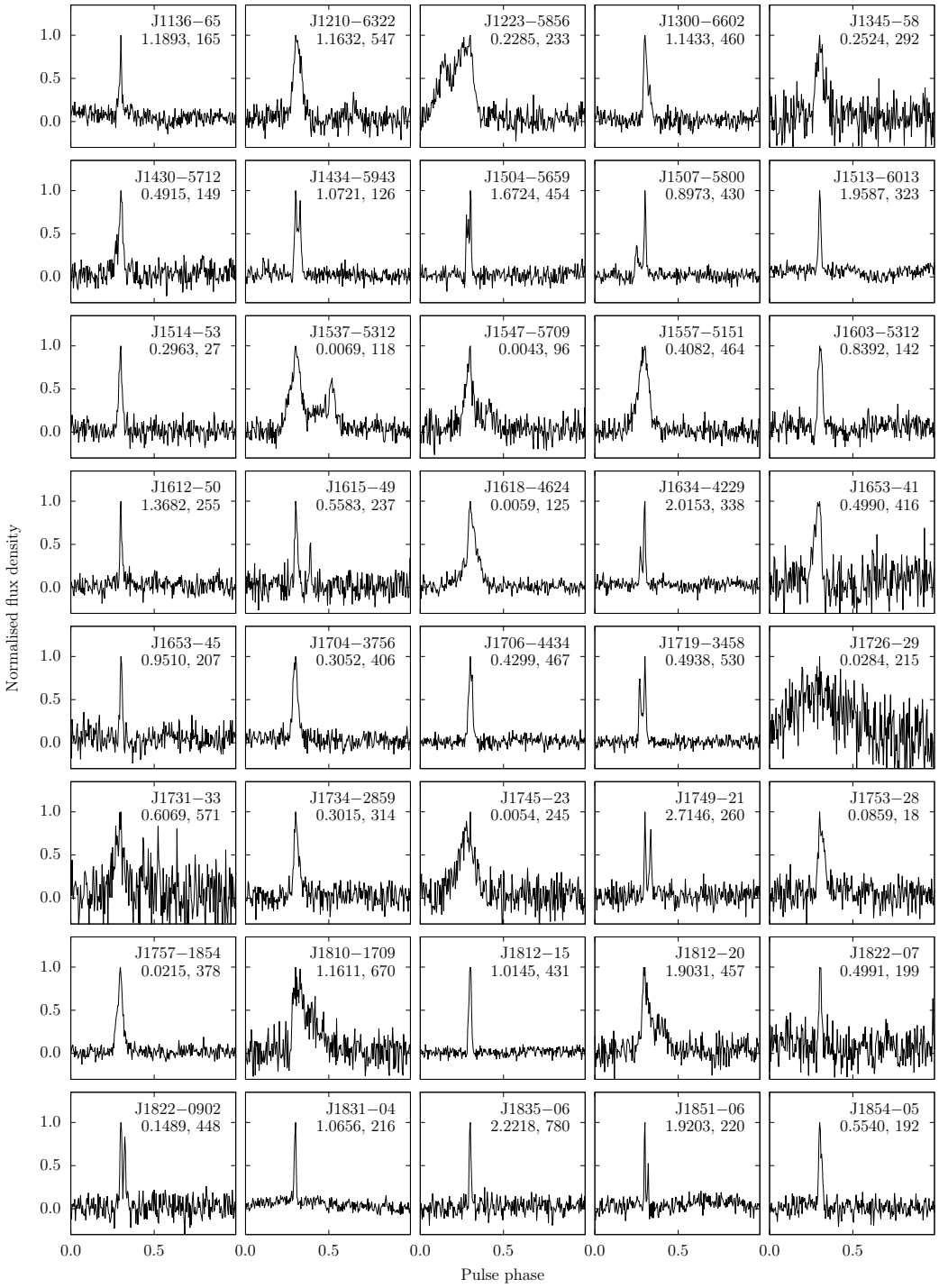

Figure 3.7: Integrated pulse profiles of the 40 newly-discovered pulsars. Each profile consists of 256 phase bins, has had its peak normalised to unity and has been rotated such that its peak is at a pulse phase of 0.3. Listed in the top right of each profile is the pulsar's current name, spin period (s) and DM ($\mathrm{cm}^{-3}\,\mathrm{pc}$).

Table 3.5: Specifications of the telescope receiver and backend combinations used for pulsar timing observations, including the antenna gain G, system temperature $T_{\rm sys}$, central observing frequency $f_{\rm c}$ and observing bandwidth B.

Telescope	Receiver	G ($\rm K\,Jy^{-1}$)	$T_{\rm sys}$ (K)	Backend	$f_{\rm c}$ (MHz)	B (MHz)
Parkes	MB20	0.74	23	BPSR[a]	1382	400
				DFB4	1369	256
				CASPSR[a]	1382	400
	H-OH	0.83	25	DFB4	1369	256
				CASPSR[a]	1382	400
Jodrell	L-band	1.00	28	DFB	1532	384
				ROACH	1527	400

[a] The usable bandwidth of BPSR and CASPSR is typically reduced to 340 MHz due to the presence of strong RFI.

pixel L-band receiver in combination with both a DFB backend and a ROACH[13] backend (Bassa et al., 2016) capable of coherent de-dispersion. A summary of the receivers and backends used in this project is presented in Table 3.5. It should be noted that the timing campaigns conducted on PSR J1757−1854 represent a special case, and the timing specifications of this pulsar are discussed separately in Section 4.3.1.

As of the time of writing, 17 of the 40 newly discovered pulsars lack sufficient TOAs for the determination of a unique phase-connected timing solution. These pulsars have been allocated temporary names listing only two digits of declination and are listed in Table 3.6. Further timing observations over the coming months will aim to to produce full timing solutions for each of these pulsars. The remaining 23 pulsars for which full timing solutions[14] have been developed are listed in Table 3.7. Pulsars in Table 3.7 for which the uncertainty in declination is greater than or equal to 0.5 arcmin have also been assigned a temporary name with only two digits of declination. Each timing solution was determined using the procedure outlined in Section 2.6 through the use of the DSPSR[15] (van Straten & Bailes, 2011), PSRCHIVE[16] (Hotan et al., 2004), SIGPROC[17] (Lorimer, 2011) and presto[18] (Ransom, 2001) pulsar data analysis packages as well as the TEMPO[19] and TEMPO2[20] (Hobbs et al., 2006) timing software packages. The development of the initial timing solutions of multiple pulsars was also aided

[13] Based on the ROACH FPGA processing board, see https://casper.berkeley.edu/wiki/ROACH

[14] Timing solutions developed by TEMPO are given in TBD (see Section 2.6.1), while TEMPO2 timing solutions are given in TCB.

[15] https://sourceforge.net/projects/dspsr

[16] http://psrchive.sourceforge.net

[17] http://sigproc.sourceforge.net

[18] http://www.cv.nrao.edu/ sransom/presto

[19] http://tempo.sourceforge.net

[20] http://www.atnf.csiro.au/research/pulsar/tempo2

by the use of a modified version of the phase-jump software technique described by Freire & Ridolfi (in prep.).

For the 20 pulsars observed using the Parkes DFB4 backend and with full phase-connected timing solutions, it is also possible to determine a calibrated 1.4-GHz flux density, S_{1400}. Each DFB4 observation was first calibrated against an observation of a pulsed noise diode in order to account for the differential gain and phase between the receiver's polarisation feeds, before being flux calibrated against an observation of Hydra A, which was typically separated in time from the pulsar observation by as much as one to two weeks. The phase-connected timing solution of each pulsar was then used to sum together the DFB4 observations so as to produce an integrated observation from which a measurement of flux density was derived. However, as the observed position of the pulsar is typically offset from the final timed position of the pulsar, an additional flux-density correction based on the offset in position (θ) was applied using Equation 3.2. The final derived values of S_{1400} are listed in Table 3.4. Also derived are the 1.4-GHz luminosities of each pulsar, $L_{1400} = S_{1400} \times d^2$, where d is the distance of each pulsar in kpc. Using the DM of each pulsar, a DM distance d can be estimated based upon two separate models of the Galactic distribution of electron density, the NE2001 model (Cordes & Lazio, 2002, 2003) and the YMW16 model (Yao et al., 2017). These distance estimates are listed both in Table 3.6 and Table 3.7, while the corresponding values of L_{1400} are listed in Table 3.4.

Figure 3.7 presents the integrated 1.4-GHz pulse profiles for each of the newly discovered pulsars, folded with 256 profile bins. In the case of the 20 pulsars timed at Parkes and with full phase-connected timing solutions, each integrated profile was produced by coherently summing the pulsar's timing observations. PSRs J1537−5312, J1547−5709, J1618−4624 and J1757−1854, for which the intrachannel dispersion smearing becomes a significant factor, the integrated profile was derived using coherently de-dispersed CASPSR data, while the remaining 16 pulsar profiles were derived from DFB4 data. Profiles for the 20 pulsars without Parkes data or without phase-connected timing solutions were produced using either their discovery HTRU observation or their subsequent confirmation observation, whichever resulted in a higher value of S/N. All pulse profiles have had their baselines subtracted and peak amplitudes normalised to unity, and have been rotated such that the profile peak is located at a pulse phase of 0.3. For each integrated profile, an analytic model profile consisting of multiple Gaussian components was derived using the PSRCHIVE application PAAS and used to measure the pulse widths at 10 % (W_{10}) and 50 % (W_{50}) of the profile peak. These pulse widths are listed in Table 3.4.

As noted previously, of the 40 newly-discovered pulsars reported in this chapter, at least 7 have been conclusively determined to be in binary systems. A further 2 pulsars display evidence which strongly suggests a binary system. These pulsars are highlighted in Tables 3.6 and 3.7. Only four of the newly-discovered binary systems have fully phase-connected timing solutions which account for their orbital properties. The orbital solutions of three of these pulsars, PSRs J1537−5312, J1547−5709 and J1618−4624, are presented in Table 3.8, along with discussions of their properties in Sections 3.4.1 and 3.4.2. The properties and timing parameters of the fourth binary pulsar for which

Table 3.6: Discovery parameters of the 17 newly-discovered pulsars for which full timing solutions are not yet available. All of these pulsars have been assigned a temporary name with only two digits of declination. The reported spin period P and DM of each pulsar is taken from its discovery observation. The reported R.A. and Dec. of each pulsar represents the best-known gridded position of the pulsar following confirmation observations. Values in parentheses represent 1-σ uncertainties on the final digit. DM distances are calculated according to the NE2001 model (left column; Cordes & Lazio, 2002) and the YMW16 model (right column; Yao et al., 2017).

PSR name	R.A. (J2000) (^{hms})	Dec. (J2000) ($^\circ$ $'$ $''$)	l ($^\circ$)	b ($^\circ$)	P (ms)	DM (cm^{-3} pc)	Dist. (kpc)	
J1136−65	11:36.3(2)	−65:30(7)	295.25	−3.76	1189.312(4)	165(12)	3.4	2.0
J1345−58	13:45.1(2)	−58:54(7)	309.82	3.25	252.39712(18)	292(3)	6.4	7.5
J1514−53	15:14.1(3)	−53:16(7)	323.39	3.83	296.2791(2)	27(3)	0.9	0.8
J1612−50	16:12.8(3)	−50:26(7)	332.30	0.60	1368.284(5)	255(14)	5.6	4.0
J1615−49	16:15.2(3)	−50:00(7)	332.88	0.64	558.2570(9)	237(6)	5.2	3.9
J1653−41	16:53.6(4)	−41:06(7)	343.96	1.72	498.9769(8)	416(6)	5.8	13.7
J1653−45[a]	16:53.9(3)	−45:17(7)	340.75	−0.97	950.977(3)	207(9)	3.6	3.5
J1726−29[b]	17:27.0(4)	−29:54(7)	357.00	2.91	28.404840(17)	215(2)	3.8	5.4
J1731−33	17:31.8(4)	−33:48(7)	354.31	−0.11	606.9003(16)	571(9)	6.1	4.3
J1745−23[a]	17:45.5(4)	−23:25(7)	4.70	2.89	5.41669986(14)	244.94(9)	4.5	7.9
J1753−28	17:53.1(4)	−28:53(7)	0.89	−1.38	85.85861(2)	18.0(9)	0.6	0.7
J1812−15[a]	18:12.6(5)	−15:31(7)	14.74	1.29	1014.529(3)	431(10)	5.9	10.0
J1822−07	18:22.3(5)	−07:20(7)	23.07	3.08	499.0748(7)	199(5)	4.2	4.6
J1831−04[b]	18:31.0(5)	−04:29(7)	26.62	2.49	1065.578(3)	216(10)	4.4	4.9
J1835−06	18:35.2(5)	−06:02(7)	25.72	0.84	2221.790(14)	780(20)	9.8	11.0
J1851−06	18:51.2(5)	−06:38(7)	27.08	−3.02	1920.312(13)	220(20)	4.8	5.7
J1854−05	18:54.7(5)	−05:24(7)	28.50	−3.19	544.0209(4)	192(3)	4.4	5.0

[a] Indicates confirmed binary pulsars.

[b] Indicates candidate binary pulsars.

Table 3.7: Best-fit TEMPO2 timing parameters for 23 newly-discovered pulsars, including the positions in both equatorial R.A. and Dec. and Galactic l and b coordinates, the spin periods P, spin-period derivative $\dot{P}$ and DM of each pulsar. Values in parentheses represent 1-σ uncertainties on the final digit. Pulsars for which the uncertainty in Dec. is greater than or equal to 0.5 arcmin have been assigned a temporary name with only two digits of declination. DM distances have been derived according to the NE2001 model (left column; Cordes & Lazio, 2002) and the YMW16 model (right column; Yao et al., 2017). Also included are fit-related parameters including the data span, the period reference epoch, the number of TOAs used to derive the timing solution, the root mean square (RMS) of the weighted TEMPO2 fit and the reduced χ^2 ($\chi^2_{\rm red}$). Derived parameters, including the characteristic age $\tau_{\rm c}$, the surface magnetic field $B_{\rm surf}$ and the spin-down energy $\dot{E}$, are calculated according to the equations presented in Section 1.2.3, and are given to a precision consistent with the measurements of P and $\dot{P}$ used to derive them.

PSR name	R.A. (J2000) ($^{\rm hms}$)	Dec. (J2000) ($^\circ\ '\ ''$)	l ($^\circ$)	b ($^\circ$)	P (ms)	$\dot{P}$ (10^{-18})	DM ($\rm cm^{-3}\,pc$)	Dist. (kpc)		Data span (MJD)	Epoch (MJD)	$n_{\rm TOA}$	RMS (μs)	$\chi^2_{\rm red}$	$\tau_{\rm c}$ (Myr)	$B_{\rm surf}$ (10^{10} G)	$\dot{E}$ ($10^{30}\,\rm erg\,s^{-1}$)
J1210−6322	12:10:47.2(5)	−63:22:18(7)	298.40	−0.86	1163.1857138(8)	9400(400)	547(5)	10.9	9.6	57531−57798	57648	22	5577	1.4	1.96	331	240
J1223−5856	12:23:40.16(4)	−58:56:49.0(4)	299.35	3.73	288.54142686(6)	5(3)	233(3)	5.3	4.8	57372−57839	57405	36	2258	1.1	900	3.8	8
J1300−6602	13:00:27.11(15)	−66:02:16.4(4)	303.85	−3.18	1143.31584212(6)	290(40)	460(3)	13.4	15.6	57373−57736	57554	33	2067	0.8	62	58	8
J1430−5712	14:30:16.17(5)	−57:12:31.2(5)	316.04	3.13	491.518803603(17)	46941(4)	149(4)	3.0	3.9	57325−57799	57562	26	1859	1.0	0.165	480	15615
J1434−5943	14:34:58.32(8)	−59:43:40.5(9)	315.65	0.56	1072.12121206(6)	32(17)	126(3)	2.4	3.2	57297−57764	57530	37	3954	1.1	500	19	1.0
J1504−5659	15:04:31.98(2)	−56:59:19.3(3)	320.33	1.32	1672.37234269(4)	1422(7)	454.2(11)	7.3	11.3	57230−57736	57483	33	1266	1.5	18.6	154	12.0
J1507−5800	15:07:03.53(4)	−58:00:56.3(2)	320.18	0.26	897.25410243(2)	253(12)	429.5(5)	6.1	5.9	57443−57766	57604	33	533	0.7	56	47.6	14
J1513−6013	15:13:53.9(3)	−60:13:25.8(17)	319.75	−2.09	1958.7370423(4)	1500(300)	322.7(16)	5.7	7.9	57501−57764	57663	35	2816	1.5	21	171	8
J1537−5312[a]	15:37:37.6954(6)	−53:12:25.066(10)	326.35	1.94	6.92709508377(5)	0.0154(5)	117.52(5)	2.9	3.1	57260−57840	57575	59	19	0.9	7100	0.0327	1830
J1547−5709[a]	15:47:24.1260(6)	−57:09:17.560(8)	325.08	−2.05	4.291146064172(5)	0.0075(2)	95.727(8)	1.9	2.7	57092−57798	57445	67	12	1.4	9000	0.0179	3700
J1557−5151	15:57:29.31(2)	−51:51:08.4(4)	329.56	1.13	408.154708459(10)	76.5(13)	464(3)	8.7	6.5	57067−57651	57359	35	1673	0.6	84.3	17.7	44
J1603−5312	16:03:50.72(15)	−53:12:45(10)	329.40	−0.53	839.2208128(2)	50000(300)	142(3)	4.2	3.1	57587−57799	57693	22	1715	0.9	0.265	648	3340
J1618−4624[a]	16:18:52.7752(4)	−46:24:34.919(7)	335.82	2.79	5.931367495288(3)	0.0045(7)	125.364(16)	2.4	3.0	57404−57870	57637	75	26	0.8	21000	0.0163	900
J1634−4229	16:34:14.66(9)	−42:29:45.2(17)	340.54	3.54	2015.26299652(14)	8010(90)	337.9(10)	6.7	18.9	57443−57764	57603	20	1242	1.2	3.98	402	38.7
J1704−3756	17:04:57.42(5)	−37:56:42.9(8)	347.80	1.95	305.234449801(13)	11292(10)	405.7(6)	5.9	15.2	57501−57799	57650	29	839	1.3	0.4271	185.65	15680
J1706−4434	17:06:23.17(2)	−44:34:29.6(6)	342.67	−2.26	429.922423266(9)	2579(5)	467.0(6)	8.8	19.4	57231−57734	57416	48	822	1.3	2.63	105	1282
J1719−3458	17:19:12.143(17)	−34:58:22.5(4)	351.89	1.39	493.774733755(7)	14(5)	530.0(3)	7.2	16.4	57474−57799	57637	34	398	1.0	600	8.3	5
J1734−2859	17:34:00.09(4)	−28:59:53(4)	358.60	2.12	301.455877933(13)	12(9)	313.9(9)	4.9	11.4	57501−57846	57674	25	856	0.9	400	6	20
J1749−21	17:49:21.2(2)	−21:46.3(9)	6.57	2.98	2714.5555611(7)	7300(300)	260(20)	4.8	9.6	57512−57848	57656	26	3551	1.8	5.9	445	14.4
J1757−1854[a]	17:57:03.78438(6)	−18:54:03.376(7)	9.97	2.88	21.497231890027(7)	2.6303(7)	378.203(2)	7.4	19.6	57405−57998	57701	3162	36	1.7	130	0.761	10500
J1810−1709	18:10:28.20(6)	−17:09:31(14)	13.05	0.96	1161.13257983(14)	330(70)	670(20)	9.3	14.6	57358−57788	57573	20	3451	1.2	56	61.9	8.3
J1812−20	18:12:36.77(5)	−20:58.3(5)	9.95	−1.32	1903.1119825(4)	-	457(19)	6.7	11.3	57513−57848	57615	30	4034	0.6	-	-	-
J1822−0902[b]	18:22:35.805(8)	−09:02:58.7(4)	21.59	2.21	148.894507042(3)	17780.8(6)	448.1(15)	7.9	15.7	57421−57847	57566	44	627	41.4	0.132308	162.710	212770

[a] Indicates binary pulsars.

[b] Timing data for J1822−0902 contains a significant degree of unexplained timing noise, and this solution should be treated with caution (see Section 3.4.7).

a phase-connected timing solution has been derived, PSR J1757−1854, are discussed in depth in Chapter 4. The remaining 3 binary pulsars for which complete timing solutions have not yet been determined, PSRs J1653−45, J1745−23, and J1812−15, as well as the 2 candidate binary systems, PSRs J1726−29 and J1831−04, are discussed separately in Section 3.4.

3.3.1 Re-detections in the PMPS

The HTRU-S LowLat survey area has a complete overlap with the survey area of the earlier PMPS (see Section 2.7). In order to determine if any of the pulsars reported in this chapter were detectable in this earlier survey, a comprehensive search of PMPS archival data was carried out. All PMPS beams within one beamwidth (0.24°) of the best known position of each pulsar were searched for matching pulsar candidates. For those pulsars with full timing solutions, a direct ephemeris fold of each observation was also produced and inspected. For those pulsars for which a detection was made, the maximum S/N derived from all inspected PMPS beams (S/N_{PMPS}) is recorded in Table 3.4.

In total, 20 pulsars were detected in the archival PMPS data. 13 of the newly-discovered pulsars were detected above the theoretical S/N cutoff for pulsars in the PMPS, $S/N_{min,PMPS} = 8$ (Manchester et al., 2001). Therefore, these pulsars were theoretically detectable in the earlier survey, but for reasons unknown were overlooked, potentially as a result of the large number of pulsar candidates produced during the survey processing or due to the presence of RFI. It should be noted that many of the pulsars detected in the PMPS using an ephemeris fold were not detected by standard searching techniques. This difficulty in detection might also partially account for the previous non-discovery of these pulsars, and may allow for further PMPS detections in the future as additional timing solutions are derived. Another 7 pulsars were detected only weakly in the PMPS, falling below the $S/N_{min,PMPS}$ cutoff. In cases where the PMPS detection is only tentative, the measured S/N_{PMPS} is set as an upper limit.

3.4 Individual pulsars of interest

Many of the pulsars discovered as part of this work warrant particular scientific scrutiny. These individual pulsars are discussed in the subsections below. As has already been noted, PSR J1757−1854, a DNS binary and by far the most scientifically interesting of the discoveries reported in this thesis, warrants sufficient attention so as to receive its own chapter. This pulsar is therefore presented in Chapter 4.

3.4.1 PSR J1537–5312 and PSR J1547–5709, a pair of He-WD binary MSPs

PSRs J1537−5312 and J1547−5709 are a pair of binary MSPs, with their binary parameters listed in Table 3.8. Based on their respective spin periods of ~ 6.93 ms and ~ 4.29 ms and their low spin-period derivatives, each of these pulsars appears to be

Table 3.8: Best-fit binary parameters for PSR J1537−5312, PSR J1547−5709 and PSR J1618−46. Values in parentheses, where available, represent 1-σ uncertainties on the final digit. Upper limits, where provided, are set at a value of 3-σ.

PSR name	J1537−5312	J1547−5709	J1618−4624
Fitting program	TEMPO2	TEMPO2	TEMPO2
Binary model	ELL1	ELL1	ELL1
Orbital period, P_b (d)	3.55014831(5)	3.07747697(3)	1.780433522(6)
Projected semi-major axis, x (lt-s)	1.982428(7)	2.668161(5)	5.329374(7)
$\lvert e\sin\omega\rvert, \lvert\varepsilon_1\rvert$ (10^{-5})	< 3.12	< 2.56	< 0.966
$\lvert e\cos\omega\rvert, \lvert\varepsilon_2\rvert$ (10^{-5})	< 3.66	< 2.10	< 0.746
Epoch of ascending node, T_{asc} (MJD)	57295.061735(7)	57297.585035(2)	57560.5896576(7)
Mass function, f ($10^{-3}\,M_\odot$)	0.664(3)	2.153(6)	51.270(16)
Minimum companion mass[a], $m_{c,min}$ ($M_\odot$)	0.11508(18)	0.17478(18)	0.58719(8)
Median companion mass[b], $m_{c,med}$ ($M_\odot$)	0.1340(2)	0.2043(2)	0.70445(10)

[a] $m_{c,min}$ is calculated for an orbital inclination of $i = 90°$ and an assumed pulsar mass of $1.4\,M_\odot$.
[b] $m_{c,med}$ is calculated for an orbital inclination of $i = 60°$ and an assumed pulsar mass of $1.4\,M_\odot$.

fully-recycled. The highly-circularised orbits and the range of companion masses implied by their mass functions (with minimum masses of $m_c = 0.11508(18)\,M_\odot$ and $m_c = 0.17478(18)\,M_\odot$ respectively) suggest that each pulsar possesses a degenerate helium white dwarf (He-WD) companion, the systems having most-likely formed out of a low-mass X-ray binary (LMXB) through Case B Roche-lobe overflow (RLO) (see e.g. Tauris, 2011), which describes a scenario where the mass-transfer and recycling process occurs during the (sub)giant phase of the companion star's evolution. No attempt at an optical confirmation of these companion WDs has yet been made, and may prove difficult given their position and estimated distance in the ISM-dense Galactic plane.

Work conducted by Tauris & Savonije (1999) and Tauris & van den Heuvel (2014) implies the existence of a significant correlation between P_b and m_c for He-WD binaries, which is approximately independent of the original mass of the donor companion star. With reference to Equation 20 of Tauris & Savonije (1999), the approximate He-WD masses for both binary systems can be calculated, taking an average between the masses derived for Pop. I and Pop. II donor stars. Furthermore, assuming a canonical pulsar mass of $m_p = 1.4\,M_\odot$, each new mass estimate can be used to determine an approximate inclination angle i via the mass function (see Equation 2.36). For PSR J1537−5312, the calculated companion mass and estimated inclination angle are $m_{c,calc} = 0.229(10)\,M_\odot$ and $i = 32°$, while for PSR J1547−5709 they are $m_{c,calc} = 0.225(10)\,M_\odot$ and $i = 52°$. Although these estimates of i are dependent on the assumed (canonical) mass of the pulsar, which has not been measured in either case, it would appear that neither binary system is significantly inclined. In combination with their low flux densities (see Table 3.4), this implies that the Shapiro delay in either pulsar is unlikely to be measurable without the use of much more sensitive future telescopes such as MeerKAT

or the SKA, rendering future mass constraints on both pulsars and their companion WDs difficult.

3.4.2 PSR J1618–4624, an unusual CO-WD binary MSP

At first glance, PSR J1618−4624 appears similar to PSRs J1537−5312 and J1547−5709, in that it also appears to be a fully-recycled MSP in a circular orbit around a WD companion. However, with a minimum companion mass of $m_c = 0.58719(8)$ as determined by the mass function, PSR J1618−4624's companion appears to be a more-massive carbon-oxygen white dwarf (CO-WD). PSR J1618−4624 therefore represents a rarer class of MSP-WD binary, with only 30 confirmed CO-WD binary systems listed on PSRCAT as of November 2017, compared to 111 binary systems conclusively identified as He-WD.

PSR J1618−4624 further stands out as a result of the unusual puzzle presented by the scenario of its formation and evolution. As described in Tauris (2011), the fully-recycled nature of this pulsar combined with a CO-WD companion favours a formation scenario involving Case A RLO, in which a long and stable mass transfer occurs while the donor companion star is still on the MS, thereby allowing the pulsar to fully spin-up. Only a handful of these systems are known to exist, including PSR J1614−2230 (Tauris et al., 2011; Lin et al., 2011; Tauris et al., 2012), PSR J1101−6424 (Ng et al., 2015) and most recently PSR J1933−6211 (Graikou et al., 2017). However, a Case A scenario does cannot account for the observed $P_b = 1.780433522(6)$ d of PSR J1618−4624 (Tauris, 2011). The loss of angular momentum required in order to produce such a short orbit implies a common-envelope (CE) evolutionary stage, during which the accreting NS becomes enveloped within the expanded outer layers of the donor star. This is known as a Case C RLO scenario, which in turn cannot account for the observed degree of recycling (Tauris, 2011). Therefore, with this apparent conflict between the Case A and Case C scenarios, PSR J1618−4624 appears to represent a new type of system which is unaccounted for by current models of MSP-WD formation.

3.4.3 PSR J1653–45, a binary system with a long orbital period

PSR J1653−45 was first discovered in an observation recorded on MJD 56128. Following its confirmation on MJD 57502, timing observations showed a monotonic increase in the pulsar's period over the following 235 days. This trend continued until timing observations on MJD 57767 resulted in a non-detection of the pulsar, and all following observations (approximately 1.6-hr of data in both timing and search modes) have failed to re-detect the pulsar. As of MJD 57838, PSR J1653−45 has yet to be re-detected.

Although a phase-connected solution for PSR J1653−45 is not yet available, the 235-day span of observations during which the pulsar was detectable is sufficient to reveal some aspects of the pulsar's behaviour. If treated as a simple spin-down, the pulsar's period change (displayed in Figure 3.8) corresponds to a spin-down rate of $\dot{P} \simeq 4.2 \times 10^{-12}$. Such a value of $\dot{P}$ would rank among the 25 highest values of $\dot{P}$ of all known pulsars. A portion of this apparent spin-down may be accounted for by the

one-year sinusoidal oscillation in apparent period introduced by an error in the pulsar's position (see Section 2.6.2). However, despite a data span of 0.64-yr, no such sinusoidal trend is visible, indicating that the contribution of this effect is likely to be at a much lower order of magnitude than the observed period change.

As shown in Figure 3.8, the apparent period of PSR J1653−45 at its discovery epoch corresponds to the pulsar's measured period shortly before its span of non-detections, indicating that the observed period change cannot be truly monotonic and implying a long-term oscillation. Considering this, it seems likely that the high value of $\dot{P}$ observed in this pulsar can be attributed to the presence of a long-period orbit, with an orbital period on the order of months to years. Hence, PSR J1653−45 may be similar to another pulsar discovered earlier in this survey, PSR J1759−24 (Ng et al., 2015), which is considered likely to be in an eclipsing binary system with a long orbital period. Another example of a similar system is PSR B1259−63 (Johnston et al., 1992b), a $\sim$ 48-ms pulsar in a $\sim$ 3.4 year orbit around a $\sim 10\,\mathrm{M}_\odot$ MS companion that experiences a $\sim$ 40-day eclipse during which it is rendered undetectable. Such eclipses, if present in PSR J1653−45, could account for the observed non-detections. However, the nature of PSR J1653−45's orbital companion and therefore the question of whether or not eclipses are possible and to what extent has yet to be determined. Additionally, the possibility that the pulsar is instead simply a nulling or intermittent pulsar cannot yet be ruled out as an explanation. Further observations will be required in order to fully resolve these questions and determine an orbital solution for the pulsar.

3.4.4 PSR J1706–4434, a glitching pulsar

PSR J1706−4434 is a $\sim$ 430-ms pulsar and was the second pulsar reported in this thesis to be discovered. Following a confirmation and gridding observation on MJD 57169, timing observations with an approximately monthly cadence between MJD 57231 and MJD 57588 (a span of 357 days) were sufficient to develop a fully phase-connected solution for the pulsar. However, all further timing observations (spanning MJD 57615 to MJD 57734) showed a clear deviation from this model, indicating a sudden decrease in the spin period of the pulsar. From this, it can be concluded that a glitch occurred in PSR J1706−4434 at some point between MJD 57588 and MJD 57615. The effect of this glitch on the timing residuals of PSR J1706−4432 are shown in Figure 3.9.

Table 3.9 lists the parameters of the observed glitch in PSR J1706−4434. Due to the limited cadence of timing observations surrounding the glitch, the precise epoch of the glitch cannot be accurately determined. A glitch epoch of MJD 57601, the approximate midway point between the epochs of the neighbouring observations, has therefore been assumed. Similarly, no evidence is detected for the presence of a post-glitch exponential decay of the spin period, likely also due to the limited observational cadence as well as the limited timing precision of this pulsar. Finally, due to the relatively short 119-day span of post-glitch timing observations, the permanent change to the spin-period derivative $\dot{P}$ (and corresponding change in the spin-frequency derivative $\dot{\nu}$) remains poorly constrained. Therefore, we present only an upper limit on this value in Table 3.9, which represents an uncertainty of $3\,\sigma$.

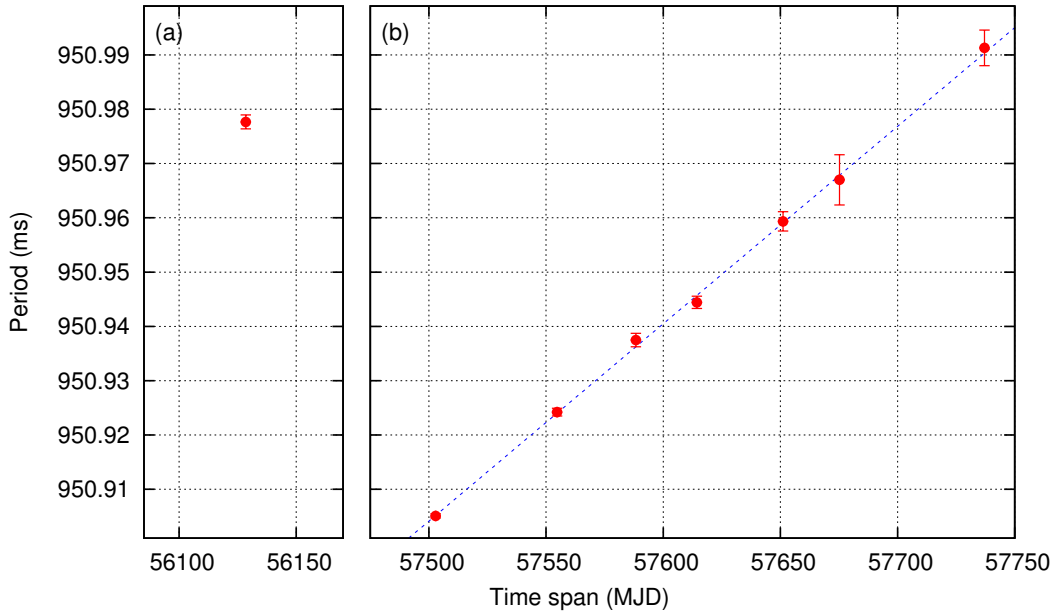

Figure 3.8: Observed changes in the apparent rotational period of PSR J1653−45. Plot (a) shows the period at the epoch of the pulsar's discovery (MJD 56128), while plot (b) shows the pulsar's changing period between MJD 57502 and MJD 57737, a span of 235 days, after which the pulsar appears to have become undetectable. The dashed blue line represents the best linear fit to the data, with the slope corresponding to a spin-down of $\dot{P} \simeq 4.2 \times 10^{-12}$. Error bars represent 1-σ uncertainties.

Table 3.9: Parameters of the glitch observed in PSR J1706−4434. Values in parentheses, where available, represent standard 1-σ uncertainties on the final digit. In the case of the permanent spin frequency derivative increment $\Delta\dot{\nu}$, an uncertainty of $3\,\sigma$ is provided as the upper limit.

Glitch parameters for PSR J1706−4434	
Estimated glitch epoch (MJD)	57601
Phase increment, $\Delta\phi$	0.010(2)
Permanent spin-frequency increment, $\Delta\nu$ (Hz)	$2.28(10) \times 10^{-8}$
Permanent spin-frequency derivative increment, $\Delta\dot{\nu}$ (s^{-2})	$< 3.8 \times 10^{-16}$

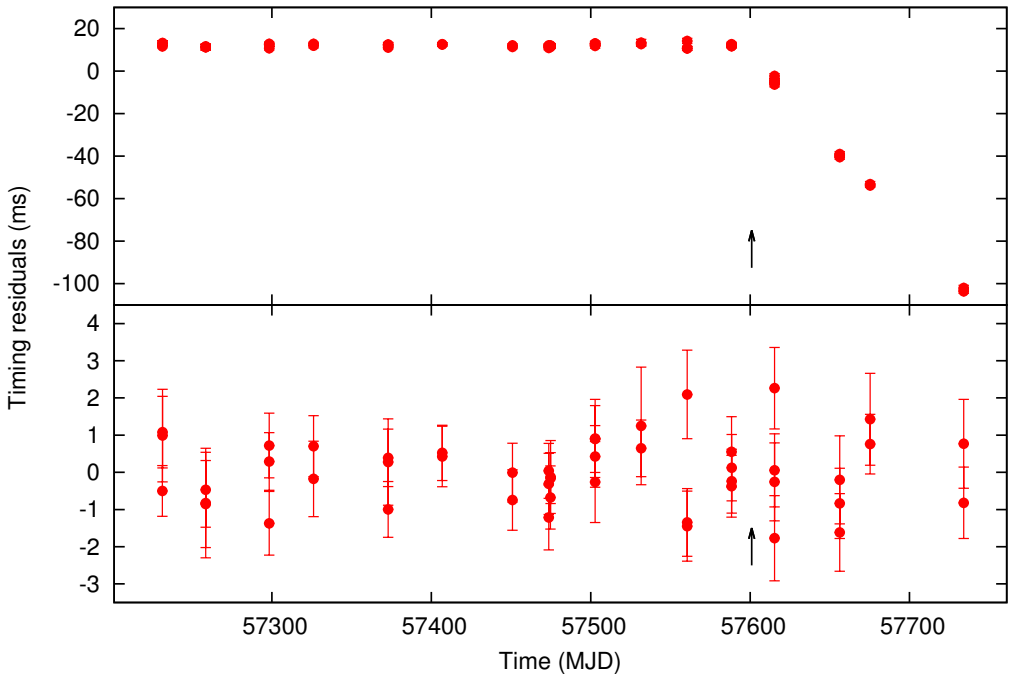

Figure 3.9: Effect of the observed glitch in PSR J1706−4434 on the pulsar's timing residuals. The top plot shows the residuals plotted using the best pre-glitch phase-connected solution for the pulsar without accounting for the glitch, the effect which can be seen in the change in slope to the right of the plot, indicating a change in spin period. The bottom plot shows the residuals plotted using the final phase-connected solution, which incorporates the glitch parameters listed in Table 3.9. In both plots the glitch epoch is indicated by the small arrow.

The magnitude of this glitch can be measured by the fractional change in its spin frequency, $\Delta\nu/\nu = 9.8(4) \times 10^{-9}$. A comparison of the magnitude of this glitch against the population of published glitches[21] (Espinoza et al., 2011) shows that this glitch magnitude is neither especially large nor especially small, with the approximate minimum, maximum and median values of $\Delta\nu/\nu$ for known glitches (considering only spin-up glitches) being 0.0025, 65000 and 29×10^{-9} respectively. Instead, the observed glitch in PSR J1706−4434 appears to be reasonably typical of the glitch population. Further observations of this pulsar will be useful in better constraining the change in the post-glitch value of $\dot{\nu}$, as well as in monitoring for future possible glitch events.

3.4.5 PSR J1745–23, a black widow pulsar

One of the more recent pulsars to emerge from the survey, PSR J1745−23 was initially identified as a ~ 5.42-ms binary MSP, with the presence of significant jerk in its discovery observation indicating a likely short orbital period. Follow-up search-mode observations with Parkes covering a 153-day span between MJD 57798 and MJD 57951 have resulted in the determination of an approximate orbital solution which is sufficiently accurate so as to be useful as a folding model at all available epochs. However, due to the low cadence of the available data, a phase-connected timing solution has yet to be determined. The estimated orbital model is presented in Table 3.10.

From the available data, PSR J1745−23 appears to have an approximate orbital period of $P_\mathrm{b} \simeq 0.166\,\mathrm{d}$, or 3.98 h, with a semi-major axis of $x \simeq 0.0624\,\mathrm{lt\text{-}s}$, indicating a particularly tight binary orbit. The orbit also appears to be highly circularised, although in the absence of a phase-connected solution, an estimate of the upper limit on the eccentricity is not yet possible. As such, any estimate of the longitude of periastron ω is also not yet possible, and has been fixed at $\omega = 0$ in our models. Based upon this orbital solution, the mass function of the binary system is approximately $f \simeq 9.53 \times 10^{-6}\,\mathrm{M}_\odot$. Assuming a canonical pulsar mass of $m_\mathrm{p} = 1.4\,\mathrm{M}_\odot$, this gives a minimum companion mass of $m_\mathrm{c,min} \simeq 0.027\,\mathrm{M}_\odot$ and a median mass of $m_\mathrm{c,med} \simeq 0.031\,\mathrm{M}_\odot$.

Follow-up observations also revealed the presence of a significant eclipse during superior conjunction. The precise duration of this eclipse is currently unknown, as while the pulsar has been directly observed entering the eclipse, a direct observation of the end of the eclipse has not yet been made. A conservative upper limit of the duration of the eclipse based upon the current coverage of the orbit is $T_\mathrm{eclipse} < 58\,\mathrm{min}$, occurring approximately between orbital phases of $0.14 < \varphi < 0.38$ as specified by the model in Table 3.10. Based upon the presence of these eclipses, it can be reasonably inferred that the orbit is close to edge-on, indicating that the mass of the binary companion is close to $m_\mathrm{c,min}$.

Based upon the lightweight companion, the presence of eclipses and the short orbital period ($P_\mathrm{b} < 24\,\mathrm{hr}$), PSR J1745−23 would appear to qualify as a black widow pulsar (see e.g., Roberts, 2013). This may in part be responsible for the difficulties that have been encountered while attempting to develop a phase-connected solution for this this

[21] http://www.jb.man.ac.uk/pulsar/glitches.html

Table 3.10: Approximate binary parameters for PSR J1745−23. Values in parentheses, where available, represent 1-σ uncertainties on the final digit. Both the eccentricity e and longitude of periastron ω have been fixed at 0 due to the evidently circular nature of the orbit, and the current inability to place further constraints on either parameter.

PSR name	J1745−23
Fitting program	TEMPO
Binary model	BT
Orbital period, P_b (d)	0.165562(10)
Projected semi-major axis, x (lt-s)	0.06247(6)
Eccentricity, e	0
Longitude of periastron, ω (°)	0
Epoch of periastron, T_0 (MJD)	57950.47559(3)
Mass function, f ($10^{-6}\,M_\odot$)	9.550(16)
Minimum companion mass[a], $m_{c,min}$ ($M_\odot$)	0.02689(2)
Median companion mass[a], $m_{c,med}$ ($M_\odot$)	0.03111(4)

[a] $m_{c,min}$ and $m_{c,med}$ are calculated as per the assumptions in Table 3.8.

pulsar, as the ongoing interaction of the pulsar with its evaporating binary companion, as well as with the resulting intra-binary debris field, has been known to introduce timing irregularities in other black widow systems, such as in PSR J2051−0827 (Shaifullah et al., 2016). A brief review indicates that both the estimated orbital period and companion mass of PSR J1745−23 are typical of the larger black widow population (Chen et al., 2013), with evolutionary scenarios suggesting that PSR J1745−23 originated from the evolution of ultra-compact LMXB (Tauris, 2011; Chen et al., 2013). At present, although the companion can be identified as both lightweight and degenerate, any further classification at this stage remains uncertain. Future observations of this pulsar will aim to derive a fully phase-connected solution through the measurement of high-cadence TOAs spaced over several consecutive orbital periods in order to remove any ambiguity in the pulsar's orbital solution over that time frame, from which a longer-span timing solution can be constructed.

3.4.6 PSR J1812–15 and PSR J1831–04, a pair of suspected binary pulsars with long rotational periods

PSR J1812−15 and PSR J1831−04 are a pair of bright, long-period pulsars with rotational periods of approximately 1014 and 1066-ms respectively. Figure 3.10 shows the discovery observation of PSR J1812−15, while Figure 3.11 shows the discovery observation of PSR J1831−04, both of which have been folded at an assumed acceleration

of $a = 0\,\mathrm{m\,s^{-2}}$. The parabolic curves visible in the sub-integrations of each of these observations clearly indicates the presence of a non-zero acceleration, from which it can be inferred that both of these pulsars are likely to be in binary systems. While PSR J1831−04 remains a candidate binary only, the binary nature of PSR J1812−15 has been confirmed via two observations recorded on MJD 58013, where the pulsar's period was observed to change from 1014.4685(3) ms to 1014.70812(6) ms over a period of $\sim 5.4\,\mathrm{h}$, with an accompanying acceleration change from $-3.9(3)\,\mathrm{m\,s^{-2}}$ to $3.75(9)\,\mathrm{m\,s^{-2}}$.

Efforts to determine full orbital solutions for both of these pulsars have been hindered by the fact that in addition to being in binary systems, both of these pulsars also appear to be either nulling or intermittent, with changes between 'on' and 'off' states having been directly observed in both pulsars. Examples of this nulling behaviour in PSR J1812−15 can be seen in Figure 3.12, while the only example of a transition between nulling/intermittency and 'normal' emission in PSR J1831−04 can be seen as part of its discovery observation in Figure 3.11. As each pulsar has only a limited number of irregularly sampled observations, with the nulling/intermittency timescale for each pulsar often exceeding the length of a typical observation ($\sim 10 - 15\,\mathrm{min}$), an approximate nulling fraction (NF) for each pulsar was determined by a visual inspection of each folded observation. This process was assisted by the program PDMP (part of the psrchive software package), in a method analogous to that described by Lyne et al. (2017a). Intervals during which the pulsar was unambiguously detectable were classified as 'on', while all other intervals were classified as 'off'. A more rigorous analysis of the NF will be provided in a following publication, ideally after the determination of a phase-connected timing solution for each pulsar.

In addition to its 1.2 h discovery observation on MJD 55845, PSR J1812−15 has been observed for a total of $\sim 4.8\,\mathrm{h}$ over 23 observations between MJD 57733 and MJD 58013, and remains undetected in a total of $\sim 2.8\,\mathrm{h}$, with 14 individual observations resulting in a non-detection. This results in a preliminary nulling fraction (including the discovery observation) of NF = 47(10) %. Less is known about PSR J1831−04, as while the pulsar's initial 1.2 h discovery observation on MJD 55923 is considered unambiguous enough to be self-confirming, the pulsar has yet to be re-detected despite having been observed for an additional $\sim$ 3h spaced over 15 observations between MJD 57798 and MJD 57984. Additionally, despite the presence of significant RFI, evidence of a null lasting several minutes is already visible approximately one hour into the pulsar's discovery observation, indicating a potentially large variety in pulsar nulling timescales. Based on the limited data available, we determine a preliminary nulling fraction of NF = 76(11) %.

However, it may be that not all of the non-detections of PSR J1812−15 and PSR J1831−04 can be attributed to nulling or intermittency. Peculiarities in the orbit of each pulsar, such as the presence of eclipses or a rapidly-changing acceleration, may yet explain some of the observed non-detections. Additional observations of both pulsars will be required in order to more accurately determine their nulling fractions and better understand their emission properties, as well as to eventually determine orbital and phase-connected timing solutions.

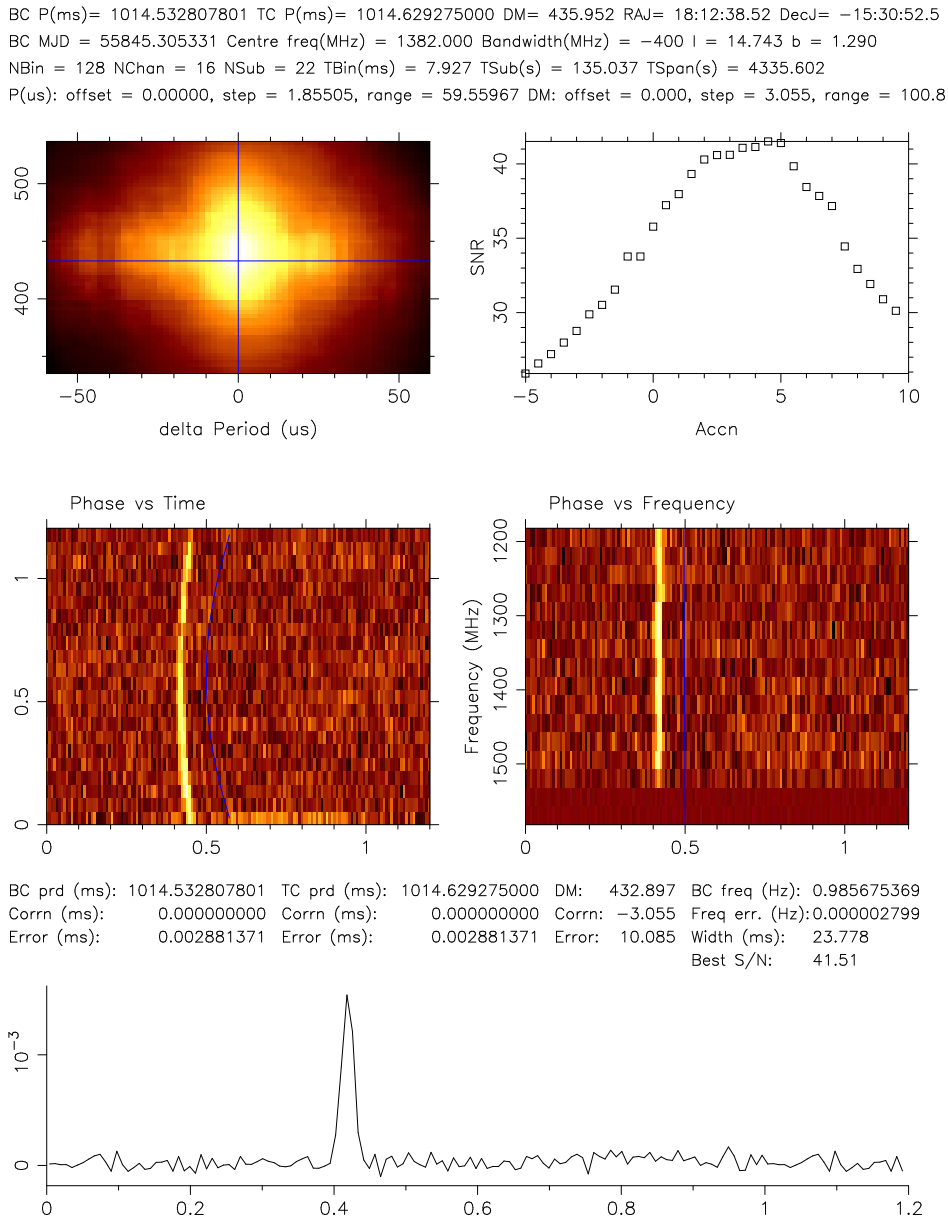

Figure 3.10: An optimised PDMP discovery plot of PSR J1812−15. The top-left plot shows the response of the pulsar's S/N to changes in spin period and DM through a colour map, with the optimal S/N marked by crosshairs. The top-right plot shows the response of the pulsar's S/N to changes in acceleration, constraining the optimal acceleration in this observation at $4.5\,\mathrm{m\,s^{-2}}$. The middle plots show the sub-integrations (left) and sub-bands (right) of the folded archive being analysed, with lines of optimal S/N indicated by the solid blue lines. The bottom plot shows the S/N-optimised profile of the pulsar.

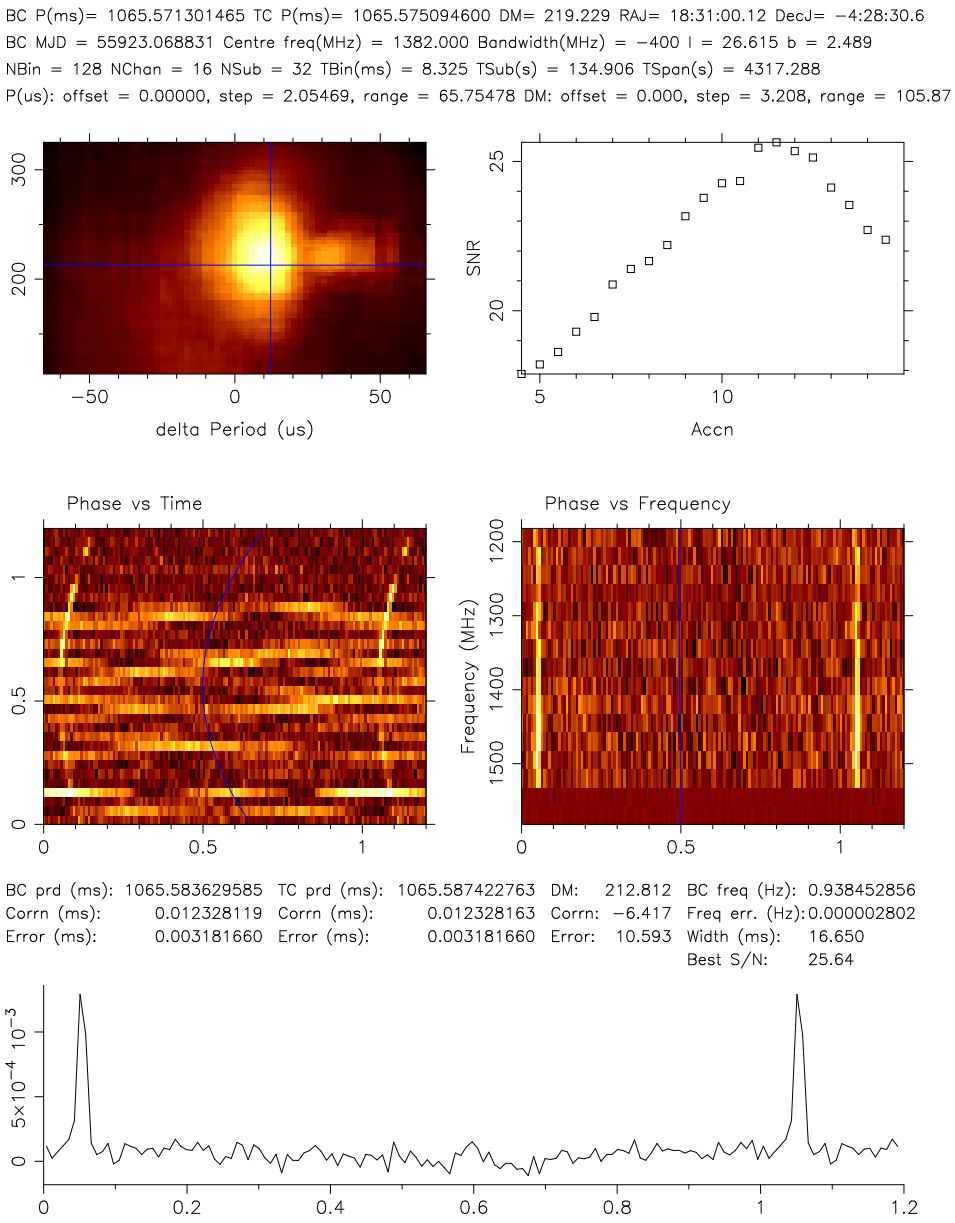

Figure 3.11: An optimised PDMP discovery plot of PSR J1831−04. The top-left plot shows the response of the pulsar's S/N to changes in spin period and DM through a colour map, with the optimal S/N marked by crosshairs. The top-right plot shows the response of the pulsar's S/N to changes in acceleration, constraining the optimal acceleration in this observation at $11.5\,\mathrm{m\,s^{-2}}$. The middle plots show the sub-integrations (left) and sub-bands (right) of the folded archive being analysed, with lines of optimal S/N indicated by the solid blue lines. A substantial amount of RFI is visible in this observation despite being cleaned by the RFI removal pipeline, however the periodic emission of the pulsar is still visible. The bottom plot shows the S/N-optimised profile of the pulsar.

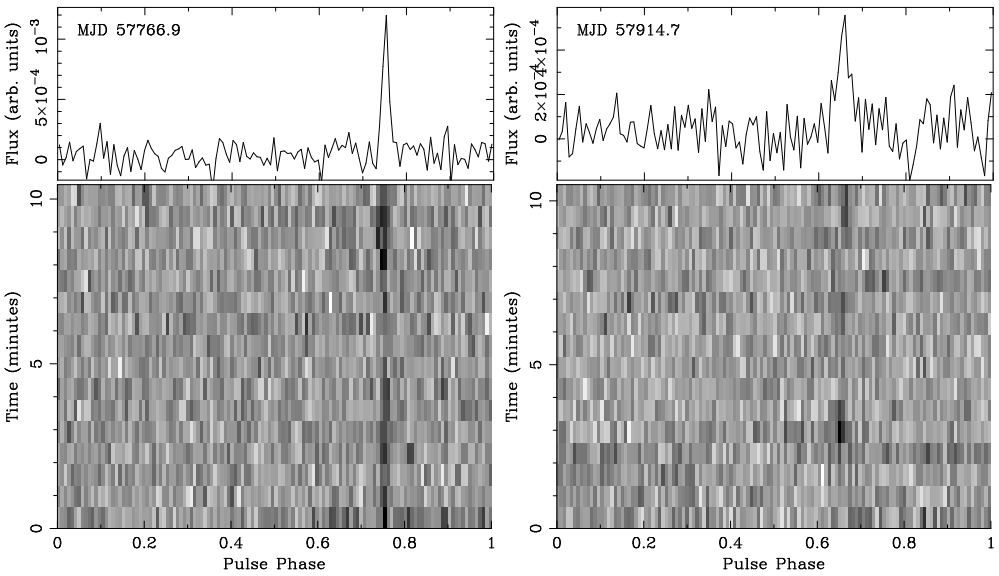

Figure 3.12: Nulling behaviour in PSR J1812−15. Shown are two epochs, MJD 57766.9 and MJD 57914.7, at which the pulsar was observed for approximately 10 min each. Variability in the pulsar signal can be seen in each instance which, given a DM of $431(10)\,\mathrm{cm}^{-3}\,\mathrm{pc}$, is unlikely to be attributable to scintillation. This nulling behaviour is in addition to other observations of similar or greater length where the pulsar is rendered entirely undetectable for the duration of the observation.

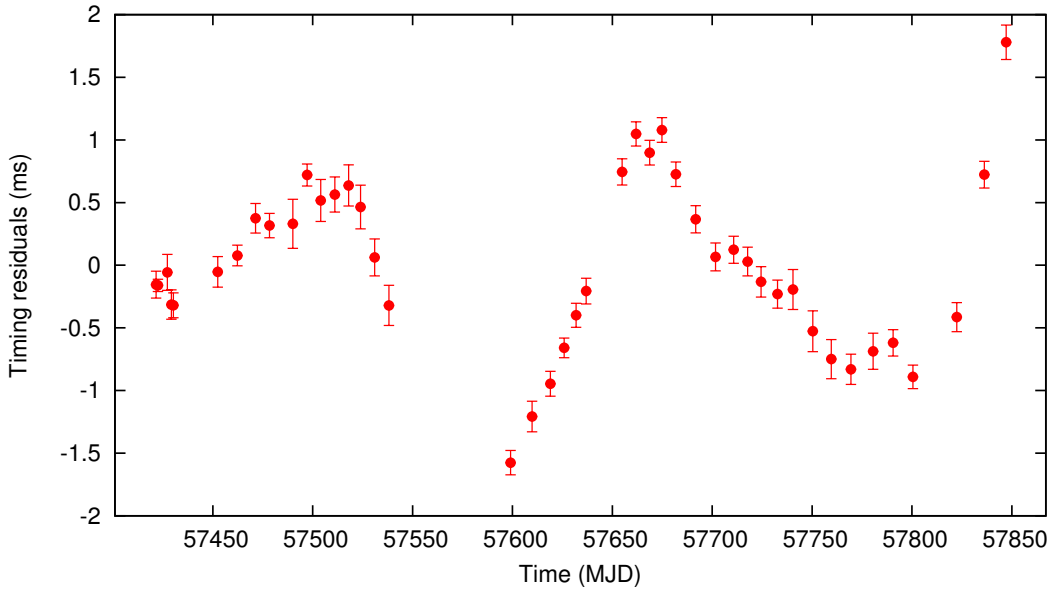

Figure 3.13: Timing residuals of PSR J1822−0902. The timing model used to derive these residuals is based on the values presented in Table 3.7, and has been fit for position, P and $\dot{P}$. The TOA uncertainties are presented without any additional weighting.

3.4.7 PSR J1822–0902, a pulsar with significant timing noise

PSR J1822−0902 is a $\sim$ 149-ms pulsar with a DM of approximately 448 $\mathrm{cm}^{-3}\,\mathrm{pc}$. The pulsar is notable in that it possesses a high spin-down rate of approximately $\dot{P} = 1.78 \times 10^{-14}$, implying both a young characteristic age τ_c and a high spin-down luminosity $\dot{E}$. In fact, the estimated characteristic age of $\tau_\mathrm{c} = 0.132\,\mathrm{Myr}$ ranks as the smallest value of τ_c presented in this thesis. The full parameters of this pulsar are available in Table 3.7.

Despite PSR J1822−0902's 426-day timing span having allowed for the development of a fully phase-connected timing solution, this pulsar appears to experience a significant amount of residual timing noise. These residuals are presented in Figure 3.13. Interestingly, the timing noise appears to be roughly periodic with an approximate timescale of 160 to 200 days. As this range includes a period of 0.5 yr, it is possible that this noise is due to an unfit timing parameter relating to the Earth's motion around the Sun. However, attempts to fit both for proper motion and parallax have been unsuccessful in removing the timing noise. Additionally, the pulsar's large DM and correspondingly large DM-distance estimates make it unlikely that either these residual timing effects would be resolvable over a timing span of only 426 days.

An alternative hypothesis for the timing noise may be that PSR J1822−0902 exists as part of a binary system. Given the long orbital period as well as the small semi-major axis implied by the observed amplitude of the oscillation of the timing noise

($x \simeq 1.5 \times 10^{-3}$ lt-s), such a binary (if present) would likely be around a very lightweight companion, potentially of planetary mass (as determined via estimates using the mass function as described in Section 2.6.3.2). However, early attempts to fit a binary model to the current data set have also been unsuccessful. It should be noted that both this and the previous hypothesis rely on the continued periodicity of any future timing noise observed in this pulsar. It may be that this apparent periodicity breaks down in the coming months and years, having only been the result of a statistical artefact. Ongoing timing of this pulsar will be essential in determining the underlying nature of this pulsar's timing noise, including whether or not it is truly periodic, and identifying any larger effect which may be present in this system.

3.4.8 PSR J1726–29, a candidate binary system and a potential aligned rotator

PSR J1726−29's most immediately identifiable feature is its extremely wide pulse profile, as shown in Figure 3.7. With a rotational period of 28.4 ms (classifying this pulsar as a likely MSP), the W_{50} and W_{10} pulse-width values listed in Table 3.4 correspond to approximately 34 % and 64 % of the period respectively, indicating emission across the majority of the pulse profile. Although it has not yet been fit for, the presence of scattering (see Section 1.3.2) may play a role in increasing the apparent width of this profile, and MSPs do typically possess wider pulse profiles than the 'normal' pulsar population (Kramer et al., 1998). However, an alternative hypothesis may be that PSR J1726−29 represents an *aligned rotator*, where the angle of misalignment (α) between the magnetic and rotational axes of the pulsar is close to zero (see Figure 1.4). A precise determination of α relies in part upon the availability of polarimetric information. However, due to the relative weakness of PSR J1726−29 as well as the lack of a full timing solution, sufficiently accurate polarimetric data is not yet available. Further complications arise from the current difficulties associated with attempts to model the geometry of the radio beams of MSPs (see e.g. Dai et al., 2015), with no clear unifying model having emerged.

For these reasons, a robust determination of α is not yet possible. Future constraint of α will be dependent upon the availability of further timing observations, which will allow both for the development of a timing solution and for the coherent integration of all available polarimetric data, improving the accuracy of the pulsar's polarised flux-density measurements. Additional multi-frequency observations may also be useful in characterising the beam geometry of this pulsar by illustrating how its profile shape and polarisation characteristics change with frequency, as well in constraining the role which scattering may play in widening the apparent pulse profile.

Additionally, PSR J1726−29 appears to be part of a binary system. An analysis of timing observations recorded between MJD 55846−57951, a span of 186 days, indicates a variation of the pulsar's spin period (see Figure 3.14). This variation does not appear sinusoidal in nature, and is of at least an order of magnitude greater than the period change expected from an error in the pulsar's on-sky position. Furthermore, the pulsar's apparent spin-down rate $\dot{P}$ also appears to fluctuate in a non-sinusoidal manner

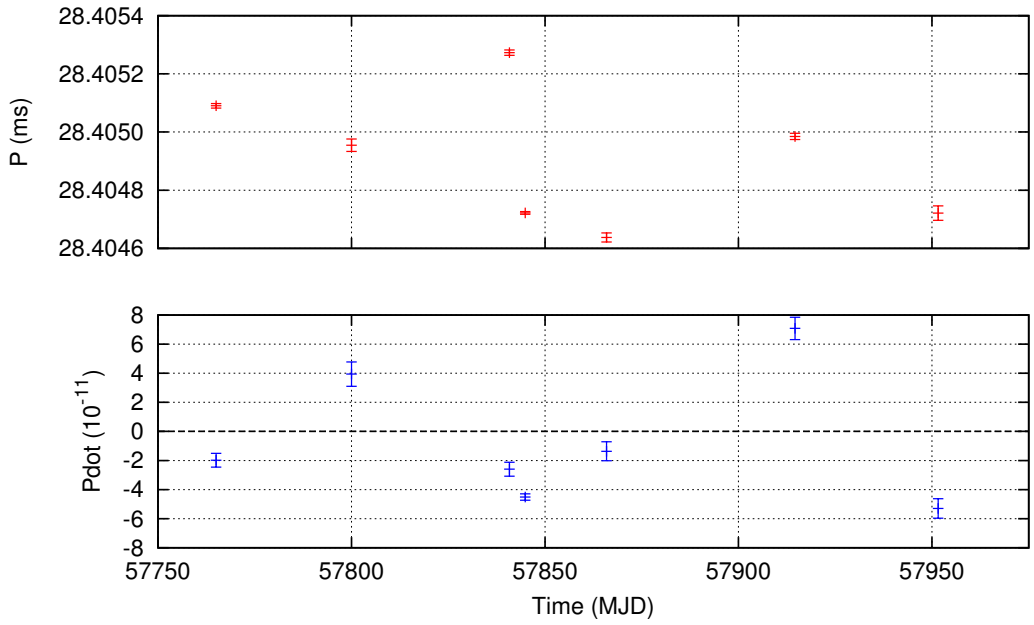

Figure 3.14: Variations in the observed spin period and spin-down rate of PSR J1726−29. The top figure shows the changing apparent period (P) of the pulsar in red, while the lower figure shows the changing spin-down rate ($\dot{P}$) of the pulsar in blue.

with each timing epoch, which is consistent with the presence of small but persistent accelerations. Based upon this information, we tentatively suggest that PSR J1726−29 exists as part of a binary system, although at present it is not possible to constrain the binary parameters. This would appear to imply that the pulsar has been partially recycled by its binary companion, although a future determination of an accurate $\dot{P}$ will be necessary in order to fully cement this pulsar as a member of the recycled-MSP population.

3.4.9 PSR J1854–05, an intermittent pulsar

The one feature of note regarding PSR J1854−05 is its apparent intermittency. Although approximately monthly confirmation observations commenced on MJD 57405, it was not until MJD 57554 that the pulsar was re-detected, and not until MJD 57609 that an observation was recorded with sufficient S/N to grid the pulsar's position. Using the same method as described in Section 3.4.6, based upon both the initial 1.2 h observation recorded on MJD 56028 and a subsequent ~ 3 h of data recorded during 9 observations from MJD 57405 to 57609, the approximate NF of PSR J1854−05 can be calculated as NF = 72(14) %. As with PSRs J1812−15 and J1831−04, a more rigorous estimate of the NF will follow in a later publication.

3.4.10 PSR J1810–1709, a nulling pulsar

Possessing a DM of $\sim$ 670 cm^{-3} pc, one of the highest DM's reported in this thesis, PSR J1810−1709 immediately stands out due to the presence of what may be a scattering tail in its profile, as seen in Figure 3.7. Alternatively, although some amount of scattering is likely, it may be that the pulsar simply has a wide inherent pulse profile. Future multi-frequency observations of the pulsar may be useful in investigating the role played by scattering in profile of this pulsar.

One feature that is not immediately evident from the pulsar profile is the nulling behaviour exhibited by PSR J1810−1709. Unlike the other intermittent pulsars reported in this thesis, the 'on'/''off' timescale of PSR J1810−1709 appears to be much shorter. The average nulling and emission timescales are 333 and 135 s respectively, with corresponding standard deviations of 291 and 122 s. Under the definitions outlined in Section 1.4.2 , this would appear to classify PSR J1810−1709 as a true nulling pulsar, as opposed to an intermittent pulsar.

Once gain, an approximate NF can be calculated by adopting the same methodology as described in Section 3.4.6. Based upon both the initial 1.2 h observation recorded on MJD 55926 and a subsequent $\sim$ 2.3 h of data recorded during 4 observations from MJD 57259 to 57407, the approximate NF of PSR J1810−1709 can be calculated as NF = 70(20) %. As with the other intermittent pulsars reported in this thesis, a more rigorous estimate of the NF will follow in a later publication.

3.5 Comparison to the known pulsar population

In order to compare the discoveries of the HTRU-S LowLat pulsar survey to the known pulsar population, this section considers the 40 pulsars reported within this thesis together with the additional 60 discoveries reported from the initial $\sim$ 50 % of the survey processing conducted by Ng et al. (2015). For the 53 pulsars in this group with well-constrained values of P and $\dot{P}$, Figure 3.15 shows their positions on a P-$\dot{P}$ diagram as compared to the previously-known pulsars within the survey region. It would seem from Figure 3.15 that the HTRU-S LowLat pulsars represent a generally older, more-evolved population. This trend appears to be shared between the discoveries reported from both portions of the survey processing, however as almost half of the reported discoveries lack a well-measured $\dot{P}$, the possibility remains that this apparent trend may be the result of small-number statistics, a caveat which will apply throughout this section. For a more specific comparison of the HTRU-S LowLat discoveries to the known pulsar population, this section will focus on three key population statistics: distance, luminosity and characteristic age.

3.5.1 Distance

As the true distance to each of the 100 HTRU-S LowLat pulsars is currently unknown, their distances have again been inferred based upon their DM values using both the NE2001 and YMW16 electron density models. The estimated DM distances for the 40

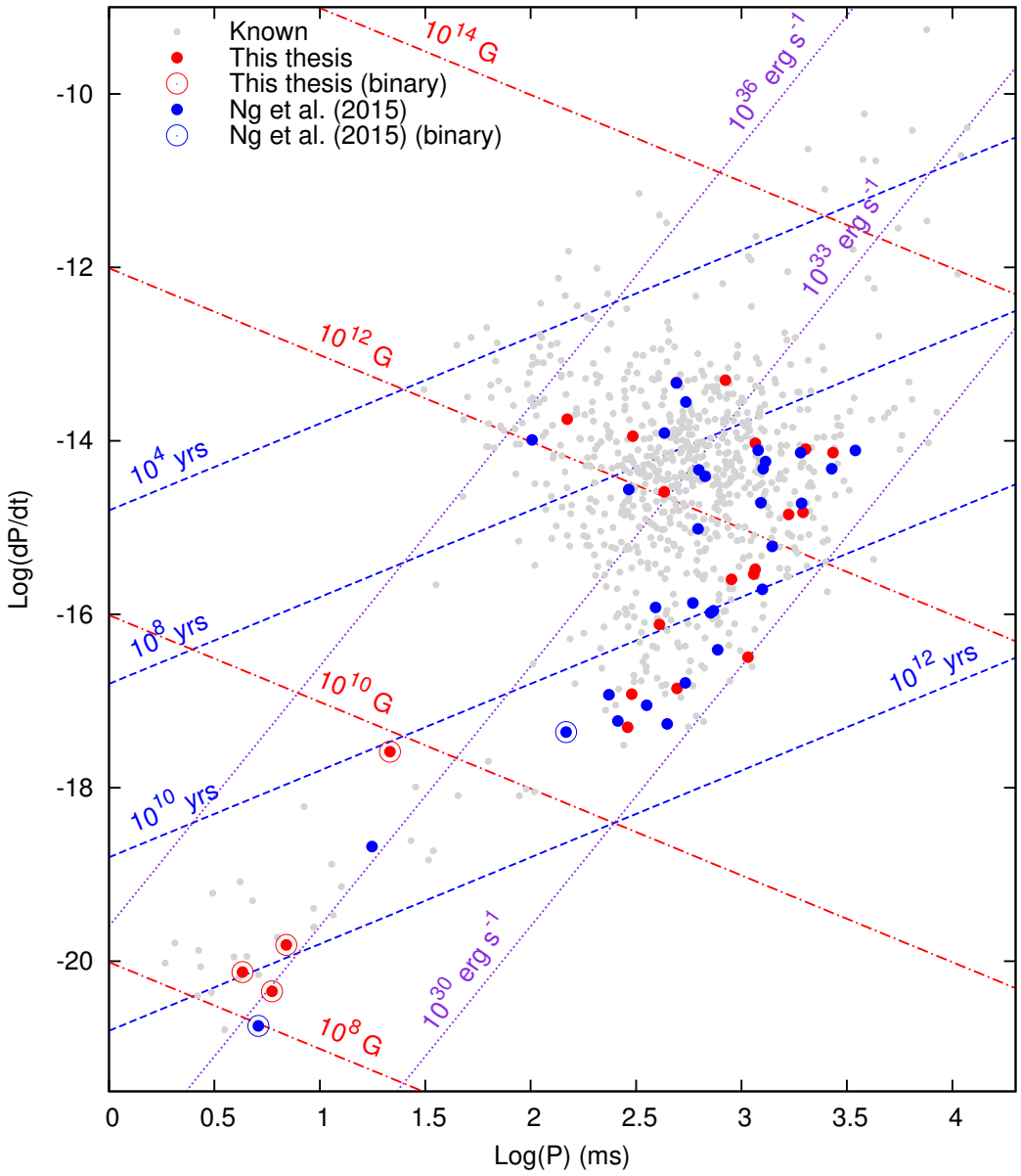

Figure 3.15: A P-$\dot{P}$ diagram displaying 53 HTRU-S LowLat discoveries with well-constrained P and $\dot{P}$ against the known Galactic pulsar population within the survey area. The 31 blue points are those pulsars with well-constrained values of P and $\dot{P}$ reported in Ng et al. (2015), while the 22 red points are those pulsars reported in Table 3.7 whose P and $\dot{P}$ are similarly well constrained. Grey points represent the population of known pulsars within the survey region. Circled points indicate binary pulsars.

pulsars reported in this thesis can be found in Tables 3.7 and 3.6, while the NE2001 distance estimates of the remaining 60 pulsars are listed in Ng et al. (2015). As per Ng et al. (2015), a typical uncertainty of 25 % is assumed for the NE2001 distance estimates, while Yao et al. (2017) report a typical uncertainty of $\sim 10\,\%$ for distance estimates from the YMW16 model. Note that it is not the intent of this comparison to render an assessment of the accuracy of either of these models, but in light of the statistical uncertainties involved in pulsar distance estimation, it is prudent to consider both of these models in this analysis.

Contrary to Ng et al. (2015), who reported the discovery of no nearby pulsars (here defined as pulsars with a distance less than $\sim 2\,\mathrm{kpc}$), this thesis reports the discovery of 2 such nearby pulsars. PSR J1753−28, with a DM of only $18.0(9)\,\mathrm{cm}^{-3}\,\mathrm{pc}$ and a DM distance of $0.6 - 0.7\,\mathrm{kpc}$, ranks as the closest pulsar detected in the HTRU-S LowLat survey, while PSR J1514−53, with a DM of only $27(3)\,\mathrm{cm}^{-3}\,\mathrm{pc}$ and a DM distance of $0.8 - 0.9\,\mathrm{kpc}$, comes in at a close second. This would indicate an approximate fraction of 'nearby' pulsars discovered within the survey of $\sim 2\,\%$ which, accounting for small-number statistical variations, is consistent with the $\sim 3.8\,\%$ expectation value calculated by Ng et al. (2015).

A more comprehensive assessment of the degree to which the distances of the HTRU-S LowLat pulsars correspond to those of the overall Galactic population can be made with a Kolmogorov-Smirnov (KS) test. Distance statistics of the known pulsars within the survey region were compiled from PSRCAT. Where precision distance measurements were unavailable from PSRCAT, DM-distance estimates were calculated once again using both the NE2001 and YMW16 models, giving two data sets consisting of distance estimates for 811 known pulsars. The distance statistics of the HTRU-S LowLat and known populations were then compared on a per-model basis. In both cases, the null hypothesis (that the distribution of distances derived for the 100 HTRU-S LowLat discoveries is drawn from the same population distribution as the known pulsars) cannot be ruled out, with both the NE2001 and YMW16 model comparisons resulting in a p-value of ~ 0.3. It would therefore appear that the distances of the HTRU-S LowLat discoveries are consistent with the background population. This consistency is shown in Figure 3.16, which shows the similarities in the distance distributions of the two populations for both the NE2001 and YMW16 models both in terms of their respective histograms and cumulative distribution functions (CDFs).

3.5.2 Luminosity

For the 74 HTRU-S LowLat pulsars with calibrated flux densities listed both here and in Ng et al. (2015), we can also use the derived DM distances (again considering both the NE2001 and YMW16 models) to calculate a set of pulsar luminosities at 1.4 GHz, as described in Section 3.3. The calculated luminosities for the the 20 flux-calibrated pulsars reported in this thesis can be found in Table 3.4. Note that these luminosity values should be treated with a degree of caution, as in addition to the uncertainty on each pulsar's measured flux density, the uncertainty on the DM distances (as outlined in Section 3.5.1) contributes an additional factor of uncertainty. For comparison, two

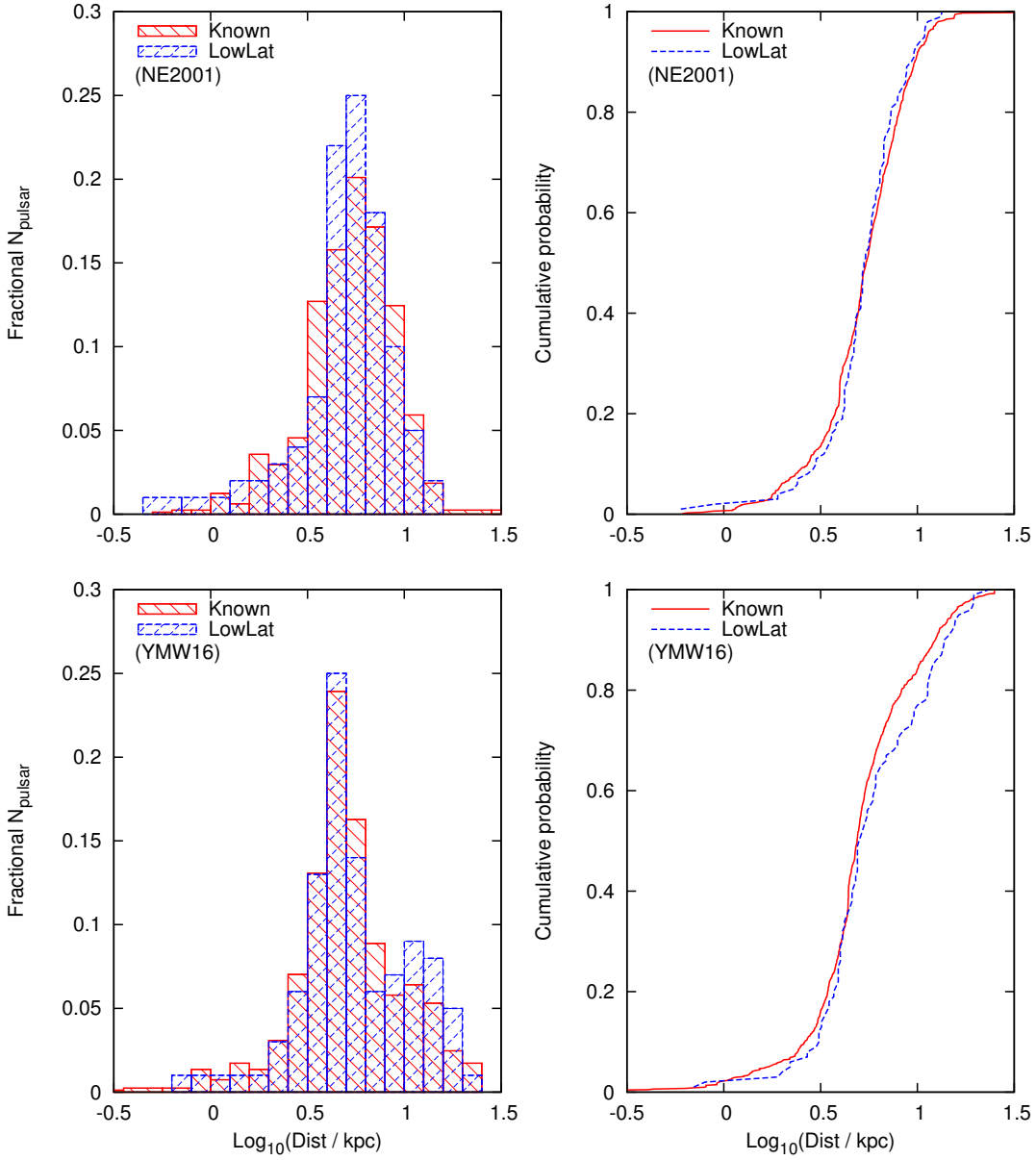

Figure 3.16: Distance distributions of the 100 HTRU-S LowLat pulsars (blue) and 811 previously-known Galactic pulsars (red). Shown on the left are histograms of the distance distributions of each population under both the NE2001 (top) and YMW16 (bottom) models, normalised by the number of pulsars in each distribution. Shown on the right are the corresponding CDFs of each distribution, again featuring the NE2001 (top) and YMW16 (bottom) models.

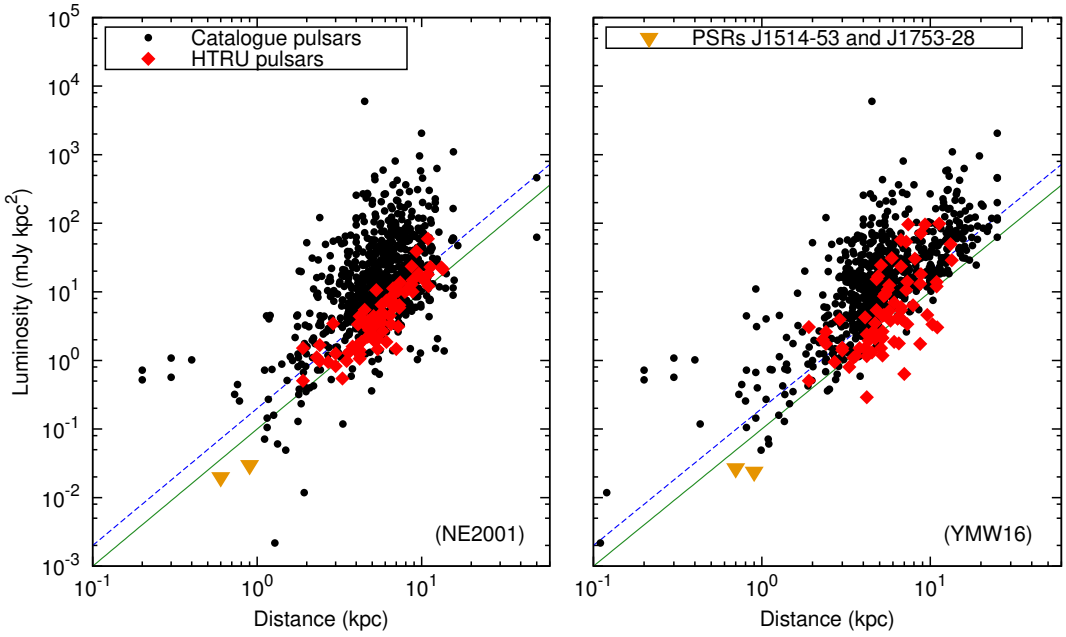

Figure 3.17: A comparison of the distances and 1.4-GHz luminosities of the 74 HTRU-S LowLat pulsars with calibrated flux densities to the background pulsar population. HTRU-S LowLat pulsars are shown in red, while the 792 known pulsars within the survey region is shown in black. The green and blue lines represent lines of constant 1.4-GHz flux density at 0.1 and 0.2 mJy respectively. Where more accurate distances are unavailable, distances and luminosities are estimates using the NE2001 (left) and YMW16 (right) electron density models. The estimated distances and luminosities of two additional pulsars without calibrated flux densities, PSRs J1753−28 and J1514−53, are indicated by gold triangles.

sets of luminosities for the 792 known pulsars with calibrated flux densities within the survey region were also compiled, using the NE2001 and YMW16 distance estimates described in Section 3.5.1.

A comparison of the HTRU-S LowLat pulsars to the background Galactic population is shown in Figure 3.17. From both the NE2001 and YMW16 luminosity estimates, it can immediately be seen that the HTRU-S LowLat survey has met its objective of discovering pulsars at the lower end of the luminosity distribution. This is verified by a KS test, which show that for both the NE2001 and YMW16 luminosity estimates, the probability of the HTRU-S LowLat luminosity distribution having being drawn from the background pulsar distribution is less than 0.01 %.

Additionally, although their absolute flux densities have not yet been calibrated, estimates based upon the radiometer equation (see Section 2.5) allow us to calculate approximate luminosities for both of the nearby pulsars reported in this thesis. For PSRs J1753−28 and J1514−53, we determine approximate luminosities of

$\sim 0.02\,\mathrm{mJy\ kpc^2}$ and $\sim 0.03\,\mathrm{mJy\ kpc^2}$ respectively. These pulsars, highlighted in Figure 3.17, indicate that there may yet be a further population of nearby, low-luminosity pulsars yet to be discovered. This inference is further strengthened by the binary MSP PSR J2322−2650, a recent discovery of HTRU-S HiLat (Spiewak et al., submitted) whose luminosity at 1.4 GHz and DM distance estimates appear extremely similar to PSRs J1753−28 and J1514−53. This, in combination with the recent discovery of the fastest-spinning pulsar in the Galactic field (PSR J0952−0607; Bassa et al., 2017), whose DM distance estimates based upon both the NE2001 and YMW16 models ranges between $0.97 - 1.74\,\mathrm{kpc}$, suggests that many exciting new discoveries may await the arrival of next-generation telescopes such as MeerKAT and the SKA, both of which will open a new window into this nearby, low-luminosity pulsar population.

3.5.3 Characteristic age

An additional comparison can be performed using the characteristic age distribution of the HTRU-S LowLat pulsars. As the characteristic age τ_c is derived from measurements of P and $\dot{P}$ (see Equation 1.11), only those pulsars for which these values are both well measured are considered in this analysis. Similarly, as τ_c becomes contaminated as a result of the recycling process, only unrecycled pulsars (here defined as those pulsars for which the surface magnetic field $B_{\mathrm{surf}} < 3.0 \times 10^{10}\,\mathrm{G}$ in order to remain consistent with the analysis performed by Ng et al. (2015)) are considered. These conditions leave a total of 46 HTRU-S LowLat pulsars and a background population of 753 known pulsars.

A KS test between these two distributions shows that they are not consistent with being drawn from the same population, to within a probability of $< 0.02\,\%$. This is also shown in Figure 3.18, which as with the distance distributions in Figure 3.16, shows both a histogram distribution and the CDF of the HTRU-S LowLat pulsars and previously known pulsars within the survey area. From both of these side-by-side comparisons, it is plain to see that the sample of 46 HTRU-S LowLat pulsars does indeed represent an older population of pulsars, with no unrecycled pulsar yet having a $\tau_c \leq 0.1\,\mathrm{Myr}$ (the typical definition of a 'young' pulsar). This reinforces the trend in the HTRU-S LowLat pulsars first noted by Ng et al. (2015), and stands in opposition to the earlier prediction of Bates et al. (2012) who, after similarly not discovering any young, unrecycled pulsars in the HTRU-S MedLat survey, predicted that such pulsars would likely be uncovered by HTRU-S LowLat due to its higher sensitivity.

While this result may still be attributable to the ambiguities of small-number statistics, it is notable that the lack of young pulsars is evident in the two portions of the survey processed both in this thesis and by Ng et al. (2015), which should express no relative bias with respect to the τ_c values of their individual set of newly-discovered pulsars. Continued timing of the remaining unrecycled and unsolved pulsars will assist in further cementing the reality of this result.

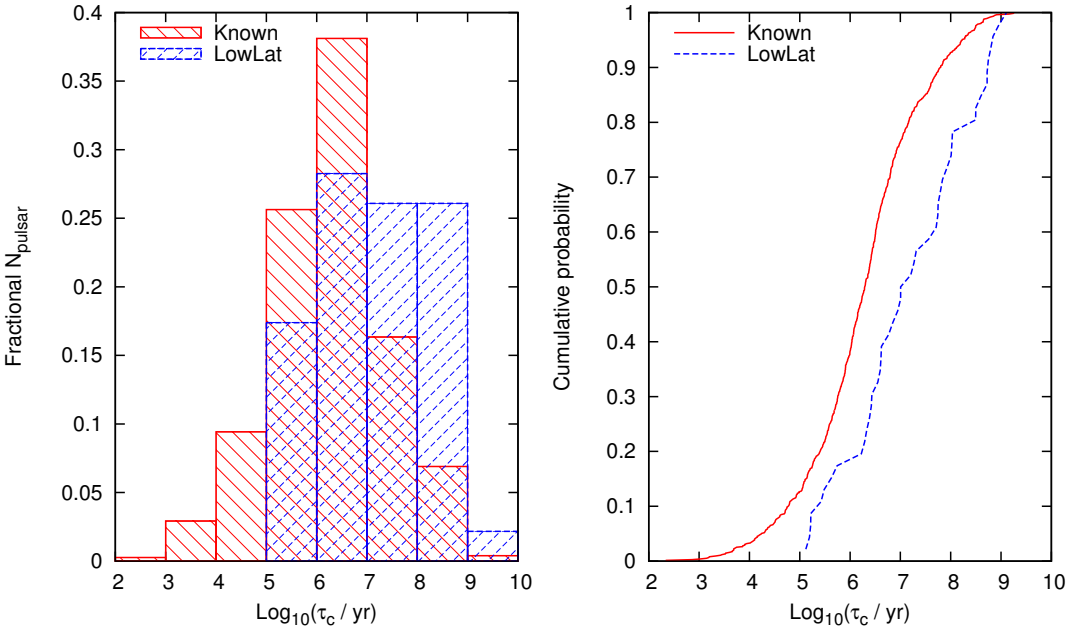

Figure 3.18: Characteristic age (τ_c) distributions of the 46 HTRU-S LowLat pulsars (blue) and 753 previously-known Galactic pulsars (red) with well-constrained values of P and $\dot{P}$. Shown on the left are the histograms of the τ_c distributions of each population, normalised by the number of pulsars in each distribution. Shown on the right are the corresponding CDFs of each τ_c distribution.

3.6 Evaluation of the survey yield

As noted in Section 3.1.4, the processing of the HTRU-S LowLat survey now stands at $\sim 94\,\%$. Therefore, it is now possible to conduct a full evaluation of the discovery yield and overall performance of the survey with respect to both earlier predictions and the earlier analysis carried out by Ng et al. (2015). Keith et al. (2010) estimated that 957 'normal' pulsars (defined for this analysis as pulsars with $P > 30\,\mathrm{ms}$ in order to maintain consistency with earlier analyses) should be detected by the HTRU-S LowLat survey, based upon simulations performed with the PSRPOP[22] software package (Lorimer et al., 2006a). Ng et al. (2015) later revised this estimate to 1020 normal pulsars, based on revised simulations using the PSRPOPPY[23] software package (Bates et al., 2014). As these two results are statistically consistent, the latter is adopted in order to maintain consistency with the earlier yield analysis in Ng et al. (2015). Rescaling this estimate to account for the small proportion of the survey yet to be processed and reviewed results in a final estimate of ~ 960 detected normal pulsars.

By comparison, as reported in Section 3.2, a total of 649 unique pulsars were re-detected in the processed $\sim 94\,\%$ of the HTRU-S LowLat survey, of which 631 are normal pulsars. This is in addition to the 58 normal pulsars reported by Ng et al. (2015) and the 34 normal pulsars reported in this thesis, giving a total of 723 normal pulsar detections. Evidently, this falls short of the projected ~ 960 detections by a factor of $\sim 25\,\%$. This result also stands in contrast to the earlier evaluation of Ng et al. (2015), who reported 485 normal pulsar detections from an expected $470 - 510$. The lower apparent detection rate in the $\sim 44\,\%$ of the survey data processed in this thesis is in part due to a common set of pulsars which were detected in both processed portions (as noted previously in Section 3.2, although this cannot fully account for the discrepancy between the predicted and actual number of detected normal pulsars.

Separate predictions were also produced for the MSP population (here defined as $P \leq 30\,\mathrm{ms}$ again in order to maintain consistency with earlier analyses), as these pulsars represent a distinct population which in turn is subject to different selection biases in a blind pulsar survey. PSRPOP and PSRPOPPY respectively predict 51 and 43 MSP detections for the HTRU-S LowLat survey region (Keith et al., 2010; Ng et al., 2015), while an in-depth study by Levin et al. (2013) predicts a higher MSP yield of 68. Taking the lower and upper limits of these estimates and rescaling to account for the $\sim 94\,\%$ completion of the survey processing gives a final estimate of $40 - 64$ detected MSPs. By comparison, only 18 of the re-detected pulsars outlined in Section 3.2 meet the $P \leq 30\,\mathrm{ms}$ criteria, along with 2 pulsars reported by Ng et al. (2015) and 6 additional pulsars reported in this thesis, giving a total of only 26 MSP detections from HTRU-S LowLat, a factor of $1.5 - 2.5$ lower than predicted.

Multiple reasons exist as to why our detections of both normal pulsars and MSPs have fallen below their initial predictions. With respect to the MSP population, Ng et al. (2015) and Eatough et al. (2013a) have already put forward a number of potential causes, including a limited understanding of the underlying Galactic MSP population

[22] http://psrpop.sourceforge.net
[23] https://github.com/samb8s/PsrPopPy

leading to inadequate model estimates, detectability limitations due to scatter broadening, and the inability of our segmented search technique to take advantage of the fully-coherent sensitivity of each 72-min observation. While only one of the HTRU-S LowLat MSP discoveries (namely PSR J1757-1854) was not initially discovered in the full-length observation (and thereby showing the strengths of our search pipeline), other pulsars such as PSRs J1802−2124 and J1141−6545 (see Section 3.2.2) which were detected much more favourably in shorter segments as a result of their short orbital periods and higher accelerations, may have been missed had they been too weak to be detected in the shorter integration times of each segment, or if they were observed at an orbital phase where the assumption of a constant acceleration was no longer applicable. Therefore, the implementation of a fully-coherent binary search remains an ongoing goal of the future reprocessing of this survey.

Additional factors exist which are likely to influence the lack of detections of both normal pulsars and MSPs. Intermittency, often a factor in longer-period pulsars (see e.g. Biggs, 1992), remains an unavoidable obstacle in blind pulsar surveys. That being said, the 72-min integration times of the HTRU-S LowLat survey have been able to partially mitigate this effect, with at least three intermittent pulsars, a nulling pulsar and one eclipsing pulsar (with one further eclipsing candidate) having been reported in this thesis. The influence of RFI also remains an ongoing problem, which although mitigated by our multiple RFI mitigation techniques, accounted for a significant number of the candidates reported by the pipeline. In particular, certain beams of the MB20 receiver would often experience extended spans of worsened interference, indicating potential hardware problems which multibeam RFI excision techniques would be unable to correct for. However, while RFI is likely to have contributed to a degraded survey sensitivity, it is difficult to quantify the precise degree of degradation.

Another problematic form of interference which is likely to have impacted the sensitivity of the survey is red noise. Figure 2.5 shows a typical example of the red noise content of a HTRU-S LowLat survey beam, with significant contamination present at the low frequency end of the Fourier spectrum. As highlighted by Lazarus et al. (2015), this increase in power is likely to mask the presence of longer-period pulsars in a Fourier-based search. Fourier searches also lose sensitivity due the fact that they are an incoherent search technique, and are only able to sum a limited number of harmonics, resulting in the loss of Fourier power. Lazarus et al. (2015) further demonstrated that in the case of the Pulsar Arecibo L-band Feed Array survey (PALFA; Cordes et al., 2006), a significant loss of sensitivity is experienced for pulsars with $P > 100\,\mathrm{ms}$, becoming especially noticeable for pulsars with $P > 1\,\mathrm{s}$, with approximately 35 % of simulated pulsars remaining undetected. One technique which may be able to counter these problems is that of the 'Fast Folding Algorithm' (FFA, Staelin, 1969). An in-depth analysis of the FFA makes up a significant portion of this thesis (see Chapter 5), and an implementation of the FFA will be applied to the HTRU-S LowLat survey as part of a future reprocessing.

Chapter 4

PSR J1757–1854: the most accelerated binary pulsar

This chapter is based on an article currently in submission to the Monthly Notices of the Royal Astronomical Society (Cameron et al., submitted). The contents have been modified only so far as to conform to the style and format of the remainder of this thesis. I am the lead author on this publication. My primary contributions include the initial discovery of PSR J1757−1854 via processing of the High Time Resolution Universe South Low Latitude (HTRU-S LowLat) survey, the coordination of the subsequent confirmation and timing campaigns, performing the data reduction and analysis involved in both solving and timing the pulsar, performing the acceleration search for the companion neutron star, and performing the timing simulations required to determine the measurement time scales of the relativistic parameters δ_θ and $\dot{x}_{\rm LT}$. I was also responsible for writing the published journal article, and I personally contributed a significant fraction of the required follow-up observing time with the Parkes, Effelsberg and Green Bank telescopes.

The full list of authors is:
A. D. Cameron, D. J. Champion, M. Kramer, M. Bailes, E. D. Barr, C. G. Bassa, S. Bhandari, N. D. R. Bhat., M. Burgay, S. Burke-Spolaor, R. P. Eatough, C. M. L. Flynn, P. C. C. Freire, A. Jameson, S. Johnston, R. Karuppusamy, M. J. Keith, L. Levin, D. R. Lorimer, A. G. Lyne, M. A. McLaughlin, C. Ng, E. Petroff, A. Possenti, A. Ridolfi, B. W. Stappers, W. van Straten, T. M. Tauris, C. Tiburzi and N. Wex.

Abstract

We report the discovery of PSR J1757−1854, a 21.5-ms pulsar in a highly-eccentric, 4.4-h orbit around a neutron star (NS) companion. PSR J1757−1854 exhibits some of the most extreme relativistic parameters of any known pulsar, including the strongest relativistic effects due to gravitational-wave (GW) damping, with a merger time of 76 Myr. Following a 1.6-yr timing campaign, we have measured five post-Keplerian (PK) parameters, yielding the two component masses ($m_{\rm p} = 1.3384(9)\,{\rm M}_\odot$ and $m_{\rm c} = 1.3946(9)\,{\rm M}_\odot$) plus three tests of general relativity (GR), which the theory passes. The large mass of the NS companion provides important clues regarding the binary formation of PSR J1757−1854. With simulations suggesting 3-σ measurements of both the contribution of Lense-Thirring precession to the rate of change of the semi-major

axis and the relativistic deformation of the orbit within $\sim 7-9$ years, PSR J1757−1854 stands out as a unique laboratory for new tests of gravitational theories.

Contents

4.1 Introduction

Since the discovery of the Hulse-Taylor pulsar (PSR B1913+16; Hulse & Taylor, 1975a), binary pulsars have played a critical role in providing key tests of GR and its alternatives. Even with the direct detection of GWs (Abbott et al., 2016) and the more recent direct observation of a double neutron star (DNS) merger (Abbott et al., 2017b), binary pulsars are still able to provide some of the most important gravity tests with strongly self-gravitating bodies, particularly in the quasi-stationary strong-field gravity regime (Wex, 2014). An example is the constraint on the leading-order GW emission in GR (as described by the quadrupole formula), for which the Double Pulsar (PSR J0737−3039; Burgay et al., 2003; Lyne et al., 2004) currently stands out as the most constraining system, surpassing LIGO by three orders of magnitude (Kramer et al., in prep.). PSR J0737−3039 currently offers five independent tests of GR (based on six PK parameters and the mass ratio), of which it passes the most stringent to within a measurement uncertainty of only 0.05 % (Kramer et al., 2006b; Breton et al., 2008). Other binary pulsars, such as the millisecond pulsar-white dwarf (MSP-WD) PSR J1738+0333, provide strong constraints on dipolar GW emission, a prediction of many alternative theories of gravity such as scalar-tensor theories (Freire et al., 2012).

Pulsar constraints on the nature of GWs, the limits of GR and on alternative gravitational theories are anticipated to provide both complementary and competitive tests against the most advanced ground-based GW detectors currently foreseen (Shao et al., 2017). However, this depends upon the discovery of additional relativistic systems capable of expanding the parameter space currently explored by binary pulsars. To this end, the HTRU-S LowLat pulsar survey (Keith et al., 2010; Ng et al., 2015), conducted using the Parkes 64-m radio telescope, was undertaken with the specific goal of discovering additional relativistic binary pulsars. This survey covers the inner

Galactic plane ($-80° < l < 30°$ and $|b| < 3.5°$) and is the region predicted to contain the highest number of relativistic binaries (Belczynski et al., 2002).

Here, we report the discovery of PSR J1757−1854, the first relativistic binary discovered in the HTRU-S LowLat survey. PSR J1757−1854 (see Figure 4.1) is a 21.5-ms pulsar in a 4.4-h orbit with an eccentricity of 0.61 and a NS companion, making the system a DNS. The compactness, high eccentricity and short orbital period of PSR J1757−1854 make it one of the most relativistic binary pulsars known, with the potential for even more rigorous constraints to be placed on GR and other gravitational theories.

4.2 Discovery

4.2.1 Candidate identification and confirmation

To search for binary pulsars, we employ the 'time-domain resampling' technique (see e.g. Middleditch & Kristian, 1984; Johnston & Kulkarni, 1991), which assumes that the binary motion can be modeled as a constant line-of-sight acceleration. For a circular orbit this assumption holds best when the quantity $r_\mathrm{b} = t_\mathrm{int}/P_\mathrm{b} \leq 0.1$ where t_int is the integration time of the observation and P_b is the orbital period (see e.g. Johnston & Kulkarni, 1991; Ng et al., 2015). Building on the technique of Eatough et al. (2013a), our 'partially-coherent segmented acceleration search' uses this principle to blindly search for pulsars in compact binary systems by progressively halving each observation into smaller time segments (as low as $t_\mathrm{int} = 537\,\mathrm{s}$) which are independently searched (to accelerations as high as $|a| = 1200\,\mathrm{m\,s^{-2}}$). This has the trade-off of increasing our sensitivity to shorter orbital periods while gradually reducing our sensitivity in flux density. Full details of the search are available in Ng et al. (2015).

PSR J1757−1854 was identified in the second 36-min half-length segment of a full 72-min observation recorded on MJD 56029, with an acceleration of $-32\,\mathrm{m\,s^{-2}}$ and a signal-to-noise ratio (S/N) of 13.3. The pulsar's signal was recoverable across the full observation to a S/N of 21.4, but with a significantly-changing acceleration (i.e. 'jerk'). Consequently, a time-domain acceleration search of the full-length observation only detected the pulsar at a reduced S/N of only 10.6, indicating that the segmented search greatly assisted in the discovery of this pulsar. At periastron, the pulsar reaches a maximum absolute acceleration of $\sim 684\,\mathrm{m\,s^{-2}}$, the highest of any known binary pulsar system.

4.2.2 Non-detection in the PMPS

The Parkes Multibeam Pulsar Survey (PMPS; Manchester et al., 2001) contains a beam coincident with the timed position of PSR J1757−1854 (see Table 4.2). However, neither acceleration searches using both time-domain resampling and matched filtering (Ransom et al., 2002) nor a fold using the ephemeris in Table 4.2 detected the pulsar in the PMPS data. Based upon the radiometer equation (see e.g. Lorimer, D. R. and Kramer, M., 2005) and the dispersive smearing introduced by the 3-MHz channel size

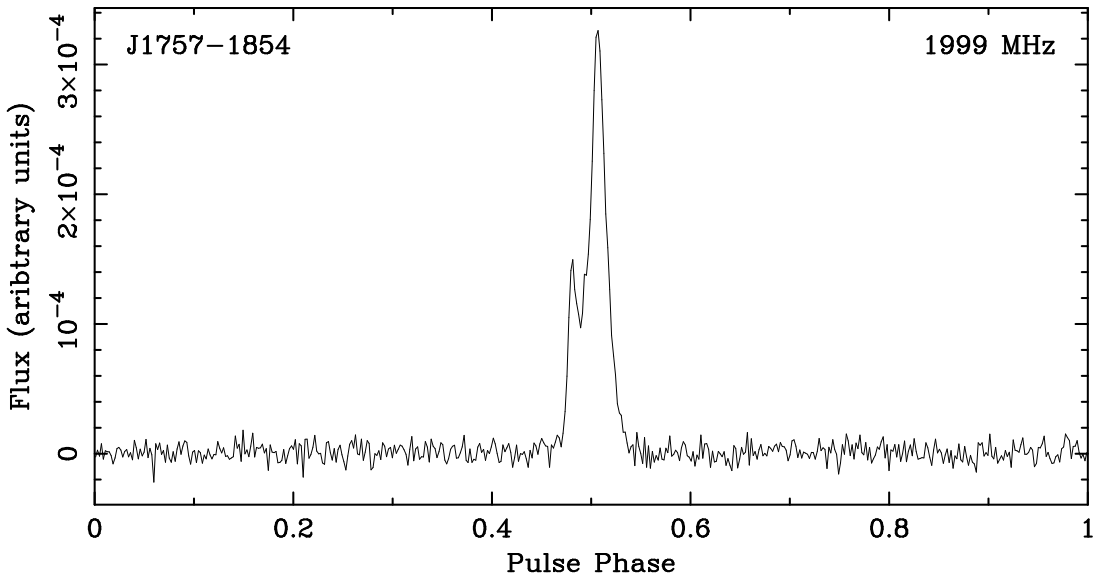

Figure 4.1: Pulse profile of PSR J1757−1854, observed with the Green Bank Telescope (GBT) on MJD 57857, integrated over approximately one full orbit.

of the PMPS, we expect a $S/N_{PMPS} \simeq 8$, rendering any detection of PSR J1757−1854 difficult. Additional factors such as geodetic precession may also play a role, but at present a precise cause cannot be determined.

4.3 Timing

4.3.1 Observations and data reduction

A summary of PSR J1757−1854's timing observations can be found in Table 4.1. Parkes (PKS) observations used the 21-cm Multibeam (MB20; Staveley-Smith et al., 1996) and H-OH receivers, in combination with the Berkeley Parkes Swinburne Recorder[1] (BPSR), the CASPER Parkes Swinburne Recorder[2] (CASPSR) and a Digital Filter Bank system (DFB4). Jodrell Bank (JBO) observations employed an L-Band receiver with a ROACH backend system (Bassa et al., 2016). Observations at Effelsberg (EFF) were performed with the 7-Beam receiver with a PSRIX backend (Lazarus et al., 2016) operating in both a folded and baseband recording mode (FOLD and BB respectively). Finally, observations with the Green Bank Telescope (GBT) were conducted using the L-Band, S-Band and Prime-Focus 800-MHz (PF1-800) receivers, all in combination with the Green Bank Ultimate Pulsar Processing Instrument (GUPPI; Ransom et al., 2009). All GBT and Effelsberg observations were designed to sample a full or significant fraction of the 4.4-h orbit.

Data reduction employed the DSPSR (van Straten & Bailes, 2011), PSRCHIVE (Hotan

[1]https://astronomy.swin.edu.au/pulsar/?topic=bpsr
[2]https://astronomy.swin.edu.au/pulsar/?topic=caspsr

Table 4.1: Telescope frontend and backend configurations, including the central frequency (f_c), bandwidth (B) of each combination and the number (n_{TOA}) and time span of the TOAs.

Receiver	Backend	f_c (B) (MHz)	n_{TOA}	Span (MJD)
PKS:				
MB20	BPSR	1382(400)	9	57405−57406
	CASPSR[a]	1382(400)	41	57734−57986
H-OH	DFB4	1369(256)	57	57553−57675
	CASPSR[a]	1382(400)	55	57596−57635
JBO:				
L-Band	ROACH[b]	1527(400)	422	57456−57958
EFF:				
7-Beam	FOLD	1360(240)	83	57573−57896
	BB[a]	1360(240)	84	57815−57986
GBT:				
PF1-800	GUPPI[a]	820(200)	25	57620−57621
L-Band	GUPPI[a,b]	1499(800)	731	57795−57950
S-Band	GUPPI[a,b]	1999(800)	1655	57627−57998

[a] Observations recorded with coherent de-dispersion.
[b] Δf split into 200 MHz sub-bands before TOA production.

et al., 2004), SIGPROC[3], PRESTO (Ransom, 2001), TEMPO[4] and TEMPO2 (Hobbs et al., 2006) software packages. During this process, the pulsar's dispersion measure (DM) appeared to vary as a function of orbital phase. This resulted from an inability of these software packages to correctly de-disperse across a large bandwidth during rapid orbital motion (cf. Ransom et al. 2004). To counteract this, Jodrell Bank and GBT (L-Band and S-Band) TOAs were produced from 200-MHz sub-bands.

4.3.2 Measured parameters and implications

The ephemeris of PSR J1757−1854, employing the DDH (Freire & Wex, 2010) binary model, is provided in Table 4.2. Based upon the spin parameters, we derive a characteristic age $\tau_c \simeq 130\,\mathrm{Myr}$ and a surface magnetic field $B_{\mathrm{surf}} \simeq 7.61 \times 10^9\,\mathrm{G}$, indicating that the pulsar has been partially recycled. Five PK parameters, including the rate of periastron advance $\dot{\omega}$, Einstein delay γ, orbital period derivative $\dot{P}_b$ and orthometric Shapiro parameters h_3 and ς, have been measured significantly. Using the DDGR model (Taylor, 1987; Taylor & Weisberg, 1989), which assumes the correctness of GR, we derive the total system mass $M = 2.73295(9)\,\mathrm{M}_\odot$ and the separate masses of the pulsar ($m_p = 1.3384(9)\,\mathrm{M}_\odot$) and its companion ($m_c = 1.3946(9)\,\mathrm{M}_\odot$). These masses, along with the high eccentricity and an implied second supernova (see Section 4.4) indicate that the system is a DNS. From m_p, m_c and the mass function we can further infer an inclination angle of $i = 84.0^{+0.4}_{-0.3}\,^\circ$ (or $96.0^{+0.3}_{-0.4}\,^\circ$, when accounting for the $i \leftrightarrow 180^\circ - i$ ambiguity of the mass function), i.e., the orbit appears to be close to edge-on.

Figure 4.2 shows the constraints on the NS masses derived from the measured PK parameters under the assumption of GR. By using the intersection of $\dot{\omega}$ and γ to fix the two NS masses, we can derive three new tests of GR from the remaining PK parameters. Based upon the $\dot{\omega}$-γ mass solution, GR predicts an orbital decay due to GW damping of $\dot{P}_b = -5.2747(6) \times 10^{-12}$, which the measured value of $\dot{P}_b$ agrees with to within a relative uncertainty of only 5 %. For ς and h_3, both observed values are within 1-σ agreement of their GR predicted values ($0.92^{+0.040}_{-0.025}$ and $5.37^{+0.72}_{-0.40}\,\mu$s respectively), indicating that GR passes all three tests.

PSR J1757−1854 exceeds many of the relativistic qualities of previous binary pulsars, setting records (among others) for the closest binary separation at periastron ($0.749\,\mathrm{R}_\odot$) and the highest relative velocity ($1060\,\mathrm{km\,s^{-1}}$) at periastron. It also shows the strongest effects of GW damping yet seen in a relativistic pulsar binary, displaying the highest value of $\dot{P}_b$ as well as the highest value of $\dot{P}_b/P_b = -3.33 \times 10^{-16}\,\mathrm{s^{-1}}$, the leading-order term in the cumulative shift in periastron time (see e.g. Taylor & Weisberg, 1982). This results in an inferred merger time of 76 Myr. Hence, PSR J1757−1854 can be seen to probe a relativistic parameter space not yet explored by previous binary pulsars.

[3] http://sigproc.sourceforge.net
[4] http://tempo.sourceforge.net

Table 4.2: Ephemeris of PSR J1757−1854. Numbers in parentheses represent 1-σ uncertainties, with TOA errors re-weighted such that the reduced χ^2 went from 1.7 to 1.0. DM distances are derived from the NE2001 (Cordes & Lazio, 2002) and YMW16 (Yao et al., 2017) models.

Right ascension, α (J2000)	17:57:03.78438(6)
Declination, δ (J2000)	−18:54:03.376(7)
Spin period, P (ms)	21.497231890027(7)
Spin period derivative, $\dot{P}$ (10^{-18})	2.6303(7)
Timing epoch (MJD)	57701
Dispersion measure, DM ($\mathrm{pc\,cm^{-3}}$)	378.203(2)
Binary model	DDH
Orbital period, P_b (d)	0.18353783587(5)
Eccentricity, e	0.6058142(10)
Projected semi-major axis, x (lt-s)	2.237805(5)
Epoch of periastron, T_0 (MJD)	57700.92599420(5)
Longitude of periastron, ω (°)	279.3409(4)
Rate of periastron advance, $\dot{\omega}$ ($^\circ\,\mathrm{yr^{-1}}$)	10.3651(2)
Einstein delay, γ (ms)	3.587(12)
Orbital period derivative, $\dot{P}_\mathrm{b}$ (10^{-12})	−5.3(2)
Orthometric amplitude, h_3 (μs)	4.6(7)
Orthometric ratio, ς	0.90(3)
Mass function, f ($\mathrm{M_\odot}$)	0.35718891(2)
Total system mass, M ($\mathrm{M_\odot}$)	2.73295(9)[a]
Pulsar mass, m_p ($\mathrm{M_\odot}$)	1.3384(9)[a]
Companion mass, m_c ($\mathrm{M_\odot}$)	1.3946(9)[a]
Inclination angle, i (°)	$84.0^{+0.4}_{-0.3}$ or $96.0^{+0.3}_{-0.4}$ [a]
Flux density at 1.4 GHz, S_{1400} (mJy)	0.25(4)
DM distance, d (kpc)	7.4 (NE2001)
	19.6 (YMW16)
Surface magnetic field, B_surf (10^9 G)	7.61
Characteristic age, τ_c (Myr)	130
Spin-down luminosity, $\dot{E}$ ($10^{30}\,\mathrm{ergs\,s^{-1}}$)	10500
Time units	TCB
Solar system ephemeris	DE421
RMS residual (μs)	36

[a] Parameters derived according to the DDGR model.

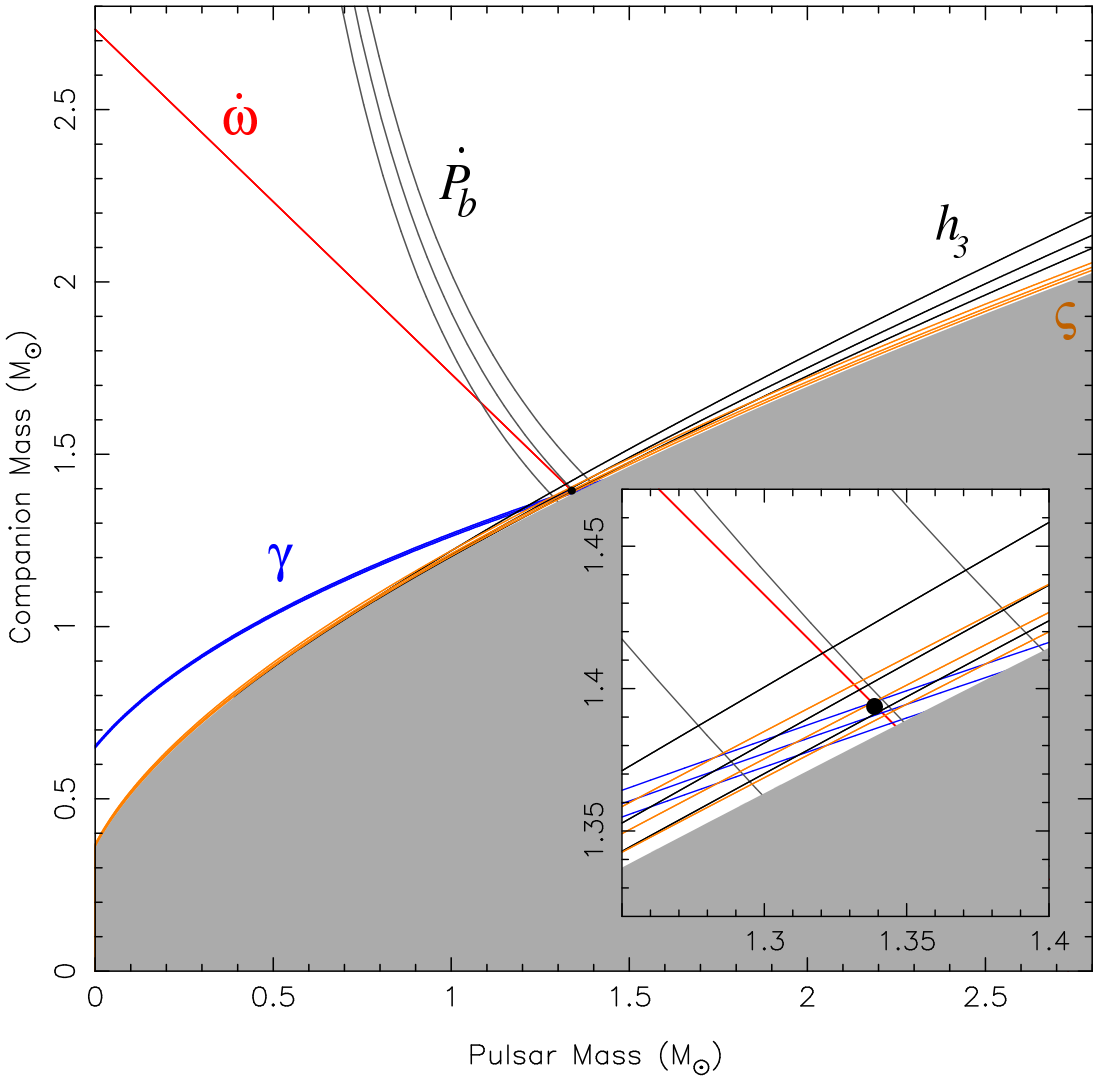

Figure 4.2: Mass-mass diagram for PSR J1757−1854. Shown are the mass constraints imposed under GR by each PK parameter, along with their 1-σ error bars. A zoomed view of the region of intersection is shown in the inset, with the black dot indicating the DDGR masses. The grey region is excluded by orbital geometry.

4.3.3 Searches for the companion neutron star

All GBT observations were recorded in coherently de-dispersed search mode, with two methods used to search for pulsations from the companion NS. The first method involved breaking each de-dispersed time series into $\sim$ 30-min segments, before performing a matched-filter acceleration search using the PRESTO program ACCELSEARCH with a filter width of $z_{\rm max} = 50$ (where z is the number of Fourier bins drifted by an accelerating pulsar). The second method (described in Martinez et al. 2015) involved resampling each time series in order to deconvolve the orbital motion of the companion NS as anticipated from the measured values of $m_{\rm c}$ and $m_{\rm p}$, before applying a PRESTO-based periodicity search. Neither method detected pulsations from the companion. As precession may move the beam of the companion into the line-of-sight in the future, we will continue to record search-mode data so as to repeat these studies regularly.

4.4 Evolutionary history

PSR J1757−1854 is remarkable given its combination of a short orbital period, a large eccentricity, a relatively massive young NS companion (more massive than the recycled pulsar, a property shared with only one other published DNS system, PSR B1534+12, Stairs et al. 2002), and a fast spinning recycled pulsar. The fast spin is expected for such a short orbital period DNS system, since in tight systems the recycling of the first-born NS is most efficient (see Case BB mass transfer modeling in Tauris et al., 2015, 2017).

Both the large eccentricity and the relatively massive young NS hint that a large kick is likely to have been imparted on the young NS at birth; see e.g. the mass–kick correlation suggested by Tauris et al. (2017). Indeed the two DNS systems B1913+16 and B1534+12, which also have relatively massive young NS companions, were shown to have experienced kicks of $\sim 200 - 400\,{\rm km\,s^{-1}}$.

To test this hypothesis for PSR J1757−1854, we performed Monte Carlo simulations of the kinematic effects of the second supernova following the method outlined in Tauris et al. (2017). As expected, we find that a large kick is most likely at work for this system (the broad distribution of solutions peaks at a value near $400\,{\rm km\,s^{-1}}$). For the mass of the exploding star, we find solutions from less than $2\,{\rm M_\odot}$ and up to our maximum input limit of $7\,{\rm M_\odot}$. However, the distribution peaks at the smallest value, supporting the idea of an ultra-stripped star exploding (Tauris et al., 2013, 2015).

4.5 Future prospects

The simulations described in Section 4.4 also produce a systemic 3D velocity distribution for PSR J1757−1854, which peaks at a value of the order $200\,{\rm km\,s^{-1}}$. Assuming a representative velocity in the plane of the sky of $150\,{\rm km\,s^{-1}}$ and the NE2001 DM distance of 7.4-kpc (see Table 4.2) produces a predicted proper motion of $4.3\,{\rm mas\,yr^{-1}}$. Furthermore, for the recycled pulsar we also obtain a distribution of misalignment an-

gles between the spin vector of the pulsar and the orbital angular momentum, with a median value of $\sim 25°$.

Consequentially, PSR J1757−1854 is also expected to allow for future measurements of Lense-Thirring precession. Due to the large estimated distance to the pulsar, which suggests that we will not be able to correct for extrinsic acceleration effects sufficiently, we expect to be unable to employ the $\dot{\omega}$-$\dot{P}_{\rm b}$ measurement technique used on PSR J0737−3039 (Kehl et al., 2016). However, the likelihood of a significant misalignment angle allows an alternate test using the contribution of Lense-Thirring precession to the rate of change of the projected semi-major axis, given by

$$\dot{x}_{\rm LT} = x \cot i \left(\frac{{\rm d}i}{{\rm d}t}\right)_{\rm LT}, \tag{4.1}$$

where $({\rm d}i/{\rm d}t)_{\rm LT}$ is given by Equation 3.27 in Damour & Taylor (1992). Adopting a typically assumed pulsar moment of inertia of $I = 1.2 \times 10^{45}\,{\rm g\,cm^2}$ (Lattimer & Schutz, 2005) and neglecting the likely slower-spinning companion NS, we calculate that $|\dot{x}_{\rm LT}|$ could be as large as $1.9 \times 10^{-14}\,{\rm lt\text{-}s\,s^{-1}}$. Based upon the continuation of our current timing setup, and assuming the addition of MeerKAT observations consisting of one orbit per month commencing in mid-2018, we predict a future measurement of $\dot{x}_{\rm LT}$ to within $3\,\sigma$ in $\sim 8-9$ years. The corresponding (geodetic) spin precession of the pulsar (expected to be $\sim 3.1\,^\circ\,{\rm yr^{-1}}$) is expected to lead to changes in the pulse profile and polarisation, which may allow a determination of the pulsar's spin orientation (see e.g. Kramer, 1998).

PSR J1757−1854 is also an ideal system for measuring the PK parameter δ_θ, which describes the relativistic deformation of the elliptical orbit (Damour & Deruelle, 1985). To date, δ_θ has been measured only in PSR B1913+16 (Weisberg & Huang, 2016) and PSR J0737−3039 (Kramer et al., in prep.), in both cases with low significance. As described in Damour & Deruelle (1986), the timing residual contribution of δ_θ can be characterised by

$$\Delta_{\delta_\theta} \simeq -\delta_\theta \frac{e^2}{\sqrt{1-e^2}}\, x \cos\omega \sin u, \tag{4.2}$$

where u is the eccentric anomaly. The strong dependence of Δ_{δ_θ} on e implies that PSR J1757−1854 (along with other high-e relativistic binaries such as PSRs B1913+16 and B2127+11C) will show the strongest timing effects due to δ_θ. However, Equation 4.2 also indicates that a measurement of δ_θ requires a significant change in ω in order to separate the residual effect of δ_θ from that of γ (for which $\Delta_\gamma = \gamma \sin u$). With its high $\dot{\omega} \simeq 10.37\,^\circ\,{\rm yr^{-1}}$, PSR J1757−1854 is therefore uniquely positioned to allow for a future measurement of δ_θ within a comparatively-short timeframe. Based on the same timing considerations as outlined for $\dot{x}_{\rm LT}$, we predict a 3-σ measurement of δ_θ will be possible within $\sim 7-8$ yr.

Finally, as noted in Section 4.3.2, PSR J1757−1854 has the largest observed $\dot{P}_{\rm b}$ and the largest shift in periastron time due to GW emission of any known binary pulsar. This promises a further high-precision test of GR's quadrupole formula for GW damping, as conducted previously with PSR B1913+16 (Weisberg & Huang, 2016) and PSR J0737−3039 (Kramer et al., 2006b; Kramer, 2016). Timing simulations indicate

a test precision of $< 1\,\%$ in only ~ 5 years. Taking the Galactic potential of McMillan (2017) and our previous systemic velocity estimates, we anticipate that our current uncertainty in the distance to PSR J1757−1854 will limit this test to within a few tenths of a percent.

Acknowledgements

The Parkes Observatory is part of the Australia Telescope National Facility which is funded by the Australian Government for operation as a National Facility managed by CSIRO. The Green Bank Observatory is a facility of the National Science Foundation operated under cooperative agreement by Associated Universities, Inc.. Pulsar research at the Jodrell Bank Centre for Astrophysics and the observations using the Lovell Telescope are supported by a consolidated grant from the STFC in the UK. This work is also based on observations with the 100-m telescope of the Max-Planck-Institut für Radioastronomie at Effelsberg. This work is supported by the ARC Centres of Excellence CE110001020 (CAASTRO) and CE170100004 (OzGrav). Survey processing was conducted in association with CAASTRO at the Australian National Computational Infrastructure high-performance computing centre at the Australian National University. The authors wish to thank Marina Berezina, Eleni Graikou, Alex Kraus and Laura Spitler for their assistance with observations at Effelsberg, along with Natalia Lewandowska and Ryan Lynch for their assistance with observations at the GBT. We also thank West Virginia University for its financial support of GBT operations, which enabled some of the observations for this project. AC acknowledges the support of both the International Max Planck Research School for Astronomy and Astrophysics at the Universities of Bonn and Cologne, and the Bonn-Cologne Graduate School of Physics and Astronomy. PCCF and AR gratefully acknowledge financial support by the European Research Council for the ERC Starting grant BEACON under contract No. 279702, and continued support from the Max Planck Society. MK, RK and RPE gratefully acknowledge support from ERC Synergy Grant 'BlackHoleCam' Grant Agreement Number 610058. MAM was supported by NSF award number AST-1517003. DRL was supported by NSF award number OIA-1458952.

Chapter 5

An investigation of pulsar searching techniques with the Fast Folding Algorithm

---

This chapter is based on an article published previously in the Monthly Notices of the Royal Astronomical Society (Cameron et al., 2017). The contents have been modified only so far as to conform to the style and format of the remainder of this thesis. I am the lead author on his publication, and my primary contributions include the development and testing of the software package FFANCY, along with the design, execution and analysis of all tests conducted on both real and simulated data. I was also responsible for writing the published journal article.

The full list of authors is:
A. D. Cameron, E. D. Barr, D. J. Champion, M. Kramer and W. W. Zhu.

Abstract

Here we present an in-depth study of the behaviour of the Fast Folding Algorithm (FFA), an alternative pulsar searching technique to the Fast Fourier Transform (FFT). Weaknesses in the FFT, including a susceptibility to red noise, leave it insensitive to pulsars with long rotational periods ($P > 1\,\mathrm{s}$). This sensitivity gap has the potential to bias our understanding of the period distribution of the pulsar population. The FFA, a time-domain based pulsar searching technique, has the potential to overcome some of these biases. Modern distributed-computing frameworks now allow for the application of this algorithm to all-sky blind pulsar surveys for the first time. However, many aspects of the behaviour of this search technique remain poorly understood, including its responsiveness to variations in pulse shape and the presence of red noise. Using a custom CPU-based implementation of the FFA, FFANCY, we have conducted an in-depth study into the behaviour of the FFA in both an ideal, white noise regime as well as a trial on observational data from the High Time Resolution Universe South Low Latitude (HTRU-S LowLat) pulsar survey, including a comparison to the behaviour of the FFT. We are able to both confirm and expand upon earlier studies that demonstrate the ability of the FFA to outperform the FFT under ideal white noise conditions, and demonstrate a significant improvement in sensitivity to long-period pulsars in real

observational data through the use of the FFA.

Contents

5.1 Introduction

The FFT is one of the most efficient and widely used techniques in pulsar searching (Lorimer, D. R. and Kramer, M., 2005). However, despite the success of this algorithm in many large-scale pulsar search campaigns, it is not without its limitations. In particular, FFT-based search pipelines remain vulnerable to the presence of red noise, which can significantly limit their sensitivity to long-period pulsars (defined in this paper as pulsars with a rotational period $P > 1\,\mathrm{s}$). A notable demonstration of these limitations was made by Lazarus et al. (2015) as part of an investigation into possible discrepancies between the theoretical and actual sensitivities of the Pulsar Arecibo L-band Feed Array survey (PALFA; Cordes et al., 2006). Through a process of attempting to recover synthetic pulsar profiles that had been injected into real observational data, it was demonstrated that significant losses in sensitivity occurred for pulsars with periods longer than $P \simeq 100\,\mathrm{ms}$. This degradation in sensitivity was seen to increase with increasing rotational period, resulting in the loss of approximately 35 % of the pulsars which PALFA may otherwise have detected. This effect has the potential to introduce a strong selection bias in our current searching pipelines, skewing our knowledge of the underlying source distribution.

An alternative approach to pulsar searching is to instead search directly in the time domain by folding an observational time series and examining the resulting folded profiles. The FFA (Staelin, 1969) is a computationally efficient means of folding multiple

trial periods. This efficiency is achieved through the removing of redundant computational steps in the folding process and by storing the results of these steps for later recall as needed.

The FFA presents a number of key advantages in searching for pulsars in the long-period regime. For example, the operational speed of the FFA increases when folding over longer periods, as the number of addition operations required during the folding process is of the order $O(N \log_2(N/P_0))$, where N is the number of samples in the original data set and P_0 is the base trial period being folded over (in units of samples). Thus for fixed N, the number of addition operations decreases as P_0 increases, giving the FFA a performance boost at longer trial periods. Furthermore, although it is not immune to red noise, the FFA is able to produce a result that is fully coherent in phase, unlike the FFT which is normally only able to incoherently sum a limited number of harmonics (Lazarus et al., 2015), typically 16 or 32 harmonics depending upon the specific FFT implementation. This results in some of the pulsar's Fourier power remaining at unsummed harmonic frequencies, reducing its overall sensitivity. Therefore, the FFA may present a viable solution for recovering some of the sensitivity previously lost in the long-period regime.

Detailed research into the properties of the FFA was previously conducted by Kondratiev et al. (2009). Through the use of a custom implementation of the FFA, FFASEARCH[1], a comparison of the performance of both the FFT and FFA was produced. This comparison was conducted both from an analytical standpoint, comparing the theoretical sensitivity of each technique, as well as from an experimental standpoint, through a simulation performed over a range of artificial pulsars created using the SIGPROC[2] program FAKE. These artificial pulsars covered a range of periods P between 2 and 14 s and duty cycles (δ) between 0.1 and 5 %, with the total per-pulse energy kept consistent for each pulsar trial. The results of both the theoretical and experimental comparisons clearly demonstrate that the in the narrow duty cycle regime ($\delta < 1\,\%$), the FFA displays a much greater sensitivity than the FFT to pulsars with periods longer than ~ 2 s, and that this remains the case for larger values of δ at even longer periods. This further builds the case for the FFA as a useful searching tool in the long-period pulsar regime.

However, unlike the FFT, to date the FFA has seen relatively little use in large-scale pulsar searches. Notable examples of its use include the discovery of PSR J2018+2839 (Craft et al., 1968), the investigation of quiescent RRAT radio emission through the folding of time series around the known period of existing RRATs (Losovsky & Dumsky, 2014), the discovery of a 7.7 s pulsar in the Parkes Multibeam Pulsar Survey (PMPS; Faulkner et al., 2004; Lorimer et al., 2006a) and a search for pulsed radio emission from the X-ray pulsar XTE J0103−728 (Crawford et al., 2009). This limited usage is primarily due to the fact that despite its inherent efficiency over other, simpler folding techniques, it has remained prohibitively computationally expensive. However, as computational power continues to increase, these concerns are gradually becoming

[1] http://astro.wvu.edu/projects/xdins
[2] https://github.com/SixByNine/sigproc

less significant. Also, the FFA is highly parallelisable, making it suitable for application to a parallel processing framework of general-purpose, many-core accelerators, allowing for further increases in performance.

Of course, the FFA is not without its own set of challenges to overcome. Chief amongst these is that unlike the FFT, which produces a power spectrum and the interpretation of which is well understood, the FFA produces a series of folded pulse profiles. Depending on the precise configuration of the FFA, these folded profiles can number in excess of several million per dispersion trial. This necessitates the development of algorithms which can evaluate the likelihood of a given folded profile representing the detection of a pulsar via a representative score or algorithm. These algorithms must themselves also be computationally efficient, as they must be applied to every single folded profile produced by the FFA, and their behaviour must be well understood in terms of their responsiveness to different pulse shapes, duty cycles, and other related parameters. The grouping of the resulting scores into appropriate lists of potential pulsar candidates must also be dealt with. Finally, the response of the FFA to the presence of red noise as well as other forms of radio frequency interference (RFI), and the degree to which this influence can be mitigated, remains to be investigated.

This challenge of pulse profile evaluation is in some ways not dissimilar to the problems facing another time-domain pulsar searching technique, the single-pulse search. This technique attempts to detect the bright individual pulses of pulsars and other radio transients (such as RRATs and fast radio bursts) through the analysis of de-dispersed time series. The basic modern technique, as presented by Cordes & McLaughlin (2003), involves the identification of significant outlying data points in a given time series, with matched-filtering used in order to tackle single pulses of varying width, with the majority of continuing single-pulse search efforts (for recent work see e.g. Burke-Spolaor et al., 2011; Devine et al., 2016; Adámek & Armour, 2016) building upon this foundation. Elements of these existing time-domain based approaches may be able to be utilised in developing profile evaluation algorithms for the FFA.

In this paper, we present the results of a new investigation into the behaviour of the FFA, building upon the work conducted by Kondratiev et al. (2009). This includes an analysis of the performance and robustness of multiple algorithms in evaluating the results of our own implementation of the FFA against a theoretical ideal FFA implementation and both an ideal and actual FFT implementation. Our investigation also includes the response of both the FFA and FFT to red noise contamination. The focus of this paper is on the computational correctness, robustness and response of the algorithms used, rather than the optimisation of their implementation. The question of designing and producing a computationally efficient implementation of the FFA and its associated evaluation algorithms (likely with the use of parallel processing) will be discussed in a future publication.

The structure of this paper is as follows: Section 5.2 outlines the mathematical theory of the FFA and our chosen algorithms, and describes the implementation of the FFA used in this study. Section 5.3 then explores the behaviour and response of each profile evaluation algorithm under a variety of controlled conditions. Section 5.4 presents a demonstration of the FFA using real-world observational data sets and explores re-

sponses of the FFA to the presence of red noise and other RFI. A brief discussion and conclusion then follow in Sections 5.5 and 5.6, respectively.

5.2 Mathematical background and implementation

As the majority of the results presented in this paper rely upon the specific details of each of the algorithms chosen for testing, as well as their specific implementation, this section will first outline the necessary background information.

5.2.1 The Fast Folding Algorithm

The full details and background of the FFA are laid out in Staelin (1969), which also includes a schematic of the algorithm's operation. Supplementary information is also available in Lovelace et al. (1969), Burns & Clark (1969) and Lorimer, D. R. and Kramer, M. (2005). Provided here is a brief outline of the fundamental aspects and behaviour of the FFA.

Consider a data set which has a length of N samples (e.g. in the case of pulsar analysis, a de-dispersed time series). A single execution of the FFA conducts a periodicity search over this data set using a base period of P_0 samples (which can be converted into units of time by multiplying by the relevant sampling interval t_{samp}). The FFA does this by breaking the data set down into segments that are P_0 samples long. Simply adding these segments together would result in a single folded profile with a period of P_0 samples, however, by applying relative offsets to each of these segments before adding them together, and by storing redundant operational results, the FFA is able to efficiently fold N/P_0 folded profiles in a single execution. These folded profiles correspond to a range of trial periods between the base period P_0 and $P_0 + 1$ inclusive, in increments of

$$\Delta P = \frac{P_0}{N - P_0} \tag{5.1}$$

samples. Therefore, the trial period P_i for any given folded profile can be given by

$$P_i = (P_0 + \frac{P_0}{N - P_0} i) \tag{5.2}$$

where $0 \leq i < (N/P_0)$ and i is an integer. By conducting multiple FFA executions for differing values of P_0, a large range of periods can be searched.

The most efficient implementation of the FFA requires that the ratio N/P_0 be equal to some power of two, that is, $\log_2(N/P_0)$ must be an integer. In order to test a wide range of arbitrary periods which do not necessarily meet this requirement, it is therefore necessary to either pad or trim the original data set of N samples (producing some new data set of length N_* samples) such that the correct relationship is maintained (i.e. $\log_2(N_*/P_0)$ is an integer). In order to preserve as much of the original data set as possible, we have chosen in our implementation to only ever increase the value of N such that $N_* \geq N$, using zero values as extra data elements so as not to introduce any additional noise into the data set. As this transition from observational data to zeroes

could potentially cause an artificial jump in the baseline of the folded profiles, a small amount of observational data at the end of the observation is also set to zero such that the length of the remaining original data set is equal to an integer multiple of P_0 for each execution of the FFA.

5.2.2 Profile evaluation algorithms

In order to evaluate the folded profiles produced by the FFA in a regular and efficient manner, we have developed multiple profile evaluation algorithms to be applied to each individual folded profile. These algorithms are able to break down a folded profile into a simple numerical score, with the aim that this score should in some way positively correlate to a profile's probability of representing a pulsar detection. These algorithm scores can then be plotted as a function of period to form a periodogram, and can be further analysed in the process of candidate selection. As previously mentioned, a critical property of any algorithm used for profile evaluation is its speed, as it will need to run over every single folded profile produced by the FFA. Therefore, while potentially 'ideal' algorithms can be imagined which can account for every single pulse profile scenario, some simplifications will be required in the algorithms chosen for implementation in order to retain a lower computational expense.

Although many algorithms were initially tested during the early research stages of this project, only the following two were selected for rigorous testing, due to the significantly higher sensitivities and robustness demonstrated by each during preliminary testing, as well as their ability to compute within a reasonable CPU time. Both algorithms work under the assumption that, aside from the presence of any pulsar in the data, the profiles to be evaluated contain normally-distributed noise. Each algorithm is designed to produce an approximation of the time-domain profile signal-to-noise ratio (S/N) as its 'score', using one of two different approaches. It should be noted that these measures of S/N are produced on a profile-by-profile basis, and that they do not represent a measure of the overall significance of a detected signal (a quantity which is dependent on the total number of evaluated profiles). The robustness of each algorithm to variations in the pulse profile is further explored in Section 5.3.

5.2.2.1 Algorithm 1: A boxcar matched-filter with median absolute deviation normalisation

Algorithm 1 employs the use of a series of scrolling boxcar matched-filters of the same style as described by Cordes & McLaughlin (2003) in an attempt to capture all of the pulse profile power within a single bin, while simultaneously capturing as little off-pulse noise as possible. Before this step however, the algorithm attempts to normalise each folded profile (reducing the off-pulse baseline of the profile to 0 and reducing the profile standard deviation σ to 1) so as to assist in later calculations. This normalisation is performed using a statistical quantity known as the median absolute deviation (MAD), which is defined for a finite set of values $x_1, x_2, \ldots x_n$ as

$$\mathrm{MAD} = \mathrm{median}(|x_i - \mathrm{median}(\vec{x})|). \tag{5.3}$$

That is, it represents the median of the absolute deviations of each value from the median of the entire data set. For large, normally distributed data sets, MAD is related to the standard deviation σ by

$$\sigma = K \cdot \mathrm{MAD}, \tag{5.4}$$

where $K \approx 1.4826$. However, unlike σ, MAD is a much more robust statistic as it remains more resilient to the presence of outliers in the data, due to the fact that it is based on the median of the data set rather than the mean. Therefore, so long as the pulse contained in a folded profile is narrow (an appropriate approximation in the case of the majority of long-period pulsars (Taylor et al., 1993), although exceptions do exist), MAD can be used to quickly normalise a folded profile as if it contained no pulse, as the 'outlying' data points of the pulse are, to a good approximation, ignored. MAD normalisation is hence performed by first subtracting the median from the folded profile (so as to reduce the baseline to 0), then by dividing all values by $\mathrm{MAD} \cdot K$ (so as to give unity variance).

Once a folded profile has been normalised in this manner, the value of any individual bin can be taken as its S/N. However, as most pulse profiles are wider than a single bin, successively larger boxcar matched-filters (up to some defined maximum filter width) are applied to the profile at each bin position in order to rebin the data at different pulse widths. In our chosen implementation, we use matched-filters at sizes of 2^n samples, where $n \geq 0$ is an integer, with the largest filter chosen as the first filter size to exceed $\delta = 20\,\%$. Normalisation is maintained by dividing each newly rebinned value by the square root of the width of the applied matched-filter. If a pulse is present in the profile, it should produce a maximum signal at the filter closest to its true pulse width, capturing as much pulse and as little noise as possible. The maximum value from all of these rebinned profiles is taken as the algorithm score, A_1, for that particular profile. An example of the response of Algorithm 1 may be found in Figure 5.1.

5.2.2.2 Algorithm 2: A boxcar matched-filter with an off-pulse window

Algorithm 2 essentially borrows its technique from the work performed by Kondratiev et al. (2009). The matched-filtering technique as described by Cordes & McLaughlin (2003) is also applied here, using the same set of filter sizes as Algorithm 1, but unlike Algorithm 1 the matched-filtering is applied first, without applying any normalisation beforehand. After the application of the matched-filter, the maximum value in the profile, I_{max}, is then identified. An exclusion window corresponding to 20 % of the profile width is then centered over the position of I_{max} on the profile, removing the 'on-pulse' data values from further consideration. The average value and standard deviation of the profile, I_{av} and σ are then calculated based on the remaining 80 % of the profile, the 'off-pulse' component. The S/N A is then given by

$$A = (I_{\mathrm{max}} - I_{\mathrm{av}})/\sigma \tag{5.5}$$

The maximum value of A over all of the matched-filters for a particular folded profile is then selected as the final algorithm score, A_2. An example of the response of Algorithm 2 may be found in Figure 5.1.

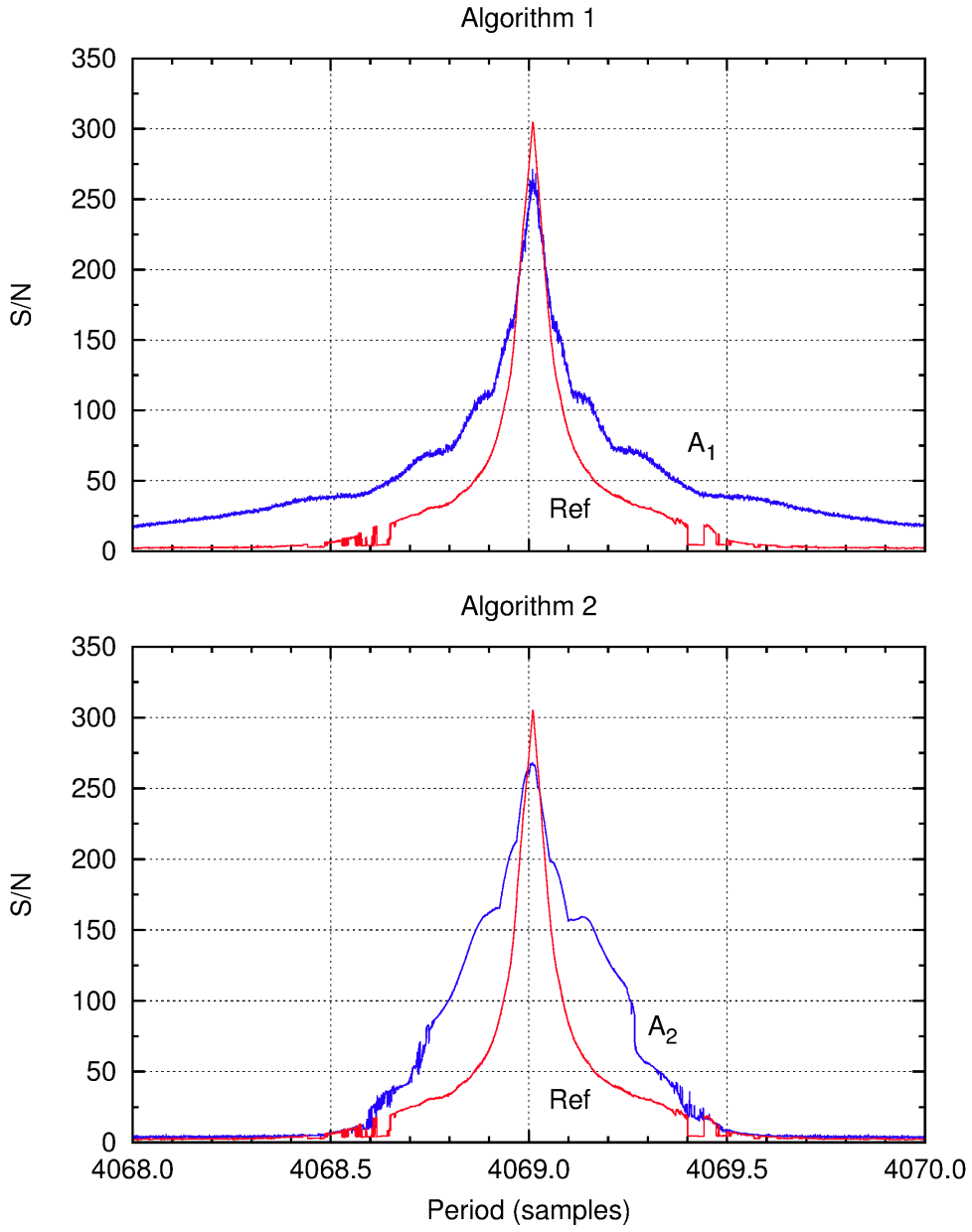

Figure 5.1: Zoomed-in view of a demonstration periodogram response for Algorithms 1 and 2 for a simulated pulsar with a top-hat pulse profile against a background of white noise. The pulsar has a period of approximately 4069 samples and a duty cycle $\delta = 1.0\,\%$. The 'bumps' in each curve indicate points where a new matched-filter gives a stronger algorithm response. The reference curve (marked 'Ref') indicates the response of a secondary version of Algorithm 2 which uses a pre-specified matched-filter in its evaluation. This filter was selected to optimally match the precise width of the top-hat pulsar, which in this case is 40 samples wide.

5.2.3 Software

5.2.3.1 FFANCY

A core part of the work of this project involved the development and testing of our own custom CPU-based implementation of the FFA, dubbed FFANCY[3]. Written in C, FFANCY was designed as a testbed program to allow for a full investigation of the FFA's behaviour. In its current version, it is capable of either generating its own simple internal data sets or reading an externally generated de-dispersed time series, before conducting the FFA over a period search range specified in units of samples. FFANCY is presently capable of reading both 8-bit unsigned-integer time series as produced by the SIGPROC pulsar software package, or 32-bit float time series as produced by the PRESTO[4] (Ransom, 2001) pulsar software package. In addition to the standard periodogram output of algorithm scores against trial period values, FFANCY is also capable of producing multiple output streams for use in testing, including the full suite of folded profiles produced by a full-scale FFA execution as well as de-reddened copies of the original input time series. FFANCY exports a simple command line interface that allows for the selection of period ranges, algorithms, etc. at runtime. It also employs a modular, extensible design that simplifies the addition and testing of new algorithms.

While the implementation of the FFA at the program's core is essentially the same as the original algorithm proposed by Staelin (1969), some additional features have also been added in order to optimise performance during testing. These include the ability to pre-downsample the data before execution of the FFA in order to increase the speed of a search by reducing the number of samples, as well as an automatic downsampling routine whereby a search conducted with a lowest trial period of P samples will automatically downsample the data set by a factor of 2 every time a period of $2^n \cdot P$ is reached, where n is an integer. A de-reddening option (which employs a dynamic running median filter) can also be selected at runtime. By default, the size of the filtering window used in the de-reddening is initially set to twice the maximum period to be searched or four times the lowest period to be searched, whichever is smaller. Alternatively, the user is able to manually specify their own window size at runtime. This de-reddening scheme is dynamic in that the de-reddening window doubles in size relative to the initial time series concurrently with each downsampling during the execution of the FFA search, such that the window size is always appropriate to the range of periods currently being searched.

5.2.3.2 PROGENY, PROSTAT and METRICTESTER

As much of the testing conducted as part of this paper involves evaluating the performance characteristics of the algorithms themselves, a separate simple program termed PROGENY was developed in order to produce simulated folded profiles as would be output by FFANCY but without the need for a full FFA execution. PROGENY is able to generate custom profiles with or without white noise, and allows the user to choose

[3] https://github.com/adcameron/ffancy
[4] https://github.com/scottransom/presto

the baseline, noise level, and number of bins in the profile, as well as the height, width and position of any seeded pulse. It has the ability to seed either top-hat pulses or Gaussian pulses, with the width of such a Gaussian pulse determined as its full width at half maximum (FWHM). The user can specify as many or as few pulse components as required, allowing for the generation of complex, multi-component pulse profiles. Finally, the program is also able to simulate the effects of scattering by convolving any seeded pulse shape with a one-sided exponential decay function. Each algorithm can be used to evaluate a PROGENY format profile using the additional application METRICTESTER, and a further application PROSTAT can be used to provide a simple statistical breakdown of the contents of each PROGENY profile.

5.2.3.3 FFA2BEST

In order to refine the large number of algorithm scores produced as part of each FFA execution down to a manageable list of candidates, an additional program termed FFA2BEST was also developed. This program is designed to accept the periodogram output produced by FFANCY and convert it into a candidate list formatted in the style of the SIGPROC program BEST. The process of candidate selection is complicated by the fact that each 'peak' in a periodogram has some finite width, with the recorded algorithm S/N rising near the optimal period of the candidate (see Figure 5.1). The basic functionality of FFA2BEST allows the seperation of candidates in the periodogram using a series of three thresholds, all of which can be specified at runtime. These thresholds determine the baseline S/N below which candidates will not be recorded, as well as a fractional and absolute threshold by which the S/N has to fall from the previous candidate before a new candidate can be recorded. More advanced functionality allows for the grouping of nearby candidates based upon the expected response of a strong pulsar whose profile is smeared due to an incorrect period (as determined from the results of the tests outlined in Section 5.3), and for the matching and removal of harmonically-related candidates. This harmonic matching is performed using each of the prime numbers up to a user-specified maximum. For each prime x, a given candidate is both multiplied and divided by each fraction n/x where $0 < n < x$ is an integer, so as to account for both higher and lower harmonic frequencies. The use of primes prevents the repetition of redundant fractions. Two candidates are treated as harmonically related if a match is obtained using this procedure to within a specified tolerance factor, with the weaker candidate being removed from the final candidate list.

5.2.4 Testing for correctness

In addition to the standard testing of code required as part of the software development process, a critical testing milestone for FFANCY was for it to demonstrate an ability to confirm the results of the simulation performed by Kondratiev et al. (2009). Our simulation was conducted by generating artificial pulsars using the SIGPROC program FAKE, with periods P between 2 and 14 s inclusive (with an increment of 0.5 s) and with duty cycles δ covering 0.1 to 1 % (increments of 0.1 %) and 2 to 5 % inclusive

(increments of 1 %). Each of the resulting 350 combinations of P and δ was generated and tested 30 times, so as to mitigate the influence of any statistical anomalies which may arise in a single data set, resulting in a total of 10500 trial pulsars. The total per-pulse energy, given by

$$E_{\mathrm{p}} = wS \tag{5.6}$$

for the top-hat pulses as seeded by FAKE (where S is the height of the pulse and $w = \delta P$ is the width of the pulse), was kept consistent between each pulsar trial. The sampling time set to $t_{\mathrm{samp}} = 491.52\,\mu\mathrm{s}$ and observation time set to $t_{\mathrm{obs}} = 3600\,\mathrm{s}$ so as to match the original simulation parameters from Kondratiev et al. (2009).

Each pulsar was processed through both the FFA and the FFT, with the resulting S/N of the detected signal at the expected period extracted and averaged over the 30 trials for each combination of P and δ. The FFA analysis was conducted using FFANCY, which conducted a narrowly targeted period search on each trial pulsar at full time resolution. The chosen algorithm was a secondary version of Algorithm 2 which employs a pre-specified matched-filter chosen to match the width of the seeded pulse, rather than the blind power-of-2 filter normally used by Algorithm 2. This most closely matches the algorithm used in the original simulation by Kondratiev et al. (2009), and should theoretically result in the maximal S/N. The FFT analysis was conducted using the SIGPROC program SEEK, with the representative S/N detection being taken from the candidate with the maximum S/N in the resulting candidate lists, regardless of the selected harmonic. It should be noted that due to software limitations with SEEK, our simulation employed only 16 harmonic sums compared to the 32 used in the original simulation. This resulted in a slight loss in sensitivity across all test cases.

In order to provide an objective baseline of sensitivity, both the FFA and the FFT were also compared against their theoretically expected S/Ns for each combination of P and δ. The analytical expressions for both the FFA and FFT were derived as part of Kondratiev et al. (2009) and will not be re-derived here. In the case of the FFA, assuming a top-hat pulse shape and the application of a matched-filter equal in size to the seeded pulse width w, for a pulsar with a period of P, duty cycle of δ and a total per-pulse energy of E_{p} recorded over a data set of length N, the theoretical maximum S/N of the detected pulsar signal is given by

$$\mathrm{S/N}_{\mathrm{ffa}} = \frac{E_{\mathrm{p}}\sqrt{N}}{P\sqrt{\delta}}. \tag{5.7}$$

In the case of the FFT, for a pulsar with a duty cycle of δ, a pulse height of S, recorded over a number of samples N and summed harmonically over H harmonics, the theoretical S/N of the detected pulsar signal is given by

$$\mathrm{S/N}_{\mathrm{fft}} = \sqrt{\frac{\pi}{H(4-\pi)}}\times \sum_{n=1}^{H}[L^0_{1/2}(-N[S(1-\delta)\mathrm{sinc}[\pi n(1-\delta)]]^2) - 1] \tag{5.8}$$

where $L^0_{1/2}(x)$ is the generalised Laguerre polynomial $L^\alpha_n(x)$ where $n = 1/2$ and $\alpha = 0$. It should be noted that although both of these equations provide the expected S/N for a given pulsar signal, Equation 5.7 represents a time domain S/N measure while Equation 5.8 represents a Fourier domain S/N measure.

The results of the simulation can be seen in Figure 5.2, which has been produced to emulate the original Figure 8 from Kondratiev et al. (2009). A comparison between these two figures demonstrates similar trends in both simulations, with the advantages of the FFA in the narrow duty cycle range extremely clear. The loss in sensitivity of the FFT due to the choice to only sum 16 harmonics is most clearly noticed in the case of $\delta = 1.0\,\%$, with the previous overlap in sensitivity at lower periods now absent. The ratio comparison of the two analytical curves also shows an increased favourability towards the FFA over the FFT in all but a few cases of shorter period pulsars with duty cycles of at least a few percent. Meanwhile, both example duty cycle plots show strong agreement between the theoretical predictions of the analytical curves described in Equations 5.7 and 5.8 and the experimental data. In summary, the results of the simulation clearly demonstrate both the ability of FFANCY to confirm the results of the previous FFA study, and once again demonstrate the broad advantages of the FFA over the FFT in the long-period pulsar regime.

5.3 Algorithm testing

As a first step towards understanding the behaviour of the FFA, it is necessary to conduct a full investigation of the behaviour of the algorithms chosen to evaluate its output. It is these algorithms that produce the fundamental data required to evaluate the presence of any potential pulsar in an observation. Therefore, any shortcomings in these algorithms in their ability to detect particular types or regimes of pulsar profiles must be understood. This section will outline the results of a series of tests intended to thoroughly probe the response patterns of both of the algorithms chosen for implementation in our study.

5.3.1 Duty cycle, pulse height and pulse energy

In the case of a simple, single-component, symmetric pulse, the three fundamental parameters of this pulse that can be modified are its width w, height S and total energy or fluence E (the area under the pulse curve). In the case of a top-hat pulse, these three parameters are linked simply by Equation 5.6, where for a single folded profile the period P is represented by the profile's length. Such a top-hat pulse results in the sensitivity equation given in Equation 5.7. Given that we are dealing in this case with a single profile, $P = N$ and this can be rewritten as

$$\mathrm{S/N_{ffa}} = \frac{E_\mathrm{p}}{\sqrt{P\delta}}. \tag{5.9}$$

Using Equation 5.6, this can also be rewritten as

$$\mathrm{S/N_{ffa}} = S\sqrt{\delta P} \tag{5.10}$$

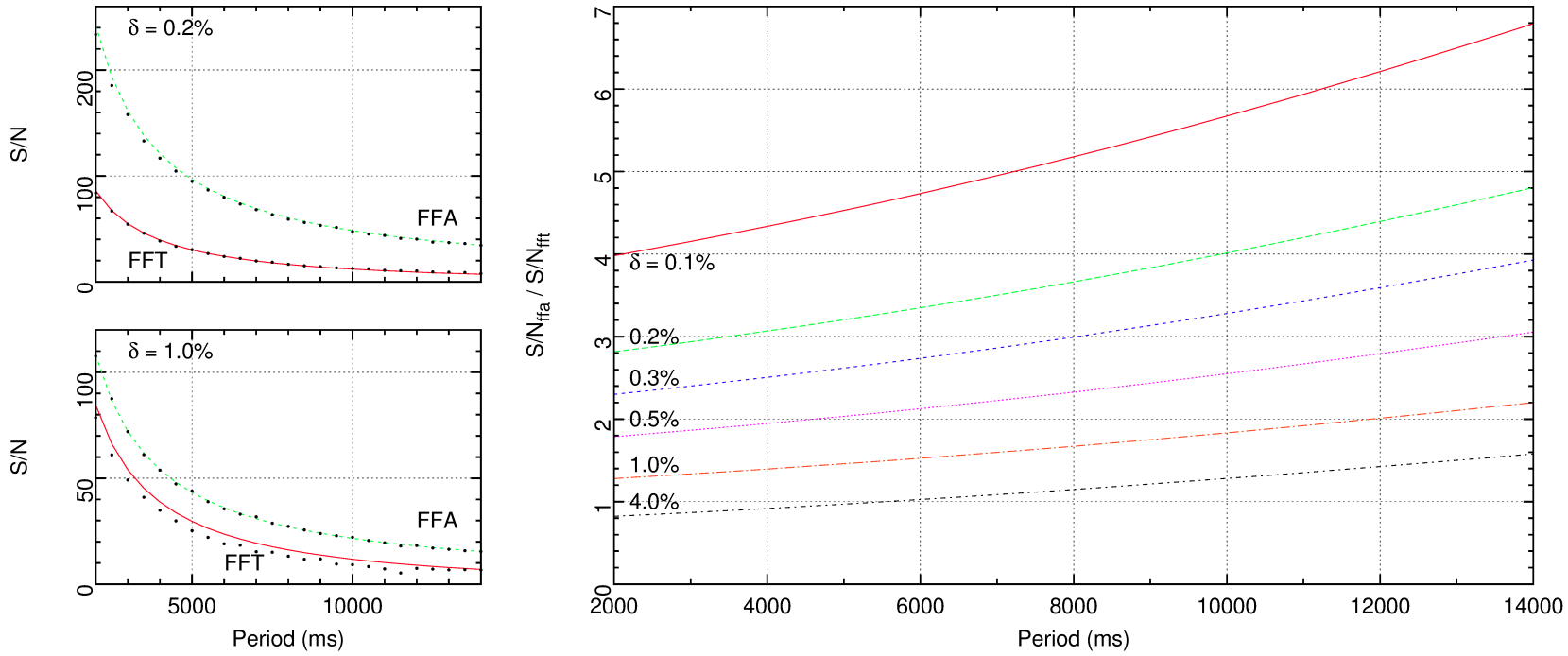

Figure 5.2: Simulation results showing confirmation of the work carried out as part of Kondratiev et al. (2009), namely Figure 8. Left: S/N of both the FFA and FFT at two different duty cycles. The analytical predictions are shown by continuous coloured lines while the experimental results from the simulation are shown as points. Right: the ratio of S/N_{FFA} to S/N_{FFT} as a function of period and duty cycle. These results are taken from the analytical expressions in equations 5.7 and 5.8.

and

$$\mathrm{S/N_{ffa}} = \sqrt{SE_{\mathrm{p}}} \tag{5.11}$$

Based upon these expressions, we can predict the theoretical behaviour of each algorithm as we vary two out of the three specified parameters, and compare the experimental behaviour of each algorithm to this prediction. Using PROGENY, a series of simulated top-hat profiles were created in order to explore this parameter space. The number of bins in each profile was kept at 1024, and each profile test was repeated 30 times using newly generated noise in each repetition, with the average taken as the overall result.

5.3.1.1 Duty cycle versus pulse height

Based upon Equation 5.10, for a constant period, the response of both algorithms should increase both with increasing duty cycle δ and with increasing pulse height S. As a reflection of the overall pulsar population (with statistics derived using the ATNF Pulsar Catalogue PSRCAT[5], Manchester et al., 2005)), duty cycle ranges of 0.1 to 1.0 % (increments of 0.1 %), 1.0 to 20.0 % (increments of 1.0 %) and 20.0 to 70.0 % (increments of 5.0 %) were selected for testing, comprising a total of 39 test values[6]. The pulse height S, specified as multiples of the standard deviation of the white noise superimposed onto the profile, was tested in a range from 0.1 to 1.0 (increments of 0.1) and from 1.0 to 10.0 (increments of 0.5), comprising a total of 28 test values. These values were chosen as representative of weaker pulsar detections, which our work with the FFA hopes to improve. Altogether, the probed parameter space consists of 1092 test cases. The results of the simulation can be found in Figure 5.3.

From these results, several key features can immediately be identified, with the two algorithms displaying markedly different response patterns. Both algorithms display a similar region of maximum response, with Algorithm 2 reaching a slightly higher maximum than Algorithm 1, but this region is constrained differently in each case. In line with our earlier prediction, at constant pulse height the algorithm response increases with increasing duty cycle, but only up to a specific point. Algorithm 1 reaches a maximum at approximately $\delta = 15$ to 25 % and then gradually weakens towards higher duty cycles, whereas Algorithm 2 reaches a maximum much earlier at approximately $\delta = 7$ to 8 %, before sharply falling off at $\delta = 12$ to 13 % and practically vanishing above $\delta = 20$ %.

In the case of Algorithm 1, this deviation can be explained as a consequence of the fact that Algorithm 1 ceases applying increasingly large matched-filters once their size exceeds $\delta = 20$ %. Hence, the algorithm loses response as pulse sizes exceed this maximum matched-filter. Additionally, increasingly wide pulses will begin to render the MAD normalisation scheme less appropriate. A wider pulse will both raise the value of the median, resulting in an incorrect baseline correction with a significant fraction of the pulse sitting below the median, as well as a raising the approximated standard

[5] http://www.atnf.csiro.au/research/pulsar/psrcat/

[6] Although pulsars with smaller duty cycles than 0.1 % are known, 0.1 % was chosen as the lower limit based upon the number of bins used in the test profiles.

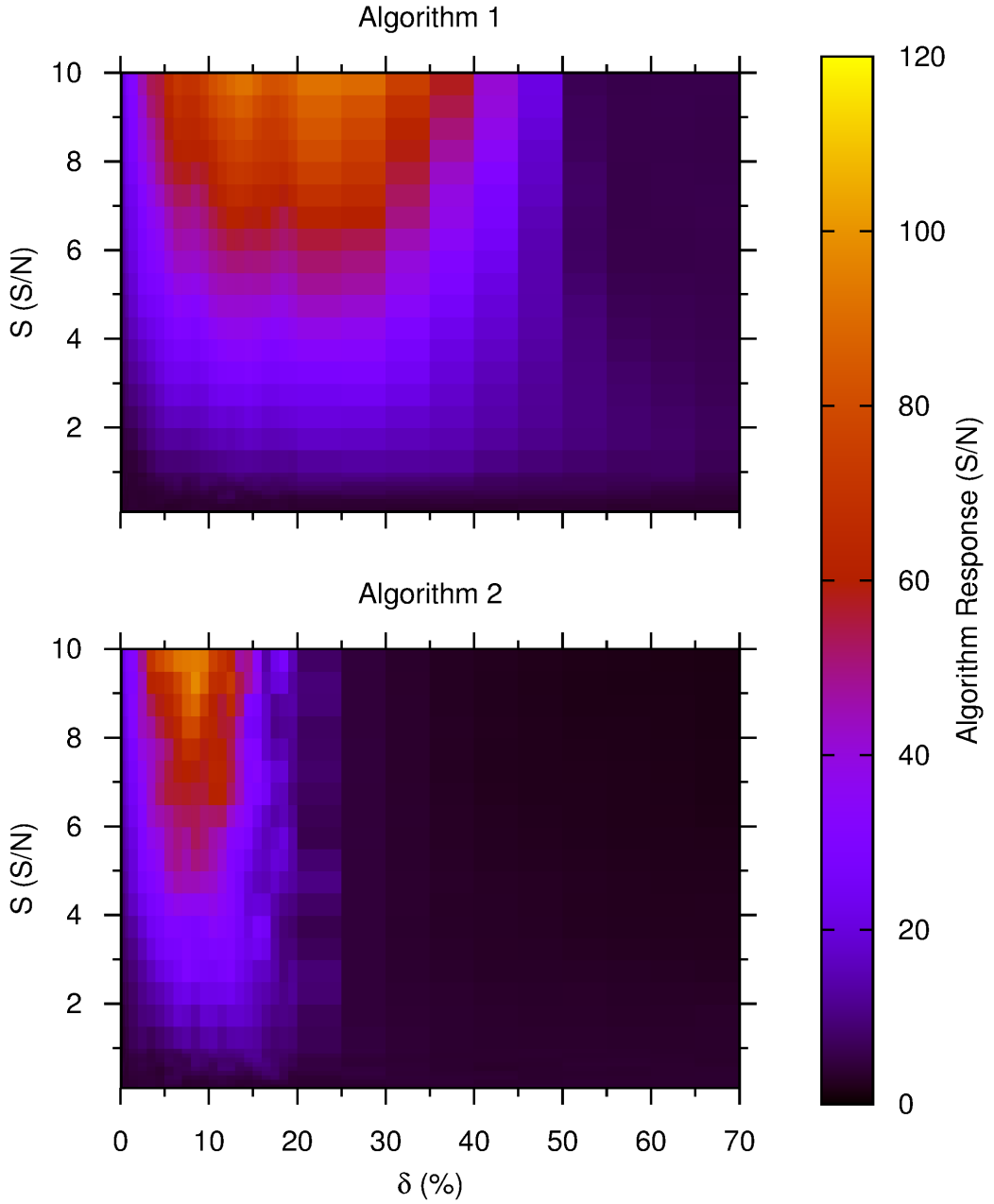

Figure 5.3: Response patterns for Algorithms 1 and 2 in relation to variations in pulse height S (in units of the standard deviation of the profile white noise) and duty cycle δ.

deviation of the profile, further decreasing Algorithm 1's responsiveness. However, the scale of this effect is sufficiently small to allow for stronger pulses to be detected up to duty cycles of $\delta \simeq 50\,\%$.

In the case of Algorithm 2, in addition to using the same limited number of matched-filter sizes as used in Algorithm 1, it also applies a 20 % duty cycle exclusion window. This is likely responsible for the vanishing response that occurs at approximately that duty cycle value. Pulses wider than this exclusion window will begin to 'contaminate' the assumed off-pulse statistics for the average intensity and standard deviation, introducing the same response restrictions as identified in Algorithm 1, but with the degradation occurring at lower values of duty cycle. However, counter-intuitively the loss of response begins at duty cycles as low as $\delta = 12$ to 13 %, smaller than the 20 % duty cycle exclusion window would suggest. This is likely a result of the maximum value in the top hat profile being detected towards one edge, a result of the random variations introduced by the superimposed profile noise. This leads to the algorithm incorrectly centering the exclusion window, leaving some of the pulse outside of the window and thus contaminating the baseline statistics.

Finally, in the region where the value of δ allows for a strong detection, our second prediction regarding the algorithm response also holds. That is, as δ is held constant, the response of both algorithms increases with increasing pulse height S.

5.3.1.2 Duty cycle versus pulse energy

As with duty cycle and pulse height, Equation 5.9 allows us to predict the effects of manipulating the duty cycle and pulse energy, namely that the algorithm response should increase with increasing energy E_p and should decrease as the duty cycle δ increases. By Equation 5.6, the values of E_p probed in Section 5.3.1.1 range between 0.0001 and 7.0 (units arbitrary). In order to probe the same parameter space, test values were chosen between 1.0 and 7.0 (increments of 0.5), 0.1 and 1.0 (increments of 0.1) and 0.01 and 0.1 (increments of 0.01), with additional tests at 0.006, 0.001, 0.0006 and 0.0001, comprising 35 test values. The same range of duty cycles as tested in Section 5.3.1.1 was re-used, producing a parameter space consisting of 1365 test cases, each of which was repeated 30 times with the average taken as the final result. The results of the simulation can be found in Figure 5.4.

From these results, similar trends as observed during the duty cycle / pulse height trials are immediately apparent. As before, Algorithm 1 and Algorithm 2 display similar yet different response patterns, Algorithm 1 displaying a broader response pattern while Algorithm 2 displays a sharper, narrower response. The same limitations in duty cycle response as noted in Section 5.3.1.1 apply here, and will not be re-discussed. At smaller duty cycles unaffected by these limitations, it can be seen that, as predicted, both algorithm response patterns increase dramatically as the pulse energy increases. It would seem clear that both algorithms prefer tall, narrow pulses rather than broader, shallower pulses with the same energy. Additionally, Algorithm 2 once again produces a marginally stronger maximum response than Algorithm 1. This is consistent with the earlier difference in algorithm strengths displayed in Section 5.3.1.1.

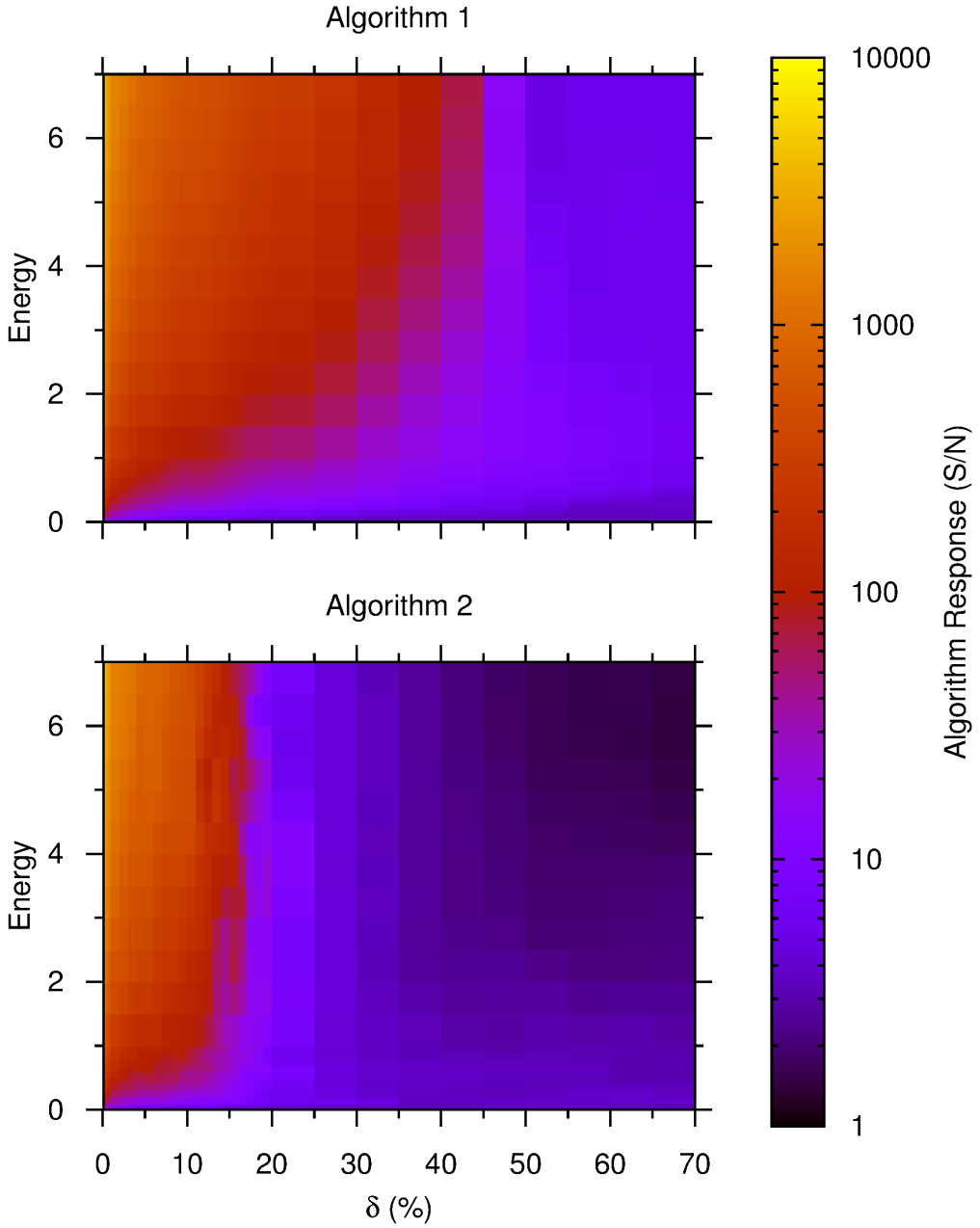

Figure 5.4: Response patterns for Algorithms 1 and 2 in relation to variations in duty cycle δ and energy. Note that the colour scale in this figure is logarithmic, due to the inversely proportional relationship between δ and algorithm response.

5.3.1.3 Pulse height versus pulse energy

Finally, using Equation 5.11 we can predict the behaviour of both algorithms as we vary pulse height and pulse energy in tandem. As both energy and height are increased, the response of both algorithms should also increase. The tested values for both pulse energy E_p and height S are those tested in Sections 5.3.1.1 and 5.3.1.2, giving a total parameter space consisting of 980 test cases, each of which was repeated 30 times with the average taken as the final result. However, some combinations had to be excluded where the combination would result in a duty cycle of $\delta \geq 100\,\%$. The results of the simulation can be found in Figure 5.5.

The displayed response patterns and relative strengths between the two algorithms are in line with those from the previous simulations. Holding E_p constant, the response of both algorithms does indeed increase with increasing pulse height, but while increasing E_p at constant pulse height S does initially cause an increase in response, this response falls off as E_p is further increased. This is because increasing the pulse energy at constant height must necessarily result in a larger duty cycle δ, re-introducing the same limitations as were previously encountered.

5.3.2 Period

To test the performance of the algorithms as a function of period, we return to the simulation conducted in Section 5.2.4. Using the same test cases and procedure (including constant pulse energy between trials), we can produce similar FFA performance plots for both Algorithm 1 and Algorithm 2. The results of this simulation can be found in Figure 5.6.

From these results, it can be seen that both algorithms obey the same trends predicted by Equation 5.7, i.e. with constant energy, duty cycle and observation length, the response of each algorithm should increase inversely proportional to the period P. Also, although the performance of both algorithms degrades slightly from the ideal analytical response, they still maintain a higher S/N result across both example duty cycles ($\delta = 0.2\,\%$ and $1.0\,\%$) and all periods than the 16-harmonic-sum FFT. This degradation from the analytic FFA curve is limited to a maximum of around 15 to 16 %, as indicated by the fractional deviation plots located beneath each S/N plot. As can be seen in each of the examples, these deviations follow a rough cycle whose period increases by a factor of 2 with each oscillation, with the shape of the curve apparently common to both algorithms for each duty cycle. This oscillation is linked to the way in which the matched-filter operates in both algorithms, increasing in size by factors of 2 such that the matched-filter whose width is closest to that of the signal in the profile should return the highest response. Minima in the deviation plots correlate with pulse widths relatively close to the size of one of these trial matched-filters, while maxima correlate with pulse widths caught almost precisely between two matched-filter sizes, neither able to truly capture the width of the pulse.

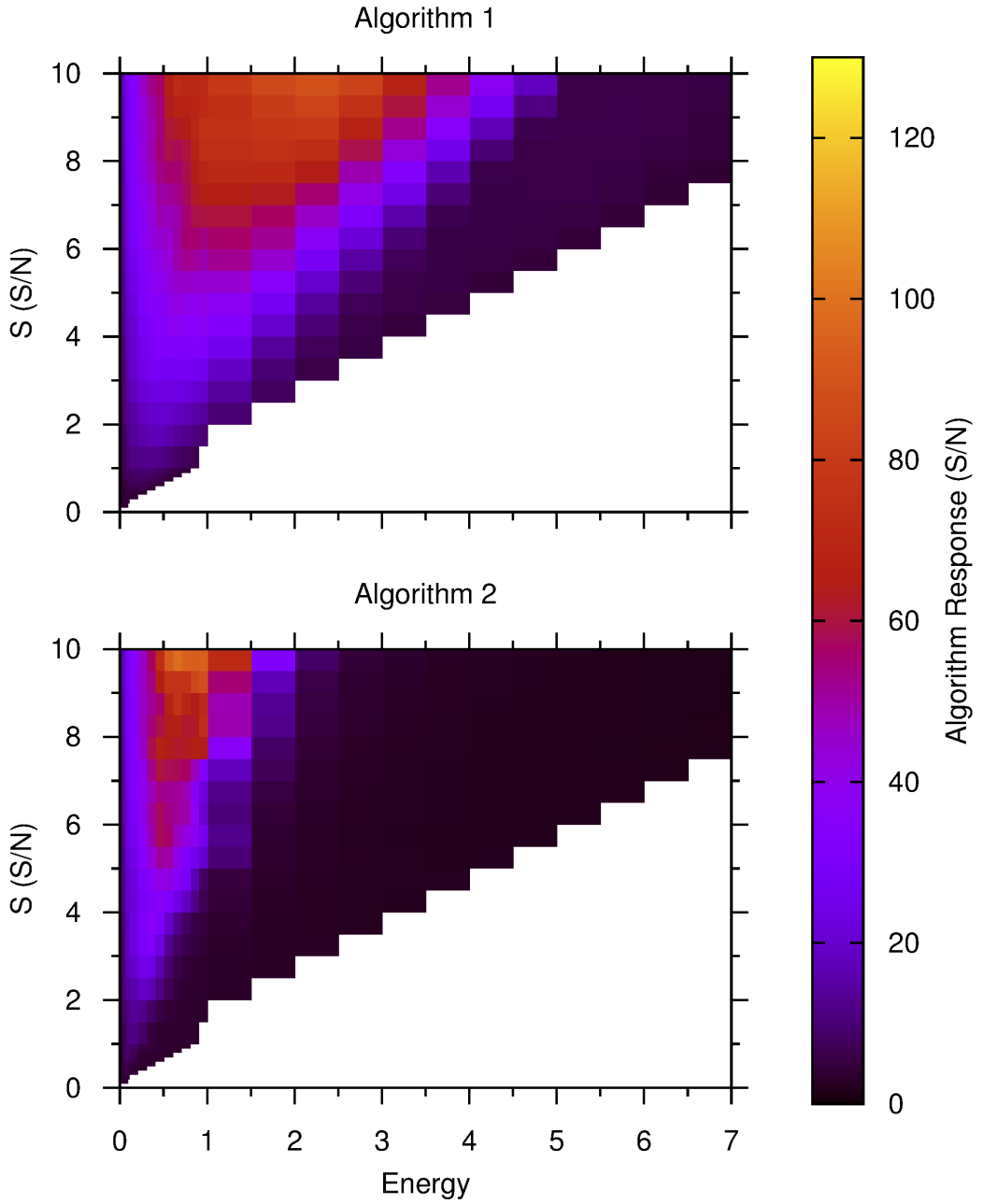

Figure 5.5: Response patterns for Algorithms 1 and 2 in relation to variations in to pulse height and energy. The empty regions in the bottom right of each plot represent regions where the duty cycle $\delta \geq 100\,\%$. This region was therefore excluded from testing.

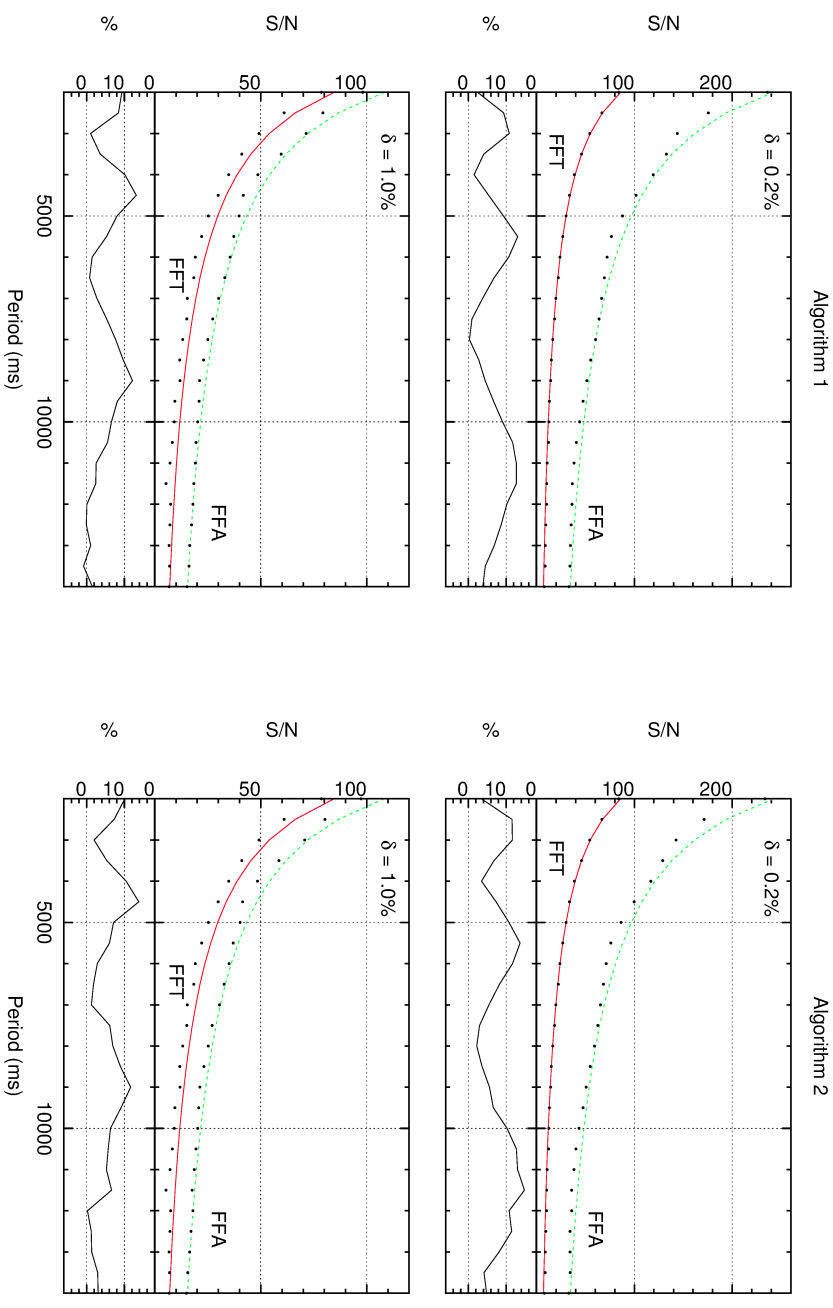

Figure 5.6: Simulation results demonstrating the performance of Algorithms 1 and 2 against the ideal FFA response and the FFT at two different duty cycles. In each figure, the solid curves represent the ideal analytical response while the point represent the experimental results of the FFA and FFT respectively. The curve beneath each plot represents the percentage deviation of each algorithm from the analytical FFA response.

5.3.3 Pulse shape

For simplicity, all tests thus far have been conducted using top-hat pulse profiles. However, although it is a useful approximation, this pulse shape is unrealistic when considering real pulsars. The morphology of pulsar profiles can range from simple single Gaussian-like curves to much more complicated shapes, and these varying profiles may influence the response of the algorithms. The taxonomy scheme proposed by Backer (1976) and refined by Rankin (1983) classifies pulse profiles into several broad categories according to the apparent shape of profile components and their associations with models of pulsar emission. However, as we are interested purely in the effects of variations in the pulse shape as well as the number of components, we can employ a simpler taxonomy scheme in our consideration of which profile types to investigate. These tests must also allow for shape variations caused by the presence of scattering (e.g. Bhat et al., 2004) and interpulses (e.g. Lorimer, D. R. and Kramer, M., 2005), which can further modify the shape of the observed profile and may affect their detectability using our chosen algorithms. Given the considerable size of the parameter space that could be explored in a full investigation of pulse shape variance, the tests chosen here are not intended to be exhaustive, but will instead serve as case examples reflective of pulsars likely to be encountered during an FFA search. The results of these tests are detailed in the following subsections.

5.3.3.1 Single-component Gaussian profile

The most obvious first step in implementing a more realistic pulse shape is to change from a top-hat pulse to a Gaussian, as this is an approximation appropriate to many known pulsars. This change in shape modifies the earlier expressions dervied for the pulse width and energy. For a Gaussian profile with maximum amplitude S and variance $c > 0$, an appropriate substitute for the duty cycle δ becomes the FWHM, defined by

$$\delta = \mathrm{FWHM} = 2\sqrt{2\ln 2}c. \tag{5.12}$$

The energy of the pulse E_g similarly becomes

$$E_\mathrm{g} = Sc\sqrt{2\pi} = \frac{S\delta\sqrt{\pi}}{2\sqrt{\ln 2}}. \tag{5.13}$$

To compare the response of both algorithms to Gaussian pulse shapes, we repeated the simulation conducted in Section 5.3.1.3, using the same energy and height combinations with 30 repetitions per test, with the average of each test taken as the final result. Energy and maximum pulse height were chosen as the defining parameters of the test space as they are both easier to define in the case of a Gaussian pulse than the duty cycle, a problem which will be only be exacerbated with the more complex pulse shapes encountered in later tests. The results of this simulation can be found in Figure 5.7. It can be seen that in comparison to the top-hat simulation in Figure 5.5 the overall response of both algorithms is similar in terms of its distribution across the energy-height plane, likely for the same reasons as discussed in Section 5.3.1.3, but in both

cases each algorithm gives an overall lower magnitude of response (note that both figures employ an identical colour scale for comparison).

5.3.3.2 Single-component Gaussian profile in the presence of scattering

Now that a baseline response to a single-component Gaussian profile has been established, the responsiveness of both algorithms to the presence of an increasingly-scattered Gaussian pulse can also be investigated. The effect of scattering can be simulated by convolving the original pulse shape with a one-sided exponential decay function with a scattering time scale of τ_s (Lorimer, D. R. and Kramer, M., 2005). As the profiles generated in these series of tests have been independent of any fixed pulsar period, τ_s is in units of profile bins. Since the effects of scattering often smear out and obscure any more complex pulse shape features (Bhat et al., 2004), it is sufficient to conduct this test with a single-component Gaussian profile.

To investigate the response of both algorithms to an increasingly scattered profile, a single test case was selected from the single-component Gaussian simulation which produced a high relative response in both algorithms, i.e., an unscattered pulse height of $S = 10$ times the profile noise level and energy $E_g = 1$. By Equation 5.13, this produces a duty cycle of $\delta \simeq 9.39\,\%$. Test profiles were generated using values of τ_s ranging from 0 to 1000 profile bins in increments of 5. As the number of bins in the profile is 1024, the maximum value of τ_s represents a pulse that has been almost completely scattered across the width of the profile. This resulted in 201 test cases, each of which was repeated 30 times. The average response of these 30 repetitions was taken as the final result for each test case. In each test case, it was ensured that the energy of the scattered pulse remained consistent with the energy of the unscattered pulse. The results of the simulation can be found in Figure 5.8.

It can be seen that both algorithms display markedly different responses to the presence of increased scattering. At very low values of τ_s both algorithms essentially provide the same response, but as the value of τ_s increases, Algorithm 2 exhibits a much more dramatic fall in response as compared to the more gentle decline in response of Algorithm 1. By $\tau_s \simeq 200$, Algorithm 2 has almost plateaued at a response of $A_2 \simeq 4$, while Algorithm 1 only begins to approach this response at the highest values of τ_s tested. This difference in behaviour between the algorithms is likely another reflection of the same difference in response exhibited to varying duty cycles as seen in prior tests. As the Gaussian pulse is increasingly scattered, it both widens asymmetrically and its maximum amplitude decreases in order to keep the pulse energy constant. Given the 20 % exclusion window imposed by Algorithm 2, it exhibits a much sharper decline in response as the pulse scatters outside of this window.

5.3.3.3 Two-component Gaussian profiles

To investigate the response of both algorithms to the presence of more complicated profiles, two further simulations were performed involving two-component Gaussian profiles. In the first simulation, profiles containing two Gaussian pulses of identical

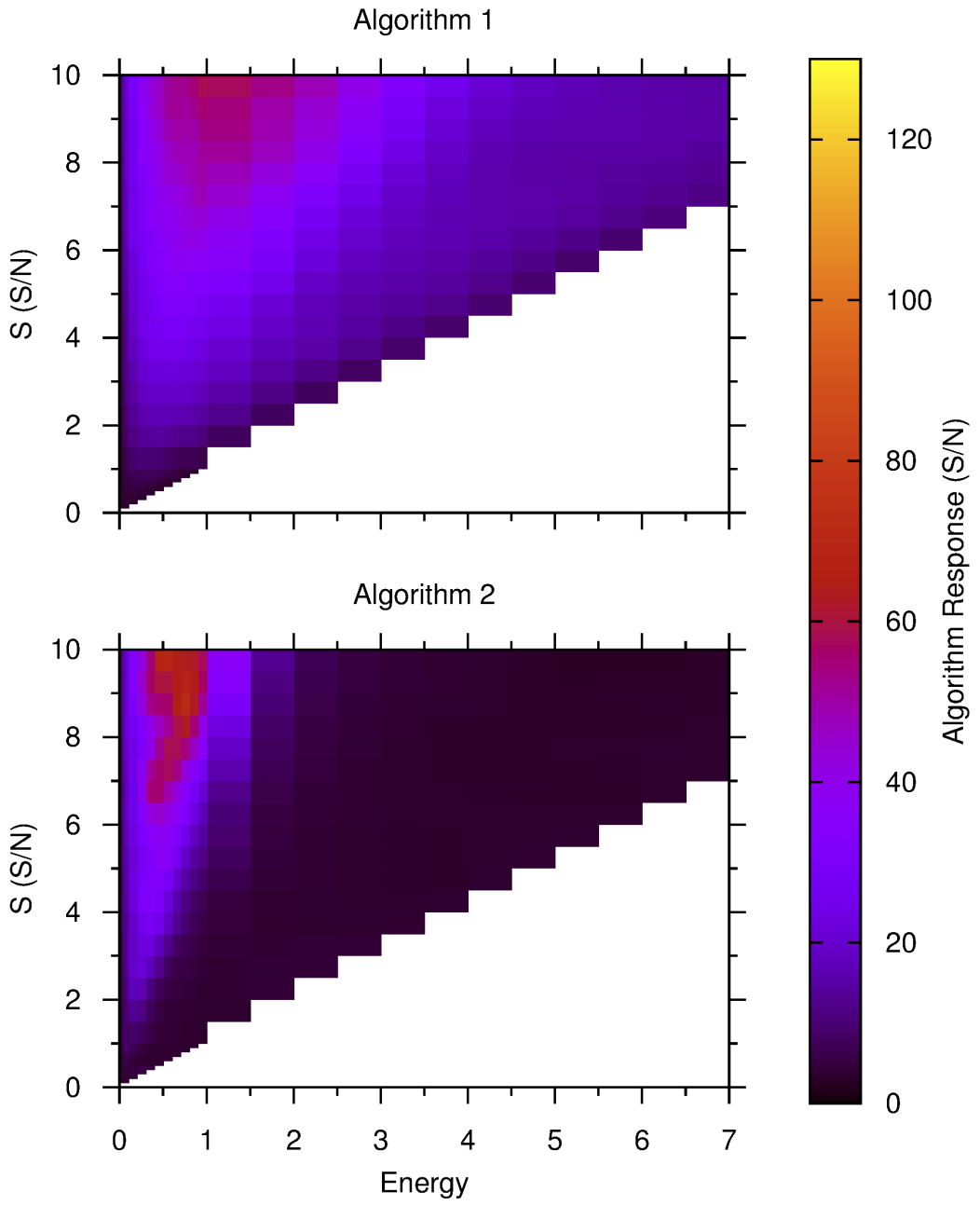

Figure 5.7: Identical to the simulation results displayed in Figure 5.5, but for a single-component Gaussian profile instead of the original top-hat profile.

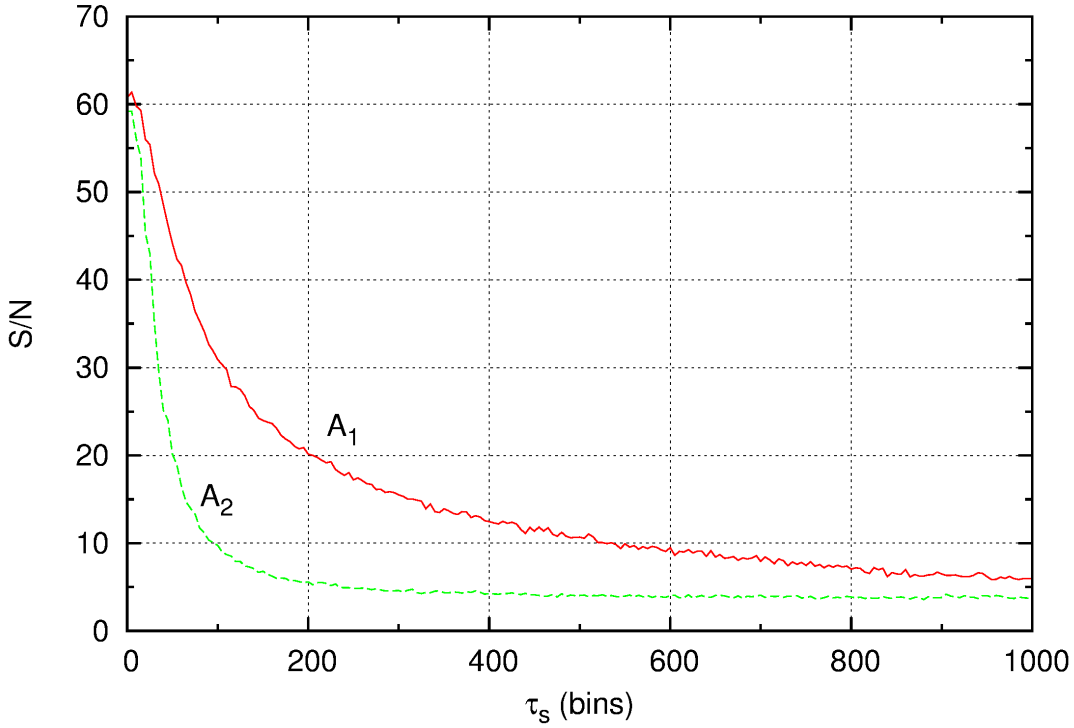

Figure 5.8: Algorithm response to an increasingly scattered single Gaussian pulse. Original pulse seeded with height 10 times the profile noise and $\delta \simeq 9.39\,\%$, producing a pulse energy $E_{\mathrm{g}} = 1$.

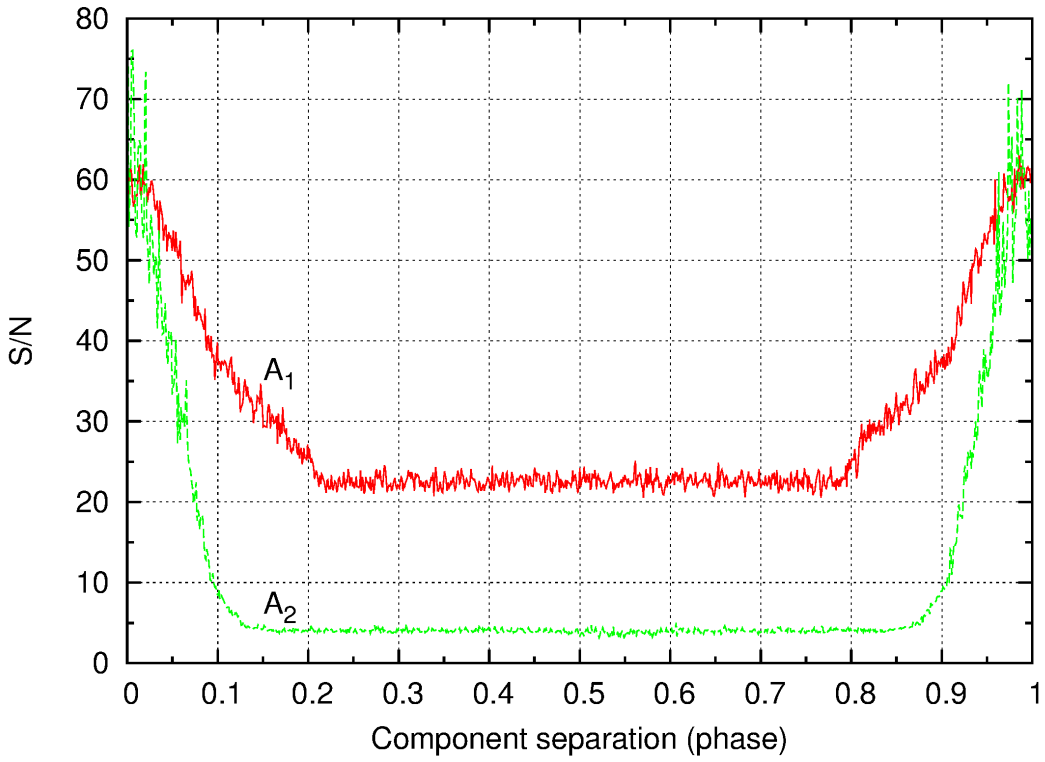

Figure 5.9: The response of Algorithms 1 and 2 to a two-component Gaussian profile, with both components being identical. The central position of the second pulse was shifted across the entire width of the profile.

strength were generated, with the separation between these pulses varied. Such a simulation encompasses the response of the algorithms both to more complicated, two-component pulse profiles (when the pulse peaks are located close together) and to harmonic detections of a pulsar folded at the wrong period (when the pulse peaks are located further apart). To produce the simulation, profiles were created containing two Gaussian pulses. Each pulse was seeded with a height of $S = 10$ times the profile noise level and energy $E_g = 0.5$. By Equation 5.13, each pulse would again have a duty cycle of $\delta \simeq 9.39\,\%$, and when added together would produce the same unscattered pulse as used in the scattering trials. One pulse was held stationary while the other was moved such that its peak was trialled at each bin position in the 1024 bin profile. Each bin position test was repeated 30 times, with the average taken as the final result for each bin position test. The results of this first simulation can be found in Figure 5.9.

In the second simulation, profiles containing two Gaussian pulses of unequal strength were generated, with the separation between these pulses once again varied. Such a simulation again encompasses the response of the algorithms both to more complicated, two-component pulse profiles (when the pulse peaks are located close together) as well as to the presence of interpulses (when the pulse peaks are located

further apart). The parameters of the test were identical to that of the previous simulation, with the exception that the stationary pulse was seeded with $S = 7.5$ and $E_g = 0.75$, while the moving pulse was seeded with each of these parameters divided by 3, such that $S = 2.5$ and $E_g = 0.25$. This would again result in two pulses with $\delta \simeq 9.39\,\%$ and that when added together would reproduce the unscattered pulse trialled as used in the scattering trials. The results of this simulation can be found in Figure 5.10.

Familiar trends can be observed in these results. Once again, as the two peaks are gradually separated, creating a wider profile with multiple components, the response of both algorithms decreases in both test cases, with Algorithm 2 decreasing and plateauing before Algorithm 1 for the reasons already outlined in earlier sections. The more interesting result can be seen in the center of the both Figures, where the two pulse components have moved far enough apart to be treated as separate features. It is clear that in this region both algorithms make no distinction about the location of the second pulse, maintaining a flat response throughout, but both algorithms plateau at different levels. Algorithm 1 maintains a stronger response in this region than Algorithm 2. This is likely due to the fact that the MAD normalisation technique is less affected by outliers (in this case the additional pulse component) than the standard deviation technique used in the evaluation of Algorithm 2. This contamination is reduced in Figure 5.10, as the second, moving pulse is relatively weaker in this case, allowing for the flat response of both algorithms to rise.

5.4 Trials on real observational data

All testing thus far has focused on evaluating the behaviour of the FFA and its associated algorithms in the white noise regime. In order to quantify the response of the FFA to the presence of red noise and other RFI and to compare its response to that of the FFT, a trial was conducted using real observational data taken from the HTRU-S LowLat survey (Keith et al., 2010), conducted with the Parkes 64-m radio telescope. Twenty telescope beams containing a selection of the longest period known pulsars present in the survey area were selected. These pulsars cover a period range from approximately 1.2 to 6.4 s, and represent a significant range of apparent flux densities and pulse shapes. For example, PSR J1307−6318 displays a striking two-component profile, while the magnetar PSR J1622−4950 displays a very wide profile (with a duty cycle as high as $\delta \simeq 50$ to $60\,\%$) which is known to vary with time (Levin et al., 2010). Table 5.1 lists the details of these pulsars as obtained through PSRCAT.

Processing was undertaken once again using software from the SIGPROC software package. Each filterbank observation file was RFI-cleaned using a process of channel and timezapping as adapted from Ng et al. (2015). Each filterbank was then dedispersed using the value of DM appropriate for its pulsar to produce a time series. The red noise present in each time series was characterised through the use of a power law fit, with the index of this power law and the frequency below which the power law fit was appropriate being listed in Table 5.1. Each time series was then processed

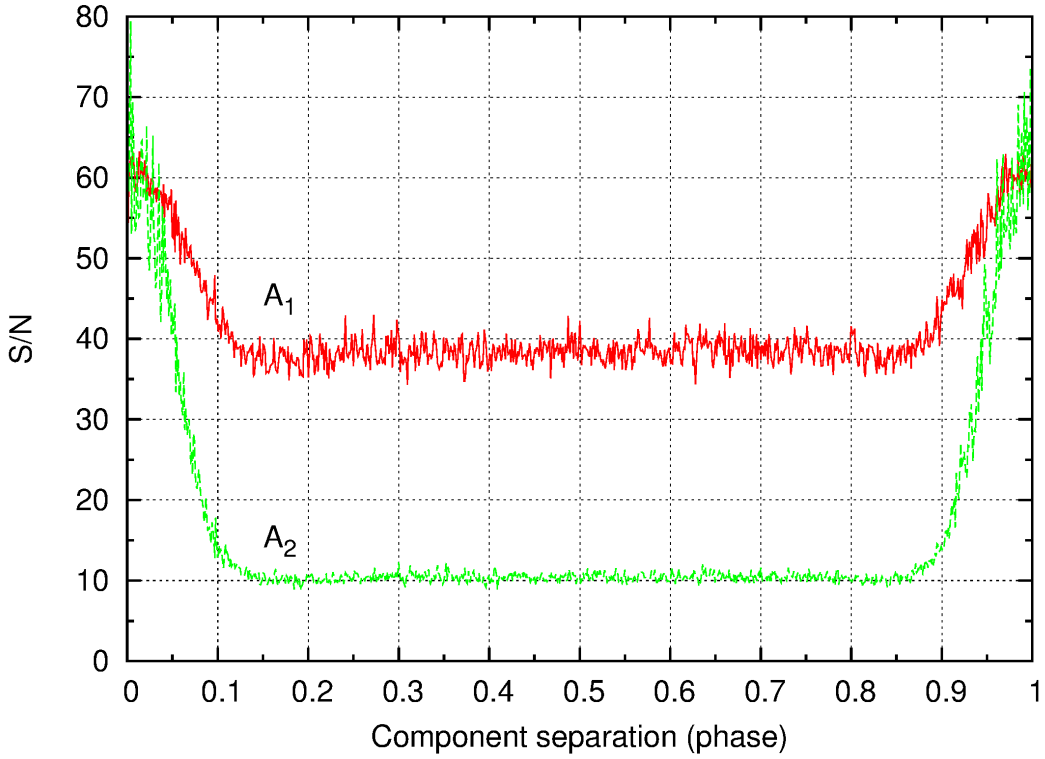

Figure 5.10: The response of Algorithms 1 and 2 to a two-component Gaussian profile, with both components being of unequal height and energy. The central position of the second, weaker pulse was shifted across the entire width of the profile.

Table 5.1: Parameters of the test pulsars selected from the HTRU-S LowLat survey as provided by PSRCAT, listed from longest to shortest barycentric period, along with the derived red noise properties of their respective observations. The Pointing/Beam combination identifies which survey observation and beam number that the pulsar was recorded in. The expected S/N is calculated based on the radiometer equation (see Equation 2.23), and takes into account the pulsar's non-central position in the beam. Duty cycle δ was derived using the FWHM (where available) as $\delta = \mathrm{FWHM}/P$. The red noise properties of each observation were determined through the use of a power law fit, with the amplitude and index of this power law (as well as the frequency below which the power law fit was appropriate) listed.

		Pulsar properties				Red noise properties		
PSR name	Pointing/Beam	P (ms)	DM ($\mathrm{cm}^{-3}\mathrm{pc}$)	δ (%)	S/N	Amplitude	Index	Cutoff Freq. (Hz)
J1736-2843	2011-07-03-13:48:57/05	6445.036	331	2.25	25.1	35.86	-1.86	1.07
J1840-0840	2013-01-01-02:30:42/10	5309.377	272	3.39	151.2	22.92	-2.00	0.90
J1307-6318	2011-12-29-14:57:57/08	4962.427	374	10.18	20.7	12.91	-2.12	0.67
J1622-4950	2010-12-31-21:03:27/08	4326.100	820	-	52.2	28.49	-2.03	1.20
J1814-1744	2013-01-01-00:04:30/08	3975.905	792	2.31	28.3	-	-	-
J1718-3718	2011-06-27-14:48:40/13	3378.574	371.1	3.85	19.1	27.54	-1.77	1.93
J1314-6101	2011-06-30-10:40:03/03	2948.390	309	2	69.6	28.39	-2.25	1.50
J1803-1857	2012-02-16-01:37:19/02	2864.338	392	0.89	98.3	98.30	-1.93	3.79
J1831-1223	2011-12-06-05:56:02/12	2857.941	342	3.43	63.9	36.09	-1.78	2.63
J1759-1956	2012-02-16-01:37:19/12	2843.389	236.4	1.33	59.2	94.92	-1.96	3.61
J1747-2802	2011-05-17-15:33:25/07	2780.079	835	0.98	14.7	5.95	-1.76	0.99
J1444-5941	2011-06-26-05:10:45/01	2760.228	177.1	1.7	17.4	37.51	-1.88	2.50
J1811-1049	2012-04-01-18:52:53/05	2623.859	253.3	-	5.3	9.97	-2.01	1.19
J1801-1855	2012-02-16-01:37:19/07	2550.498	484	1.64	86.1	76.22	-1.90	3.85
J1822-0848	2012-04-02-18:07:28/13	2504.518	186.3	1.24	1.74	14.88	-1.99	1.55
J1324-6302	2011-12-08-02:26:00/13	2483.804	497	0.72	43.0	6.21	-1.91	1.05
B1658-37	2012-04-02-14:27:04/07	2454.609	303.4	1.75	393.0	9.06	-1.98	1.24
B1740-31	2011-10-13-10:01:19/13	2414.576	193.05	1.86	207.0	-	-	-
J1817-1938	2013-04-08-18:54:20/10	2046.838	519.6	-	15.6	1.67	-2.03	0.63
J1838-1046	2011-07-14-15:08:44/07	1218.354	208	1.36	15.5	9.98	-2.01	2.58

through an FFT and FFA analysis in the following manner:

- **FFT:** Each time series was processed through the SIGPROC program SEEK, with the use of the default AGN spectral-whitening de-reddening scheme and the summation of 16 harmonics. A spectral bin-zapping mask, or 'birdie' mask, was also applied. This mask takes advantage of the 13 simultaneous beams recorded during each HTRU-S LowLat observation, and was generated through the use of the multibeam RFI-excision technique described in Ng et al. (2015). The resulting candidate file was then evaluated by eye to find the strongest detection which was harmonically related to the relevant pulsar.

- **FFA:** Each time series was processed through FFANCY using a search from 1 to 20 s. An initial downsampling factor of $2^6 = 64$ was applied to each time series before the search began, so as to reduce the required processing time. FFANCY's dynamic de-reddening scheme was activated for each time series, using the default values described in Section 5.2.3.1. This process was repeated with both Algorithm 1 and Algorithm 2. Finally, the resulting periodograms for each pulsar and algorithm were processed through the candidate selection program FFA2BEST. No candidate was accepted with an S/N of less than 9, and both candidate grouping and harmonic matching were used so as to lower the number of overall candidates. Harmonic matching was conducted using the complete set of primes up to and including 31, with a matching tolerance of 0.001 % for Algorithm 1 and 0.01 % for Algorithm 2. These values were chosen as during testing they produced an optimal balance between correctly grouping related candidates and incorrectly grouping unrelated candidates.

As a control test on each pulsar's detectability, each clean time series was also folded using an optimal ephemeris as obtained using PSRCAT and visually inspected. The optimally-folded profile of each pulsar at its fundamental period as produced using Algorithm 1 of the FFA was also produced for comparison.

The best detections made by each technique are given in Table 5.2. It should be noted that the periods detected by both the FFT and the FFA do not align precisely with the recorded PSRCAT values in Table 5.1. This is partly due both to the resolution of each searching technique, as well as the change in epoch between the catalogue period and each HTRU observation. Also, in many instances, these detections were made at harmonics of the true pulsar period. In the case of the FFT, five detections were made at various harmonics, and these occurrences are indicated in Table 5.2. In the case of the FFA, Algorithm 1 produced three detections at half of the true pulsar period which were stronger than the fundamental detection, while Algorithm 2 produced six stronger harmonic detections, one of which was at the quarter period harmonic while the others were at the half period harmonic. These detection S/Ns are compared against the fundamental S/Ns in Table 5.3.

Table 5.2: Results from the analysis of all 20 pulsars by the FFT and FFA using both Algorithms 1 and 2. [a]FFT harmonic detections. Due to the nature of the operation of `seek`, the fundamental S/Ns are unavailable. [b]FFA harmonic detections. For a comparison of these detections to the fundamental detections made by the FFA, refer to Table 5.3. All listed periods are topocentric.

	FFT		FFA (Algorithm 1)		FFA (Algorithm 2)	
PSR name	P (ms)	S/N	P (ms)	S/N	P (ms)	S/N
J1736-2843	6445.421864	28.0	6445.254194	32.8	1611.298383[b]	26.7
J1840-0840	5309.085587	76.7	5309.441001	108.2	5309.200766	61.1
J1307-6318	4962.142906	15.4	4962.334029	19.5	4962.253951	12.2
J1622-4950	4326.605589	21.1	4326.513110	15.9	-	-
J1814-1744	3976.188776	30.0	1988.062367[b]	32.6	1988.058366[b]	14.8
J1718-3718	3378.580197	8.2	3378.917862	15.6	-	-
J1314-6101	2948.479585	23.0	1474.271930[b]	39.7	2948.527711	26.8
J1803-1857	954.705686[a]	31.1	2864.106490	52.1	2864.102488	35.6
J1831-1223	2858.101443	51.6	2858.039527	50.5	1429.008879[b]	31.2
J1759-1956	1421.593545[a]	17.6	2843.160262	30.4	2843.156260	20.2
J1747-2802	2779.942215	14.6	2779.949397	14.7	2779.937391	11.3
J1444-5941	2760.400348	9.3	2760.303805	13.9	2760.335820	11.3
J1811-1049	2623.606783	11.1	2623.633071	17.7	2623.601055	15.7
J1801-1855	1275.139081[a]	21.6	2550.285256	34.3	2550.285256	24.9
J1822-0848	1252.114308[a]	9.0	2504.226767	14.4	2504.218763	11.4
J1324-6302	620.930604[a]	7.0	1241.868190[b]	20.4	1241.861189[b]	14.7
B1658-37	2454.376590	116.6	2454.390433	304.8	2454.466470	178.2
B1740-31	2414.874382	127.7	2414.851127	165.8	1207.415779[b]	99.5
J1817-1938	2046.638718	22.7	2046.615662	21.6	1023.330918[b]	19.8
J1838-1046	1218.392631	22.6	1218.376455	25.2	1218.377455	22.3

Table 5.3: Instances where the FFA detected a harmonic as the strongest detection using either Algorithm 1 or 2, as compared to the strength of the fundamental detection.

	FFA (Algorithm 1)				FFA (Algorithm 2)			
	Strongest Detection		Fundamental Detection		Strongest Detection		Fundamental Detection	
PSR name	P (ms)	S/N	P (ms)	S/N	P (ms)	S/N		
J1736-2843	-	-	-	-	1611.298383	26.7	6445.222162	25.8
J1814-1744	1988.062367	32.6	3976.077444	23.0	1988.058366	14.8	3976.145477	8.7
J1314-6101	1474.271930	39.7	2948.527711	35.5	-	-	-	-
J1831-1223	-	-	-	-	1429.008879	31.2	2858.039527	25.8
J1324-6302	1241.868190	20.4	2483. 732760	18.6	1241.861189	14.7	2483.728758	13.0
B1740-31	-	-	-	-	1207.415779	99.5	2414.775089	46.5
J1817-1938	-	-	-	-	1023.330918	19.8	2046.621663	16.3

5.4.1 Analysis

Both the FFT and Algorithm 1 of the FFA were able to successfully recover all 20 of the test pulsars. However, Algorithm 2 was only able to recover 18 of the 20 pulsars, with PSR J1622−4950 and PSR J1718−3718 remaining undetected. A likely explanation for the non-detection of PSR J1622−4950 lies in the pulsar's unusually high duty cycle ($\delta \simeq$ 50 to 60 %), because as demonstrated in Section 5.3.1, Algorithm 2 is largely insensitive to wide pulse profiles. Following a visual inspection of the folded profile produced by the FFA at the fundamental period, the non-detection of pulsar PSR J1718−3718 appears to be due to a combination of an inherently low S/N combined with noise contamination of the baseline, which persisted despite the application of FFANCY's red noise removal system and other RFI mitigation techniques. The reduction in sensitivity caused by the contaminated baseline was again likely a result of Algorithm 2's insensitivity to wide pulsar profiles, or in this instance, wide baseline variations.

A comparison of the best detections made by both the FFA and the FFT shows a clear trend towards the FFA typically either matching or exceeding the performance of the FFT, especially in the case of Algorithm 1. This trend, expected for long-period pulsars, can be seen in Figure 5.11. All but three pulsars were detected with a higher S/N through the use of Algorithm 1, the most notable of which was PSR J1324−6302, which was detected using Algorithm 1 at a S/N approximately 2.9 times that of its FFT detection. Of the three remaining pulsars which were detected more strongly in the FFT, two (PSRs J1817−1938 and J1831−1223) were detected by Algorithm 1 within 5 % of their FFT S/N values. This could potentially be a result of the approximations introduced into both Algorithms 1 and 2 as described in Section 5.3.2 and the resultant losses documented in Figure 5.6. The third pulsar (PSR J1622−4950) shows a much more notable loss of sensitivity in its Algorithm 1 detection, reaching only 75 % of its FFT detection. As with this pulsar's non-detection by Algorithm 2, the cause would again seem to be the unusually wide pulse shape of PSR J1622−4950.

Algorithm 2 displays a much less favourable response than Algorithm 1, on average only approximately matching the performance of the FFT. Of the 18 pulsars detected using Algorithm 2, only 9 were detected with higher S/N values than their FFT detections. The highest of these was again PSR J1324−6302, which was detected at a S/N approximately 2.1 times higher than its FFT detection. At the other extreme, Algorithm 2 was only able to detect PSR J1814−1744 with approximately 49 % of the S/N of the FFT detection.

In each of the 18 pulsars detected by both algorithms, Algorithm 1 was able to obtain a higher S/N detection. This relationship is demonstrated in Figure 5.12, and appears to indicate evidence of an approximately linear trend between the two algorithms. While this relation is only tentative given the limited number of data points, a simple least-squares fit to a linear curve (including a forced intercept at the origin) gives

$$\mathrm{S/N}_{\mathrm{A1}} \simeq 1.668 \times \mathrm{S/N}_{\mathrm{A2}}, \tag{5.14}$$

with a coefficient of determination of $R^2 = 0.994$.

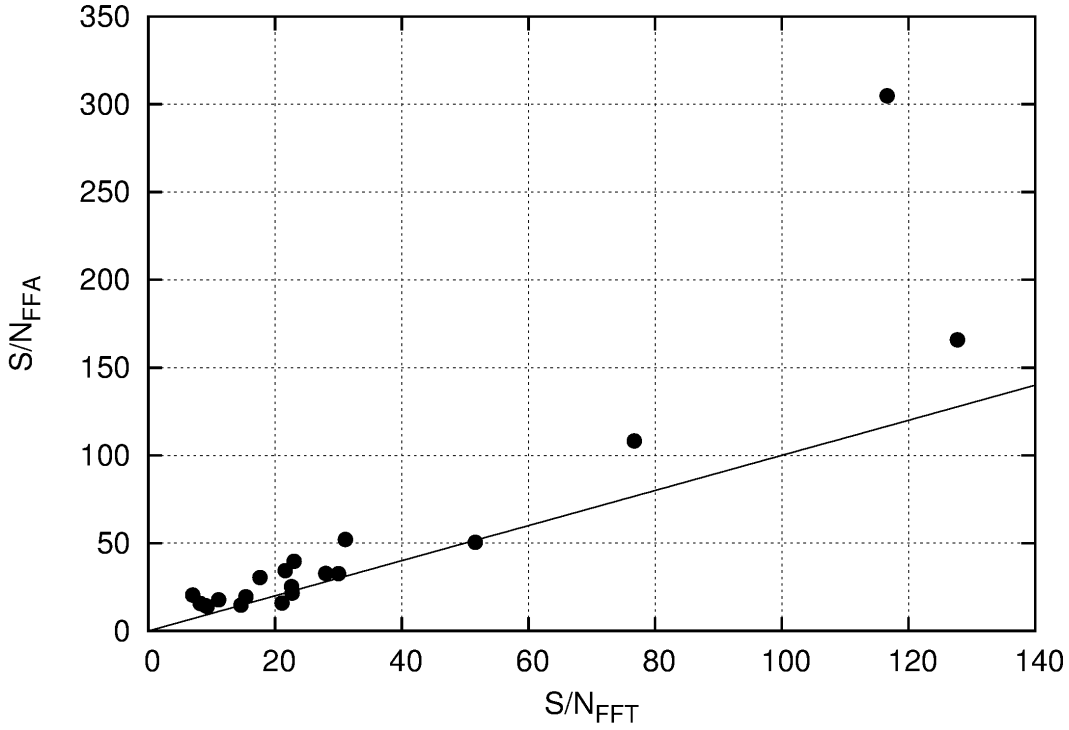

Figure 5.11: Comparison of the sensitivity of FFA Algorithm 1 to the FFT across all 20 pulsars, using the best detections of each technique (including fundamental and harmonic detections). The solid line indicates a relationship of 1:1.

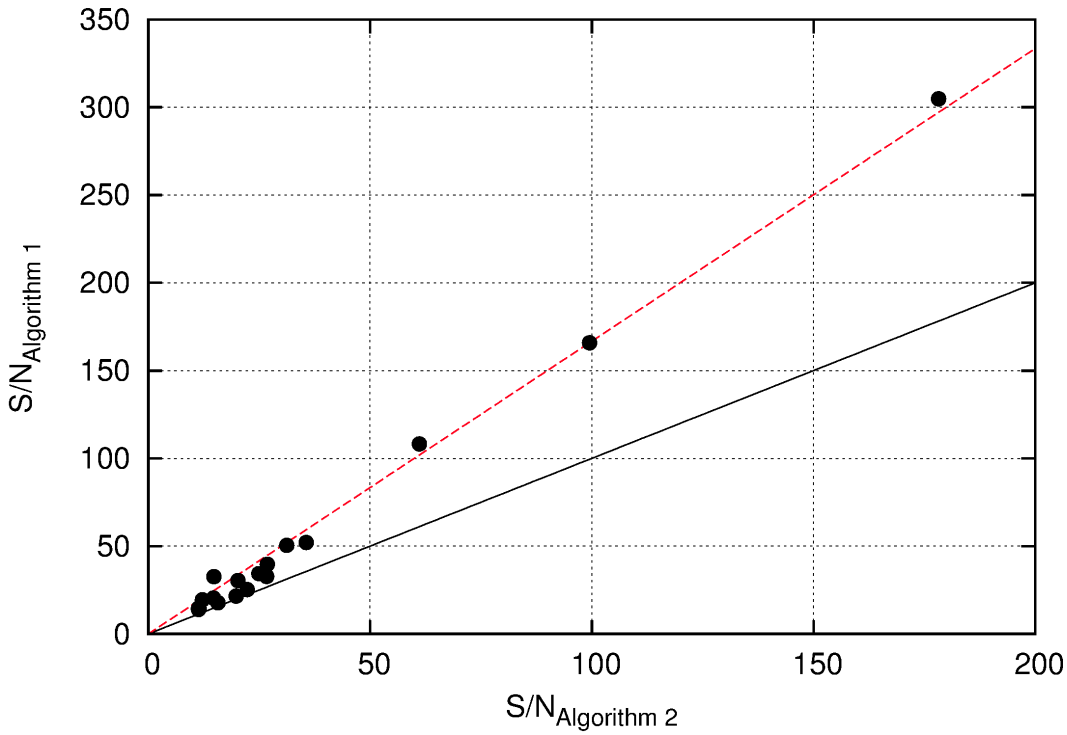

Figure 5.12: Comparison of the sensitivity of Algorithm 1 against Algorithm 2 across the 18 pulsars for which both algorithms were able to make a detection, using the best detections of each technique (including fundamental and harmonic detections). The solid line indicates a relationship of 1:1, while the dashed line indicates a least squares fit to the scatter plot, defined in Equation 5.14.

5.4.1.1 Influence of red noise and other RFI

Despite our chosen methods of mitigating both red noise and general RFI, some element of both of these contaminants is likely to still remain in the analysed data. A visual inspection of the folded profiles produced by FFANCY indicates only two pulse profiles, PSR J1814−1744 and PSR J1718−3718, which appear to be suffering from visible baseline contamination. An inspection of a manually-folded set of sub-integrations reveal this to be caused primarily by persistent RFI which was not removed during the preliminary cleaning procedures. While in the case of PSR J1718−3718 this contamination is likely to have contributed to the pulsar's non-detection by Algorithm 2, both algorithms were able to detect PSR J1814−1744 despite the profile contamination. This is likely due to the higher S/N of the pulse profile being able to stand out against the contaminated baseline.

A more analytical presentation of the remaining influence of red noise may potentially be determined by comparing the improvement in detectability of each pulsar against the red noise content of each data set at the pulsar's fundamental period. This red noise content can be calculated using the parameters listed in Table 5.1, and the results for both Algorithms 1 and 2 are plotted in Figure 5.13. However, inspection of this figure shows no apparent correlation between the improvement in detectability and red noise content. This could again be a result of the limited size of the data set employed in this study, as other unaccounted factors may be playing into the detectability of each pulsar. Future comparisons using larger data sets may assist in revealing any underlying trend.

The persistence of the influence of red noise even in the FFA is also evident upon an examination of the periodograms resulting from each FFA execution. This is particularly the case with Algorithm 1, as its higher response to wider pulse shapes means that it is likely to be more sensitive (in the absence of a stronger true pulsar signal) to the longer profile baseline variations which typically characterise red noise. This effect is demonstrated in Figure 5.14, which shows the Algorithm 1 periodogram for pulsar PSR J1831−1223. Note that at longer periods, the average value of the periodogram appears to rise. This is caused by the continued persistence of red noise creating a pulsar-like signal and causing an undesired response in the algorithm. However, this effect does not persist in the periodograms of Algorithm 2, due to the reasons already described in relation to its pulsar non-detections.

5.4.1.2 Signal significance and false-alarm statistics

Up until this point, we have been considering the response of both the FFT and the FFA only in terms of either the spectral or profile-based S/N of each pulsar or candidate signal. However, it is worth considering the statistics of each of these candidate distributions in order to evaluate the detection significance afforded by each technique, as well as the expected corresponding false-alarm rates. When combined with the number of trials conducted or candidates produced as part of a given FFT or FFA search, these will allow for the true significance of a candidate to be determined. The statistics for the FFT of normally-distributed white noise are reasonably well understood, and will

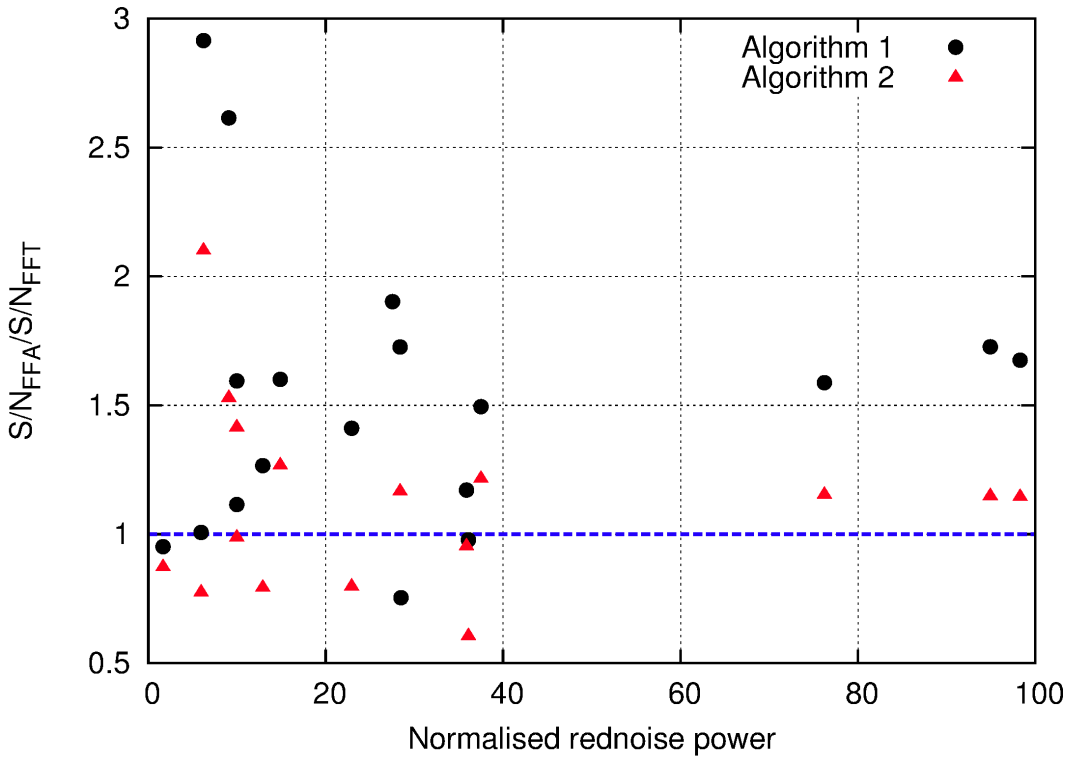

Figure 5.13: Comparison of the ratio of the sensitivity of both FFA Algorithms 1 and 2 to the FFT against red noise content at each pulsar's fundamental frequency, across all 18 pulsars for which the red noise content could successfully be characterised. The blue line indicates the 1:1 relationship between the FFA and FFT. Above the line, the FFA performs better, while below the line the FFT performs better. The best detections of each technique (including fundamental and harmonic detections) were used.

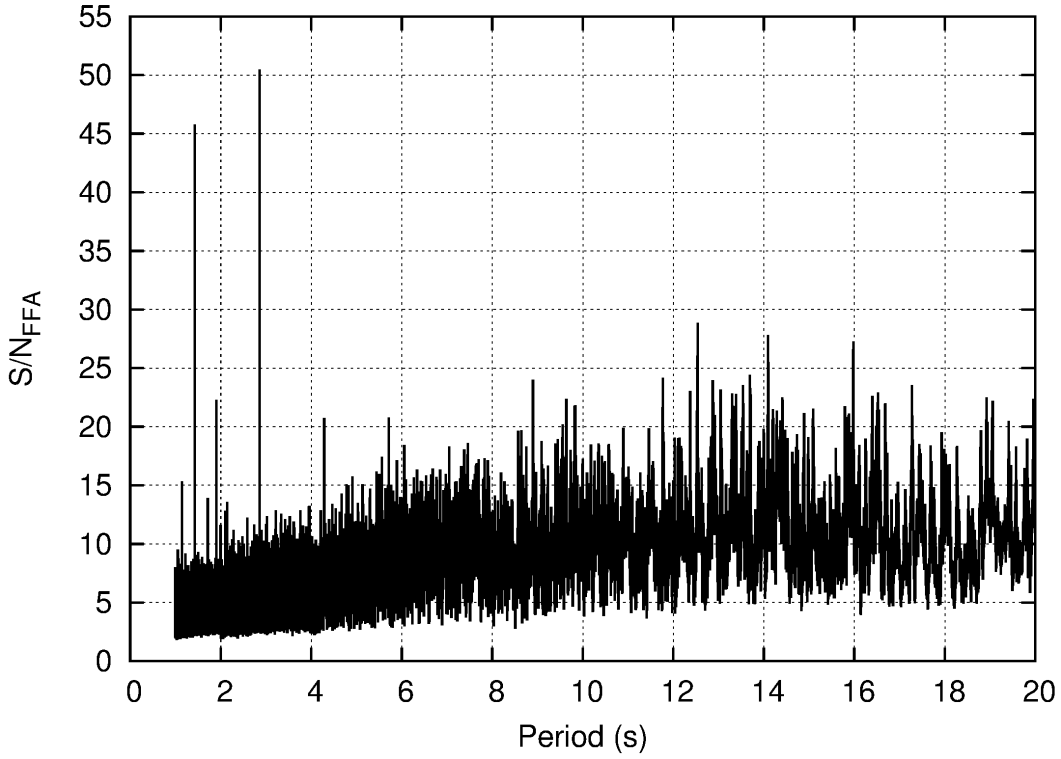

Figure 5.14: Periodogram of a search conducted using Algorithm 1 on pulsar PSR J1831−1223. The pulsar is visible as the strong peak near 2.858 s, along with its half harmonic.

not be re-derived here (see Lorimer, D. R. and Kramer, M. (2005) for a basic overview). However, a more in-depth study of the FFA is required.

We can evaluate the significance of an FFA algorithm score by studying the distribution of S/N values produced by each algorithm over a large number of trials. For a given operation of the FFA (N/P_0 period trials for a given base period P_0) conducted across a time series constructed from normally-distributed values, the evaluation of the S/N of a single folded profile can approximately be thought of as the maximum of $n_{\mathrm{bin}} \times n_{\mathrm{fil}}$ independent normally distributed variables, where n_{bin} is the number of bins in the profile and n_{fil} is the number of applied matched filters. However, while these values remain constant for each incremental period trial in a single FFA execution, these numbers vary significantly across different FFA executions. For example, the specific implementation of the FFA in FFANCY causes n_{bin} to vary by as much as a factor of 2.

In order to characterise these distributions, 26 normally-distributed filterbank files built to match HTRU specifications were created using FAKE. These were then integrated in frequency into single-channel time series at a DM of $0\,\mathrm{cm}^{-3}\mathrm{pc}$ which were run through FFANCY using both Algorithms 1 and 2 over a search from 1 to 20 s and an initial downsampling factor of $2^5 = 32$, such that the total number of produced S/N trials was approximately 10^8. An identical analysis was also performed using 26 representative beams from HTRU-S LowLat which had previously been found to be devoid of pulsars, so as to determine the influence of RFI and other red noise on the distribution. In order to minimise the influence of local RFI (producing a close to best case scenario), these beams were de-dispersed at a DM of $200,\mathrm{cm}^{-3}\mathrm{pc}$. Due to the increasing presence of red noise with increasing period, these HTRU distributions were divided into period ranges of 1 to 2 s and 2 to 20 s, with each range containing approximately the same number of trials (5×10^7). Each value of S/N was converted into a Gaussian Equivalent Sigma (σ_{gauss}) by mapping its probability to a normal quantile function. The resulting distributions can be seen in Figure 5.15.

While the distributions of the two algorithms are largely similar in their response to the white noise distributions generated with FAKE, significant differences can be observed in their response to the real HTRU data and in their response to longer periods and corresponding red noise. As encountered previously, Algorithm 2 appears to be far more robust in its sensitivity to red noise, with its 2 to 20 s distribution varying very little from its 1 to 2 s distribution, with only a small increase in S/N at the highest values of σ_{gauss} (and a corresponding decrease in S/N at the lowest values of σ_{gauss}). A 5-σ_{gauss} detection moves from an S/N of 7.1 in the fake case to 11.7 and to 14.5 in the 1 to 2 s and 2 to 20 s distributions respectively.

In contrast, Algorithm 1 shows a much more pronounced response to the transition to real HTRU data and to the increasing presence of red noise. This is likely a reflection of the same response seen in Figure 5.14, once again a result of Algorithm 1's more favourable response to wider pulse profiles. While the responses below $\sigma_{\mathrm{gauss}} = 0$ are very similar, a 5-σ_{gauss} detection moves from an S/N of 6.6 in the fake case to 18.0 and to 30.9 in the 1 to 2 s and 2 to 20 s distributions respectively, indicating that at longer periods, pulsar signals may suffer from a reduced apparent significance due to

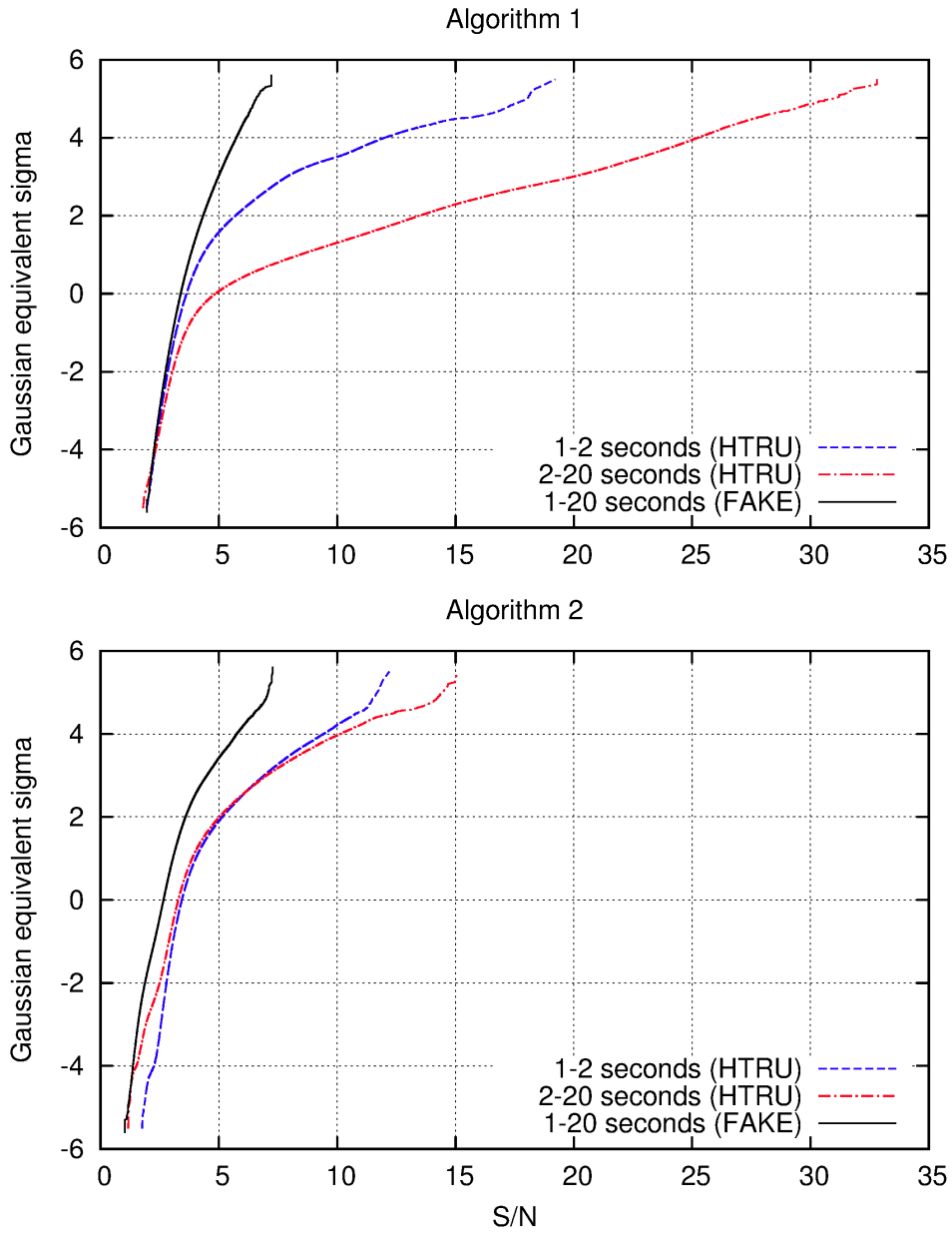

Figure 5.15: A demonstration of the the S/N distribution curves for Algorithms 1 and 2 map against detection significance, expressed as Gaussian Equivalent Sigma (σ_{gauss}). The FAKE distributions were constructed by deploying FFANCY across multiple artificial filterbanks seeded with normally-distributed noise using the SIGPROC program FAKE. The HTRU distributions were constructed by deploying FFANCY over a set of HTRU-S LowLat filterbanks which were devoid of pulsars, de-dispersed using a DM of $200\,\text{cm}^{-3}\text{pc}$.

the presence of spurious detections caused by red noise and other interference.

Unfortunately, due to the lack of an appropriate analytic model of red noise which can be applied generally to multiple telescope configurations, it is presently impractical to develop an analytic expression for deriving these false-alarm statistics for general observational data. At this stage, generation of statistical distributions such as the one presented in Figure 5.15, using data devoid of strong pulsar signals, remains the best solution for producing observation-specific false-alarm and significance thresholds.

5.5 Discussion

It is clear that from a theoretical standpoint, the FFA presents many clear advantages over the FFT in the search for long-period pulsars. In the case of clean, white data, the two algorithms which have been presented for consideration in this paper demonstrate a robust ability to detect pulsars typical of the long-period population, over and above the performance of the FFT. However, while the real-world trials demonstrate that this outperformance persists after the transition to real, noisy data sets, there remains considerable room for improvement.

One area which deserves particular scrutiny is improving our ability to discriminate against and remove forms of interference, including red noise. As noted in our methods, our analysis involved the use of thresholded time and frequency zapping as well as multibeam RFI excision. In addition, we have applied a dynamic red noise removal system through the use of a series of time domain median-filters. While these techniques are well tested and show demonstrable improvement in the resulting signal quality, our analysis shows that they are not entirely successful in the removal of interference.

A particular shortcoming of FFANCY (and the FFA in general) in relation to RFI is its inability to discriminate between a signal which is more or less continuous throughout the observation, and a bright, sporadic burst of RFI. A single short instance of strong interference could potentially contaminate a large number of folded profiles with an apparent pulsar-like signal. As the FFA currently only evaluates folded profiles which have been collapsed in time, removing these false positives poses a challenge. One immediate solution which could be applied to future versions of the FFA is a simple clipping mechanism which would cap the values in the initial time series and thereby mitigate any potential contamination. This feature is already available in many pulsar searching packages and could be easily applied to an FFA-based search.

Another proposed solution is to incorporate an additional 'persistence score' into the FFA. This technique would involve scoring each bin (either in the original time series or in one of the subsequent folding steps of the FFA, depending on the expected strength of the pulsar being searched for) with either a 1 or 0 based upon whether it exceeded a particular cutoff value. In this manner, the combined persistence scores in the bins of a folded profile should rank a continuous pulsar signal more highly than a single burst of strong RFI folded into noise. These scores could either be used to weight the folded profiles, or be written out to be used in later determining which candidates to consider for further investigation. Such 'persistence' measures could be

easily determined during the subsequent folding and inspection (either by person or machine) of each selected candidate from the original observation after the execution of the FFA, but by the incorporation of this step into the FFA itself, the number of false alarm candidates could potentially be reduced at an earlier stage. Such a technique has already been implemented in other pulsar searching algorithms, such as the Pulsar Evaluation Algorithm for Candidate Extraction (Lee et al., 2013).

There is also room for improvement in the profile evaluation algorithms themselves. Both FFA algorithms were designed to favour pulsars with a narrow duty cycle, and although this is typically the case for long-period pulsars, exceptions to this general rule were encountered even among the test set of 20 pulsars chosen for study. The most notable example of this was the magnetar PSR J1622−4950, which was missed by Algorithm 2 and suffered a loss of sensitivity in Algorithm 1 because of its large duty cycle. It is these types of scientifically interesting sources that we would most hope to find with future FFA-based searches, and so future versions of these algorithms may need to be modified to allow for better detection of larger duty cycles.

However, Algorithm 1's existing sensitivity to larger duty cycles caused it to detect a large number of false positive candidates, typically on the order of hundreds for each searched time series. As noted in Sections 5.4.1.1 and 5.4.1.2, Algorithm 1 is more sensitive to the pulsar-like profile baseline variations induced by red noise at longer periods and it tends to produce candidates with an apparent higher significance. This is the source of the reported false positives, and any increase in its duty cycle response is only likely to increase this number of false positive detections. Therefore, significant improvements in this algorithm may not be possible without the implementation of better red noise mitigation techniques.

In theory, the median-filtering technique used by FFANCY should have been capable of filtering out the red noise present in the data. However, this technique is only capable of filtering out those red noise signals with periods longer than that of the pulsar itself. Lower periods cannot be easily removed using this technique without potentially removing the desired pulsar signal, and it is this form of red noise which is likely to be producing the red noise detected by Algorithm 1. The multibeam RFI excision technique we have used on sporadic, ground based interference is also not an applicable technique, as the properties responsible for the generation of red noise (such as thermal variability) will be independent to each beam of the receiver.

An alternative approach to red noise removal potentially lies in the use of interferometers for pulsar observations. While the same problem of independent receiver noise will remain, by forming beams onto multiple adjacent sky locations using the same telescope information, the red noise component which will be common to all beams may be able to be removed while a pulsar, located in only a single beam, would remain. The investigation of such a technique is of particular interest with the development of new, large scale interferometers such as MeerKAT[7] and the Square Kilometre Array[8] (SKA), and may lend these systems an advantage in the search for long-period pulsars

[7] http://www.ska.ac.za/science-engineering/meerkat/
[8] https://skatelescope.org/

(see e.g. Stappers & Kramer, in press).

In addition to the two algorithms presented here, the challenge of evaluating a large number of folded candidate profiles is one which has already been partly addressed through machine learning techniques. These techniques have had a history of successful application to pulsar surveys, including the PMPS (Eatough et al., 2010b) and HTRU (Bates et al., 2012). In particular, we have followed on from work conducted by Zhu et al. (2014), which involves the processing of large numbers of pulsar candidate diagnostic plots through a Pulsar Image-based Classification System (PICS). PICS consists of an ensemble of classifiers based on different machine learning techniques. The system is trained on how to recognise good candidates using a set of human-selected candidate detection plots, and its use has resulted in the discovery of at least six pulsars in the PALFA survey. As part of a preliminary exploration of the application of this technique to the FFA, a newly discovered pulsar from the HTRU-S LowLat survey (Cameron et al. in prep.) with a period of $\simeq 1.7\,\mathrm{s}$ and a FFT S/N of $\simeq 14$ was processed through a FFA search (from approximately 1 to 10 s) with FFANCY. The resulting 1.9 million folded profiles from this search were then passed through PICS. The pipeline was able to detect the pulsar as the top ranked candidate after 36 s of processing time using a neural net classifier running across 20 processing cores, and 600 s using a support vector machine classifier running on only a single core (giving a similar per-core processing performance). Room exists for further speed optimisation through the use of further parallel processing. Although of limited scope, this test demonstrates a potential usefulness of this technique in future versions of the FFA. However, FFA-specific training sets would also need to be developed in order for this method to proceed further.

Finally, it should be noted that the FFA technique bears strong similarities to image processing and pattern recognition techniques involving the use of the Radon transform that have been developed in parallel in recent years (e.g. Götz & Druckmüller, 1996; Brady, 1998; Press, 2006). These techniques (collectively labeled as the fast or discrete Radon transform) use a similar strategy to the FFA in order to remove redundant computations in the processing of the Radon transform, transforming an $N \times N$ size image through a series of integrals taken along a complete set of lines through the image. This results in the same order of computational complexity as the FFA for a given period, $O(N \log_2(N))$. The analogy of treating aspects of pulsar searching as an image-processing problem is not new, and further investigation of the work done in this field may produce valuable further insights into extracting further performance gains from the FFA.

In the immediate future, this work will now be turning to focus on improving the performance and efficiency of our FFA search techniques. A second, GPU-based FFA software package known as FFASTER has been developed in parallel with the CPU-based FFANCY, and will incorporate the results of the tests conducted in this study. FFASTER should be able to take full advantage of the parallelisability of the FFA so as to gain a significant increase in performance, and will help to cement the FFA as a practical pulsar searching technique for future large-scale pulsar surveys.

5.6 Conclusions

In this paper, we have conducted an intensive study of the behaviour of FFA against the behaviour of the FFT in both an ideal white noise regime and in a real-world observational regime using data from the HTRU-S LowLat pulsar survey. In the ideal white noise regime, two separate profile evaluation algorithms have been characterised and tested in their response to a wide variety of possible pulse shapes, including variances in pulse height, width and total pulse energy as well as the presence of scattering and multiple pulse components, including interpulses. Algorithm 1, a boxcar matched-filter with MAD normalisation, showed response patterns which were significantly more sensitive to wider pulse shapes (including pulses exhibiting scattering tails, as well as to multiple pulse components and to interpulses) than Algorithm 2, a boxcar matched-filter with an off-pulse window. However, both algorithms demonstrated an ability to significantly exceed the performance of the FFT under similar testing regimes, confirming and building upon the results demonstrated by Kondratiev et al. (2009).

Trials on real observational data, coupled with a dynamic de-reddening scheme employing a running median filter, showed that over a test set of 20 long period pulsars, the FFA has the ability to match and often exceed the performance of the FFT by a maximum factor of almost 3, despite the presence of red noise and other contamination. Algorithm 1 was demonstrated as being the more sensitive of the two tested algorithms, exceeding the performance of the FFT in all but 3 of the test pulsars, but suffered from a large number of false positive candidates, largely due to the influence of red noise. Algorithm 2 was on average only able to match the performance of the FFT when tested on real data, and was unable to detect two of the 20 pulsars in the test sample.

Room for improvement remains on both of the presented profile evaluation algorithms as well as the noise removal techniques used in partnership with the FFA. Opportunity also remains for additional evaluation techniques to be developed which can be coupled with the FFA, including neural network pattern recognition. However, this paper clearly demonstrates the ability of the FFA to recover the sensitivity lost by the FFT in the long-period pulsar regime, and lays a strong foundation for future research into the behaviour of this technique. The custom FFA software package FFANCY produced as part of this work will allow for further investigation and testing of the FFA to be conducted as we move forwards towards a faster, GPU-based implementation of the algorithm for use on large-scale pulsar surveys.

Acknowledgements

Observational data used in this paper was made available thanks to the HTRU scientific collaboration. The Parkes Observatory, used in the collection of this data, is part of the Australia Telescope National Facility (ATNF), which is funded by the Commonwealth of Australia for operation as a National Facility managed by CSIRO. Processing for this paper was largely performed using the 'Hercules' computing cluster operated by the Max Planck Computing & Data Facility (MPCDF). The authors would like to thank Patrick Lazarus for the use of his code in evaluating red noise content, and Vladislav

Kondratiev for sharing his expertise on both the FFA and FFT and the MPCDF help desk for their constant assistance. AC acknowledges the support of both the International Max Planck Research School (IMPRS) for Astronomy and Astrophysics at the Universities of Bonn and Cologne and the Bonn-Cologne Graduate School of Physics and Astronomy (BCGS). Both AC and EB gratefully acknowledge the support of the Deutscher Akademischer Austauschdienst and Universities Australia as part of the Australia-Germany Joint Research Cooperation Scheme under contract no. 57218648.

Chapter 6

Conclusions and future work

Contents

6.1 Summaries and conclusions

6.1.1 The HTRU-S LowLat pulsar survey

The primary scientific motivation of this thesis has been the processing and analysis of the High Time Resolution Universe South Low Latitude (HTRU-S LowLat) pulsar survey, which was undertaken with the goal of discovering short-P_b, relativistic binary pulsars, as well as pulsars situated at the low end of the luminosity distribution. In both of these respects, the results derived from the processing of approximately 44 % of the survey as part of this thesis have shown the HTRU-S LowLat survey to have been successful in achieving these goals, with the survey now standing at a total of 100 newly-discovered pulsars. Not only has this survey and its 'partially-coherent segmented acceleration search' pipeline (originally designed and implemented by Ng et al., 2015) resulted in the discovery of an exceptional relativistic binary pulsar (PSR J1757−1854, see Section 6.1.2 for a more detailed summary), it has also uncovered the population of lower-luminosity pulsars it was designed to explore (see Section 3.5.2). This achievements come as a direct consequence of the longer integration times, larger bandwidth and finer time resolution employed by this survey in comparison to previous search efforts such as those undertaken with the Parkes Multibeam Pulsar Survey (PMPS; Manchester et al., 2001).

An evaluation of the processing of the HTRU-S LowLat survey, as documented in Section 3.2, has shown that the 44 % of the survey analysed in this thesis has been

processed consistently with the 50 % processed earlier by Ng et al. (2015). This includes 755 individual re-detections from 390 unique known pulsars within the survey region, a majority of which were detected at the signal to noise (S/N) anticipated based upon the radiometer equation and other considerations as presented in Section 3.2. Of the 21 non-detections of expected pulsars (none of which were binary pulsars), only 9 remain unaccounted for, giving a miss-rate of only $\sim 2\,\%$, again consistent with the $\sim 1\,\%$ reported by Ng et al. (2015).

The segmented acceleration search, which is designed to optimise the search for binaries with orbital periods $P_\mathrm{b} \leq P_\mathrm{b,crit} = 12\,\mathrm{h}$, also re-detected 17 unique binary pulsars spanning 28 individual re-detections. As discussed in Section 3.2.2, the majority of these pulsars did not require the segmented search aspect of the pipeline in order to be re-detected due to their long orbital periods. However, those pulsars whose orbital periods approached or fell below $P_\mathrm{b,crit}$ were able to highlight both the strengths and weaknesses of the segmented acceleration search pipeline used on this survey. While the strong half-segment detection of the relativistic binary PSR J1141−6545 showed the clear advantages of a segmented-search technique in the short-P_b, relativistic binary regime, PSRs J1435−6100 and J1810−2124 showed the pipeline's potential insensitivity to pulsars with $P_\mathrm{b} > P_\mathrm{b,crit}$ whose orbital accelerations were higher than anticipated. These latter two pulsars also showed the dependence of the S/N of each detection on the orbital phase φ at which each pulsar was observed, particularly in relation to the presence of jerk.

The $\sim 44\,\%$ of the survey processed in this thesis resulted in the discovery of 40 new pulsars, at least 7 of which appear to be in binary systems, with an additional 2 potentially falling into this category although at present their binary nature cannot be confirmed. 23 of the 40 pulsars have been sufficiently timed so as to develop fully phase-connected timing solutions, while the remaining 17 require additional observations. At least 20 of the new pulsars were re-detected in archival PMPS data, 13 with $\mathrm{S/N_{PMPS}}$ above the original noise floor of the survey, highlighting the value of continued re-analysis of older survey data as well as the value of re-observing regions of sky with ever-more sensitive survey and search techniques in order to detect new pulsars.

Of these 40 pulsars, a number stand out as objects of particular scientific interest (see Section 3.4). To name a few, PSRs J1537−5312 and J1547−5709 were both identified as fully-recycled millisecond pulsars (MSPs) with helium-white dwarf (He-WD) companions, and appear to be typical of members of this particular class of binary pulsar, possessing highly circular orbits with likely low angles of orbital inclination. PSR J1618−4624 was identified as a rarer MSP-WD binary class, possessing a likely carbon-oxygen-white dwarf (CO-WD) binary companion. The fully-recycled nature of PSR J1618−4624 (which has a spin period of only 5.93 ms), combined with a relatively short orbital period of only 1.78 d, appear to defy conventional models for the formation of such a CO-WD binary system, with PSR J1618−4624 possessing characteristics indicative of both Case A and Case C Roche lobe overflow (RLO) formation scenarios, presenting a significant puzzle regarding its evolutionary development. Meanwhile PSR J1653−45, while lacking a full timing solution, appears to be part of a binary system with a long orbital period on the order of months or years. The long apparent

eclipse experienced by this pulsar indicate that it may be similar to both PSR B1259−63 and PSR J1759−24, long-P_b binary pulsars around suspected or confirmed main sequence (MS) companions. PSR J1706−4434 was observed to experience a glitch close to MJD 57601, making it one of the ~ 170 pulsars known to have experienced glitches. PSR J1745−23 appears to be a 'black widow' MSP, which exists in a circular ~ 0.166-d orbit around a low-mass companion ($m_{c,min} \simeq 0.027\,M_\odot$) and experiences eclipses spanning approximately a quarter of its orbital period. Finally, PSRs J1812−15 and J1831−04 represent a pair of $\sim$ 1-s pulsars which both appear to experience either nulling or intermittent behaviour, and additionally both appear to exist in binary systems, although only the binary nature of PSR J1812−15 can be confirmed at present. Collectively, these and the remaining pulsar discoveries presented in this thesis represent a significant diversity of pulsar behaviour. They have the potential to shed new scientific insights into a number of astrophysical fields of research, including processes of binary evolution, plasma physics under extreme conditions and the behaviour of ultra-dense nuclear material, thereby demonstrating the merits of continuing to search for new pulsars, in that only by doing so can our understanding of these and other fields be further extended.

As already noted, the HTRU-S LowLat survey has been successful in exploring the low-luminosity region of the pulsar population, with two particular pulsars (PSRs J1753−28 and J1514−53) standing out as examples of a potentially unexplored population of nearby, very low-luminosity pulsars ripe for exploitation by next generation telescopes such as MeerKAT[1] and the Square Kilometre Array[2] (SKA). Additionally, the 46 pulsar discoveries reported within both this thesis and by Ng et al. (2015) for which characteristic ages (τ_c) can be determined appear to represent an older population of pulsars, standing in contrast to the background population of known pulsars within the survey region. Constrained measurements of P and $\dot{P}$ will allow for the characteristic ages of other pulsars from the survey to be calculated, which will assist in determining whether this old population is an artefact of small-number statistic or a genuine property of the survey discovery population. Finally, an evaluation of the survey yield (see Section 3.6) concludes that, as the processing of the HTRU-S LowLat survey nears completion, its final pulsar re-detection and discovery counts for both the 'normal' pulsars and MSPs have fallen below the earlier predictions of Keith et al. (2010), Levin et al. (2013) and Ng et al. (2015), with reasons for this deficit potentially including inadequate modeling of the anticipated pulsar population, the presence of radio frequency interference (RFI), red noise and other contaminating factors. The survey yield may also have been hindered by potential limitations in the search techniques themselves, including known limitations in the Fast Fourier Transform (FFT) (see Section 6.1.3).

[1] http://www.ska.ac.za/science-engineering/meerkat/
[2] https://skatelescope.org/

6.1.2 PSR J1757–1854

As the only relativistic binary to have been discovered in the HTRU-S LowLat survey, PSR J1757−1854 stands out as the flagship discovery both of the survey as a whole and of this thesis in particular. A 21.5-ms pulsar in a 4.4-hr orbit around a neutron star (NS) companion and with an eccentricity of $e = 0.61$, PSR J1757−1854 represents the most accelerated binary pulsar known to date, as well as one of the most relativistic, exceeding many of the properties of both the Hulse Taylor pulsar (PSR B1913+16 Hulse & Taylor, 1975a) and the Double Pulsar (PSR J0737−3039; Burgay et al., 2003; Lyne et al., 2004). Indeed, PSR J1757−1854 displays the strongest relativistic effects due to gravitational-wave (GW) damping yet seen in a binary pulsar, with a merger time of only 76 Myr. Its initial discovery in a half-segment of its HTRU-S LowLat discovery observation further validates the 'partially-coherent segmented acceleration search' technique as a means of detecting short-P_b, relativistic binary pulsars, especially given that later acceleration searches of the full-length observation showing a significant reduction in the detected S/N due to the presence of high jerk.

Following a 1.6-yr multi-frequency, multi-telescope campaign involving the Parkes 64-m Radio Telescope, the Jodrell Bank 76-m Lovell Telescope, the 100-m Effelsberg Radio Telescope and the 100-m Green Bank Telescope (GBT), five of PSR J1757−1854's post-Keplerian (PK) orbital parameters have already been measured significantly, including the rate of periastron advance $\dot{\omega}$, Einstein delay γ, orbital period derivative $\dot{P}_\mathrm{b}$ and orthometric Shapiro parameters h_3 and ς. These five PK parameters have allowed for three tests of gravity to be carried out which, although not as constraining as the tests available from other longer-studied relativistic pulsars such as PSR J0737−3039, the theory of general relativity (GR) still passes. The measured PK parameters also allow for the masses of the pulsar ($m_\mathrm{p} = 1.3384(9)\,\mathrm{M}_\odot$) and companion ($m_\mathrm{c} = 1.3946(9)\,\mathrm{M}_\odot$) NSs to be separated, along with an estimate of the inclination angle, $i = 84.0^{+0.4}_{-0.3}$ or $96.0^{+0.3}_{-0.4}$. The more-massive companion NS (which so far shows no evidence of radio pulsations) and the high orbital eccentricity provide additional clues as to likely formation scenarios for the neutron star, indicating a Case BB RLO scenario and a large kick from the second supernova explosion.

Combining the high eccentricity of the PSR B1913+16 combined with the shorter and more compact orbit of PSR J0737−3039, the properties of PSR J1757−1854 promise future tests of gravity in regimes which remain unexplored by earlier relativistic binary pulsars. In particular, the likelihood of a significant angle of misalignment between the spin vector of the pulsar and the orbital angular momentum means that PSR J1757−1854 is well suited to a measurement of the as-yet unmeasured Lense-Thirring precession effect via a measurement of its contribution to the rate of change of the semi-major axis, $\dot{x}_\mathrm{LT}$. Although an alternate Lense-Thirring test is available for PSR J0737−3039 (Kehl et al., 2016), the $\dot{x}_\mathrm{LT}$ test cannot be conducted using PSR J0737−3039 due to its extremely edge-on orbit. Similarly, the high eccentricity and high rate of periastron advance makes PSR J1757−1854 a uniquely suitable system for measuring the PK parameter δ_θ, which to date has only been measured to low significance in both PSR B1913+16 (Weisberg & Huang, 2016) and PSR J0737−3039

(Kramer et al., in prep.). With future timing observations (see Section 6.2.2.1), both of these measurements are expected to become possible within approximately $7-9$ years, allowing for significant new contributions to be made to the study of gravitational theories through the use of this relativistic binary pulsar.

6.1.3 The Fast Folding Algorithm

As highlighted by Lazarus et al. (2015), despite its widespread use as a fundamental component of most pulsar searching pipelines, the FFT is subject to significant limitations which hinder its ability to detect long-period pulsars ($P > 1\,\mathrm{s}$, in some cases for pulsars with $P > 100\,\mathrm{ms}$). This inherent bias in the FFT may have skewed our understanding of the underlying pulsar population. These limitations stem from the FFT's ability to only incoherently sum a limited number of harmonic frequencies, and its vulnerability to red noise. The final science chapter of this thesis presents a detailed study and evaluation of an alternative pulsar searching technique, the Fast Folding Algorithm (FFA) (Staelin, 1969), a time-domain searching technique with the potential to overcome these limitations of the FFT.

Following the development of a custom software implementation of the FFA, FFANCY, two algorithms were designed in order to evaluate the folded pulse profiles produced by the FFA and assess the likelihood of a pulsar detection. Both of these algorithms were extensively tested in the white-noise regime (describing the statistical distribution of the background, un-pulsed radio signal) under a variety of conditions, including changes in pulse height, width, shape, scattering and the number of pulse components in order to evaluate their behaviour. As implemented, Algorithm 1 (a boxcar matched-filter with median absolute deviation [MAD] normalisation) and Algorithm 2 (a boxcar matched-filter with an off-pulse window) showed markedly different performance characteristics, with the most significant difference being Algorithm 1's typically more-favourable response to wider pulse profiles than Algorithm 2. Large-scale tests designed to confirm and expand upon the earlier exploration of the FFA by Kondratiev et al. (2009) showed that both of these algorithms were capable of outperforming the FFT in the detection of long-period pulsars under the assumption of white noise.

In order to characterise the performance of the FFA and the chosen algorithms on real data, which is typically subject to additional contamination from sporadic RFI and the influence of red noise, a comparison against the FFT over a test set of 20 long-period pulsars selected from the HTRU-S LowLat pulsar survey was conducted. Coupled with a dynamic de-reddening scheme designed to combat the influence of red noise, the FFA was typically able to produce higher S/N detections of these pulsars than were produced by the FFT. Algorithm 1 exceeded the performance of the FFT in all but 3 cases, but also suffered from a large number of false-positive candidates, while Algorithm 2 typically only matched the performance of FFT, and was unable to re-detect 2 of the test pulsars. Based upon these results, and with continual advances in distributed-computing now opening the way for large-scale applications of the FFA to blind pulsar surveys, it is clear that the FFA has the potential to uncover a significant

population of pulsars to which the FFT was previously insensitive. With this in mind, a method of analysing the statistical significance of the S/N values produced by the FFA, a critical step in assessing the likelihood of pulsar candidates produced by the FFA when applied to a blind pulsar survey, was also presented.

6.2 Future work

6.2.1 Survey processing, and improvements in reprocessing

As noted in Section 3.1.4, the work conducted in this thesis brings the total amount of the HTRU-S LowLat survey which has been processed and searched for pulsars to $\sim 94\,\%$. Bringing the processed total to $100\,\%$ (while accounting for portions of the survey which may be unsearchable due to data corruption) is therefore a priority goal for ongoing work, as is reviewing the results of this processing for additional pulsar candidates. However, the $94\,\%$ of the survey processed to date also includes $\sim 15\,\%$ of the survey data which has yet to have been processed through the partially-coherent segmented acceleration search pipeline. As such, it is possible that this portion of the data may contain additional relativistic pulsars which, like PSR J1757−1854, are rendered much more easily detectable through the use of the segmented acceleration search technique and may have escaped earlier scrutiny. Therefore, reprocessing this portion of the survey with the segmented search pipeline so as to achieve a uniform first-pass processing of the HTRU-S LowLat survey will also form a priority goal for future work.

Following the completion of the first-pass processing, attention will naturally turn to additional reprocessing of the HTRU-S LowLat survey. Even with the ongoing Survey for Pulsars and Extragalactic Radio Bursts (SUPERB; Keane et al., 2018) and the advent of the next generation of pulsar surveys which will be enabled by telescopes such as MeerKAT and the SKA (see Section 6.2.4), the steady production of new pulsar discoveries and other key scientific results from the multiple reprocessings of the PMPS (see e.g. Keane et al., 2010; Eatough et al., 2010a, 2013a) clearly demonstrates the value in reprocessing legacy surveys with a variety of search techniques. These reprocessing efforts can aim to improve upon the shortcomings of previous search efforts, or to employ new search techniques which may be sensitive to different portions of the pulsar population.

With regard to the first of these goals, it is clear that despite the benefits presented by the partially-coherent segmented acceleration search technique in the search for short-P_b, relativistic binary pulsars, there remains room for further improvement. Some of these shortcomings, which were originally implemented as a means of improving the computational efficiency of the survey, can be trivially corrected for in future processing efforts. For example, as noted in Section 3.1.2.3, a significant portion of the survey has been processed with an acceleration-search gap between $|a| < 200\,\mathrm{m\,s^{-2}}$ in the quarter-segments. Although this gap was closed during later processing of the $44\,\%$ of the survey presented in this thesis, this represents a parameter space to which the partially-coherent segmented acceleration search was insensitive during much of the processing.

Similarly, although the design of this pipeline was specifically targeted towards the discovery of binary systems with $P_{\mathrm{b}} \leq P_{\mathrm{b,crit}} = 12\,\mathrm{h}$, the examples in Section 3.2.2 of PSRs J1435−6100 and J1802−2124 demonstrate that the acceleration search range of $|a| \leq 1\,\mathrm{m\,s^{-2}}$ applied to the full-segment search may be insufficiently large, and represents another parameter space to which the current design of the HTRU-S LowLat pipeline is insensitive. With continued advances in the computational processing power available for the processing of pulsar surveys, increasing the full-segment acceleration search range is unlikely to pose a significant problem in future reprocessing efforts.

However, perhaps the key shortcoming of this technique is its incoherent nature, in that it is not yet possible to coherently recombine the Fourier spectra (or the pulsar candidates themselves) from the individually-searched segments, so as to regain the flux-density sensitivity lost during the segmentation process. As a result, a highly-accelerated, short-P_{b} pulsar which (according to Equation 2.22) would be optimally detected by the time-domain resampling technique in a quarter- or eighth-segment, may still be undetected in those segments if it lacks sufficient flux density to be detectable above the noise floor of the survey, even if its flux density would have been sufficient for a detection when integrated across the entire 72-min observation. Currently, the development of a means of coherently searching the HTRU-S LowLat survey using a segmented search approach remains an ongoing research task.

Alternatively, it may soon to be possible to efficiently search the HTRU-S LowLat survey without the need for segmentation at all. With continued advances in available computational processing power (particularly the implementation of large-scale distributed-computing frameworks), future reprocessing of the HTRU-S LowLat survey may be able to search in terms of both acceleration *and* jerk, the mitigation of which was the primary motivation behind the segmentation process. Such a search technique would allow for each 72-min observation to be searched coherently and without the limitation of the $r_{\mathrm{orb}} \simeq 0.1$ rule-of-thumb imposed by Equation 2.22. Research efforts exploring the properties and limitations of such a technique are currently underway at the MPIfR and other research institutions. The application of this and other binary search techniques (which may also open up the $P_{\mathrm{b}} < 1.5\,\mathrm{h}$ parameter space currently unexplored by the partially-coherent segmented acceleration search) will form a core part of any future reprocessing of the HTRU-S LowLat survey.

Finally, although the search for relativistic binary pulsars will always remain a primary goal for future reprocessing, additional pulsar discoveries are likely to be enabled by the application of alternative searching techniques. For example, a single-pulse search of the HTRU-S LowLat survey, sensitive to transient sources such as rotating radio transient pulsars (RRATs) and fast radio bursts (FRBs) is already underway (Bhandari et al., in prep.), and has already resulted in the discovery of at least two (as-yet unpublished) pulsars in the $\sim 50\,\%$ of the survey processed using this search technique. Additionally, as has been noted throughout this thesis, limitations in the FFT are likely to have limited the detection of long-period pulsars due in part to red-noise contamination, a particular problem in the case of the 72-min observations of the HTRU-S LowLat survey. Future reprocessing by the FFA (further described in Section 6.2.3) is likely to allow for the discovery of yet-more pulsars within the HTRU-S

LowLat survey.

6.2.2 Ongoing pulsar timing and additional follow-up

Another region in which there is clear scope for ongoing scientific work is in the follow-up and continued scientific exploitation of the 40 newly-discovered pulsars reported in this thesis. Much of this work will rely upon the availability of continued timing observations of these pulsars, as 17 of the discovered pulsars so far lack full timing solutions which can only be developed with the incorporation of additional pulse times of arrival (TOAs). In the majority of these unsolved pulsars, constructing and refining their solutions will rely less on increasing the sensitivity of each observation than it will rely on observing each pulsar with a sufficiently-high cadence over a sufficiently-long timespan so as to separate and solve the effects of each unconstrained timing parameter. The current lack of solutions for these 17 pulsars limits our ability to determine their individual underlying behaviour and, as discussed in Section 3.5, also limits our understanding of the properties of the pulsar population which the HTRU-S LowLat survey has uncovered. Determining additional phase-connected timing solutions, incorporating well-constrained measurements of P and $\dot{P}$, will for example assist in resolving the question (raised in Section 3.5.3) of whether the pulsars discovered by the HTRU-S LowLat survey truly represent an older population of pulsars, or whether this apparent trend is simply a result of small-number statistics. This scientific need for the development of additional timing solutions also applies to the 27 as-yet unsolved pulsars reported by Ng et al. (2015), although it is likely that sufficient timing data to solve these pulsars now exists, with only the analysis itself remaining.

The need for full timing solutions is particularly important in the case of the three unsolved binary pulsars reported in this thesis (PSRs J1653−45, J1745−23 and J1812−15), as well the two suspected binary pulsars (PSRs J1726−29 and J1831−04). In the case of PSR J1653−45, ongoing monitoring will be necessary until the pulsar becomes detectable once again, after which its long apparent orbital period means that monthly-cadence observations should be sufficient in order to develop both an orbital and timing solution. Such a solution, combined with a constrained duration of the suspected eclipse, will shed additional light on the nature of the binary companion. For the black widow PSR J1745−23, high-cadence observations spanning several orbits within a timescale of days or weeks will be critical in obtaining an initial orbital solution, and a timing model such as the BTX model (see e.g. Shaifullah et al., 2016) will likely be required in order to handle the long-timescale orbital variabilities inherent in a black widow system. Finally, in the cases of PSRs J1812−15 and J1831−04, both of which experience either nulling or intermittent behaviour, the development of binary and timing solutions will require as high a cadence of follow-up observations as can be justified in order to successfully detect them during their ‘on’ phase. While this is likely to be an easier endeavour in the case of PSR J1812−15 given its lower nulling fraction (NF), it is important that both of these pulsars eventually be solved, as along with PSR J1753−45, they represent a rarer class of long-P binary pulsar (see e.g. Figure 1.7). Given the significant accelerations detected in both PSR J1812−15 and

PSR J1831−04, and an inferred P_b range for each pulsar on the order of days to weeks (based on Equation 2.22), it is possible that both PSR J1812−15 and PSR J1831−04 may represent objects of some scientific interest at the very least in terms of their evolutionary history.

Ongoing timing observations of those pulsars for which phase-coherent solutions already do exist may also be useful in shedding further scientific insight on their behaviour. For example, the observed glitch in PSR J1706−4434 may not have been an isolated event, and ongoing monitoring may detect the presence of additional glitches, contributing further to the body of knowledge regarding glitching pulsars. If PSR J1706−4434 is seen to glitch regularly, higher cadence observations may be warranted so as to better localise each glitch in time as it occurs and hopefully measure the presence of the exponential relaxation in spin period which is typically observed immediately following a glitch event (see Section 1.4.3). Meanwhile, ongoing monitoring of PSR J1822−0902 will assist in modeling the timing noise so far observed in this pulsar. Should the apparent periodicity present in the timing noise continue, it may represent an additional unsolved binary system. Finally, the curious evolutionary history CO-WD MSP posed by PSR J1618−4624 suggests that this pulsar may also benefit from additional timing follow-up. Although upper limits on the eccentricity of this pulsar have been measured (see Table 3.8), constraining a precise value of the eccentricity may provide additional clues in determining its evolutionary past, as would any future constraint on the pulsar's proper motion. These measurements will likely require higher-precision TOAs than are currently available from the Parkes timing setup as described in Table 3.5. Instead, new receivers such as the ultra-wideband receiver (UWB; Manchester, 2015) currently being commissioned at Parkes (which covers a frequency range between $0.7 - 4$ GHz), as well as potential timing campaigns with next-generation telescopes such as MeerKAT and the SKA, may be able to provide the required increase in timing precision.

A number of additional follow-up projects for the 40 pulsars reported within this thesis also extend beyond mere timing observations. For example, the majority of the pulsars reported in this thesis have only been observed at a central frequency of 1.4 GHz, also known as 'L-band'. Multi-wavelength studies focusing both on higher (e.g. ~ 2 GHz) and lower (e.g. ~ 800 MHz) radio frequencies may assist in constraining the role played by scattering in producing some of the wider pulse profiles observed among the pulsars reported in this thesis (see Figure 3.7). As with the example of PSR J1757−1854 (for which the majority of TOAs are derived from observations at the ~ 2 GHz 'S-band' frequency range), such multi-wavelength studies may also indicate additional frequencies suitable for pulsar timing. Considering observations beyond just the radio frequencies, optical observations may also be useful in a number of cases. In the case of the three MSP-WD binary systems reported in this thesis, it may be possible to optically identify their WD candidates (see e.g. Cadelano et al., 2015; Swiggum et al., 2017). Such observations may be able to provide significant additional information regarding the evolutionary and binary properties of each of these systems, but as noted in Section 3.4.1, the location of these three MSP-WD binary systems within the ISM-dense Galactic plane may make optical identification of their WD companions

difficult. A similar optical identification should also be attempted of the suspected MS companion to PSR J1653−45, however as an accurate position for this pulsar has not yet been determined via timing measurements, such an identification should ideally be left until after the development of a phase-connected timing solution in order to reduce the potential for confusion when identifying potential optical counterparts.

Finally, with regard to the discussion of the properties of the HTRU-S LowLat pulsar population presented in Section 3.5, two additional analyses remain to be performed as part of future work. The first of these involves an investigation of potential high-energy counterpart sources to the pulsars reported in this thesis, particularly with regard to gamma-ray sources detected by the Large Area Telescope (LAT; Abdo et al., 2009) installed on the *Fermi Gamma-Ray Space Telescope*. Gamma-ray associations are typically expected for those pulsars with high spin-down luminosities, in the case of young pulsars where $\dot{E} \gtrsim 10^{34}\,\mathrm{erg\,s^{-1}}$ (see e.g. Thompson, 2008; Abdo et al., 2013). A search for Fermi-counterpart sources which are spatially coincident with the 23 solved pulsars reported in this thesis, along with evidence of periodicity matching the phase-connected timing models developed for these pulsars, is currently underway and will be reported on in a future publication. In addition, cross-checking the 40 pulsars reported in this thesis for the presence of any supernova remnant (SNR) associations is also planned for a future publication, although given that none of the pulsars with a well-measured P and $\dot{P}$ display a $\tau_\mathrm{c} < 10^5\,\mathrm{yr}$, and the anticipated lifetime of an SNR is typically on the order of $10^4\,\mathrm{yr}$ (Frail et al., 1994), such an association appears unlikely.

6.2.2.1 Follow-up of PSR J1757–1854

By far the most important follow-up work to be conducted revolves around the relativistic binary PSR J1757−1854. As highlighted in Chapter 4, PSR J1757−1854 promises to deliver a number of significant new scientific results within the coming years, including constrained measurements of the PK parameter δ_θ and the Lense-Thirring contribution to the rate of change of the semi-major axis, $\dot{x}_\mathrm{LT}$. The predicted $7-9$ year timeframe for measuring both of these parameters assumes both a continuation of the current timing setup used in the observations of this pulsar across all four telescopes employed in its ongoing timing, as well as the inclusion of monthly MeerKAT timing observations (employing the MeerKAT S-band receivers with an available bandwidth between $1.7-35\,\mathrm{GHz}$)) from mid-2018 onwards. The availability of the high-precision TOAs afforded by additional MeerKAT (and eventually SKA) observations, which comes as a direct result of the additional gain and bandwidth provided by the setup, will be a fundamental determinant in the timescale required for the measurement of both $\dot{x}_\mathrm{LT}$ and δ_θ. Backing up these MeerKAT observations will be the improved TOA-precision afforded both by the Versatile GBT Astronomical Spectrometer (VEGAS), a new GBT backend capable of pulsar timing across a 1.5-GHz bandwidth, and (to a lesser extent) the aforementioned Parkes UWB. However, the problems in correctly de-dispersing the signal of a relativistic binary pulsar such as PSR J1757−1854 across increasingly large bandwidths (as discussed briefly in Section 4.3.1) may limit the degree to which these new and increasingly-sensitive observing setups may be exploited in the study of this

pulsar.

Beyond these high-priority goals, ongoing regular observations of PSR J1757−1854 will also enable a number of other important projects to be pursued. For example, the same higher-precision TOAs from future timing campaigns will be advantageous in further constraining the five PK parameters which have already been measured, particularly in the case of the Shapiro delay parameters h_3 and ς, for which each newly-observed orbit of the pulsar adds additional constraint. Constraints on the other PK parameters, such as ω and $\dot{P}_\mathrm{b}$, will be more strongly dependent on the duration over which the pulsar continues to be observed, as the parameters of its orbit continue to evolve with time. Refining each of these PK parameters will assist in further constraining the 3 tests of gravity already available from the system. In addition, PSR J1757−1854 is predicted under GR to geodetically precess at a rate of approximately $\Omega_\mathrm{SO} = 3.1^\circ\,\mathrm{yr}^{-1}$. Although no evidence of this effect has yet been seen, ongoing timing observations should eventually reveal the presence of the secular profile changes expected from this effect, allowing for a measurement of Ω_SO to be made and a fourth test of gravity to be conducted.

Finally, as noted in Section 4.3.3, no pulsations from PSR J1757−1854's companion NS have been detected thus far, despite an exhaustive search effort. Multiple reasons for this non-detection exist, the most straightforward being that the unrecycled companion NS has simply evolved through the P-$\dot{P}$ diagram to the point where it is no longer capable of producing radio pulsations (see Section 1.4). However, as demonstrated by the existence of PSR J0737−3039B (the unrecycled NS in the Double Pulsar), this may not necessarily be the case. The companion NS could either possess too low a luminosity to be detectable by current instrumentation and search techniques, or it may emit only at certain orbital phases (see e.g. PSR J0737−3039B; Lyne et al., 2004), or it may precess into view in the future due to the effects of geodetic precession (Perera et al., 2010). In each of these scenarios, the only means by which the companion NS may eventually be detected as a pulsar is to continue regular search-mode observations, which will once again benefit from the same technology improvements and next-generation telescopes already outlined with regard to the other future research goals of PSR J1757−1854. Should a detection of the companion NS be made it would greatly enhance the scientific utility of this particular binary system.

6.2.3 Developing the Fast Folding Algorithm

A discussion regarding the potential future work to be carried out in developing and implementing the FFA has already been largely presented in Sections 5.5 and 5.6. To summarise, immediate future steps include the implementation of more advanced RFI-mitigation techniques, including options for multibeam excision and possible 'persistence' scores used to isolate pulse-profile contamination from sporadic RFI, as well as researching and implementing additional red-noise mitigation techniques. Additionally, despite their success of the profile evaluation algorithms developed for this thesis, both Algorithms 1 and 2 still contain room for improvement. Both algorithms were designed to search for pulsars with narrow duty cycles, which while typical of the long-period

pulsar population (Taylor et al., 1993) may cause scientifically-interesting candidates with naturally-wide pulse profiles such as the magnetar PSR J1622−4950 to be overlooked. Algorithm 1 was also noted to be susceptible to the influence of red noise due its more favourable response to wider pulse profiles than Algorithm 2, producing large numbers of false-positive pulsar candidates. The development of additional, improved pulsar searching algorithms, and the potential future incorporation of machine-learning techniques as an alternative means of profile evaluation, remain promising avenues of further research.

With these caveats for future development of the FFA in mind, the next logical step is to begin the application of the FFA onto large-scale, blind pulsar surveys. While FFANCY (the implementation of the FFA developed for this thesis) was not designed or optimised with this task in mind, other implementations of the FFA designed to take advantage of the power of distributed-computing frameworks are already being deployed. This includes the planned GPU-based successor to FFANCY (known as ffaster) which remains under development, as well as the FFA implementation currently in operation in the processing of the SUPERB survey (Keane et al., 2018) which has already resulted in the discovery of 9 new pulsars (Morello et al., submitted). Therefore, it would seem that with continuing development and implementation, the FFA is poised to make a significant scientific contribution to the current and next generation of pulsar surveys.

6.2.4 Next generation surveys

The field of radio astronomy is currently at a turning point, with a new generation of radio telescopes currently under development. These next-generation telescopes promise to revolutionise the sensitivity of future pulsar surveys well beyond the capabilities of current-generation surveys such as HTRU and SUPERB, but also present considerable challenges both in terms of their physical engineering requirements and in terms of processing the formidable volumes of data that they are expected to produce. The first of these projects is the Five-hundred-meter Aperture Spherical Telescope[3] (FAST), a Chinese, Arecibo-style telescope on which construction has only recently been completed. With its sheer physical dimensions giving the telescope a significantly higher gain over the Arecibo telescope, and equipped with both a wideband single-pixel receiver (with a frequency range from 270 MHz to 1.6 GHz) and a (shortly-anticipated) 19-beam receiver (configured in 3 hexagonal rings with one central beam), FAST is already making its first pulsar discoveries (Li et al., in prep., Champion & Cruz, private communication). Future pulsar surveys are currently in the planning stages, and are expected to commence within the very near future. However, at present the telescope remains in a testing and commissioning phase, and is currently capable of only limited source tracking.

While FAST will be capable of observing the northern skies, the MeerKAT array currently under construction and commissioning in South Africa will open up new

[3] http://fast.bao.ac.cn/en/

windows on pulsar and transient searching in the southern skies. An array of 64, 13.5-m offset-Gregorian dishes, with a maximum baseline between these dishes of 8 km, MeerKAT will be the most sensitive radio telescope in the southern hemisphere, with a sensitivity equivalent to a single 110-m dish (Kramer et al., 2015) and a frequency range spanning $0.58 - 14.5$ GHz (Brederode et al., 2016). The Transients and Pulsars with MeerKAT[4] (TRAPUM) search project has already been allocated significant observing time on MeerKAT even as it comes online, and the full array is expected to commence operations in mid-2018.

MeerKAT itself is the precursor telescope to the long-proposed SKA, the result of an international collaboration spanning 10 core member countries. Components of the telescope will be built in both South Africa (upgrading and expanding the existing MeerKAT array) and Australia (hosting the low-frequency component of the telescope), with construction implemented across two phases (Shao et al., 2015). The unprecedented sensitivity of the telescope is expected to uncover approximately 10−30,000 new pulsars (Keane et al., 2015), vastly improving our understanding of the pulsar population, with a similar improvement expected in pulsar timing capabilities. Initial observations are expected to begin using a limited subset of the telescope in 2020, with full operations commencing in the mid 2020's.

6.3 Final remarks

As with all science, continued innovation and experimentation lie at the heart of the ongoing scientific progress and achievements that have been made in the field of pulsar astronomy. This thesis has explored two such innovative techniques that are designed for pulsar searching, the partially-coherent segmented acceleration search and the FFA. The application of the former technique to the HTRU-S LowLat survey has demonstrated both its merits and limitations in the search for relativistic binary pulsars for which it was designed, and has resulted in the discovery of one of the most relativistic binary pulsars discovered to date, a pulsar which promises significant future contributions to the study and constraint of gravitational theories. 39 other pulsars, many with their own individual scientific merits, have also been discovered through the work conducted on the HTRU-S LowLat survey using this search technique. Meanwhile the FFA, while itself an older search technique, has been shown to be a viable means of discovering additional pulsars in a parameter space to which other search techniques are insensitive, with continued progress in computational technology finally allowing the technique an opportunity to meet its full potential. With the lessons learned and scientific progress made within this thesis, along with the dawn of the next-generation of radio telescopes and pulsar surveys, ongoing innovation in pulsar searching techniques will ensure that the field of pulsar astronomy continues to produce new and exciting scientific results for many years to come.

[4] http://www.trapum.org/

Bibliography

Abbott B. P., et al., 2016, Phys. Rev. Lett., 116, 061102 (Cited on pages 16, 37 and 152.)

Abbott B. P., et al., 2017a, preprint, (arXiv:1710.09320) (Cited on page 37.)

Abbott B. P., et al., 2017b, Phys. Rev. Lett., 119, 161101 (Cited on pages 16, 37 and 152.)

Abdo A. A., et al., 2009, Science, 325, 840 (Cited on pages 33 and 216.)

Abdo A. A., et al., 2013, ApJS, 208, 17 (Cited on page 216.)

Ables J. G., Manchester R. N., 1976, A&A, 50, 177 (Cited on page 24.)

Adámek K., Armour W., 2016, preprint, (arXiv:1611.09704) (Cited on pages 48 and 166.)

Alpar M. A., Anderson P. W., Pines D., Shaham J., 1981, ApJ, 249, L29 (Cited on page 35.)

Alpar M. A., Cheng A. F., Ruderman M. A., Shaham J., 1982, Nature, 300, 728 (Cited on page 30.)

Anderson P. W., Itoh N., 1975, Nature, 256, 25 (Cited on page 35.)

Antoniadis J., 2014, ApJ, 797, L24 (Cited on pages 33 and 38.)

Antoniadis J., van Kerkwijk M. H., Koester D., Freire P. C. C., Wex N., Tauris T. M., Kramer M., Bassa C. G., 2012, MNRAS, 423, 3316 (Cited on page 15.)

Antoniadis J., et al., 2013, Science, 340, 448 (Cited on pages 15 and 37.)

Archibald A. M., et al., 2009, Science, 324, 1411 (Cited on page 34.)

Armstrong J. W., Rickett B. J., Spangler S. R., 1995, ApJ, 443, 209 (Cited on page 26.)

Baade W., Zwicky F., 1934, Physical Review, 46, 76 (Cited on page 8.)

Bachetti M., et al., 2014, Nature, 514, 202 (Cited on page 10.)

Backer D. C., 1970a, Nature, 228, 42 (Cited on page 34.)

Backer D. C., 1970b, Nature, 228, 1297 (Cited on page 35.)

Backer D. C., 1975, A&A, 43, 395 (Cited on page 28.)

Backer D. C., 1976, ApJ, 209, 895 (Cited on page 183.)

Backer D. C., Kulkarni S. R., Heiles C., Davis M. M., Goss W. M., 1982, Nature, 300, 615 (Cited on pages 9 and 87.)

Bailes M., et al., 2011, Science, 333, 1717 (Cited on pages 94 and 95.)

Barker B. M., O'Connell R. F., 1975, Phys. Rev. D, 12, 329 (Cited on page 15.)

Barr E. D., et al., 2013, MNRAS, 435, 2234 (Cited on pages 66, 91, 94 and 95.)

Barr E. D., Freire P. C. C., Kramer M., Champion D. J., Berezina M., Bassa C. G., Lyne A. G., Stappers B. W., 2017, MNRAS, 465, 1711 (Cited on pages 33 and 38.)

Bassa C. G., et al., 2016, MNRAS, 456, 2196 (Cited on pages 122 and 154.)

Bassa C. G., et al., 2017, ApJ, 846, L20 (Cited on page 146.)

Bates S. D., et al., 2011, MNRAS, 416, 2455 (Cited on page 94.)

Bates S. D., et al., 2012, MNRAS, 427, 1052 (Cited on pages 94, 146 and 204.)

Bates S. D., Lorimer D. R., Verbiest J. P. W., 2013, MNRAS, 431, 1352 (Cited on page 42.)

Bates S. D., Lorimer D. R., Rane A., Swiggum J., 2014, MNRAS, 439, 2893 (Cited on page 148.)

Bates S. D., et al., 2015, MNRAS, 446, 4019 (Cited on page 94.)

Baym G., Pethick C., Pines D., Ruderman M., 1969, Nature, 224, 872 (Cited on page 35.)

Belczynski K., Kalogera V., Bulik T., 2002, ApJ, 572, 407 (Cited on pages 101 and 153.)

Berezina M., et al., 2017, MNRAS, 470, 4421 (Cited on page 95.)

Berti E., et al., 2015, Classical and Quantum Gravity, 32, 243001 (Cited on page 11.)

Bertotti B., Iess L., Tortora P., 2003, Nature, 425, 374 (Cited on page 15.)

Bhat N. D. R., Cordes J. M., Camilo F., Nice D. J., Lorimer D. R., 2004, ApJ, 605, 759 (Cited on pages 26, 183 and 184.)

Bhat N. D. R., Bailes M., Verbiest J. P. W., 2008, Phys. Rev. D, 77, 124017 (Cited on page 116.)

Bhattacharya D., van den Heuvel E. P. J., 1991, Phys. Rep., 203, 1 (Cited on pages 30 and 32.)

Bhattacharyya B., et al., 2016, ApJ, 817, 130 (Cited on page 97.)

Biggs J. D., 1992, ApJ, 394, 574 (Cited on page 149.)

Bignami G. F., Caraveo P. A., De Luca A., Mereghetti S., 2003, Nature, 423, 725 (Cited on page 23.)

Bisnovatyi-Kogan G. S., Komberg B. V., 1974, Soviet Ast., 18, 217 (Cited on page 32.)

Blandford R., Teukolsky S. A., 1976, ApJ, 205, 580 (Cited on page 80.)

Bombaci I., 1996, A&A, 305, 871 (Cited on page 19.)

Bower G. C., et al., 2015, ApJ, 798, 120 (Cited on page 36.)

Brady M. L., 1998, SIAM Journal on Computing, 27, 107 (Cited on page 204.)

Brederode L. R., van den Heever L., Esterhuyse W., Jonas J. L., 2016, in Ground-based and Airborne Telescopes VI. p. 990625, doi:10.1117/12.2231602 (Cited on page 219.)

Breton R. P., et al., 2008, Science, 321, 104 (Cited on pages 15 and 152.)

Burbidge E. M., Burbidge G. R., Fowler W. A., Hoyle F., 1957, Rev. Mod. Phys., 29, 547 (Cited on page 18.)

Burgay M., et al., 2003, Nature, 426, 531 (Cited on pages 12, 32, 91, 101, 152 and 210.)

Burgay M., et al., 2006, MNRAS, 368, 283 (Cited on page 91.)

Burgay M., et al., 2013a, MNRAS, 429, 579 (Cited on page 91.)

Burgay M., et al., 2013b, MNRAS, 433, 259 (Cited on page 94.)

Burke-Spolaor S., et al., 2011, MNRAS, 416, 2465 (Cited on pages 48, 94 and 166.)

Burns W. R., Clark B. G., 1969, A&A, 2, 280 (Cited on pages 56 and 167.)

Cadelano M., Pallanca C., Ferraro F. R., Salaris M., Dalessandro E., Lanzoni B., Freire P. C. C., 2015, ApJ, 812, 63 (Cited on page 215.)

Cameron A. D., Barr E. D., Champion D. J., Kramer M., Zhu W. W., 2017, MNRAS, 468, 1994 (Cited on page 163.)

Camilo F., Nice D. J., Taylor J. H., 1996, ApJ, 461, 812 (Cited on page 33.)

Camilo F., Lorimer D. R., Freire P., Lyne A. G., Manchester R. N., 2000, ApJ, 535, 975 (Cited on pages 63 and 65.)

Camilo F., et al., 2001, ApJ, 548, L187 (Cited on page 116.)

Camilo F., Manchester R. N., Gaensler B. M., Lorimer D. R., 2002, ApJ, 579, L25 (Cited on pages 30, 113 and 115.)

Camilo F., Ransom S. M., Halpern J. P., Reynolds J., Helfand D. J., Zimmerman N., Sarkissian J., 2006, Nature, 442, 892 (Cited on page 36.)

Camilo F., Ransom S. M., Halpern J. P., Reynolds J., 2007, ApJ, 666, L93 (Cited on pages 36, 113 and 115.)

Cerutti B., Beloborodov A. M., 2017, Space Sci. Rev., 207, 111 (Cited on page 38.)

Chamel N., Haensel P., Zdunik J. L., Fantina A. F., 2013, International Journal of Modern Physics E, 22, 1330018 (Cited on page 19.)

Champion D. J., et al., 2008, Science, 320, 1309 (Cited on pages 33 and 96.)

Champion D. J., et al., 2016, MNRAS, 460, L30 (Cited on page 95.)

Chandrasekhar S., 1931, ApJ, 74, 81 (Cited on page 18.)

Chen K., Ruderman M., 1993, ApJ, 402, 264 (Cited on pages 29 and 30.)

Chen H.-L., Chen X., Tauris T. M., Han Z., 2013, ApJ, 775, 27 (Cited on page 133.)

Clifton T. R., Lyne A. G., 1986, Nature, 320, 43 (Cited on page 87.)

Clifton T. R., Lyne A. G., Jones A. W., McKenna J., Ashworth M., 1992, MNRAS, 254, 177 (Cited on page 87.)

Coburn W., Heindl W. A., Rothschild R. E., Gruber D. E., Kreykenbohm I., Wilms J., Kretschmar P., Staubert R., 2002, ApJ, 580, 394 (Cited on page 23.)

Coenen T., et al., 2014, A&A, 570, A60 (Cited on page 97.)

Cooley J. W., Tukey J. W., 1965, 19, 297 (Cited on page 56.)

Cordes J. M., 2002, in Stanimirovic S., Altschuler D., Goldsmith P., Salter C., eds, Astronomical Society of the Pacific Conference Series Vol. 278, Single-Dish Radio Astronomy: Techniques and Applications. pp 227–250 (Cited on page 28.)

Cordes J. M., Lazio T. J. W., 2002, ArXiv Astrophysics e-prints, (Cited on pages 26, 120, 123, 124, 125 and 157.)

Cordes J. M., Lazio T. J. W., 2003, ArXiv Astrophysics e-prints, (Cited on pages 26 and 123.)

Cordes J. M., McLaughlin M. A., 2003, ApJ, 596, 1142 (Cited on pages 166, 168 and 169.)

Cordes J. M., et al., 2006, ApJ, 637, 446 (Cited on pages 96, 149 and 164.)

Craft H. D., Sutton J. M., Comella J. M., 1968, Nature, 219, 1237 (Cited on page 165.)

Crawford F., Lorimer D. R., Devour B. M., Takacs B. P., Kondratiev V. I., 2009, ApJ, 696, 574 (Cited on page 165.)

Dai S., et al., 2015, MNRAS, 449, 3223 (Cited on page 139.)

Damour T., Deruelle N., 1985, Ann. Inst. Henri Poincaré Phys. Théor., 43, 107 (Cited on pages 83, 86 and 160.)

Damour T., Deruelle N., 1986, Ann. Inst. Henri Poincaré Phys. Théor., 44, 263 (Cited on pages 83, 84, 86 and 160.)

Damour T., Schafer G., 1988, Nuovo Cimento B Serie, 101, 127 (Cited on page 15.)

Damour T., Taylor J. H., 1992, Phys. Rev. D, 45, 1840 (Cited on pages 11, 16, 83, 84 and 160.)

Davies J. G., Large M. I., 1970, MNRAS, 149, 301 (Cited on page 86.)

Davies J. G., Large M. I., Pickwick A. C., 1970, Nature, 227, 1123 (Cited on page 86.)

Davies J. G., Lyne A. G., Seiradakis J. H., 1973, Nature Physical Science, 244, 84 (Cited on page 86.)

DeCesar M. E., Ransom S. M., Kaplan D. L., Ray P. S., Geller A. M., 2015, ApJ, 807, L23 (Cited on page 66.)

Demorest P. B., Pennucci T., Ransom S. M., Roberts M. S. E., Hessels J. W. T., 2010, Nature, 467, 1081 (Cited on page 37.)

Deneva J. S., Stovall K., McLaughlin M. A., Bates S. D., Freire P. C. C., Martinez J. G., Jenet F., Bagchi M., 2013, ApJ, 775, 51 (Cited on page 97.)

Deneva J. S., et al., 2016, ApJ, 821, 10 (Cited on page 97.)

Desvignes G., Kramer M., Cognard I., Kasian L., van Leeuwen J., Stairs I., Theureau G., 2013a, in van Leeuwen J., ed., IAU Symposium Vol. 291, Neutron Stars and Pulsars: Challenges and Opportunities after 80 years. pp 199–202 (arXiv:1211.3937), doi:10.1017/S1743921312023630 (Cited on page 15.)

Desvignes G., Cognard I., Champion D., Lazarus P., Lespagnol P., Smith D. A., Theureau G., 2013b, in van Leeuwen J., ed., IAU Symposium Vol. 291, Neutron Stars and Pulsars: Challenges and Opportunities after 80 years. pp 375–377 (arXiv:1211.3936), doi:10.1017/S1743921312024179 (Cited on page 96.)

Devine T. R., Goseva-Popstojanova K., McLaughlin M., 2016, MNRAS, 459, 1519 (Cited on pages 48 and 166.)

Dewey R. J., Taylor J. H., Weisberg J. M., Stokes G. H., 1985, ApJ, 294, L25 (Cited on page 72.)

Duncan R. C., Thompson C., 1992, ApJ, 392, L9 (Cited on page 36.)

Dyson F. W., Eddington A. S., Davidson C., 1920, Philosophical Transactions of the Royal Society of London Series A, 220, 291 (Cited on page 11.)

Eatough R. P., Molkenthin N., Kramer M., Noutsos A., Keith M. J., Stappers B. W., Lyne A. G., 2010a, MNRAS, 407, 2443 (Cited on pages 90 and 212.)

Eatough R. P., Molkenthin N., Kramer M., Noutsos A., Keith M. J., Stappers B. W., Lyne A. G., 2010b, MNRAS, 407, 2443 (Cited on page 204.)

Eatough R. P., Kramer M., Lyne A. G., Keith M. J., 2013a, MNRAS, 431, 292 (Cited on pages 64, 66, 90, 105, 148, 153 and 212.)

Eatough R. P., et al., 2013b, Nature, 501, 391 (Cited on page 36.)

Edwards R. T., Bailes M., van Straten W., Britton M. C., 2001, MNRAS, 326, 358 (Cited on page 91.)

Edwards R. T., Hobbs G. B., Manchester R. N., 2006, MNRAS, 372, 1549 (Cited on pages 72 and 74.)

Einstein A., 1915a, Sitzungsberichte der Königlich Preußischen Akademie der Wissenschaften (Berlin), Seite 844-847., (Cited on page 10.)

Einstein A., 1915b, Sitzungsber. preuss.Akad. Wiss., vol. 47, No.2, pp. 831-839, 1915, 47, 831 (Cited on page 11.)

Einstein A., 1916, Annalen der Physik, 354, 769 (Cited on page 11.)

Espinoza C. M., Lyne A. G., Stappers B. W., Kramer M., 2011, MNRAS, 414, 1679 (Cited on pages 35 and 132.)

Espinoza C. M., Lyne A. G., Stappers B. W., 2017, MNRAS, 466, 147 (Cited on page 22.)

Faucher-Giguère C.-A., Kaspi V. M., 2006, ApJ, 643, 332 (Cited on pages 30 and 39.)

Faulkner A. J., et al., 2004, MNRAS, 355, 147 (Cited on pages 33, 67, 90 and 165.)

Ferdman R. D., et al., 2010, ApJ, 711, 764 (Cited on page 116.)

Foster R. S., Fairhead L., Backer D. C., 1991, ApJ, 378, 687 (Cited on page 73.)

Frail D. A., Goss W. M., Whiteoak J. B. Z., 1994, ApJ, 437, 781 (Cited on pages 30 and 216.)

Freire P. C. C., 2013, in van Leeuwen J., ed., IAU Symposium Vol. 291, Neutron Stars and Pulsars: Challenges and Opportunities after 80 years. pp 243–250 (arXiv:1210.3984), doi:10.1017/S1743921312023770 (Cited on page 38.)

Freire P. C. C., Wex N., 2010, MNRAS, 409, 199 (Cited on pages 86 and 156.)

Freire P. C., Kramer M., Lyne A. G., 2001, MNRAS, 322, 885 (Cited on pages 80 and 81.)

Freire P. C. C., et al., 2011, MNRAS, 412, 2763 (Cited on page 33.)

Freire P. C. C., et al., 2012, MNRAS, 423, 3328 (Cited on pages 15 and 152.)

Fruchter A. S., Stinebring D. R., Taylor J. H., 1988, Nature, 333, 237 (Cited on page 34.)

Glendenning N. K., 1992, Phys. Rev. D, 46, 4161 (Cited on page 19.)

Gold T., 1968, Nature, 218, 731 (Cited on page 8.)

Goldreich P., Julian W. H., 1969, ApJ, 157, 869 (Cited on pages 20 and 38.)

Gonthier P. L., Ouellette M. S., Berrier J., O'Brien S., Harding A. K., 2002, ApJ, 565, 482 (Cited on page 28.)

Gotthelf E. V., Vasisht G., Boylan-Kolchin M., Torii K., 2000, ApJ, 542, L37 (Cited on page 30.)

Götz W., Druckmüller H., 1996, Pattern Recognition, 29, 711 (Cited on page 204.)

Goussard J.-O., Haensel P., Zdunik J. L., 1998, A&A, 330, 1005 (Cited on page 19.)

Graikou E., Verbiest J. P. W., Osłowski S., Champion D. J., Tauris T. M., Jankowski F., Kramer M., 2017, MNRAS, 471, 4579 (Cited on page 128.)

Han J., 2013, in van Leeuwen J., ed., IAU Symposium Vol. 291, Neutron Stars and Pulsars: Challenges and Opportunities after 80 years. pp 223–228 (arXiv:1210.7029), doi:10.1017/S174392131202371X (Cited on page 38.)

Hankins T. H., 1971, ApJ, 169, 487 (Cited on page 47.)

Hankins T. H., Rickett B. J., 1975, in Alder B., Fernbach S., Rotenberg M., eds, Vol. 14, Methods in Computational Physics. Volume 14 - Radio astronomy. pp 55–129 (Cited on page 47.)

Haslam C. G. T., Klein U., Salter C. J., Stoffel H., Wilson W. E., Cleary M. N., Cooke D. J., Thomasson P., 1981, A&A, 100, 209 (Cited on page 93.)

Heger A., Fryer C. L., Woosley S. E., Langer N., Hartmann D. H., 2003, ApJ, 591, 288 (Cited on page 17.)

Hessels J. W. T., Ransom S. M., Stairs I. H., Freire P. C. C., Kaspi V. M., Camilo F., 2006, Science, 311, 1901 (Cited on pages 9 and 19.)

Hewish A., Bell S. J., Pilkington J. D. H., Scott P. F., Collins R. A., 1968, Nature, 217, 709 (Cited on pages 7, 8, 24 and 86.)

Ho W. C. G., Andersson N., 2012, Nature Physics, 8, 787 (Cited on page 23.)

Hobbs G., et al., 2004, MNRAS, 352, 1439 (Cited on page 90.)

Hobbs G. B., Edwards R. T., Manchester R. N., 2006, MNRAS, 369, 655 (Cited on pages 74, 122 and 156.)

Hobbs G., Lyne A. G., Kramer M., 2010, MNRAS, 402, 1027 (Cited on page 22.)

Hotan A. W., van Straten W., Manchester R. N., 2004, PASA, 21, 302 (Cited on pages 68, 122 and 154.)

Hulse R. A., Taylor J. H., 1974, ApJ, 191, L59 (Cited on page 87.)

Hulse R. A., Taylor J. H., 1975a, ApJ, 195, L51 (Cited on pages 8, 12, 87, 152 and 210.)

Hulse R. A., Taylor J. H., 1975b, ApJ, 201, L55 (Cited on page 87.)

Ihm C. M., Kalogera V., Belczynski K., 2006, ApJ, 652, 540 (Cited on page 32.)

Israel G. L., et al., 2017a, Science, 355, 817 (Cited on page 10.)

Israel G. L., et al., 2017b, MNRAS, 466, L48 (Cited on page 10.)

Jackson J. D., 1962, Classical Electrodynamics (Cited on page 22.)

Jacoby B. A., Bailes M., Ord S. M., Edwards R. T., Kulkarni S. R., 2009, ApJ, 699, 2009 (Cited on page 91.)

Jenet F. A., Hobbs G. B., Lee K. J., Manchester R. N., 2005, ApJ, 625, L123 (Cited on page 37.)

Jia K., Li X.-D., 2015, ApJ, 814, 74 (Cited on page 34.)

Johnston S., Karastergiou A., 2017, MNRAS, 467, 3493 (Cited on page 28.)

Johnston H. M., Kulkarni S. R., 1991, ApJ, 368, 504 (Cited on pages 63, 64 and 153.)

Johnston S., Lyne A. G., Manchester R. N., Kniffen D. A., D'Amico N., Lim J., Ashworth M., 1992a, MNRAS, 255, 401 (Cited on page 87.)

Johnston S., Manchester R. N., Lyne A. G., Bailes M., Kaspi V. M., Qiao G., D'Amico N., 1992b, ApJ, 387, L37 (Cited on page 129.)

Jouteux S., Ramachandran R., Stappers B. W., Jonker P. G., van der Klis M., 2002, A&A, 384, 532 (Cited on page 67.)

Kaspi V. M., 2004, in Camilo F., Gaensler B. M., eds, IAU Symposium Vol. 218, Young Neutron Stars and Their Environments. p. 231 (`arXiv:astro-ph/0402175`) (Cited on page 36.)

Kaspi V. M., et al., 2000, ApJ, 543, 321 (Cited on page 90.)

Keane E. F., Ludovici D. A., Eatough R. P., Kramer M., Lyne A. G., McLaughlin M. A., Stappers B. W., 2010, MNRAS, 401, 1057 (Cited on pages 90 and 212.)

Keane E. F., Kramer M., Lyne A. G., Stappers B. W., McLaughlin M. A., 2011, MNRAS, 415, 3065 (Cited on page 90.)

Keane E., et al., 2015, Advancing Astrophysics with the Square Kilometre Array (AASKA14), p. 40 (Cited on page 219.)

Keane E. F., et al., 2018, MNRAS, 473, 116 (Cited on pages 66, 95, 212 and 218.)

Kehl M. S., Wex N., Kramer M., Liu K., 2016, preprint, (arXiv:1605.00408) (Cited on pages 16, 37, 160 and 210.)

Keith M. J., Kramer M., Lyne A. G., Eatough R. P., Stairs I. H., Possenti A., Camilo F., Manchester R. N., 2009a, MNRAS, 393, 623 (Cited on page 90.)

Keith M. J., Eatough R. P., Lyne A. G., Kramer M., Possenti A., Camilo F., Manchester R. N., 2009b, MNRAS, 395, 837 (Cited on page 90.)

Keith M. J., et al., 2010, MNRAS, 409, 619 (Cited on pages 17, 39, 41, 50, 88, 91, 94, 102, 107, 111, 148, 152, 188 and 209.)

Keith M. J., et al., 2012, MNRAS, 419, 1752 (Cited on page 94.)

King A. R., Beer M. E., Rolfe D. J., Schenker K., Skipp J. M., 2005, MNRAS, 358, 1501 (Cited on page 34.)

Kluzniak W., Ruderman M., Shaham J., Tavani M., 1988, Nature, 334, 225 (Cited on page 34.)

Knispel B., et al., 2013, ApJ, 774, 93 (Cited on page 90.)

Kocz J., Bailes M., Barnes D., Burke-Spolaor S., Levin L., 2012, MNRAS, 420, 271 (Cited on pages 53 and 102.)

Kondratiev V. I., McLaughlin M. A., Lorimer D. R., Burgay M., Possenti A., Turolla R., Popov S. B., Zane S., 2009, ApJ, 702, 692 (Cited on pages x, 165, 166, 169, 172, 173, 174, 175, 205 and 211.)

Kramer M., 1998, ApJ, 509, 856 (Cited on pages 15 and 160.)

Kramer M., 2016, International Journal of Modern Physics D, 25, 1630029 (Cited on page 160.)

Kramer M., Champion D. J., 2013, Classical and Quantum Gravity, 30, 224009 (Cited on page 37.)

Kramer M., Stairs I. H., 2008, ARA&A, 46, 541 (Cited on page 38.)

Kramer M., Wielebinski R., Jessner A., Gil J. A., Seiradakis J. H., 1994, A&AS, 107, 515 (Cited on page 73.)

Kramer M., Xilouris K. M., Lorimer D. R., Doroshenko O., Jessner A., Wielebinski R., Wolszczan A., Camilo F., 1998, ApJ, 501, 270 (Cited on pages 72 and 139.)

Kramer M., et al., 2003, MNRAS, 342, 1299 (Cited on page 90.)

Kramer M., Lyne A. G., O'Brien J. T., Jordan C. A., Lorimer D. R., 2006a, Science, 312, 549 (Cited on page 35.)

Kramer M., et al., 2006b, Science, 314, 97 (Cited on pages 12, 16, 86, 152 and 160.)

Kramer M., et al., 2006c, Annalen der Physik, 518, 34 (Cited on page 86.)

Kramer M., Kraus A., Wieching G., 2015, IAU General Assembly, 22, 2256564 (Cited on page 219.)

Lange C., Camilo F., Wex N., Kramer M., Backer D. C., Lyne A. G., Doroshenko O., 2001, MNRAS, 326, 274 (Cited on page 80.)

Large M. I., Vaughan A. E., Mills B. Y., 1968a, Nature, 220, 340 (Cited on page 8.)

Large M. I., Vaughan A. E., Wielebinski R., 1968b, Nature, 220, 753 (Cited on pages 86 and 87.)

Large M. I., Vaughan A. E., Wielebinski R., 1969, Astrophys. Lett., 3, 123 (Cited on page 86.)

Lattimer J. M., Prakash M., 2001, ApJ, 550, 426 (Cited on pages 18 and 19.)

Lattimer J. M., Schutz B. F., 2005, ApJ, 629, 979 (Cited on pages 37 and 160.)

Lattimer J. M., Prakash M., Masak D., Yahil A., 1990, ApJ, 355, 241 (Cited on page 19.)

Lazarus P., et al., 2014, MNRAS, 437, 1485 (Cited on page 33.)

Lazarus P., et al., 2015, ApJ, 812, 81 (Cited on pages 39, 50, 72, 96, 149, 164, 165 and 211.)

Lazarus P., Karuppusamy R., Graikou E., Caballero R. N., Champion D. J., Lee K. J., Verbiest J. P. W., Kramer M., 2016, MNRAS, 458, 868 (Cited on page 154.)

Lee K. J., et al., 2013, MNRAS, 433, 688 (Cited on page 203.)

Levin L., et al., 2010, ApJ, 721, L33 (Cited on pages 36, 94, 95 and 188.)

Levin L., et al., 2013, MNRAS, 434, 1387 (Cited on pages 33, 148 and 209.)

Lewandowski W., Dembska M., Kijak J., Kowalińska M., 2013, MNRAS, 434, 69 (Cited on page 26.)

Lin J., Rappaport S., Podsiadlowski P., Nelson L., Paxton B., Todorov P., 2011, ApJ, 732, 70 (Cited on page 128.)

Lorimer D. R., 2008, Living Reviews in Relativity, 11 (Cited on page 31.)

Lorimer D. R., 2011, SIGPROC: Pulsar Signal Processing Programs, Astrophysics Source Code Library (ascl:1107.016) (Cited on pages 47 and 122.)

Lorimer, D. R. and Kramer, M. 2005, Handbook of Pulsar Astronomy. Cambridge University Press (Cited on pages 7, 18, 19, 20, 21, 26, 28, 32, 35, 43, 46, 55, 60, 61, 62, 64, 69, 72, 73, 75, 80, 83, 153, 164, 167, 183, 184 and 200.)

Lorimer D. R., et al., 2004, MNRAS, 347, L21 (Cited on page 33.)

Lorimer D. R., et al., 2006a, MNRAS, 372, 777 (Cited on pages 33, 90, 148 and 165.)

Lorimer D. R., et al., 2006b, ApJ, 640, 428 (Cited on pages 15 and 96.)

Lorimer D. R., Bailes M., McLaughlin M. A., Narkevic D. J., Crawford F., 2007, Science, 318, 777 (Cited on page 95.)

Lorimer D. R., Camilo F., McLaughlin M. A., 2013, MNRAS, 434, 347 (Cited on page 91.)

Losovsky B. Y., Dumsky D. V., 2014, Astronomy Reports, 58, 537 (Cited on page 165.)

Lovelace R. V. E., Sutton J. M., Salpeter E. E., 1969, Nature, 222, 231 (Cited on page 167.)

Lynch R. S., Bank North Celestial Cap Survey Collaborations 2013, in van Leeuwen J., ed., IAU Symposium Vol. 291, Neutron Stars and Pulsars: Challenges and Opportunities after 80 years. pp 41–46 (arXiv:1303.5316), doi:10.1017/S1743921312023113 (Cited on page 97.)

Lynch R. S., et al., 2013, ApJ, 763, 81 (Cited on page 15.)

Lyne A. G., Rickett B. J., 1968, Nature, 219, 1339 (Cited on page 28.)

Lyne A. G., Brinklow A., Middleditch J., Kulkarni S. R., Backer D. C., 1987, Nature, 328, 399 (Cited on page 9.)

Lyne A. G., et al., 1998, MNRAS, 295, 743 (Cited on page 87.)

Lyne A. G., et al., 2000, MNRAS, 312, 698 (Cited on page 90.)

Lyne A. G., et al., 2004, Science, 303, 1153 (Cited on pages 12, 32, 91, 101, 152, 210 and 217.)

Lyne A., Hobbs G., Kramer M., Stairs I., Stappers B., 2010, Science, 329, 408 (Cited on pages 35 and 38.)

Lyne A. G., Stappers B. W., Keith M. J., Ray P. S., Kerr M., Camilo F., Johnson T. J., 2015, MNRAS, 451, 581 (Cited on page 33.)

Lyne A. G., et al., 2017a, ApJ, 834, 72 (Cited on page 134.)

Lyne A. G., et al., 2017b, ApJ, 834, 137 (Cited on page 96.)

Lyon R. J., Stappers B. W., Cooper S., Brooke J. M., Knowles J. D., 2016, MNRAS, 459 (Cited on pages 68 and 97.)

Maggiore M., 2000, Phys. Rep., 331, 283 (Cited on page 37.)

Maitia V., Lestrade J.-F., Cognard I., 2003, ApJ, 582, 972 (Cited on page 38.)

Manchester R. N., 2015, IAU General Assembly, 22, 2256190 (Cited on page 215.)

Manchester R. N., IPTA 2013, Classical and Quantum Gravity, 30, 224010 (Cited on page 37.)

Manchester R. N., Taylor J. H., 1972, ApL, 10, 67 (Cited on page 24.)

Manchester R. N., Lyne A. G., Taylor J. H., Durdin J. M., Large M. I., Little A. G., 1978, MNRAS, 185, 409 (Cited on page 87.)

Manchester R. N., et al., 1996, MNRAS, 279, 1235 (Cited on page 87.)

Manchester R. N., et al., 2001, MNRAS, 328, 17 (Cited on pages 66, 88, 90, 95, 107, 126, 153 and 207.)

Manchester R. N., Hobbs G. B., Teoh A., Hobbs M., 2005, AJ, 129, 1993 (Cited on pages 7, 103 and 176.)

Manchester R. N., et al., 2010, ApJ, 710, 1694 (Cited on page 15.)

Manchester R. N., et al., 2013, PASA, 30, e017 (Cited on page 37.)

Martinez J. G., et al., 2015, ApJ, 812, 143 (Cited on page 159.)

McCulloch P. M., Hamilton P. A., Ables J. G., Hunt A. J., 1983, Nature, 303, 307 (Cited on page 10.)

McLaughlin M. A., 2013, Classical and Quantum Gravity, 30, 224008 (Cited on page 37.)

McLaughlin M. A., et al., 2006, Nature, 439, 817 (Cited on page 90.)

McMillan P. J., 2017, MNRAS, 465, 76 (Cited on page 161.)

Middleditch J., Kristian J., 1984, ApJ, 279, 157 (Cited on pages 63 and 153.)

Middleditch J., Deich W., Kulkarni S., 1993, in van Riper K. A., Epstein R. I., Ho C., eds, Isolated Pulsars. p. 372 (Cited on page 57.)

Morris D. J., et al., 2002, MNRAS, 335, 275 (Cited on page 90.)

Ng C. W. Y., 2014, PhD thesis, Rheinische Friedrich-Wilhelms-Universität, Bonn (Cited on pages 30, 53, 60, 92, 93, 94, 101, 104 and 106.)

Ng C., et al., 2014, MNRAS, 439, 1865 (Cited on page 94.)

Ng C., et al., 2015, MNRAS, 450, 2922 (Cited on pages 4, 17, 48, 53, 64, 65, 66, 94, 99, 101, 102, 105, 107, 109, 110, 111, 113, 114, 115, 116, 128, 129, 141, 142, 143, 146, 148, 152, 153, 188, 191, 207, 208, 209, 214, 241 and 248.)

Nice D. J., Fruchter A. S., Taylor J. H., 1995, ApJ, 449, 156 (Cited on page 87.)

Nice D. J., et al., 2013, ApJ, 772, 50 (Cited on page 96.)

Olausen S. A., Kaspi V. M., 2014, ApJS, 212, 6 (Cited on pages 29 and 36.)

Ollivier M., Maurel M.-C., 2014, BIO Web of Conferences, 2, 00001 (Cited on page 10.)

Oppenheimer J. R., Volkoff G. M., 1939, Physical Review, 55, 374 (Cited on page 18.)

Özel F., Freire P., 2016, ARA&A, 54, 401 (Cited on pages 18 and 19.)

Pacini F., 1967, Nature, 216, 567 (Cited on page 8.)

Perera B. B. P., et al., 2010, ApJ, 721, 1193 (Cited on pages 15 and 217.)

Peters P. C., 1964, Physical Review, 136, 1224 (Cited on page 12.)

Petroff E., et al., 2014, ApJ, 789, L26 (Cited on page 96.)

Petroff E., et al., 2015a, MNRAS, 447, 246 (Cited on page 95.)

Petroff E., et al., 2015b, MNRAS, 451, 3933 (Cited on page 49.)

Petroff E., et al., 2015c, MNRAS, 454, 457 (Cited on page 95.)

Phinney E. S., Kulkarni S. R., 1994, ARA&A, 32, 591 (Cited on pages 30 and 32.)

Portegies Zwart S., van den Heuvel E. P. J., van Leeuwen J., Nelemans G., 2011, ApJ, 734, 55 (Cited on page 33.)

Press W. H., 2006, Proceedings of the National Academy of Sciences, 103, 19249 (Cited on page 204.)

Prinz T., Becker W., 2015, preprint, (`arXiv:1511.07713`) (Cited on page 115.)

Radhakrishnan V., Manchester R. N., 1969, Nature, 222, 228 (Cited on page 35.)

Rankin J. M., 1983, ApJ, 274, 333 (Cited on page 183.)

Ransom S. M., 2001, PhD thesis, Harvard University (Cited on pages 47, 67, 122, 156 and 171.)

Ransom S. M., Greenhill L. J., Herrnstein J. R., Manchester R. N., Camilo F., Eikenberry S. S., Lyne A. G., 2001, ApJ, 546, L25 (Cited on page 66.)

Ransom S. M., Eikenberry S. S., Middleditch J., 2002, AJ, 124, 1788 (Cited on pages 57, 58, 66 and 153.)

Ransom S. M., Cordes J. M., Eikenberry S. S., 2003, ApJ, 589, 911 (Cited on page 67.)

Ransom S. M., Backer D. C., Demorest P., Kaspi V. M., Ramachandran R., Arons J., Spitkovsky A., 2004, ArXiv Astrophysics e-prints, (Not cited.)

Ransom S. M., Demorest P., Ford J., McCullough R., Ray J., DuPlain R., Brandt P., 2009, in American Astronomical Society Meeting Abstracts #214. p. 605.08 (Cited on page 154.)

Ransom S. M., et al., 2014, Nature, 505, 520 (Cited on pages 33 and 38.)

Reardon D. J., et al., 2016, MNRAS, 455, 1751 (Cited on page 32.)

Roberts M. S. E., 2013, in van Leeuwen J., ed., IAU Symposium Vol. 291, Neutron Stars and Pulsars: Challenges and Opportunities after 80 years. pp 127–132 (arXiv:1210.6903), doi:10.1017/S174392131202337X (Cited on pages 34 and 132.)

Rohlfs K., Wilson T. L., 2000, Tools of radio astronomy (Cited on page 43.)

Ruderman M., 1976, ApJ, 203, 213 (Cited on page 35.)

Ruderman M., Shaham J., Tavani M., 1989, ApJ, 336, 507 (Cited on page 34.)

Scheuer P. A. G., 1968, Nature, 218, 920 (Cited on pages 26 and 28.)

Segelstein D. J., Rawley L. A., Stinebring D. R., Fruchter A. S., Taylor J. H., 1986, Nature, 322, 714 (Cited on page 87.)

Seidelmann P. K., Fukushima T., 1992, A&A, 265, 833 (Cited on page 74.)

Sesana A., 2013, Classical and Quantum Gravity, 30, 244009 (Cited on page 37.)

Shaifullah G., et al., 2016, MNRAS, 462, 1029 (Cited on pages 133 and 214.)

Shannon R. M., Cordes J. M., 2010, ApJ, 725, 1607 (Cited on page 22.)

Shao L., et al., 2015, Advancing Astrophysics with the Square Kilometre Array (AASKA14), p. 42 (Cited on page 219.)

Shao L., Sennett N., Buonanno A., Kramer M., Wex N., 2017, Physical Review X, 7, 041025 (Cited on pages 16 and 152.)

Shapiro I. I., 1964, Physical Review Letters, 13, 789 (Cited on pages 11 and 84.)

Shapiro S. L., Teukolsky S. A., Wasserman I., 1983, ApJ, 272, 702 (Cited on page 9.)

Shemar S. L., Lyne A. G., 1996, MNRAS, 282, 677 (Cited on page 35.)

Shibazaki N., Murakami T., Shaham J., Nomoto K., 1989, Nature, 342, 656 (Cited on page 32.)

Sigurdsson S., Richer H. B., Hansen B. M., Stairs I. H., Thorsett S. E., 2003, Science, 301, 193 (Cited on page 33.)

Sobey C., et al., 2015, MNRAS, 451, 2493 (Cited on page 35.)

Spitler L. G., et al., 2016, Nature, 531, 202 (Cited on page 95.)

Spruit H., Phinney E. S., 1998, Nature, 393, 139 (Cited on page 20.)

Staelin D. H., 1969, IEEE Proceedings, 57, 724 (Cited on pages 60, 62, 149, 164, 167, 171 and 211.)

Staelin D. H., Reifenstein III E. C., 1968, Science, 162, 1481 (Cited on pages 8 and 30.)

Stairs I. H., Splaver E. M., Thorsett S. E., Nice D. J., Taylor J. H., 2000, MNRAS, 314, 459 (Cited on page 46.)

Stairs I. H., Thorsett S. E., Taylor J. H., Wolszczan A., 2002, ApJ, 581, 501 (Cited on page 159.)

Stairs I. H., Thorsett S. E., Arzoumanian Z., 2004, Physical Review Letters, 93, 141101 (Cited on page 15.)

Staveley-Smith L., et al., 1996, PASA, 13, 243 (Cited on pages 88, 102 and 154.)

Steiner A. W., Lattimer J. M., Brown E. F., 2013, ApJ, 765, L5 (Cited on page 19.)

Stokes G. H., Taylor J. H., Welsberg J. M., Dewey R. J., 1985, Nature, 317, 787 (Cited on page 87.)

Stokes G. H., Segelstein D. J., Taylor J. H., Dewey R. J., 1986, ApJ, 311, 694 (Cited on page 87.)

Stovall K., et al., 2014, ApJ, 791, 67 (Cited on pages 66 and 97.)

Stovall K., et al., 2016, ApJ, 833, 192 (Cited on page 23.)

Sutton J. M., 1971, MNRAS, 155, 51 (Cited on page 28.)

Swiggum J. K., et al., 2017, ApJ, 847, 25 (Cited on page 215.)

Tauris T. M., 2011, in Schmidtobreick L., Schreiber M. R., Tappert C., eds, Astronomical Society of the Pacific Conference Series Vol. 447, Evolution of Compact Binaries. p. 285 (arXiv:1106.0897) (Cited on pages 127, 128 and 133.)

Tauris T. M., 2012, Science, 335, 561 (Cited on page 23.)

Tauris T. M., Savonije G. J., 1999, A&A, 350, 928 (Cited on page 127.)

Tauris T. M., van den Heuvel E. P. J., 2006, Formation and evolution of compact stellar X-ray sources. pp 623–665 (Cited on pages 30, 32 and 33.)

Tauris T. M., van den Heuvel E. P. J., 2014, ApJ, 781, L13 (Cited on page 127.)

Tauris T. M., Langer N., Kramer M., 2011, MNRAS, 416, 2130 (Cited on page 128.)

Tauris T. M., Langer N., Kramer M., 2012, MNRAS, 425, 1601 (Cited on page 128.)

Tauris T. M., Langer N., Moriya T. J., Podsiadlowski P., Yoon S.-C., Blinnikov S. I., 2013, ApJ, 778, L23 (Cited on page 159.)

Tauris T. M., Langer N., Podsiadlowski P., 2015, MNRAS, 451, 2123 (Cited on page 159.)

Tauris T. M., et al., 2017, ApJ, 846, 170 (Cited on pages 32 and 159.)

Tayler, R. J. 1994, The Stars: their structure and evolution. Cambridge University Press (Cited on page 17.)

Taylor J. H., 1987, in MacCallum M. A. H., ed., General Relativity and Gravitation. pp 209–222 (Cited on pages 86 and 156.)

Taylor J. H., Huguenin G. R., 1969, Nature, 221, 816 (Cited on page 58.)

Taylor J. H., Stinebring D. R., 1986, ARA&A, 24, 285 (Cited on page 9.)

Taylor J. H., Weisberg J. M., 1982, ApJ, 253, 908 (Cited on pages 12 and 156.)

Taylor J. H., Weisberg J. M., 1989, ApJ, 345, 434 (Cited on pages 83, 86 and 156.)

Taylor J. H., Hulse R. A., Fowler L. A., Gullahorn G. E., Rankin J. M., 1976, ApJ, 206, L53 (Cited on page 12.)

Taylor J. H., Fowler L. A., McCulloch P. M., 1979, Nature, 277, 437 (Cited on page 12.)

Taylor J. H., Manchester R. N., Lyne A. G., 1993, ApJS, 88, 529 (Cited on pages 169 and 218.)

Thompson D. J., 2008, Reports on Progress in Physics, 71, 116901 (Cited on page 216.)

Thompson C., Duncan R. C., 1995, MNRAS, 275, 255 (Cited on page 36.)

Thornton D., et al., 2013, Science, 341, 53 (Cited on page 95.)

Thorsett S. E., Arzoumanian Z., Camilo F., Lyne A. G., 1999, ApJ, 523, 763 (Cited on page 33.)

Tiburzi C., et al., 2013, MNRAS, 436, 3557 (Cited on pages 113 and 115.)

Torne P., et al., 2017, MNRAS, 465, 242 (Cited on page 36.)

Turtle A. J., Vaughan A. E., 1968, Nature, 219, 689 (Cited on page 86.)

Vaughan A. E., Large M. I., 1972, MNRAS, 156, 27P (Cited on page 86.)

Wang Z., Archibald A. M., Thorstensen J. R., Kaspi V. M., Lorimer D. R., Stairs I., Ransom S. M., 2009, ApJ, 703, 2017 (Cited on page 34.)

Weber F., 2005, Progress in Particle and Nuclear Physics, 54, 193 (Cited on page 20.)

Weisberg J. M., Huang Y., 2016, ApJ, 829, 55 (Cited on pages 12, 13, 84, 160 and 210.)

Weisberg J. M., Romani R. W., Taylor J. H., 1989, ApJ, 347, 1030 (Cited on page 15.)

Weisberg J. M., Nice D. J., Taylor J. H., 2010, ApJ, 722, 1030 (Cited on page 12.)

Weltevrede P., et al., 2010, ApJ, 708, 1426 (Cited on page 115.)

Wex N., 2014, preprint, (arXiv:1402.5594) (Cited on pages 10, 11, 12, 15, 16, 36 and 152.)

Wielebinski R., Vaughan A. E., Large M. I., 1969, Nature, 221, 47 (Cited on page 87.)

Will C. M., 2014, Living Reviews in Relativity, 17, 4 (Cited on pages 11 and 12.)

Wolszczan A., 1994, Science, 264, 538 (Cited on page 10.)

Wolszczan A., Frail D. A., 1992, Nature, 355, 145 (Cited on page 10.)

Woods P. M., Thompson C., 2006, Soft gamma repeaters and anomalous X-ray pulsars: magnetar candidates. pp 547–586 (Cited on page 36.)

Woosley S. E., Weaver T. A., 1986, ARA&A, 24, 205 (Cited on page 17.)

Yao J. M., Manchester R. N., Wang N., 2017, ApJ, 835, 29 (Cited on pages 26, 120, 123, 124, 125, 143 and 157.)

Young M. D., Manchester R. N., Johnston S., 1999, Nature, 400, 848 (Cited on page 30.)

Young N. J., Weltevrede P., Stappers B. W., Lyne A. G., Kramer M., 2015, MNRAS, 449, 1495 (Cited on page 35.)

Yuan J. P., Manchester R. N., Wang N., Wang J. B., Zhou X., Yan W. M., Liu Z. Y., 2017, MNRAS, 466, 1234 (Cited on page 35.)

Yuen R., Melrose D. B., 2017, MNRAS, 469, 2049 (Cited on page 38.)

Zhang B., Harding A. K., Muslimov A. G., 2000, ApJ, 531, L135 (Cited on page 30.)

Zhu W. W., et al., 2014, ApJ, 781, 117 (Cited on pages 68 and 204.)

Zolotukhin I. Y., Bachetti M., Sartore N., Chilingarian I. V., Webb N. A., 2017, ApJ, 839, 125 (Cited on page 10.)

van Heerden E., Karastergiou A., Roberts S. J., 2017, MNRAS, 467, 1661 (Cited on page 53.)

van Straten W., Bailes M., 2011, PASA, 28, 1 (Cited on pages 122 and 154.)

van Straten W., Demorest P., Oslowski S., 2012, Astronomical Research and Technology, 9, 237 (Cited on page 68.)

van der Klis M., 1989, in Ögelman H., van den Heuvel E. P. J., eds, NATO Advanced Science Institutes (ASI) Series C Vol. 262, NATO Advanced Science Institutes (ASI) Series C. p. 27 (Cited on page 57.)

Appendices

Appendix A

Known pulsar re-detections in 44 % of the HTRU-S Low Latitude Survey

Table A.1: Catalogue of the 390 unique pulsars re-detected in the 44 % of the HTRU-S LowLat survey processed for this thesis project. For each pulsar, we list the published galactic longitude (l) and latitude (b), as well as the survey beam in which the pulsar was detected and the offset (θ) in position between the pulsar and the center of the beam. Also listed are the observed spin period ($P_{\rm obs}$) and dispersion measure ($\mathrm{DM_{obs}}$), along with the expected apparent pulsar flux density at 1.4 GHz ($S_{\rm exp}$) and the expected S/N ($\mathrm{S/N_{exp}}$), which are calculated via the method described in Section 3.2. Finally, the observed S/N ($\mathrm{S/N_{obs}}$) of each re-detection is also listed. In the case where a pulsar was detected in multiple telescope beams, the detection with the smallest offset is listed. For those pulsars where the positions of all telescope beams in which the pulsar was re-detected are sufficiently ambiguous to prevent the calculation of an accurate offset, the detection with the highest observed $\mathrm{S/N_{obs}}$ is listed instead. Instances where either the offset, $S_{\rm exp}$ or $\mathrm{S/N_{exp}}$ were unable to be calculated (either due to position ambiguity or due to the pulsar having no published flux density) are marked by an asterix (*). Finally, we also indicate instances where the pulsar was detected at a harmonic period, as well as instances where a re-detection with a smaller θ was achieved in the 50 % of the survey processed by Ng et al. (2015).

PSR name	l (°)	b (°)	Pointing/Beam	θ (°)	$P_{\rm obs}$ (ms)	$\mathrm{DM_{obs}}$ ($\mathrm{cm^{-3}\,pc}$)	$S_{\rm exp}$ (mJy)	$\mathrm{S/N_{exp}}$	$\mathrm{S/N_{obs}}$
B1011−58[a]	283.706	−2.144	2012-09-05-20:01:28/04	0.174	819.924	379.0	0.4	108.0	83.9
B1015−56[a]	282.732	0.341	2012-07-23-23:59:36/09	0.112	503.462	433.2	1.5	354.0	265.3
B1030−58[a]	285.907	−0.98	2012-09-24-21:37:39/04	0.189	464.210	415.2	0.2	38.6	40.2
B1044−57[a]	287.065	0.733	2012-09-05-21:14:20/08	0.120	369.428	240.0	0.5	92.8	89.7
B1046−58	287.425	0.577	2012-08-05-00:16:37/03	0.119	123.714	127.8	3.2	484.0	498.7
B1056−57	288.345	1.948	2012-07-22-02:45:38/02	0.103	1185.003	102.1	0.7	187.0	155.7
B1112−60[a]	291.443	−0.322	2011-10-10-19:28:50/09	0.343	880.854	679.3	0.0	0.7	26.6
B1124−60[a]	292.834	0.292	2011-10-10-19:28:50/06	0.135	202.737	280.3	0.4	82.1	108.6
B1131−62	294.213	−1.296	2011-12-29-13:44:28/06	0.142	1022.887	563.5	1.0	59.5	114.8
B1143−60[a]	294.977	1.343	2012-07-16-04:15:06/09	0.289	273.374	110.0	0.1	7.0	72.6
B1154−62[a]	296.705	−0.199	2011-07-14-02:00:27/01	0.178	400.525	321.1	1.2	255.0	204.8
B1221−63	299.984	−1.415	2012-04-13-09:24:34/07	0.187	216.480	95.8	0.7	128.0	234.6
B1222−63[a]	300.131	−1.414	2012-04-13-09:24:34/07	0.176	419.619	409.8	0.1	18.5	27.8
B1302−64	304.411	−2.092	2012-04-09-10:16:41/10	0.090	571.651	494.9	1.1	160.0	152.5
B1303−66	304.462	−3.463	2011-12-13-00:15:24/10	0.076	473.033	438.3	1.9	230.0	325.3
B1323−62[a]	307.074	0.204	2011-07-14-03:13:57/11	0.141	529.927	316.9	5.8	1110.0	1330.4
B1323−627[a]	306.966	−0.429	2011-12-08-02:26:00/07	0.135	196.480	295.9	1.3	223.0	139.6
B1323−63	306.748	−1.534	2011-12-07-17:28:25/11	0.084	792.671	494.9	1.0	230.0	137.7

B1334−61	308.373	0.305	2011-12-14-16:44:34/10	0.063	1239.000	652.0	3.1	305.0	332.6
B1336−64	308.047	−2.557	2012-07-25-07:03:11/09	0.075	378.627	74.9	0.8	118.0	84.8
B1338−62	308.73	−0.035	2011-10-10-21:55:27/04	0.113	193.448	720.4	1.0	128.0	114.8
B1353−62	310.474	−0.565	2011-12-30-15:53:41/08	0.033	455.778	417.8	8.2	1080.0	977.7
B1356−60[a]	311.239	1.126	2011-12-13-17:27:21/08	0.129	127.508	293.9	3.2	510.0	604.3
B1436−63	314.646	−3.384	2012-02-18-22:54:57/03	0.020	459.606	124.8	0.8	173.0	197.3
B1449−64	315.733	−4.427	2012-08-04-04:17:32/13	0.393	179.487	70.5	0.0	1.0	41.3
B1508−57[a]	320.772	−0.108	2012-04-10-11:32:06/01	0.183	128.699	628.0	1.1	152.0	208.7
B1509−58	320.321	−1.162	2012-04-12-10:21:05/13	0.082	151.674	254.6	0.7	54.3	59.7
B1518−58[a]	321.63	−1.215	2012-08-01-10:10:14/13	0.149	395.354	195.6	1.4	204.0	205.3
B1530−53[a]	325.716	1.944	2012-01-18-17:03:10/08	0.126	1368.888	18.4	3.0	759.0	214.1
B1530−539	325.463	1.483	2012-04-01-12:46:07/09	0.116	289.690	191.1	0.6	116.0	88.7
B1535−56[a]	324.621	−0.806	2011-12-13-02:44:07/12	0.167	243.395	175.8	1.1	160.0	101.0
B1541−52[a]	327.271	1.32	2012-04-02-12:00:23/11	0.338	178.554	33.3	0.0	1.8	22.4
B1550−54	327.186	−0.901	2011-12-27-03:23:56/04	0.112	1081.344	227.0	0.4	95.9	31.7
B1555−55	327.238	−2.024	2012-07-26-04:53:20/05	0.099	957.262	211.3	0.4	150.0	127.7
B1556−57[a]	325.971	−3.697	2012-08-06-09:44:21/05	0.175	194.456	179.6	0.3	39.6	45.1
B1557−50	330.69	1.631	2011-12-06-20:26:28/07	0.081	192.604	263.2	12.1	2380.0	1197.0
B1558−50	330.688	1.286	2011-10-11-00:22:09/10	0.059	864.275	170.8	4.8	1390.0	347.1
B1600−49	332.152	2.442	2012-07-24-05:18:06/02	0.105	327.418	141.4	3.1	895.0	416.4
B1601−52	329.732	−0.484	2012-08-03-05:51:26/03	0.095	658.014	34.5	8.2	867.0	894.6
B1607−52	330.923	−0.482	2012-08-03-05:51:26/11	0.151	182.495	128.8	0.4	94.8	52.4
B1609−47[a]	334.573	2.835	2011-12-28-19:51:40/06	0.175	382.377	161.3	0.3	64.9	33.2
B1610−50	332.206	0.172	2012-07-24-09:40:05/12	0.079	231.917	583.0	1.8	219.0	150.4
B1626−47	336.403	0.562	2011-12-30-19:34:06/01	0.111	575.985	493.3	2.1	193.0	185.5
B1630−44[a]	338.725	1.982	2011-05-18-12:25:52/07	0.190	436.511	472.6	0.3	65.2	55.4
B1634−45	338.478	0.761	2012-04-12-12:47:43/06	0.114	118.773	194.4	0.6	105.0	91.2
B1635−45[a]	338.5	0.459	2012-04-12-12:47:43/06	0.197	88.187[d]	258.3	0.1	27.7	14.9
B1636−47	337.714	−0.439	2012-07-22-07:39:34/01	0.117	517.433	580.7	0.6	98.3	63.2
B1641−45[a]	339.193	−0.195	2012-08-04-06:14:26/11	0.604	455.076	475.7	0.0	0.0	14.3
B1643−43	341.105	0.968	2011-10-11-01:35:22/10	0.067	231.671	501.1	0.8	89.3	64.1
B1648−42	342.457	0.923	2012-09-24-05:30:04/02	0.164	844.083	476.7	4.0	347.0	320.3
B1650−38	345.878	3.268	2012-04-01-15:12:32/09	0.120	305.039	206.4	0.6	146.0	127.8
B1657−45[a]	341.36	−2.18	2012-11-28-23:45:14/12	*	322.911	528.3	*	*	46.9
B1658−37	347.756	2.834	2012-04-02-14:27:04/07	0.109	2454.619	286.9	1.6	393.0	304.8
B1703−40[a]	345.758	−0.198	2012-07-24-06:31:40/08	0.401	581.021	346.0	0.0	0.2	13.4
B1706−44[a]	343.098	−2.686	2012-07-25-10:44:51/05	0.159	102.507	76.3	2.0	267.0	327.8
B1713−40	346.82	−1.73	2012-10-04-06:49:53/04	0.059	887.718	305.9	4.2	1138.7	217.4
B1714−34	352.12	2.205	2011-10-11-02:48:47/10	0.093	656.303	583.1	2.1	403.0	199.6
B1715−40[a]	347.653	−1.533	2012-09-26-07:30:59/05	0.237	189.096	386.8	0.1	10.7	14.0
B1718−32[a]	354.561	2.525	2012-08-01-13:50:07/08	0.312	477.155	125.8	0.0	4.5	29.2
B1718−35[a]	351.687	0.67	2012-12-29-20:33:59/10	0.182	280.434	492.9	2.0	176.0	131.7
B1718−36	350.934	−0.001	2012-12-29-20:33:59/09	0.084	399.184	411.2	1.1	129.0	153.0
B1719−37	350.49	−0.507	2012-08-03-08:18:01/08	0.086	236.180	99.0	2.2	466.0	322.2
B1730−37	351.577	−2.284	2012-09-30-04:28:47/12	0.097	337.596	154.3	2.1	432.0	171.5
B1734−35[a]	353.175	−2.268	2012-07-25-11:58:21/12	0.197	397.589	85.4	0.1	21.6	16.2
B1735−32	356.466	−0.491	2012-07-21-10:23:16/08	0.171	768.500	49.6	0.6	139.0	81.6
B1736−29	359.206	1.064	2012-12-14-23:03:48/10	0.190	161.443[b]	137.4	0.3	61.3	45.9
B1736−31	357.096	−0.22	2011-12-22-22:10:51/02	0.176	529.453	597.9	1.0	163.0	103.1
B1737−30	358.294	0.238	2011-12-29-21:35:52/11	0.194	606.932	152.8	0.9	281.0	226.7
B1740−31[a]	357.299	−1.148	2012-07-21-10:23:16/13	0.160	2414.631	180.0	0.5	105.0	123.2
B1742−30[a]	358.553	−0.963	2011-12-22-22:10:51/12	0.224	367.434	86.8	1.0	189.0	168.2
B1746−30	359.459	−1.244	2013-02-01-01:43:53/11	0.144	609.877	494.9	1.3	128.0	81.3
B1749−28[a]	1.54	−0.961	2012-09-27-05:18:25/10	0.429	562.564	50.4	0.0	0.3	66.1
B1756−22[a]	7.472	0.81	2011-10-12-04:24:15/09	0.193	460.979	177.8	0.2	58.8	33.2
B1758−29	1.436	−3.249	2012-07-23-13:57:57/10	0.025	1081.910	113.3	1.7	217.0	196.0
B1800−21	8.395	0.146	2011-10-12-04:24:15/08	0.117	133.689	234.2	6.9	565.8	298.5
B1800−27[a]	3.494	−2.532	2012-10-01-06:42:41/10	0.125	334.412	165.0	0.4	52.7	54.8
B1805−20	9.446	−0.4	2011-12-22-23:24:21/03	0.113	918.420	600.1	1.4	150.0	75.9
B1806−21	9.415	−0.72	2011-12-29-22:49:20/07	0.076	702.417	377.2	0.6	152.0	100.7
B1809−173	13.109	0.538	2012-12-29-23:00:17/06	0.175	1205.379	252.4	0.2	54.7	24.8
B1809−176	12.904	0.387	2011-12-31-22:59:57/01	0.085	538.340	490.3	2.3	222.0	140.5

B1813−17[a]	13.433	−0.424	2012-11-21-04:47:34/11	*	782.320	516.5	*	*	52.3
B1815−14	16.405	0.61	2011-05-09-15:10:12/08	0.158	291.490	619.4	2.0	211.0	153.1
B1817−18	13.202	−1.72	2012-07-20-14:45:40/05	0.032	309.905	436.6	1.1	149.0	143.2
B1820−11[a]	19.767	0.946	2011-12-23-01:58:46/13	0.141	279.821	428.0	1.2	101.0	91.2
B1821−11	19.809	0.741	2011-12-23-01:58:46/13	0.164	435.762	602.1	0.3	39.0	36.1
B1821−19[a]	12.279	−3.106	2012-07-23-15:11:13/03	0.142	189.338	224.6	1.7	464.0	574.8
B1822−09[a]	21.449	1.324	2012-12-03-00:34:57/12	*	769.012	16.7	*	*	385.1
B1823−11[a]	19.8	0.293	2011-12-23-01:58:46/07	0.227	2093.127	310.9	0.1	5.9	18.9
B1823−13[a]	18.001	−0.691	2012-11-21-06:00:28/05	*	101.500	231.8	*	*	23.3
B1824−10[a]	21.286	0.798	2012-12-03-00:34:57/06	*	245.759	430.9	*	*	99.0
B1826−17	14.604	−3.418	2012-09-28-11:04:43/04	0.242	307.136	216.7	0.4	57.3	31.3
B1828−11[a]	20.812	−0.478	2012-11-21-07:28:40/07	*	405.077	160.8	*	*	76.4
B1829−08	23.272	0.298	2012-12-30-00:13:40/04	0.201	647.330	301.4	0.3	84.6	55.2
B1829−10[a]	21.587	−0.597	2011-12-15-05:18:52/03	0.199	330.356	476.2	0.2	35.2	20.1
B1830−08	23.386	0.063	2012-01-01-00:13:22/01	0.026	85.289	409.1	3.5	499.0	372.9
B1831−03	27.657	2.272	2011-12-29-01:58:30/08	0.056	686.723	232.5	2.4	634.0	287.1
B1831−04	27.042	1.749	2011-12-29-01:58:30/09	0.113	290.109	80.9	2.6	114.0	390.0
B1832−06[a]	25.093	0.552	2011-10-11-07:58:09/01	0.131	305.852	465.2	0.5	56.2	48.5
B1834−04	27.167	1.13	2011-12-31-01:40:51/07	0.091	354.238	236.0	1.2	241.0	171.9
B1834−06	25.191	0.002	2011-10-11-07:58:09/02	0.064	1905.808	325.5	2.0	280.0	210.8
B1841−05	27.073	−0.941	2012-08-03-13:11:46/08	0.068	255.705	413.2	1.7	172.0	232.2
B1846−06	26.773	−2.497	2012-08-04-14:47:04/12	0.052	1451.350	160.1	1.2	133.0	215.8
J1001−5559[a]	280.691	−0.648	2012-03-26-09:49:47/10	0.181	1661.161	153.7	0.1	33.1	25.2
J1013−5934[a]	284.13	−2.596	2012-08-06-07:03:31/06	0.214	442.901	375.9	0.2	47.1	46.5
J1016−5857[a]	284.079	−1.88	2012-09-05-20:01:28/01	0.151	107.410	395.3	0.1	18.2	25.8
J1020−5921	284.719	−1.944	2012-09-05-20:01:28/07	0.043	1238.322	76.0	0.4	109.0	63.3
J1021−5601	283.041	0.935	2012-07-23-23:59:36/03	0.070	670.027	212.3	0.3	33.0	31.8
J1043−6116[a]	288.221	−2.106	2012-08-06-08:16:28/13	0.171	288.606	445.5	0.2	36.3	52.5
J1049−5833	287.628	0.649	2012-08-03-03:00:51/02	0.064	2202.325	438.1	0.6	157.0	116.4
J1054−5943	288.729	−0.1	2012-07-26-23:19:48/04	0.031	346.911	328.8	0.3	82.7	79.0
J1054−5946	288.701	−0.174	2012-07-26-23:19:48/04	0.058	228.312	254.6	0.2	36.3	12.5
J1055−6022	289.109	−0.65	2012-07-26-06:23:38/01	0.100	947.586	580.6	0.1	21.5	18.9
J1055−6028	289.133	−0.745	2012-07-26-06:23:38/01	0.033	99.665	636.8	0.7	103.0	121.8
J1056−5709	287.835	2.311	2012-08-01-07:29:33/07	0.045	676.082	436.1	0.1	21.2	22.3
J1058−5957	289.241	−0.123	2012-07-26-23:19:48/05	0.020	616.270	339.4	0.5	102.0	101.5
J1103−6025[a]	289.994	−0.294	2012-07-26-06:23:38/10	0.165	396.587	274.2	0.0	9.9	20.1
J1115−6052[a]	291.564	−0.126	2011-10-10-19:28:50/09	0.188	259.779	228.3	0.1	12.1	15.4
J1119−6127[a]	292.151	−0.537	2011-10-04-18:53:15/11	0.188	409.255	706.8	0.1	14.7	21.3
J1123−6102	292.509	0.049	2011-12-09-18:06:17/01	0.092	640.235	437.2	0.3	97.0	114.6
J1123−6259[a]	293.183	−1.783	2011-12-05-17:38:00/11	0.189	271.437	225.9	0.1	16.2	17.2
J1124−6421	293.747	−3.036	2011-12-12-15:05:41/13	0.072	479.099	296.0	0.1	24.5	26.4
J1125−5825	291.893	2.602	2011-12-27-13:47:20/07	0.128	3.102	124.9	0.4	37.2	24.8
J1130−5826	292.46	2.778	2011-10-04-20:14:39/13	0.115	162.323	262.2	0.1	16.2	23.1
J1130−5925	292.755	1.83	2011-10-11-19:50:26/01	0.061	680.984	265.3	0.1	22.7	17.8
J1138−6207[a]	294.506	−0.463	2012-01-28-13:25:24/10	0.153	117.570	518.6	0.1	12.4	16.4
J1141−6545	295.791	−3.863	2012-02-18-20:27:49/05	0.076	394.152	114.8	2.5	771.0	285.9
J1142−6230	295.11	−0.675	2012-01-28-13:25:24/01	0.096	558.382	348.9	0.2	24.1	25.7
J1144−6146	295.116	0.073	2012-01-28-13:25:24/11	0.060	987.786	75.6	0.4	56.5	30.5
J1144−6217	295.186	−0.438	2012-01-28-12:12:44/04	0.112	850.675	284.2	0.1	32.3	29.3
J1148−6415	296.177	−2.214	2012-04-05-13:33:51/06	0.038	1620.513[b]	236.0	0.1	17.2	11.8
J1159−6409	297.295	−1.865	2012-04-11-09:08:53/09	0.097	667.485	162.8	0.3	12.0	35.5
J1201−6306	297.309	−0.793	2011-12-10-15:41:16/07	0.044	592.135	678.0	0.1	26.2	23.0
J1211−6324	298.47	−0.888	2011-10-10-20:41:56/08	0.110	433.084	326.8	0.2	35.9	61.6
J1216−6410	299.096	−1.561	2012-04-13-09:24:34/09	0.021	3.540	47.4	0.0	1.4	41.5
J1220−6318	299.444	−0.652	2012-04-10-09:05:15/04	0.123	789.212	350.5	0.3	37.1	26.7
J1225−6035	299.748	2.117	2011-12-10-21:56:55/10	0.116	626.325	176.6	0.1	46.3	37.9
J1255−6131	303.466	1.348	2011-12-28-16:11:33/01	0.130	657.974	207.6	0.1	16.9	14.8
J1303−6305[a]	304.24	−0.241	2011-12-29-14:57:57/02	0.159	2306.659	349.9	0.1	25.4	26.9
J1306−6242	304.686	0.119	2011-12-22-15:34:56/01	0.074	981.911	470.6	0.1	20.2	15.5
J1307−6318	304.781	−0.497	2011-12-29-14:57:57/08	0.184	4962.527	262.7	0.2	20.7	17.2
J1309−6415	304.867	−1.462	2012-04-05-14:47:06/13	0.138	619.459	566.2	0.1	10.7	11.2
J1312−6400	305.195	−1.235	2012-04-05-14:47:06/07	0.077	2437.433	79.1	0.6	155.0	76.2

J1317−6302	305.908	−0.328	2012-04-03-18:02:10/08	0.015	261.271	677.7	1.0	125.0	146.4
J1322−6241	306.489	−0.041	2011-07-14-03:13:57/10	0.094	506.060	619.4	0.2	49.7	43.0
J1324−6302	306.638	−0.404	2011-12-08-02:26:00/13	0.105	2483.772	501.9	0.1	43.0	20.7
J1334−5839	308.52	3.749	2011-12-24-15:55:06/11	0.272	107.718	119.1	0.0	2.0	11.2
J1337−6423	307.889	−1.958	2012-01-02-01:12:28/09	0.085	9.425	259.3	0.2	19.4	16.5
J1339−6618	307.786	−3.889	2012-07-25-07:03:11/06	0.120	558.180	243.7	0.1	16.5	17.8
J1341−6023	309.035	1.889	2011-12-11-17:35:46/04	0.011	627.293	359.8	0.6	171.0	149.8
J1344−6059	309.341	1.216	2012-02-16-21:34:55/01	0.080	540.103	426.6	0.1	20.4	15.4
J1345−6115	309.414	0.928	2012-01-19-14:43:25/02	0.082	1253.080	277.3	0.4	94.1	94.5
J1347−5947	309.914	2.318	2012-01-18-19:31:16/12	0.090	609.965	291.8	0.4	293.4	92.5
J1348−6307[a]	309.353	−0.962	2012-04-10-10:18:45/10	0.137	927.769	600.4	0.2	17.8	23.3
J1349−6130[a]	309.813	0.587	2011-12-30-15:53:41/10	0.136	259.365	285.4	0.2	40.5	36.6
J1354−6249[a]	310.07	−0.832	2012-04-10-10:18:45/04	0.142	1475.989[b]	275.3	0.1	20.4	10.6
J1355−5747	311.425	4.022	2011-12-21-16:53:53/11	0.145	679.558[c]	247.4	0.1	28.5	14.8
J1355−5925[a]	311.069	2.431	2011-12-13-17:27:21/04	0.208	1213.371	359.2	0.1	15.3	11.5
J1355−6206[a]	310.332	−0.156	2011-12-30-15:53:41/02	0.125	276.602	544.1	0.2	29.8	28.9
J1357−6429	309.923	−2.514	2011-12-12-01:36:25/02	0.085	166.200	124.7	0.3	32.1	31.3
J1416−6037	313.179	0.535	2011-10-11-22:17:28/09	0.179	295.582	287.6	0.1	17.8	26.0
J1418−5945	313.706	1.287	2011-10-11-22:17:28/04	0.123	1672.596	310.4	0.1	13.9	12.5
J1425−5723	315.382	3.186	2011-12-23-16:52:20/03	0.099	353.263	45.4	0.1	34.0	24.9
J1425−5759	315.217	2.613	2012-01-19-16:45:38/08	0.118	707.867	318.9	0.0	10.5	11.6
J1425−6210[a]	313.63	−1.258	2012-01-03-02:01:35/13	0.105	501.730	426.4	0.1	20.2	19.3
J1431−5740	315.962	2.66	2011-12-23-16:52:20/07	0.102	4.111	131.3	0.2	32.4	18.7
J1433−6038	315.092	−0.197	2011-12-29-16:42:22/01	0.055	1954.443	414.4	0.2	51.8	20.7
J1434−6006	315.396	0.256	2011-12-29-16:42:22/05	0.035	306.368	334.2	0.2	55.3	29.9
J1434−6029	315.31	−0.13	2011-12-14-19:52:54/05	0.059	963.347	287.9	0.1	27.5	15.9
J1435−5954	315.577	0.391	2011-12-30-17:07:26/08	0.114	472.995	46.3	1.9	254.0	49.3
J1435−6100	315.186	−0.641	2011-12-14-19:52:54/06	0.096	9.351	114.1	0.2	14.3	20.9
J1437−6146	315.101	−1.422	2012-01-03-02:01:35/09	0.090	467.619	196.3	0.2	22.8	31.1
J1452−6036	317.296	−1.169	2012-04-05-16:00:36/07	0.021	154.992	349.8	1.4	272.0	208.3
J1453−6413	315.73	−4.43	2012-07-31-11:22:27/11	*	179.512	72.4	*	*	51.5
J1454−5846	318.272	0.391	2012-12-30-17:34:08/06	0.067	45.244	115.6	0.2	24.2	19.9
J1457−5900[a]	318.561	−0.027	2012-12-30-17:34:08/13	0.074	1498.648	160.0	0.2	24.5	22.1
J1457−5902	318.538	−0.037	2012-12-30-17:34:08/13	0.074	390.744	475.7	0.2	37.1	39.0
J1502−5653	320.186	1.505	2012-02-16-22:48:27/02	0.080	535.028	190.4	0.3	80.4	29.7
J1502−5828	319.395	0.133	2011-12-11-03:30:47/08	0.052	668.116	589.1	0.4	66.0	44.4
J1502−6128	317.921	−2.483	2012-01-02-02:25:54/03	0.099	842.103	261.2	0.3	59.8	42.5
J1509−6015	319.228	−1.815	2012-07-20-09:47:33/03	0.147	339.040	417.8	0.1	9.4	11.8
J1511−5414	322.598	3.177	2011-12-27-17:49:32/06	0.078	200.384	84.8	0.5	105.0	165.6
J1511−5835	320.289	−0.508	2012-04-10-11:32:06/08	0.096	301.511	331.4	0.3	36.8	35.0
J1512−5431	322.486	2.92	2011-12-28-18:38:14/05	0.031	2040.534	207.4	0.4	50.4	63.8
J1513−5739	321.097	0.104	2012-04-10-11:32:06/04	0.191	973.470	473.6	0.1	26.6	28.6
J1514−5925	320.284	−1.482	2012-07-24-08:26:32/02	0.101	148.797	193.1	0.2	29.3	18.8
J1529−5355	325.006	2.009	2011-10-11-23:30:49/01	0.075	891.266	300.7	0.3	38.0	38.1
J1530−5327[a]	325.328	2.347	2011-10-11-23:30:49/04	0.163	278.959	49.2	0.2	22.1	35.2
J1532−5308	325.78	2.434	2011-10-11-23:30:49/11	0.070	443.824	180.8	0.2	21.9	26.6
J1535−5450	325.194	0.757	2011-12-30-18:20:50/08	0.133	566.740	220.4	0.1	14.8	21.6
J1536−5433	325.374	0.98	2011-12-30-18:20:50/02	0.091	881.445	150.3	0.8	137.0	131.5
J1537−5153	327.088	3.035	2011-12-23-18:06:55/12	0.084	1528.128	97.5	0.0	11.0	17.0
J1538−5438	325.645	0.679	2011-12-30-18:20:50/07	0.048	276.727	135.3	0.2	34.9	26.2
J1538−5551	324.912	−0.299	2011-12-29-17:55:52/09	0.090	104.676	603.9	0.2	13.5	16.6
J1541−5535	325.424	−0.337	2011-12-29-17:55:52/03	0.064	295.864	424.1	0.2	26.6	30.7
J1543−5013	328.925	3.725	2012-01-03-17:57:10/09	0.041	644.258	222.1	0.2	28.3	28.4
J1543−5459	326.024	−0.044	2011-12-10-02:14:58/11	0.088	377.140	345.4	0.4	57.4	40.3
J1548−4927	329.956	3.9	2012-01-03-17:57:10/04	0.180	602.741	141.5	0.1	30.6	43.0
J1548−5607	325.858	−1.359	2012-04-14-12:27:49/09	0.042	170.938	315.4	0.9	119.0	110.6
J1549−5722	325.198	−2.42	2011-12-12-20:12:12/01	0.082	497.775	102.1	0.1	15.3	14.5
J1556−5358	328.117	−0.436	2012-04-12-11:34:25/10	0.102	994.686	428.4	0.3	50.6	57.9
J1601−50	330.985	1.846	2012-03-31-18:42:58/04	0.025	430.357[b]	73.6	0.4	12.9	12.2
J1602−4957	331.374	2.07	2011-12-06-20:26:28/05	0.030	410.001[b]	320.3	0.2	28.2	16.1
J1603−5657[a]	326.884	−3.309	2012-01-02-03:39:14/11	0.137	496.078	264.2	0.2	58.5	63.5
J1605−5215	330.201	0.031	2011-12-31-18:06:48/07	0.045	1013.617	535.3	0.2	40.6	24.9

J1617−5055	332.499	−0.275	2012-11-30-00:36:14/10	*	69.421	470.6	*	*	12.9
J1610−5006	332.278	1.05	2012-04-11-12:49:10/05	0.128	481.125	417.1	0.7	74.1	75.0
J1611−4949	332.59	1.14	2012-07-24-09:40:05/04	0.084	666.436	556.2	0.4	80.7	60.8
J1611−5209	330.92	−0.48	2012-11-25-21:17:32/09	*	182.495	126.9	*	*	20.9
J1612−55	328.99	−2.78	2012-11-24-21:43:39/02	*	846.905	287.2	*	*	12.9
J1613−5211	331.197	−0.784	2012-11-30-00:36:14/06	*	457.512	351.8	*	*	19.9
J1615−5444[a]	329.578	−2.768	2012-02-20-00:08:17/01	0.188	360.958	311.1	0.1	25.4	20.0
J1616−5109	332.23	−0.34	2012-11-25-21:17:32/11	*	1219.592	1189.1	*	*	38.7
J1616−5208	331.524	−1.038	2012-11-30-00:36:14/05	*	1025.847	475.7	*	*	17.5
J1618−4723[a]	335.037	2.184	2011-10-12-00:44:05/03	0.174	203.554	134.8	0.2	29.6	21.6
J1621−5243[a]	331.718	−2.045	2011-12-12-04:03:41/08	0.144	371.922	362.9	0.1	11.9	15.4
J1622−4802[a]	335.139	1.17	2011-12-22-00:16:31/05	0.174	265.072	367.9	0.2	25.0	19.4
J1624−4613	336.616	2.265	2012-04-02-13:13:43/02	0.057	871.014	225.0	0.3	22.3	11.1
J1626−4537	337.346	2.367	2011-12-23-19:20:21/05	0.094	370.142	235.2	0.7	127.0	77.4
J1628−4804[a]	335.766	0.461	2011-12-22-19:44:15/02	0.209	865.980	954.0	0.1	15.7	17.4
J1630−4719	336.497	0.787	2011-12-29-19:09:15/03	0.101	559.076	483.3	0.3	67.4	51.7
J1632−4621	337.527	1.1	2012-04-12-12:47:43/02	0.200	1709.190	567.7	0.1	41.4	21.9
J1632−4757	336.296	0.08	2011-12-22-19:44:15/07	0.088	228.569	574.9	0.2	21.1	19.1
J1632−4818	336.08	−0.209	2012-08-05-04:55:47/10	0.104	813.714	783.8	0.2	26.6	18.1
J1635−4944	335.391	−1.57	2011-12-13-04:39:04/11	0.106	671.974	478.1	0.2	25.2	15.3
J1636−4803[a]	336.7	−0.515	2011-12-29-19:09:15/13	0.129	1204.660	506.9	0.5	67.7	44.4
J1636−4933	335.641	−1.561	2011-12-13-04:39:04/11	0.146	430.369	538.1	0.2	20.8	15.7
J1637−4642	337.788	0.312	2012-07-22-07:39:34/10	0.039	154.050	420.1	0.7	57.3	44.7
J1637−4721	337.304	−0.117	2012-04-14-13:41:06/03	0.029	1165.745	440.2	0.4	98.7	42.5
J1637−4816	336.71	−0.831	2012-04-14-13:41:06/08	0.160	837.371	741.0	0.2	19.0	17.8
J1638−42	341.019	2.91	2012-01-19-19:12:22/05	0.105	510.928	406.5	*	*	20.5
J1638−4608[a]	338.343	0.544	2012-04-12-12:47:43/06	0.152	278.157	423.3	0.1	20.0	18.3
J1640−4648	338.114	−0.215	2012-08-04-06:14:26/04	0.116	178.352	470.7	0.1	14.4	12.4
J1640−4951	335.829	−2.218	2012-08-05-13:18:12/07	0.086	739.098	409.2	0.1	25.6	22.2
J1644−4657	338.435	−0.808	2012-08-04-06:14:26/05	0.098	125.962	722.4	0.4	17.5	28.5
J1646−4308	341.603	1.374	2012-07-24-10:53:22/04	0.115	840.697	448.9	0.2	10.5	13.0
J1648−4458	340.349	0.009	2011-12-31-19:20:07/02	0.083	629.632	928.8	0.4	48.0	30.4
J1649−4349	341.36	0.596	2011-10-11-01:35:22/04	0.118	870.726	403.9	0.4	70.1	19.1
J1649−4653[a]	339.019	−1.38	2012-12-09-21:55:05/04	*	557.040	332.5	*	*	18.2
J1649−4729[a]	338.54	−1.76	2012-12-09-21:55:05/01	*	297.697	554.4	*	*	13.1
J1650−4126	343.291	1.997	2012-09-24-04:17:22/01	0.103	308.918	252.7	0.2	37.6	31.0
J1650−4341	341.623	0.485	2011-12-31-19:20:07/11	0.010	309.396	674.3	0.3	27.5	16.1
J1650−4502	340.559	−0.351	2011-12-31-19:20:07/07	0.098	380.877	319.1	0.2	50.8	53.2
J1650−4921[a]	337.25	−3.11	2012-11-25-22:40:38/13	*	156.401	227.5	*	*	13.3
J1651−4519[a]	340.506	−0.719	2012-11-28-23:45:14/10	*	517.447	544.2	*	*	13.8
J1652−4406	341.564	−0.088	2011-12-23-04:46:35/09	0.093	3853.557[b]	853.9	*	*	16.3
J1653−4249	342.636	0.629	2012-09-24-05:30:04/01	0.034	612.560	419.3	1.2	284.0	183.2
J1655−3844	346.046	2.906	2012-04-01-15:12:32/02	0.034	1193.429	341.2	0.2	26.5	34.2
J1656−3621	348.013	4.245	2012-04-02-14:27:04/10	0.149	730.133	223.8	0.1	15.6	14.4
J1657−4432	341.743	−1.006	2012-11-30-01:50:13/07	*	609.610	377.2	*	*	34.9
J1659−4316[a]	343	−0.547	2012-11-30-01:50:13/10	*	474.380	639.7	*	*	17.2
J1659−4439	341.881	−1.361	2012-11-30-01:50:13/06	*	353.293	532.2	*	*	38.8
J1700−3611	348.679	3.672	2012-04-02-14:27:04/11	0.066	1494.091	227.7	0.7	168.8	99.2
J1700−3919	346.161	1.826	2011-12-10-04:41:41/07	0.074	560.505	355.8	0.2	36.0	32.7
J1700−4012	345.488	1.234	2011-12-30-20:47:14/02	0.067	283.792	389.2	0.1	14.0	16.6
J1700−4422	342.23	−1.36	2012-07-26-10:07:30/05	0.047	755.534	404.5	0.4	49.6	20.6
J1702−3932	346.203	1.401	2011-10-12-01:57:23/05	0.087	390.328	534.2	0.2	35.2	29.4
J1702−4428	342.378	−1.701	2011-12-12-05:16:53/12	0.046	2123.520	403.1	0.3	50.2	50.9
J1703−4442[a]	342.23	−1.92	2012-11-30-01:50:13/12	*	1747.310	275.7	*	*	14.5
J1705−3936	346.548	0.845	2012-07-21-09:08:53/12	0.016	854.487	598.0	0.3	56.1	33.1
J1705−3950	346.341	0.718	2012-08-04-07:27:37/09	0.035	318.965	205.8	1.4	243.0	118.8
J1705−4331	343.428	−1.515	2012-09-24-06:43:27/08	0.049	222.561	186.6	0.4	63.9	47.8
J1706−3839	347.387	1.301	2012-04-12-14:00:55/07	0.051	586.289	621.6	0.2	27.1	20.9
J1707−4341	343.521	−1.915	2012-07-25-10:44:51/02	0.066	890.596	393.2	0.4	105.0	68.1
J1708−3426	351.083	3.407	2012-01-19-20:25:43/10	0.166	692.110	192.1	0.4	55.6	73.3
J1708−3827	347.776	1.123	2012-04-14-14:54:34/09	0.048	1225.784	785.8	0.4	56.9	38.4
J1709−3841	347.709	0.832	2012-04-12-14:00:55/13	0.051	586.990	361.7	0.3	41.5	33.2

J1711−3826	348.197	0.591	2012-07-22-08:53:05/02	0.076	465.367	382.1	0.1	16.9	16.6
J1713−3844	348.101	0.207	2012-07-22-08:53:05/08	0.129	800.094[b]	538.2	0.1	30.0	15.3
J1715−3859	348.194	−0.348	2012-09-26-07:30:59/08	0.540	928.101	817.9	0.4	44.0	39.9
J1715−3903	348.101	−0.321	2012-09-26-07:30:59/08	0.033	278.496	315.4	0.0	68.7	47.5
J1715−4034[a]	346.912	−1.277	2012-10-04-06:49:53/03	0.201	2072.153	259.6	0.2	32.9	25.2
J1716−4005[a]	347.418	−1.155	2012-09-26-07:30:59/06	0.227	311.814	433.5	0.1	7.6	14.9
J1716−4111	346.53	−1.79	2012-11-26-01:06:38/06	*	1036.079	244.2	*	*	24.4
J1717−3737	349.491	0.182	2012-07-22-08:53:05/12	0.072	682.419	526.5	0.5	81.1	46.6
J1717−3953	347.655	−1.157	2012-09-26-07:30:59/06	0.010	1085.515	434.5	1.3	68.5	47.6
J1717−4043[a]	347.02	−1.7	2012-11-26-01:06:38/12	*	397.864	454.9	*	*	23.9
J1718−3825[a]	348.951	−0.432	2011-07-13-08:46:45/13	0.130	74.675	247.8	0.5	65.1	37.0
J1719−4006	347.65	−1.53	2012-11-25-01:22:55/08	*	189.096	387.4	*	*	126.1
J1723−3659[a]	350.682	−0.409	2012-08-03-08:18:01/08	0.212	202.726	247.4	0.2	21.4	12.5
J1725−4043	347.874	−2.92	2012-10-02-05:59:18/01	0.142	1465.075	195.5	0.1	22.8	21.9
J1726−3635	351.442	−0.802	2012-12-29-20:33:59/07	0.049	287.432	538.1	0.3	51.1	27.6
J1726−4006	348.481	−2.711	2012-10-02-05:59:18/04	0.118	882.779	272.2	0.1	22.5	23.2
J1727−2946	357.14	2.92	2011-10-12-03:10:49/04	0.134	27.086	61.3	0.1	12.4	15.1
J1728−3733	350.842	−1.656	2012-09-30-04:28:47/01	0.118	615.538	282.4	0.1	28.5	19.5
J1728−4028	348.375	−3.218	2012-10-01-05:23:50/11	0.023	866.344	228.7	0.9	67.9	71.8
J1730−2900	358.123	2.819	2011-12-07-03:42:23/05	0.074	1538.442	294.2	0.1	26.5	22.1
J1732−3729	351.29	−2.21	2012-11-30:03:03:36/04	*	2184.009	293.4	*	*	56.5
J1733−3322[a]	354.917	−0.238	2012-09-30-07:17:21/03	0.191	1245.923	523.3	0.1	24.6	14.6
J1736−3511[a]	353.61	−1.6	2012-12-13-23:21:32/10	*	502.803	101.0	*	*	11.6
J1737−3137	356.744	0.145	2011-12-29-21:35:52/09	0.073	450.488	487.8	0.6	88.1	40.7
J1738−2647	0.94	2.544	2011-06-30-16:47:36/06	0.048	349.591	180.9	0.4	69.1	62.9
J1739−3023	358.086	0.336	2012-07-21-10:23:16/11	0.064	114.372	169.7	0.8	95.6	38.6
J1739−3049	357.68	0.152	2011-12-29-21:35:52/04	0.085	239.318	572.4	0.3	39.3	22.2
J1739−3159	356.739	−0.547	2012-07-21-10:23:16/08	0.125	877.562	357.8	0.5	49.8	39.4
J1740−2540	2.212	2.633	2012-04-10-16:25:21/03	0.059	1692.660	336.5	0.1	33.3	22.5
J1740−3052	357.811	−0.132	2012-07-21-10:23:16/05	0.030	570.380	738.0	0.7	177.0	83.2
J1741−2719	0.907	1.604	2011-06-30-16:47:36/04	0.076	346.797	361.8	0.1	24.2	20.6
J1741−2733[a]	0.636	1.582	2012-01-19-21:39:10/08	0.098	892.943	138.5	0.7	85.2	69.8
J1741−2945	358.798	0.38	2012-12-14-23:03:48/03	0.117	223.560	299.7	0.3	44.2	13.0
J1741−3016	358.346	0.13	2011-12-22-22:10:51/11	0.105	1893.761	384.6	1.3	252.0	68.8
J1743−2442	3.333	2.64	2012-04-13-16:45:09/06	0.113	1242.510	252.0	0.1	9.6	15.4
J1744−2335[a]	4.463	2.937	2012-12-09-23:10:30/04	*	1683.508	87.1	*	*	22.4
J1744−3130	357.641	−1.059	2011-12-22-22:10:51/13	0.148	1066.067	183.6	0.2	51.6	36.5
J1745−2229	5.47	3.422	2012-12-09-23:10:34/11	*	1160.594	295.1	*	*	17.9
J1747−2647	2.054	0.758	2011-12-31-21:46:41/07	0.118	500.255	566.5	0.8	64.7	76.1
J1748−2444	3.955	−0.075	2012-12-29-21:47:09/01	0.113	442.837	201.6	0.2	57.8	32.1
J1748−3009	359.272	−1.147	2012-11-30-04:17:16/08	*	19.367[e]	418.6	*	*	11.7
J1749−2629	2.505	0.593	2011-12-31-21:46:41/06	0.059	1335.391	397.5	0.6	103.0	60.6
J1750−3157	357.98	−2.52	2012-11-25-02:37:28/04	*	910.382	208.9	*	*	62.9
J1751−2516	3.852	0.692	2012-12-29-21:47:09/13	0.064	394.834	554.2	0.2	18.4	16.8
J1751−2857	0.646	−1.124	2012-12-14-00:34:43/05	*	3.915	43.0	*	*	16.0
J1753−1914	9.251	3.412	2012-07-22-11:20:16/11	0.142	62.955	101.8	0.0	2.8	14.4
J1755−2025	8.48	2.416	2012-04-14-17:21:47/03	0.099	322.232	362.2	0.1	26.5	25.8
J1755−2521[a]	4.255	−0.15	2012-07-26-12:48:29/02	0.120	1176.005	256.5	0.3	104.0	11.9
J1758−1931	9.544	2.353	2012-04-02-22:08:42/09	0.092	692.557	196.4	0.2	38.9	18.1
J1758−2846[a]	1.556	−2.294	2012-07-20-13:32:01/01	0.135	766.706	60.3	0.1	36.8	17.8
J1759−1903	10.142	2.26	2012-02-16-01:37:19/13	0.076	731.512	464.1	0.1	15.1	18.2
J1759−1940	9.634	1.901	2012-08-02-14:26:50/06	0.074	254.720	301.5	0.7	78.4	95.4
J1759−1956	9.366	1.845	2012-02-16-01:37:19/12	0.100	2844.465	207.2	0.2	59.2	37.2
J1759−2922	1.202	−2.887	2012-07-23-13:57:57/04	0.088	574.402	80.3	0.4	94.0	77.7
J1800−2114	8.306	1.073	2011-10-12-04:24:15/01	0.005	1799.266	628.4	0.3	46.2	29.6
J1801−1855	10.447	1.978	2012-02-16-01:37:19/07	0.082	2550.507	458.6	0.3	86.1	44.3
J1801−1909	10.295	1.781	2012-08-04-09:54:39/05	0.091	1108.727	265.2	0.3	56.1	31.0
J1802−2124	8.382	0.611	2011-12-30-23:14:07/02	0.165	12.652	148.8	0.2	36.8	17.0
J1803−1616	13.02	2.827	2012-04-13-17:58:32/13	0.123	536.596	387.7	0.1	10.8	13.0
J1803−1857	10.73	1.428	2012-02-16-01:37:19/02	0.083	2864.416	368.6	0.3	98.3	33.1
J1805−1504[a]	14.246	3.093	2012-04-10-17:38:53/10	0.131	1181.266	223.8	1.8	101.1	130.8
J1806−2125	8.843	−0.261	2012-07-21-11:36:47/12	0.136	481.833	750.5	0.4	49.5	15.8

J1808−1517	14.472	2.239	2012-04-10-17:38:53/02	0.139	544.548	208.4	0.1	21.4	13.4
J1808−1726	12.599	1.188	2011-07-05-13:09:31/08	0.094	241.033	522.6	0.2	11.3	14.5
J1809−1429[a]	15.306	2.393	2012-09-28-09:51:42/07	0.169	895.287	402.4	0.1	41.3	31.1
J1810−1441	15.272	2.035	2012-09-28-09:51:42/02	0.077	217.214	303.9	0.2	19.6	14.8
J1810−1820	12.604	0.289	2012-12-29-23:00:17/09	0.070	153.716	451.5	0.5	48.9	32.6
J1811−1049	18.712	3.83	2012-04-01-18:52:53/05	0.111	2623.890	251.7	0.2	5.3	18.6
J1811−1736	12.821	0.435	2011-12-31-22:59:57/01	0.046	104.148	475.2	1.2	76.7	40.5
J1811−2405	7.073	−2.559	2012-08-05-14:33:10/04	0.070	2.661	60.8	0.3	46.2	24.9
J1812−2102	9.859	−1.303	2011-12-22-23:24:21/08	0.111	1223.366	544.2	0.7	114.0	60.0
J1813−2113[a]	9.853	−1.656	2012-07-21-15:18:42/02	0.164	426.467	463.3	0.2	28.4	21.7
J1814−1649[a]	13.82	0.245	2011-10-11-06:44:35/10	0.209	957.466	766.1	0.1	19.2	13.8
J1815−1738[a]	13.18	−0.27	2012-11-25-06:09:30/09	*	198.462	728.1	*	*	13.8
J1818−1116	19.144	2.068	2012-07-22-12:33:52/04	0.012	544.801	419.5	0.5	75.2	38.8
J1819−0925	20.935	2.633	2012-04-02-18:07:28/01	0.062	852.054	372.7	0.6	135.0	103.3
J1819−1008	20.287	2.337	2012-04-02-18:07:28/09	0.131	301.490	407.8	0.1	22.2	19.6
J1819−1114	19.291	1.857	2011-12-24-00:13:43/02	0.027	294.161	314.0	1.0	49.9	56.7
J1822−0848	21.828	2.262	2012-04-12-17:41:06/13	0.055	2504.459	185.5	0.0	8.6	66.9
J1823−1126[a]	19.568	0.935	2011-12-31-00:27:33/12	0.149	1846.555	597.7	0.2	40.9	22.3
J1824−1159[a]	19.253	0.324	2011-12-23-01:58:46/01	0.165	362.494	468.7	0.2	35.4	20.0
J1826−1334	18	−0.69	2012-11-25-07:22:18/11	*	101.500	231.2	*	*	151.3
J1827−0750	23.176	1.803	2012-07-23-11:27:36/03	0.092	270.502	371.4	1.8	297.0	167.5
J1827−0934	21.724	0.841	2011-07-05-14:23:23/10	0.028	512.550	260.4	0.3	39.3	43.8
J1828−0611[a]	24.78	2.279	2012-08-04-12:20:54/04	0.086	269.415	365.0	0.8	140.0	111.4
J1828−1101	20.495	0.042	2012-10-01-09:10:12/12	0.173	72.058	604.4	0.6	44.4	24.6
J1828−1336	18.25	−1.24	2012-11-25-07:22:18/04	*	860.329	483.8	*	*	39.9
J1829−0734	23.647	1.478	2012-12-15-02:43:57/03	0.063	318.402	318.2	0.4	81.1	34.2
J1830−1135[a]	20.193	−0.59	2012-10-01-09:10:12/01	0.211	6221.630	284.2	0.1	40.3	20.9
J1831−0823	23.211	0.548	2012-01-01-00:13:22/04	0.115	612.132	241.4	0.5	107.0	60.4
J1831−1223	19.618	−1.217	2012-10-01-09:10:12/10	0.050	2857.928	347.0	1.1	157.0	112.4
J1831−1329[a]	18.72	−1.88	2012-11-25-07:22:18/09	*	1082.842[b]	344.8	*	*	32.7
J1832−0644[a]	24.806	1.07	2011-10-11-07:58:09/05	0.196	744.308	554.1	0.1	16.8	16.8
J1833−0556	25.623	1.232	2012-04-02-19:20:27/08	0.077	1521.555	451.2	0.1	19.0	15.7
J1833−0559	25.514	1.321	2012-04-14-19:48:16/09	0.102	483.467	344.9	0.4	32.1	26.1
J1834−0602[a]	25.64	0.965	2011-10-11-07:58:09/13	0.125	487.914	444.6	0.4	53.7	34.7
J1834−0731	24.288	0.366	2012-12-30-00:13:40/12	0.125	513.004	291.8	0.4	50.4	37.4
J1834−1202[a]	20.287	−1.743	2012-10-01-09:10:12/09	0.153	610.257	334.8	0.2	17.5	25.8
J1835−0522	26.296	1.164	2011-12-31-01:40:51/04	0.099	1087.746	447.4	0.1	31.6	19.9
J1836−1324	19.348	−2.91	2012-07-22-15:27:14/03	0.117	178.756	158.7	0.0	14.2	18.2
J1838−0453	27.07	0.709	2011-12-31-01:40:51/02	0.098	380.870	616.7	0.2	36.0	25.5
J1838−0549	26.295	0.183	2012-08-03-13:11:46/12	0.114	235.313	277.2	0.1	23.9	17.8
J1839−0436	27.407	0.654	2011-12-31-01:40:51/08	0.075	149.461	290.8	0.2	22.8	23.4
J1839−0643	25.547	−0.35	2012-07-21-14:03:32/11	0.122	449.550	494.9	0.7	86.9	52.2
J1839−0905[a]	23.533	−1.591	2012-09-27-10:47:54/07	0.085	418.977	343.0	0.1	17.9	18.0
J1841−0157	30.099	1.216	2011-10-11-09:11:02/02	0.061	663.324	475.6	0.7	123.0	156.5
J1841−0524	27.024	−0.333	2012-07-21-14:03:32/13	0.109	445.824	289.7	0.1	17.6	11.3
J1842−0612	26.413	−0.898	2012-08-03-13:11:46/02	0.131	564.476	474.3	0.2	23.1	23.5
J1842−0905	23.81	−2.136	2012-09-27-10:47:54/08	0.153	344.647	345.8	0.2	45.8	32.9
J1843−0211[a]	30.084	0.768	2011-10-11-09:11:02/09	0.197	2027.536	433.8	0.1	33.0	17.0
J1843−0702	25.741	−1.426	2012-08-04-13:34:30/12	0.116	191.615	229.5	0.1	15.1	13.1
J1843−0744	25.092	−1.68	2012-10-02-09:50:46/11	0.068	475.395	318.8	0.1	27.2	27.4
J1845−0545	27.15	−1.337	2011-12-23-03:12:09/05	0.059	1092.360	309.8	0.4	101.0	57.0
J1845−0635	26.348	−1.603	2012-07-21-14:03:32/09	0.052	340.528	415.9	0.3	29.7	53.4
J1845−0743	25.429	−2.304	2012-10-02-09:50:46/04	0.170	104.695	281.3	0.6	94.1	76.5
J1846−0749[a]	25.386	−2.431	2012-08-04-13:34:30/04	0.179	350.110	389.9	0.1	15.5	22.0
J1846−07492	25.366	−2.386	2012-08-04-13:34:30/04	0.151	861.380	184.6	0.1	13.1	27.6
J1847−0438[a]	28.371	−1.268	2011-12-23-03:12:09/13	0.204	957.996	238.6	0.1	15.2	18.9
J1847−0605	27.048	−1.867	2011-12-30-01:16:00/03	0.106	778.166	202.4	0.5	115.0	72.8
J1848−0511	27.945	−1.659	2011-12-23-03:12:09/07	0.112	1637.125	409.6	0.2	27.5	29.9
J1848−0601	27.221	−2.054	2011-12-23-03:12:09/03	0.136	225.005	494.9	0.1	3.1	15.7
J1849−0614	27.182	−2.469	2012-07-23-12:40:40/03	0.124	953.401	117.1	0.3	73.7	61.5
J1852−0635	27.225	−3.34	2012-08-04-14:47:04/07	0.050	524.155	175.1	5.2	379.0	395.4
J1856−0526	28.636	−3.575	2012-04-11-21:49:28/02	0.112	370.483	125.1	0.2	7.0	29.4

[a] Pulsar was detected with a smaller offset in the portion of the survey processed by Ng et al. (2015).
[b] Spin period detected at the second harmonic, i.e. half of the fundamental spin period.
[c] Spin period detected at the third harmonic, i.e. one third of the fundamental spin period.
[d] Spin period detected at the sixth harmonic, i.e. one sixth of the fundamental spin period.
[e] Spin period detected at the half harmonic, i.e. double the fundamental spin period.

Erklärung

Ich versichere, dass ich die von mir vorgelegte Dissertation selbständig angefertigt, die benutzten Quellen und Hilfsmittel vollständig angegeben und die Stellen der Arbeit- einschlielich Tabellen, Karten und Abbildungen –, die anderen Werken im Wortlaut oder dem Sinn nach entnommen sind, in jedem Einzelfall als Entlehnung kenntlich gemacht habe; dass diese Dissertation noch keiner anderen Fakultät oder Universität zur Prfung vorgelegen hat; dass sie noch nicht verffentlicht worden ist sowie, da ich eine solche Veröffentlichung vor Abschluss des Promotionsverfahrens nicht vornehmen werde. Die Bestimmungen dieser Promotionsordnung sind mir bekannt. Die von mir vorgelegte Dissertation ist von Prof. Dr. Michael Kramer betreut worden.

Unterschift:

_____

Datum:

_____

Publications accounting for major parts of the thesis

Refereed

- **Cameron A. D.**, Barr E. D., Champion D. J., Kramer M., Zhu W. W., *'An investigation of pulsar searching techniques with the fast folding algorithm'*, Monthly Notices of the Royal Astronomical Society, 2017, Volume 468, Issue 2, p.1994-2010

Submitted

- **Cameron A. D.**, Champion D. J., Kramer M., Bailes M., Barr E. D., Bassa C. G., Bhandari S., Bhat N. D. R., Burgay M., Burke-Spolaor S., Eatough R. P., Flynn C. M. L., Freire P. C. C., Jameson A., Johnston S., Karuppusamy R., Keith M. J., Levin ,L., Lorimer D. R., Lyne A. G., McLaughlin M. A., Ng C., Petroff E., Possenti A., Ridolfi A., Stappers B. W., van Straten W., Tauris T. M., Tiburzi C., Wex N.,
  'The High Time Resolution Universe Pulsar Survey - XIII. PSR J1757−1854, the most accelerated binary pulsar',
  submitted to the Monthly Notices of the Royal Astronomical Society, 2017

- **Cameron A. D.**, on behalf of the HTRU Collaboration and additional collaborators,
  'The Discovery of the Most Accelerated Binary Pulsar',
  submitted to the Proceedings of the International Astronomical Union, 2017, Volume 337

Publication History

Refereed

- **Cameron A. D.**, Barr E. D., Champion D. J., Kramer M., Zhu W. W.,
  'An investigation of pulsar searching techniques with the fast folding algorithm',
  Monthly Notices of the Royal Astronomical Society, 2017, Volume 468, Issue 2, p.1994-2010

- **Cameron A. D.**, Keith M., Hobbs G., Norris R. P., Mao M. Y., Middelberg E.,
  'Are the infrared-faint radio sources pulsars?',
  Monthly Notices of the Royal Astronomical Society, 2017, Volume 415, Issue 1, pp.845-848

Submitted

- **Cameron A. D.**, Champion D. J., Kramer M., Bailes M., Barr E. D., Bassa C. G., Bhandari S., Bhat N. D. R., Burgay M., Burke-Spolaor S., Eatough R. P., Flynn C. M. L., Freire P. C. C., Jameson A., Johnston S., Karuppusamy R., Keith M. J., Levin ,L., Lorimer D. R., Lyne A. G., McLaughlin M. A., Ng C., Petroff E., Possenti A., Ridolfi A., Stappers B. W., van Straten W., Tauris T. M., Tiburzi C., Wex N.,
  'The High Time Resolution Universe Pulsar Survey - XIII. PSR J1757−1854, the most accelerated binary pulsar',
  submitted to the Monthly Notices of the Royal Astronomical Society, 2017

- **Cameron A. D.**, on behalf of the HTRU Collaboration and additional collaborators,
  'The Discovery of the Most Accelerated Binary Pulsar',
  submitted to the Proceedings of the International Astronomical Union, 2017, Volume 337

- Spiewak R., Bailes M., Barr E. D., Bhat N. D. R., Burgay M., **Cameron A. D.**, Champion D. J., Flynn C. M. L., Jameson A., Johnston S., Keith M. J, Kramer M., Kulkarni S. R., Levin L., Lyne A. G., Morello V., Ng C., Possenti A., Ravi V., Stappers B. W., van Straten W., Tiburzi C.,
  'PSR J2322−2650 - A low-luminosity millisecond pulsar with a planetary-mass companion',
  submitted to the Monthly Notices of the Royal Astronomical Society, 2017

- Ng C., Kruckow M. U., Tauris T. M., Lyne A. G., Freire P. C. C., Ridolfi A., Caiazzo I., Heyl J., Stappers B., **Cameron A. D.**, Champion D. J., Kramer M.,

'PSR J1755−2550: A young radio pulsar with a massive compact companion', to be submitted to the Monthly Notices of the Royal Astronomical Society